

# **Spectral function at high energy and momentum from (e,e'p) experiment**

Habilitationsschrift

zur Erlangung der Venia docendi  
vorgelegt der Philosophisch-Naturwissenschaftlichen Fakultät  
der Universität Basel

von  
Daniela Rohe  
aus Koblenz

2004



# Contents

|          |   |           |
|----------|---|-----------|
| <b>1</b> | <b>Introduction</b>   | <b>1</b>  |
| 1.1      | Indirect evidence for Short–Range Correlations . . . . .                            | 1         |
| 1.2      | Theoretical framework . . . . .   | 10        |
| 1.2.1    | The $(e,e'p)$ –reaction . . . . .   | 10        |
| 1.2.2    | Fermi gas model and Independent Particle Shell Model                                | 12        |
| 1.2.3    | Hartree–Fock approximation . . . . .  | 15        |
| 1.2.4    | Brückner–Bethe–Goldstone approach . . . . .   | 17        |
| 1.2.5    | Green’s function approach for finite nuclei . . . . .                               | 19        |
| 1.2.6    | Self–consistent Green’s function for nuclear matter at finite temperature . . . . . | 25        |
| 1.2.7    | Correlated Basis Function theory for nuclear matter and finite nuclei . . . . .     | 26        |
| 1.2.8    | Conclusions . . . . .   | 30        |
| 1.3      | Occupation numbers . . . . .  | 33        |
| 1.3.1    | $n^{occ}$ from theory . . . . .   | 33        |
| 1.3.2    | $n^{occ}$ from experiment . . . . .   | 35        |
| 1.4      | Different approaches to search for SRC . . . . .                                    | 36        |
| 1.5      | Design of the present experiment . . . . .  | 39        |
| 1.5.1    | Kinematics . . . . .  | 41        |
| <b>2</b> | <b>Experimental Setup</b>   | <b>43</b> |
| 2.1      | Electron accelerator . . . . .  | 43        |
| 2.2      | Hall C beam line and instrumentation . . . . .                                      | 44        |
| 2.2.1    | Beam Position Monitor . . . . .   | 45        |
| 2.2.2    | Beam Current Monitor . . . . .  | 46        |
| 2.2.3    | Beam Raster . . . . .   | 47        |
| 2.2.4    | Beam energy measurement . . . . .   | 48        |
| 2.3      | Targets . . . . .   | 49        |
| 2.3.1    | Solid targets . . . . .   | 50        |
| 2.3.2    | Cryo targets . . . . .  | 51        |
| 2.4      | Spectrometers . . . . .   | 52        |

|          |   |            |
|----------|---|------------|
| 2.4.1    | High Momentum Spectrometer . . . . .                    | 53         |
| 2.4.2    | Short Orbit Spectrometer . . . . .                      | 53         |
| 2.4.3    | Detector package . . . . .                              | 54         |
| 2.4.4    | Trigger logic and Data Acquisition . . . . .            | 57         |
| 2.4.5    | Dead time . . . . .                                     | 59         |
| <b>3</b> | <b>Basics of the analysis</b>                           | <b>62</b>  |
| 3.1      | Hall C analysis code . . . . .                          | 62         |
| 3.1.1    | Tracking algorithm . . . . .                            | 63         |
| 3.1.2    | Reconstruction of target quantities . . . . .           | 66         |
| 3.1.3    | Optics check . . . . .                                  | 68         |
| 3.2      | Particle Identification . . . . .                       | 70         |
| 3.2.1    | Blocking correction . . . . .                           | 72         |
| 3.3      | Experimental yield . . . . .                            | 74         |
| <b>4</b> | <b>The Monte Carlo Simulation</b>                       | <b>75</b>  |
| 4.1      | Basic structure of SIMC . . . . .                       | 75         |
| 4.1.1    | The cross section . . . . .                             | 76         |
| 4.1.2    | Models of the spectral function and its implementation  | 79         |
| 4.1.3    | Radiative corrections . . . . .                         | 81         |
| 4.1.4    | Energy loss and multiple scattering . . . . .           | 86         |
| 4.1.5    | Coulomb corrections . . . . .                           | 87         |
| <b>5</b> | <b>Correction to the tracking efficiency</b>            | <b>91</b>  |
| 5.1      | Idea and method . . . . .                               | 91         |
| 5.2      | Inelastic cross section . . . . .                       | 92         |
| <b>6</b> | <b><math>H(e,e'p)</math> analysis</b>                   | <b>96</b>  |
| 6.1      | Proton transmission . . . . .                           | 96         |
| 6.2      | Efficiency of the $\beta$ -cut . . . . .                | 99         |
| 6.3      | Determination of the spectrometer offsets . . . . .     | 101        |
| 6.4      | Comparison to Monte Carlo simulation . . . . .          | 107        |
| 6.4.1    | Experimental resolution in $E_m$ and $p_m$ . . . . .    | 114        |
| 6.5      | Penetration of protons through the collimator . . . . . | 115        |
| <b>7</b> | <b>Single-particle region</b>                           | <b>118</b> |
| 7.1      | Comparison with Monte Carlo simulation . . . . .        | 118        |
| 7.2      | Nuclear transparency . . . . .                          | 120        |
| 7.2.1    | Discussion of the results . . . . .                     | 121        |

|   |            |
|---|------------|
| <b>8 Analysis of the production runs</b>  | <b>127</b> |
| 8.1 Extraction of the spectral function . . . . .   | 127        |
| 8.1.1 Phasespace–Analysis . . . . .   | 128        |
| 8.1.2 Yield–Analysis . . . . .  | 129        |
| 8.2 Model and analysis dependence of the result . . . . .                                       | 133        |
| 8.2.1 Sensitivity to kinematical offsets . . . . .  | 133        |
| 8.2.2 Check of the $p_m$ –binning . . . . .   | 134        |
| 8.2.3 Dependence on Coulomb corrections . . . . .   | 134        |
| 8.2.4 Sensitivity to radiative corrections . . . . .  | 135        |
| 8.2.5 Choice of the off–shell cross section . . . . .   | 136        |
| 8.3 Results for $^{12}\text{C}$ . . . . .   | 139        |
| 8.3.1 Systematic uncertainties . . . . .  | 143        |
| 8.4 Comparison with theory . . . . .  | 144        |
| 8.5 Results for $^{27}\text{Al}$ , $^{56}\text{Fe}$ and $^{197}\text{Au}$ . . . . .             | 150        |
| 8.6 Rescattering contribution . . . . .   | 155        |
| 8.6.1 Framework of the rescattering calculation . . . . .                                       | 156        |
| 8.6.2 Results and comparison with experiment . . . . .  | 160        |
| 8.6.3 Discussion of possible multi–step processes . . . . .                                     | 163        |
| 8.7 The resonance region . . . . .  | 165        |
| 8.7.1 Formalism for pion–electroproduction . . . . .  | 166        |
| 8.7.2 The MAID–model . . . . .  | 169        |
| 8.7.3 Comparison to experimental data . . . . .   | 172        |
| 8.7.4 Separation of resonance and correlated region . . . . .                                   | 177        |
| <b>9 Summary</b>  | <b>180</b> |
| <b>A The off–shell cross sections <math>\sigma_{cc1b}</math> and <math>\sigma_{cc1c}</math></b> | <b>183</b> |

# 1 Introduction

The Nuclear Shell Model was invented in its original form by Goeppert-Mayer and Jensen in 1949. Its success in predicting the ground-state properties like the angular momentum, the parity of the states, the magic numbers and the right sequence of energy levels came as a surprise. It had been expected that in a dense system such as the nucleus the nucleons will perform many collisions and no independent-particle orbits are allowed. It turned out that due to the Pauli Principle, which prohibits scattering of nucleons to occupied states, collisions between the nucleons are suppressed and therefore the gross features can be described by the shell model. But already in the early seventies it became clear that the precise data from elastic electron scattering can not be described by mean field theory alone. The theoretical description has to account for Short-Range and tensor Correlations (SRC); high momentum components in the nuclear wave function are generated due to the repulsive part of the N-N interaction at short N-N distance. In sec. 1.1 an overview of key-experiments will be given.

In the following sections the main features of the Independent Particle Shell Model (IPSM) as well as modern many-body theories, which treat short-range correlations explicitly, are described and compared. Further recent experimental approaches and results are presented. Finally the aim and the design of the present experiment is given.

## 1.1 Indirect evidence for Short-Range Correlations

The first experiments, which were done to investigate the structure of nuclei and the validity of the mean field theory, were single nucleon transfer reactions, pick-up as well as stripping reactions (for a review s. [82]). Due to the strong absorption of projectiles and ejectiles these reactions could investigate only the surface of the nucleus. Therefore they are not sensitive to the dense

region in the nuclear interior. These experiments were done with the aim to obtain the spectroscopic factor of various states. The spectroscopic factor is a measure of the strength of the transition from one state in the nucleus A to another state in the nucleus A-1, when removing one nucleon (sec. 1.3). These experiments seemed to indicate that the occupation of states was close to the one predicted by the IPSM. However, the result was misleading due to incorrect assumption made in the analysis. It will be discussed at the end of this section in more detail. A much better probe for this purpose are electrons, which are sensitive to the distribution of magnetic and electric charge even in the interior of the nucleus. An overview of key-experiments investigating correlations can be found in [144]. In the following a few electron scattering experiments will be mentioned, which became important for the further progress in the investigation of nuclear structure and the search for SRC.

In the course of 35 years a large amount of precise elastic scattering electron cross sections on  $^{208}\text{Pb}$ , measured in Saclay, Stanford, Mainz and Darmstadt for momentum transfers between 100–800 MeV/c, were collected [71]. For target nuclei with  $J^\pi = 0^+$  the cross section is determined by the charge form factor, which is related to the charge density by a Fourier transformation. Whereas the mean field theory could describe the outer region of the charge distribution quite well it overestimates the experimental charge density in the central region. In addition, the strong fluctuations in the interior as predicted by the theory are hardly visible in the data. This is likely due to a overestimation of the contribution of the  $3s_{1/2}$ -shell as it was observed by the measurement of the charge density difference between  $^{206}\text{Pb}$  and  $^{205}\text{Tl}$  [40], nuclei which differ by a proton in the  $3s_{1/2}$  orbit. The shape of the charge density difference can be clearly identified as being due to the additional proton in the  $3s_{1/2}$ -orbit in  $^{206}\text{Pb}$ . It can be well described by the mean field theory except that the theoretical prediction has to be scaled by a factor  $0.64 \pm 0.06$ . Thus on the one hand the concept of the IPSM, where the charge distribution is simply the sum of the squared single-proton wave functions, is confirmed even in the nuclear interior. On the other hand the failure of the IPSM in predicting the observed strength became obvious. It should be mentioned that interpretation of these data require accounting for configuration-mixing and core-polarization effects.

A pilot experiment to investigate the shell structure of medium-light nuclei via quasi-elastic electron scattering was done in the seventies at Frascati [5], but this experiment suffered from the poor energy resolution ( $\approx 12$  MeV). Due to the low duty factor of the electron beam only a few points of the momentum distribution were measured for low missing momentum ( $< 100$  MeV/c). First systematic studies with high resolution of  $\approx 1$  MeV

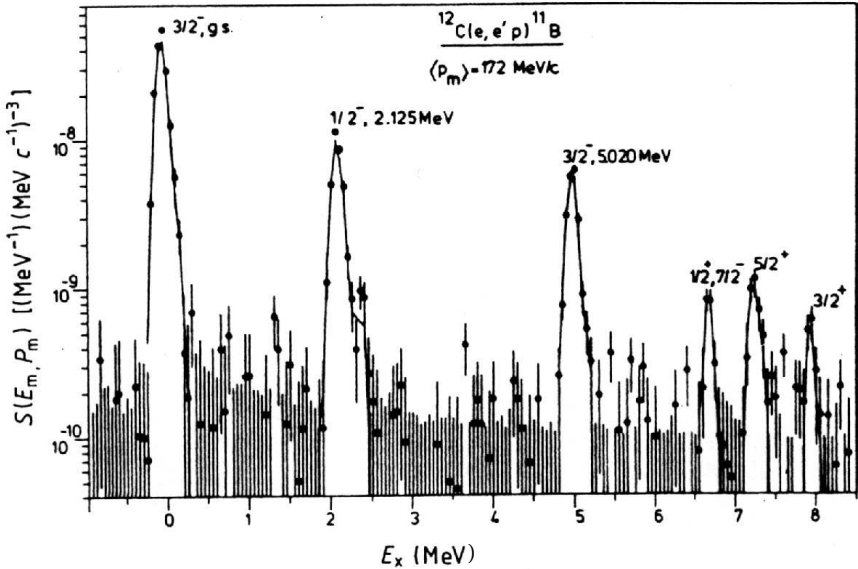


Figure 1.1: Excitation spectrum of  $^{11}\text{B}$  obtained in the reaction  $^{12}\text{C}(\text{e},\text{e}'\text{p})$  at NIKHEF [188].

were done at Saclay on C, Si, Ca and Ni [125]. Most of the shells could be separated and the momentum distributions were extracted and compared in different kinematics (parallel and perpendicular). These experiments clearly showed the occurrence of shells also for the more deeply bound nucleons. The results were later confirmed with better statistics at NIKHEF. For an overview of the status of  $(\text{e},\text{e}'\text{p})$ -experiments up to the eighties see [72]. In the nineties detailed nuclear structure investigations became feasible with the development of high-resolution detectors for both the electron and the proton. Later  $(\text{e},\text{e}'\text{p})$  experiments benefit from improved electron machines with higher duty cycle, higher electron energy and more intense electron beams. In addition better control over the energy spread of the electron beam is a prerequisite for high-resolution experiments. Different targets ranging from deuterium to lead were investigated with  $(\text{e},\text{e}'\text{p})$  coincidence experiments at NIKHEF-K. These experiments were limited to the single-particle region, i.e. small missing energy ( $< 30$  MeV) and moderate missing momentum ( $< 250$  MeV/c). Definitions of the quantities and terms will be given in the next section.

At NIKHEF-K a very good energy resolution of 100 keV was achieved due to a dispersion-matching technique between electron beam and spectrometer. Therefore the states occupied according to the shell model could be

energetically separated. In Fig. 1.1 the excitation spectrum of  $^{11}\text{B}$  obtained in the reaction  $^{12}\text{C}(\text{e},\text{e}'\text{p})$  is shown. The orbits are labelled with quantum numbers  $\alpha = (n)l_j$  ( $n$  = main radial,  $l$  = orbital angular momentum,  $j$  = total angular momentum) or alternatively with  $j^{\text{parity}}$  (parity = + for  $l$  even). The first peak at excitation energy  $E_x = 0$  corresponds to the ground state of  $^{11}\text{B}$ . It is remarkable that the transition to the final state with spin-parity  $5/2^-$  at  $E_x = 4.45$  MeV is missing whereas it was seen in  $(\text{p},2\text{p})$ -experiments with a momentum distribution characteristic for a proton from the p-shell. Because the  $f_{5/2}$  state in  $^{12}\text{C}$  is empty the  $5/2^-$  in  $^{11}\text{B}$  can not be populated by a 1-step process [165]. Additional excitation of the target nucleus in the initial or final state could explain the appearance in the  $(\text{p},2\text{p})$  reaction. This indicates that electron scattering experiments offer a way to examine the nucleus under much cleaner conditions than hadronic processes, which are suffering more from multi-step processes. The observation of the  $1/2^-$  state in  $^{11}\text{B}$  is due to a mixing of the  $1p_{3/2}$  with the  $1p_{1/2}$  orbit, which would be empty without the presence of residual interactions (in particular long range correlations - LRC). A study of different nuclei leads to the result that on average 7 % of the strength is located in the shells above, but close to the Fermi edge. The positive parity states at around 7 MeV excitation energy are due to the excitation of the  $(1s_{1/2})^4$  configuration, the  $\alpha$ -core in  $^{12}\text{C}$ . The knock-out of a proton from the deep-lying orbit  $s_{1/2}$  requires a removal energy of around 38 MeV and can not be seen on Fig. 1.1 due to the limited range in excitation energy.

From the  $(\text{e},\text{e}'\text{p})$  cross section measurements the momentum distribution  $n(p_m)$  is obtained for each orbit. The outgoing proton, of a kinetic energy around 100 MeV in the case of the NIKHEF data, is strongly affected by the interaction with the residual nucleus; the momentum distribution extracted from the data is therefore distorted. Thus a comparison to the predictions obtained in PWIA is not useful. Instead, the Distorted Wave Impuls Approximation (DWIA) is used. Here both the bound state and the final (continuum) state are modelled using the optical potential of a Wood-Saxon shape. Its main parts are a complex central potential, an imaginary surface term and a spin-orbit term. The imaginary part accounts for inelastic reactions in the  $\text{p}-(\text{A}-1)$  system and reduces the outgoing flux.

The parameters of the optical potential are fixed by total, differential and reaction cross sections from nucleon-nucleus scattering with nucleon energies of less than 300 MeV. The depth of the central potential is adjusted to reproduce the measured single-particle energy. The only parameter, which is varied freely, is the radius  $R$  of the Wood-Saxon well. The rms-radius obtained from the fit agrees within 5 % with mean field theories using effective forces, whose parameters are fitted to binding energies and charge radii. The

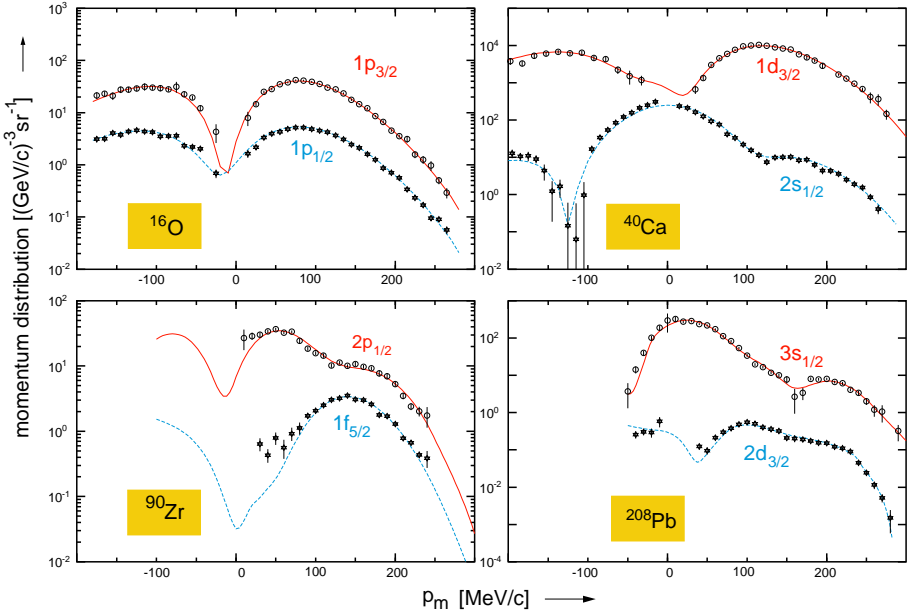


Figure 1.2: Momentum distribution in the single-particle region obtained at NIKHEF for different nuclei and quantum states as indicated, compared to the fit from DWIA.

shape of the bound-state wave function from DWIA is nearly identical to the Hartree-Fock single-particle wave function.

The momentum distribution of DWIA is compared to the experimental one in Fig. 1.2. The shape of the momentum distribution is characteristic for the shell and can be used to identify the angular momentum of the orbit. The agreement of the shapes of the momentum distribution from experiment and theory is excellent, but the amplitude from DWIA had to be scaled by a factor of  $\approx 0.65$  for states close to the Fermi edge. This factor is called the spectroscopic factor (sec. 1.2). Whereas the relative strengths of the different orbits are in good agreement with the shell model [188], the IPSM fails to give the correct absolute normalization. This indicates that the major part of the depletion in a shell is independent of the missing momentum and does not depend on the location of the nucleon in the nucleus. The spectroscopic factors for light and heavy nuclei measured at NIKHEF are shown in Fig. 1.3. They are integrated up to an excitation energy of  $\approx 20$  MeV using the l-decomposition method<sup>1</sup>. Nuclei, which have a specially stable closed shell

<sup>1</sup>Fit of the shape of the momentum distribution for the different angular momenta to the continuum in the excitation spectrum.

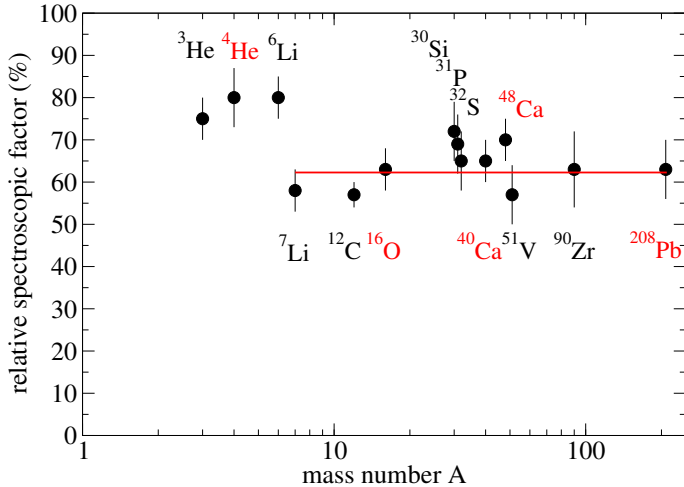


Figure 1.3: Spectroscopic factors measured at NIKHEF and integrated to an excitation energy of  $\approx 20$  MeV are shown relative to the IPSM expectation value. Nuclei marked in red are doubly magic. The line indicates the average of 62 % for  $A \geq 7$ .

configuration for protons and neutrons (doubly magic), are marked in red. No significant difference between magic and non-magic nuclei is found. For nuclei with  $A \geq 7$  the depletion of the single-particle shells is nearly constant. A fit gives an average spectroscopic factor of 62 % for valence states summed up over the single-particle region. The difference of the spectroscopic factors between  $^6\text{Li}$  and  $^7\text{Li}$  is remarkable. The value for  $^7\text{Li}$  is in perfect agreement with a Variational Monte Carlo (VMC) calculation [103], which predicts a spectroscopic factor of 0.60. For  $^6\text{Li}$  a three-body calculation of the  $(\alpha-n-p)$  system, where the  $\alpha$ -core is assumed to be inert and structureless, gives a spectroscopic factor of 0.87. This agrees within the error bars with the experimental result [188]. This difference might be an indication that the additional neutron in  $^7\text{Li}$ , which leads to an increased number of n-p pairs, results in a larger depletion due to the strong tensor force (sec. 1.2).

Later experiments at NIKHEF cover a larger  $E_m$ -range and could also measure the strength which resides in deep-lying states. In Fig. 1.4 the spectroscopic factors of the single-particle states up to 30 MeV are shown for the doubly magic nucleus  $^{208}\text{Pb}$  [151]; one can clearly see that the depletion is more pronounced for states closer to the Fermi surface. Here the binding energy is small and approximately equal to the energy required for the excitation of collective modes (LRC). In contrast nucleons which reside in the interior, have larger binding energies and are therefore more difficult to

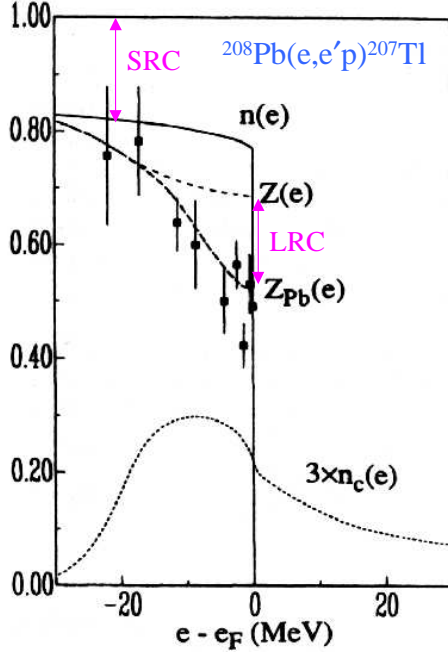


Figure 1.4: Spectroscopic factor as a function of the single-particle energy measured on  $^{208}\text{Pb}$  at NIKHEF [151]. The solid lines are calculations performed in CBF theory [22][21] (sec. 1.2.7).

excite. The spectroscopic factors of the deep-hole states are approaching the occupation number of  $\approx 0.8$  calculated for nuclear matter in the Correlated Basis Function theory (CBF) [22] (sec. 1.2.7). This confirms the view that lead should behave like nuclear matter in the interior, because the proton density of lead reaches almost 90 % of the one for nuclear matter. To take surface effects approximately into account in the CBF theory the imaginary part of the self-energy was modified to reproduce the experimental width of the hole state [21]. This accounts effectively for LRC, which leads due to the coupling of single-particle states and collective modes to a smearing out of the strength and thus to a spreading in width. The result is shown as dashed line in Fig. 1.4 and labelled with  $Z_{\text{Pb}}$ . The experimental data follow this curve remarkable well. The relation of spectroscopic factor and occupation number as well as the meaning of the correlated part will be explained in the following section.

A comparison of the binding energies predicted by Hartree–Fock calculation with the experimental values for lead and thallium isotopes gives a difference of 3 MeV for the deep-lying hole states ( $|\epsilon_B| > 20$  MeV) [151]. This

deviation could be explained by taking into account dynamical corrections due to core-polarization and ground state correlations in the Hartree-Fock calculation [112].

The large depletion of the single-particle states found in (e,e'p)- experiments appeared to be in contradiction to the results of nuclear transfer reactions, whose results were in agreement with the shell model. It turns out that the spectroscopic factor  $Z$  from nuclear transfer reactions is very sensitive to the rms-radius in the bound-state wave function ( $\Delta Z/Z \approx 7\Delta r_{rms}/r_{rms}$ ). Due to the strong absorption the transfer reaction measures only the asymptotic normalization of the bound-state wave function. In the usual analyses the rms-radii were chosen such as to fulfill the sum rule  $n_{particle} + n_{hole} = (2j+1)$  according to the IPSM limit. In the small range of missing energy accessible to the experiment (10–20 MeV) the sum rule is not fulfilled, however, because the missing strength is spread out over a large range of initial energy and momentum. In the reanalysis [101] [99] of transfer reaction data the rms-radii as derived from the fit to the (e,e'p)-data were used. Further the local potential and zero-range approximation were replaced by a non-local potential<sup>2</sup> including a full finite-range analysis<sup>3</sup>. With these ingredients the spectroscopic factors were reduced to  $\approx 60\%$  of the IPSM limit in agreement with the result from the (e,e'p) analysis.

It has been [81] claimed that the consistency of the spectroscopic factors from the two reactions obtained when using the same rms-radius does not prove the correctness of the results. For example, if one uses for the (d,  $^3\text{He}$ ) data on  $^{51}\text{V}$  the smaller rms-radius obtained from elastic magnetic scattering [147] (4.06(5) fm instead of 4.20 fm from (e,e'p)) one obtains a significantly larger spectroscopic factor ( $\approx 70\%$ ) from the (d,  $^3\text{He}$ ) data. The rms-radius was corrected for MEC and agrees well with the density-dependent Hartree-Fock-Bogoliubov calculation of Dechargé and Gogny [47], also for other nuclei measured in the same experiment. However, it might be that the MEC contribution is still underestimated.

Further, in [147] 90 % of the IPSM value was found. Here one has to

---

<sup>2</sup>A non-local potential depends not only on the coordinates of the interacting particles, but also on their velocity; this is equivalent to a energy dependence and can also introduce high-momentum components in the wave function [124]. Further as Perey [146] pointed out the wave function of a non-local potential is systematically smaller in the nuclear interior than the wave function of the local potential with an equivalent description of the nuclear scattering data. This is also confirmed by theories trying to reproduce the charge distribution of nuclei in the nuclear interior [161].

<sup>3</sup>In the zero-range analysis the ejectile is assumed to be emitted at the same position, where the absorption of the projectile took place. The spectroscopic factor obtained from a zero-range approximation is larger than from a finite-range analysis. One can account for finite-range effects by the local energy approximation.

keep in mind that this factor corresponds to a weighted sum of spectroscopic factors over all final states [52] and therefore should not be compared to the spectroscopic factor measured in  $(e,e'p)$  experiments but rather to the occupation number.

The analyses of the  $(e,e'p)$  data rely on the description of the reaction mechanism in DWIA. It turns out that DWIA can not describe the whole set of data taken in different kinematics. It fails to account for the enhanced yield observed in antiparallel kinematics. Therefore a factor  $\eta^4$  of  $1.2 - 1.3$  depending on the optical potential was introduced to enhance the transverse response function (and the interference terms) with respect to the longitudinal one (e.g. [166]). This reproduced the observed ratio of transverse to longitudinal cross section but lead to a reduction of the spectroscopic factor of  $\approx 10\%$ . Even with the factor  $\eta$  included data taken in perpendicular kinematics would result in a  $10\%$  higher spectroscopic factor. This indicates the sensitivity of the perpendicular kinematics to other reaction mechanisms not taken explicitly into account, such as MEC. In addition the influence of channel-couplings on the extracted value of the spectroscopic factor from  $^{12}C(e,e'p)$  was examined in ref. [166]. There are two kinds of couplings. The 2-step processes  $(p,d')+(d',p')$  and  $(p,p'')+(p'',p')$  affect the momentum distribution measured in parallel and perpendicular in a different way. Its effect is accounted for in parallel kinematics by a reduction of the real part of the optical potential by 5 MeV. Further the interference between the direct knock-out and the excitation in  $^{11}B$  was taken into account. It leads to an increase of the spectroscopic factor of the  $p_{1/2}$  state by  $15\%$  and a decrease of  $10\%$  in  $\eta$ .

The  $(e,e'p)$  experiments at NIKHEF measured the spectroscopic factor at low  $Q^2 < 0.4$  ( $GeV/c$ ) $^2$ . Recently an experiment at Jlab was performed [76], which investigated the reaction  $^{16}O(e,e'p)$  at  $Q^2 = 0.8$  ( $GeV/c$ ) $^2$ . From the determination of the response functions the spectroscopic factors were obtained. It was shown that a relativistic approach can describe the data well. The use of a relativistic potential in the Dirac equation leads to a reduction of the normalization of the wave function. Therefore the spectroscopic factor is enhanced by  $10-15\%$ . The spectroscopic factors found in the experiment are  $\approx 0.7$  for the p-state in  $^{16}O$ . The increased spectroscopic factor is also in better agreement with the prediction of modern many-body theories. In addition the left-right asymmetry was extracted from the data. It was shown that a fully relativistic approach is necessary to describe the experimental results.

In [152] it was shown that in a relativistic approach using non-relativistic

---

<sup>4</sup>The factor  $\eta$  is defined as the ratio of  $G_m/G_e$  for bound and free protons.

ingredients, like the hole spectral function from the Green's function formalism to account for SRC and an eikonal description for FSI, consistent spectroscopic factors at low and high  $Q^2$  are obtained (0.644 for  $1p_{1/2}$  and 0.537 for  $1p_{3/2}$ ). In an analysis of high and low  $Q^2$  data using RDWIA spectroscopic factors of  $Z_{p1/2} = 0.708$  and  $Z_{p3/2} = 0.602$  were obtained independently of  $Q^2$  [153] and in agreement with [175]. The difference between spectroscopic factors from relativistic and non-relativistic analyses is still an unsolved problem.

Recently spectroscopic factors were determined using the heavy ion reactions  $^{12}\text{C}(^{16}\text{O}, ^{15}\text{N})$  and  $^{12}\text{C}(^{12}\text{C}, ^{11}\text{B})$  [36]. The experimental cross sections were compared to the theoretical single-particle removal cross section calculated from parameter set constrained by the experiment. The spectroscopic factors for the p-shell found for  $^{16}\text{O}$  and  $^{12}\text{C}$  were 0.49–0.68 and in agreement with the one obtained from the  $(e, e'p)$ -experiments. An advantage of the heavy ion reactions is that also short-lived isotopes can be studied using radioactive beams. For the halo proton in  $^8\text{B}$  a larger spectroscopic factor of 0.88(4) was obtained. In a halo nucleus SRC are expected to be reduced due to the larger average internucleon distance. In addition also the number of n-p pairs is significantly smaller.

## 1.2 Theoretical framework

### 1.2.1 The $(e, e'p)$ -reaction

Protons bound in a nucleus are in motion, subject to the interplay of the attractive and repulsive part of the N–N interaction. This motion of the proton, which is the subject of interest in the present work, can be characterized by a distribution in energy  $E$  and momentum  $k$ . In the following we distinguish between  $k$ ,  $E$  as theoretical values and  $p_m$ ,  $E_m$ , which are accessible in the experiment. When a proton is knocked out from a bound state in a nucleus A by an electron in quasi-elastic kinematics, the residual nucleus A–1 can be left in an excited state with excitation energy  $E_x$ . The total amount of energy to remove a proton is given by

$$E = E_o^A - E_n^{A-1} \quad (1.1)$$

$$= E_x + \epsilon_S \quad (1.2)$$

Here  $E_o^A$  denotes the energy of the ground state for A nucleons and  $E_n^{A-1}$  indicates that the residual nuclei remains in the state n. The separation energy  $\epsilon_S$  can be obtained from the mass difference of initial and residual

nucleus

$$\epsilon_S = (M_{A-1} + M_p) - M_A. \quad (1.3)$$

When comparing to theory, we will occasionally deal with spectral functions from infinite nuclear matter. Here the Fermi energy  $\epsilon_F$  plays an important role (sec. 1.2.2). In application of such calculations to finite nuclei, the Fermi edge can be identified with the topmost filled shell, with the removal energy  $\epsilon_S$ .

The quantity  $E$  corresponds to the theoretical definition of the missing energy and appears in the energy conserving  $\delta$ -function of Eq. 1.12 when defining the spectral function. Experimentally it is difficult to determine the energy  $E$  directly via Eq. 1.1. Instead of it one measures the missing energy  $E_m$ . The missing energy  $E_m$  and the missing momentum  $p_m$  can be reconstructed from the measured quantities in the detectors, the momentum and angles of both the proton and the electron

$$E_m = E_e - E'_e - T_p - T_{A-1} \quad (1.4)$$

$$\vec{p}_m = \vec{q} - \vec{p}'_p, \quad (1.5)$$

where  $E_e$  is the beam energy,  $E'_e$  the energy of the scattered electron and  $T_p$ ,  $T_{A-1}$  the kinetic energy of the knocked-out proton and the residual nucleus. The momentum transfer  $\vec{q}$  is obtained from the initial and final electron momentum,  $\vec{k}_e - \vec{k}'_e$ , and  $\vec{p}'_p$  is the 3-momentum of the knocked out proton. In Plane Wave Impuls Approximation (PWIA), where no distortions of the initial and final particles are considered, the residual nucleus has the opposite momentum of the initial proton due to momentum conservation. Then  $E_m$  and  $p_m$  can be directly related to the initial energy  $E$  and momentum  $k$  of the proton in the nucleus and therefore be compared to theoretical predictions.

In PWIA the nuclear current factorizes into an one-body (nucleon) current times a matrix element, which is the Fourier transform of the overlap between the target ground state wave function and the wave function of the residual nucleus. Then the 6-fold cross section for electron scattering on a bound nucleon can be written as

$$\frac{d^6\sigma}{d\Omega_e dE'_e d\Omega_p dE'_p} = p' E'_p \sigma_{ep} S(E, \vec{k}) \quad (1.6)$$

Corrections to PWIA as for example due to the Coulomb field of the nucleus and rescattering inside the nucleus will be considered later (sec. 4.1.5 and 8.6). The spectral function  $S(E, \vec{k})$  contains the nuclear structure information and gives the joint probability to find a proton with energy  $E$  and momentum

$\vec{k}$  in the nucleus. The momentum distribution  $n(\vec{k})$  is obtained from the integral of the spectral function over the energy:

$$n(\vec{k}) = \int S(E, \vec{k}) dE \quad (1.7)$$

For a specific shell  $\alpha$  with vanishing width the integral is replaced by a delta-function. Then the momentum distribution  $n_\alpha(\vec{k})$  is the square of the Fourier transformation of the bound-state wave function

$$n_\alpha(\vec{k}) = \left| \int \exp(i\vec{k}\vec{r}) \phi_\alpha(\vec{r}) d\vec{r} \right|^2 \quad (1.8)$$

The spectroscopic factor  $Z$  is usually obtained by comparing the integral of the measured momentum distribution to the one obtained from DWIA. This is justified because the treatment of final state interactions by means of an optical potential without spin-dependent forces leads also to a factorized expression as in Eq. 1.6 [30]. In addition the shape of the momentum distributions from DWIA and experiment are in good agreement. The spectroscopic factor  $Z$  is a measure of the strength of the transition from one state of nucleus A to another discrete state of nucleus (A-1). Experimentally the energy is often integrated over a range of energy (Fig. 1.3), i.e. some of the fragments produced by residual interaction (sec. 1.2.5) are already included. In the analysis only fragments, which exhibit the characteristic momentum distribution for the shell of interest (sec. 1.2), are summed up. One then obtains a quantity that is neither a spectroscopic factor nor a true occupation number. One might call it a "spectroscopic factor over the IPSM region".

The definition of the occupation number requires knowledge about the momentum distribution for *all* final states. It will be given below together with measurements of the occupation number (sec. 1.3).

After the description of the formalism from the experimental point of view an overview of modern microscopic theories as well as the IPSM and the Hartree-Fock approach will be given. Some of the expressions above will be replaced by their definitions in the theoretical framework.

### 1.2.2 Fermi gas model and Independent Particle Shell Model

The observation that the average nuclear binding energy per nucleon is nearly independent of the number of nucleons reminds of the properties of an ideal gas. On the other hand the nucleon-nucleon distance at the minimum of the N-N potential is 1.8 fm. This is of the same order as the diameter of a

nucleon and contradicts the concept of an ideal gas. However, if one assumes that the nucleons have a hard core of  $\approx 0.4$  fm radius, which can not be penetrated, the ratio of the minimal space needed for  $A$  nucleons to the nuclear volume is around 0.03. From this naive point of view the picture of independently moving nucleons in the nucleus could be justified. In addition, the Pauli blocking helps to fulfill this condition, because it prevents scattering of nucleons into already occupied states.

Such a simple model can only describe infinite symmetric nuclear matter, because no details of the shell structure are included. Any correlations are forbidden by definition.

Due to the translational invariance in nuclear matter the single-particle wave functions are plane waves with energy eigenvalues  $k^2/2M$ . Because no potential is present the hamiltonian reduces to the kinetic energy term. Under such conditions the diagonal elements of the density matrix  $\rho(\vec{r}, \vec{r}')$  are equal to the density distribution  $\rho(\vec{r})$ , which is a constant ( $= \rho_o$ ). Therefore the momentum distribution  $n(\vec{k})$

$$n(\vec{k}) = \int \exp[i\vec{k}(\vec{r} - \vec{r}')] \rho(\vec{r}, \vec{r}') d\vec{r} d\vec{r}', \quad (1.9)$$

is a step function  $\theta(k_F - |\vec{k}|)$ . This means that in the ground state all momentum states are fully occupied according to the Pauli principle up to the highest momentum, which is called the Fermi momentum  $k_F = (\frac{3}{2}\pi^2\rho_o)^{1/3}$ . In terms of energy the levels are filled up to the Fermi energy  $\epsilon_F = k_F^2/2M$ . No particles above the Fermi energy and no high momentum components are allowed for. This will change, when correlations are included. But even then the discontinuity at the Fermi energy remains for infinite nuclear matter (Fig. 1.5).

The main assumption of the Independent Particle Shell Model is that the nucleons move independently from each other in a mean field. The mean field is generated by the average interaction between a nucleon and the other nucleons. This leads to a typical self-consistency problem, which can be solved in the Hartree-Fock approximation (sec. 1.2.3). Usually simple approximations to the exact mean field are taken, e.g. the isotropic harmonic-oscillator potential or the Wood-Saxon potential. A common procedure is to adjust the depth of the potential for each shell to reproduce the energy eigenvalue. As in the Fermi model no correlations are taken into account and therefore all levels below the Fermi energy are fully occupied in the ground state. Then the many-body wave function  $\Psi(\vec{r}_1, \dots, \vec{r}_A)$  is the solution of the Schrödinger equation and it can be written as a Slater determinant

$$\Psi(\vec{r}_1, \dots, \vec{r}_A) = \frac{1}{\sqrt{A!}} \det |\phi_i(\vec{r}_j)| \quad i, j = 1, \dots, A \quad (1.10)$$

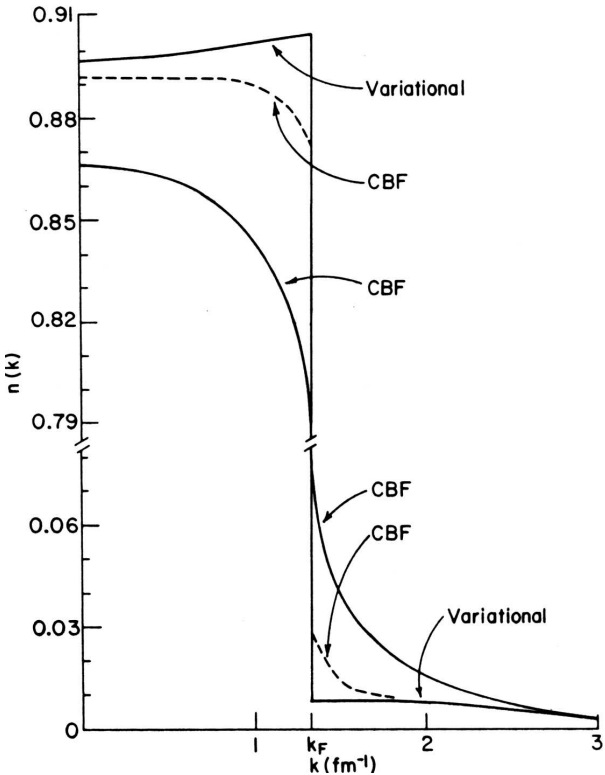


Figure 1.5: Occupation probability for infinite matter as predicted by the Variational and CBF calculation. The full and broken line (CBF) show results of second-order CBF calculation with and without the tensor operator [64]. For definition of the occupation probability see Eq. 1.33.

using the single-particle wave functions  $\phi_i$ . This reduces the many-body problem to a single-particle problem, which is a great simplification. Contrary to the Fermi model for nuclear matter the momentum distribution contains no discontinuity, because the shell model is applied to finite nuclei. The momentum distribution exhibits a steeply falling slope at large momentum. This can be seen in Fig. 1.6, where the momentum distribution of the IPSM is compared to modern many-body theories, which treat correlations.

For practical purpose the spectral function in IPSM is separated into a momentum and energy distribution. The energy distribution for each shell is parametrized as lorentzian around the single-particle energy with a width  $\Gamma$ . Usually width and energy are taken from the experiment (sec. 4.1.2).

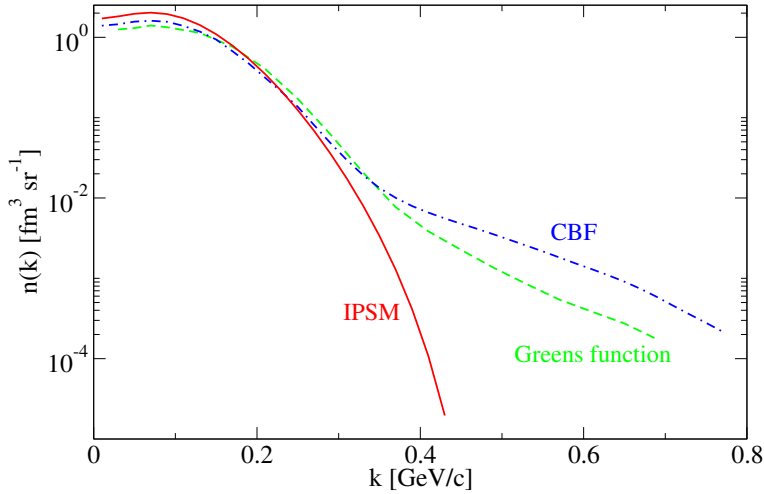


Figure 1.6: Momentum distribution for  $^{12}\text{C}$  as predicted by the IPSM (solid line), Green's function approach (dashed) [128] and CBF theory (dot-dashed) [20]. The upper energy limit in the integration of the spectral function is 300 MeV.

### 1.2.3 Hartree–Fock approximation

The Hartree–Fock (HF) approximation, one special version of mean–field theory, is used for constructing the mean field from the N–N interaction. Self–consistency is achieved, when the density calculated from the single–particle wave functions via

$$\rho(\vec{r}) = \sum_i |\phi_i(\vec{r})|^2 \quad (1.11)$$

is the same as used in the density–dependent Hartree–Fock potential, which in turn leads to the particle wave functions via the Schrödinger equation. This Hartree–Fock potential is then called mean field. It consists of two terms: A direct local potential (Hartree term) and a non-local exchange term, which is related to the Pauli principle (Fock term). It depends on the density distribution  $\rho(\vec{r})$  as well as on the density matrix  $\rho(\vec{r}, \vec{r}')$  and is static . The main ingredient for the HF approximation is the choice of the N–N interaction. Unfortunately using realistic potentials the HF procedure does not lead to a bound state. This is due to the strong repulsive part in the N–N interaction at short distances ( $< 0.4$  fm), which is required to describe N–N scattering data. Due to this singularity integration over the wave function and the potential diverges, because there is no mechanism, which

suppresses the contribution from the strong repulsive part of the N–N potential at short distances. Therefore the mean field can not be derived from the bare interaction. To overcome this problem usually effective phenomenological interactions like the Skyrme or Gogny force are used, whose parameters are fitted to binding energies and charge radii of several nuclei. It should be mentioned that the HF approximation does not only fail in nuclear systems but also in describing atomic  $^3\text{He}$  liquid drops bound by the Van–der–Waals interaction, which has also a repulsive core.

It is important to note that, independently from the interaction used, the HF approximation leads to fully occupied states below the Fermi energy. The hole spectral function, which is in general defined as

$$S_h(E, \vec{k}) = \sum_n | \langle \Psi_{A-1}^n | a_k^- | \Psi_A \rangle |^2 \delta(E - (E_o^A - E_n^{A-1})), \quad (1.12)$$

reduces to a collection of  $\delta$ –functions centered at the single–particle energies with occupation probability one. Obviously neither the width of the states nor their strength are in agreement with the experimental results. The sum in Eq. 1.12 runs over all possible eigenstates of the final nucleus A-1 with energy  $E_n^{A-1}$ . Often the sum is omitted in the definition, when non–degenerate eigenstates in the final state are assumed. The hole spectral function gives the probability to remove a particle with  $(E, k)$  from the ground state of the nucleus A with energy  $E_o^A$ , whereas the particle spectral function  $S_p$  gives the probability of adding a particle with  $(E, k)$  to the ground state of A. Analogously to Eq. 1.12 the particle spectral function is defined as

$$S_p(E, \vec{k}) = \sum_n | \langle \Psi_{A+1}^n | a_k^+ | \Psi_A \rangle |^2 \delta(E - (E_n^{A+1} - E_o^A)). \quad (1.13)$$

Since the density dependence of the effective N–N interaction has been fitted to experimental charge densities, the density distribution is in much better agreement with the data than the momentum distribution, which depends on the non–diagonal elements in the density matrix. The results obtained in the HF approximation are quite similar to the one from the IPSM.

Approaches beyond the Hartree–Fock approximation have to include the effect of short–range correlations. Because of the strong repulsive term in the N–N interaction a perturbative calculation will not converge. To avoid the singularity in the bare N–N potential the interaction has first to be properly renormalized. This was originally the idea of Brückner and is realized in the approaches described below.

### 1.2.4 Brückner–Bethe–Goldstone approach

When using realistic potentials to account for correlations one has to take care that the potential acting on the wave function does not diverge for relative distances smaller than the hard–core radius. There exist two solutions to avoid this problem. One solution includes the correlations directly into the wave function as it is done in the Variational and CBF theory (sec. 1.2.7); the other uses an effective interaction<sup>5</sup>, which together with the uncorrelated wave function yields the same result as the bare interaction with the correlated wave function.

For free nucleons the effective interaction is obtained by the Lippman–Schwinger equation and is represented by the reaction matrix  $T$ . For nucleons in the medium, the dressed nucleons, the effective interaction is the solution of the Bethe–Goldstone (BG) integral equation

$$G(E) = V + V \frac{Q}{E - Q H_o Q} G(E), \quad (1.14)$$

where Brückner’s scattering matrix  $G$  contains the sum of all two–particle correlations to infinite order. The nuclear medium effects are appearing in the Pauli operator  $Q$ , which prevents scattering into occupied states. Further the unperturbed Hamiltonian  $H_o$  acts not on free but intermediate states, which involves a sum of single–particle energies  $\epsilon_m + \epsilon_n$  of the interacting nucleons. If the starting energy  $E$  is chosen equal to the unperturbed one the  $G$ -matrix is called on–shell. The main point of the Brückner–Bethe–Goldstone (BBG) or hole–line expansion is that the perturbation series is ordered in terms of the number of hole–lines, not in the bare interaction  $V$ . Hole–lines are intermediate single–particle states with momentum less than the Fermi momentum. The number of  $n$  hole–lines describes  $n$ –particle correlations in the system. In a diagrammatic approach the set of terms summed in the  $G$ –matrix is called ladder diagrams.

Several choices for  $H_o$  can be made. In fact the solution of the BG equation should not depend on the choice of  $H_o = T + U$ , but it is convenient to choose it as close as possible to the exact solution, which should lead to a better convergence of the perturbation series. In the Hartree–Fock theory  $U$  is determined from the bare potential  $V$ . In analogy one replaces the bare interaction by the  $G$ –matrix. In the BHF approximation where only pp correlations are taken into account, the energy for the hole states are

---

<sup>5</sup>This effective interaction should not be mistaken for the phenomenological interactions fitted to experimental data, which are also called effective.

determined from the on-shell condition (quasi-particle spectrum)

$$\epsilon(k) = \frac{k^2}{2M} + \text{Re } \Sigma(k, \epsilon(k)). \quad (1.15)$$

Here the real part of the on-shell self energy can be interpreted as a momentum dependent quasi-particle or optical potential. The self energy is obtained from the G-matrix.

For the particle states above the Fermi energy two prescriptions are in use. In the conventional choice  $U$  is set to zero for the states above the Fermi energy, which leads to a large gap of 50 MeV in the energy spectrum at the Fermi surface. Therefore the so called continuous choice was introduced, using the same definition Eq. 1.15 for the hole as well as for the particle states. The solution of the BG equation requires self-consistency. As input for the BG equation single-particle energies and states are needed. On the other hand the solution of the BG equation, the G-matrix, has to be known to get these ingredients.

The two choices for the ansatz give different results in the two-hole line approximation. Baldo [164] showed that, when including the three-hole line contribution, one gets remarkable agreement between the two approaches. This might indicate the convergence of the BBG expansion. The result of this three-hole line calculation is closer to the solution obtained with the two-hole line expansion using the continuous choice. For the inclusion of three-hole lines one has to solve the Bethe–Faddeev equation. The BHF approximation contains only two-hole line contribution and is therefore often called the lowest order Brückner theory. No self-energy insertions into particle lines are made.

The relativistic extension of the Brückner theory is referred to as the Dirac–Brückner–Hartree–Fock (DBHF) approach. The relativistic version of the BBG equation is derived from the Bethe–Salpeter equation. Instead of the Schrödinger equation the Dirac equation is used to describe the single-particle motion. The main progress is that the saturation point of nuclear matter is shifted off the Coester band (sec. 1.2.5) in such a way that the empirical saturation density can be better reproduced without the need to introduce a three-body force [33] [129]. The need of three-nucleon forces in non-relativistic approaches seems to indicate the importance of relativity. For finite nuclei also an improvement in the charge radius and the binding energy is obtained [127].

It is important to note that the BHF approach does not lead to partial occupation of states which are empty in the mean field approximation. The reason is that only particle–particle correlations are considered and no hole–hole propagation. This lack in the theory is removed in the Green’s function

formalism.

### 1.2.5 Green's function approach for finite nuclei

The single-particle propagator or Green's function  $g(k_1, k_2, E)$  gives direct access to all single-particle properties like the spectral function, the density matrix and the optical potential. Whereas in the BHF approach only particle-particle propagation is considered the Green's function approach puts the hole-hole and the particle-particle correlations on an equal footing. This leads to a coupling of the single-hole states to 2p1h and more complicated states, which results in a depletion and fragmentation of the single-particle states.

For realistic calculations finite nuclei have to be considered instead of nuclear matter. The main complication in a calculation for finite nuclei is the fact that one needs first to determine a complete and appropriate set of single-particle wave functions; these are more difficult to handle than the plane waves in nuclear matter. Further, both the Green's function and the self energy are no longer diagonal in the momentum. In addition also long range correlations have to be treated in a complete calculation.

Because a calculation of the ladder diagrams directly in the single-particle basis is not feasible one starts from the G-matrix obtained in BHF approximation. Using vector bracket transformation coefficients the G-matrix is rewritten in the basis of single-particle states. The hole states are represented by oscillator functions, where the oscillator length is chosen appropriately for the nucleus of interest; the single-particle energy are taken from the experiment. Particles are described by plane waves and their energy eigenvalues are equal to the kinetic energy. Next a "Hartree-Fock" type self energy  $\Sigma^{HF}$  is calculated from the G-matrix. In general the self energy is a non-local energy-dependent potential with a real and imaginary part, which takes into account the strong interactions felt by the nucleons when propagating through the medium. In the case of  $\Sigma^{HF}$  it is independent of the energy and real, which does not lead to depletion. To take correlations into account second-order corrections to the self-energy are introduced,

$$\Sigma = \Sigma^{HF} + \Sigma^{2p1h} + \Sigma^{2h1p} \quad (1.16)$$

$$= \Sigma^{HF} + \Delta\Sigma. \quad (1.17)$$

The 2p1h-term is responsible for the depletion of strength in the single-particle region. The coupling of particle-states to 2h1p states is essential for accumulation of strength in the high-momentum region. A graphical representation of the self energy up to second order is shown in Fig. 1.7.

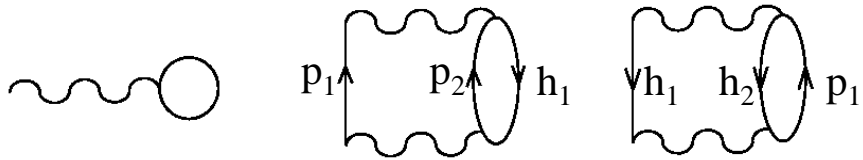


Figure 1.7: Graphical representation of the self energy up to second order. The wiggled line represents the G-matrix, the solid with arrow up (down) are particles (holes).

The imaginary part is calculated from the G-matrix whereas the real part of the self energy is obtained from the imaginary part using dispersion relations. To avoid double-counting the real part of  $\Sigma^{2p_1h}$  already included in  $\Sigma^{HF}$  has to be subtracted. The Green's function is obtained via the Dyson equation,

$$g(k_1, k_2, E) = g^o(k_1, k_2, E) + \int dk_3 \int dk_4 g^o(k_1, k_3, E) \Delta\Sigma(k_3, k_4, E) g(k_4, k_2, E) \quad (1.18)$$

from the part of the self energy, which goes beyond the HF approximation. The Dyson equation contains the self-consistency directly, which corresponds to the fact that the properties of a particle in the medium are determined by its interaction with the medium. The unperturbed Green's function  $g^o(k_1, k_2, E)$  is obtained from the Hartree-Fock part of the self energy. The Dyson equation is solved by a discretization technique, which leads to an eigenvalue problem in a spherical box with a radius chosen much larger than the radius of the nucleus (e.g. 15 fm for  $^{16}\text{O}$ ). For nuclear matter the Dyson equation simplifies considerably. There it becomes diagonal in the momentum.

The spectral function is obtained from the imaginary part of the Green's function

$$S(E, k) = \frac{1}{\pi} \text{Im } g(k, k, E). \quad (1.19)$$

This spectral function contains the correlated or continuous part of the spectral function via  $\Delta\Sigma$  in Eq. 1.18, which has only a significant contribution below the lowest single-particle energy in this approximation. In addition the spectral function receives the contributions from the quasi-hole part.

For finite nuclei long range correlations have to be included. Contrary to SRC, where the special shell structure of the nucleus is not relevant due to the high momenta and energies involved, for LRC excitation modes at low energies are important. Therefore the shell structure has to be taken into

account. This is done in a finite model space, which contains oscillator states up to the 2p– and 1f–shell for  $^{16}\text{O}$  (up to  $\approx 100$  MeV). SRC in this region are not disregarded but taken into account by an effective interaction  $G_{eff}$ . The effective interaction is derived from the BG equation similar to Eq. 1.14, but with a modified Pauli operator, which ensures that no double–counting of SRC and LRC in the model space occurs. This method is called doubly partitioned Hilbert space [73]. It turns out that states lying close to the Fermi level, the valence states, still show a strong peak at certain energies and therefore exhibit quasi–particle properties; their strength is considerably reduced, however. The remainder of the strength is spread over a large energy range. Here the quasi–particle picture is still valid to some extent.

In contradistinction, the strongly bound states are totally fragmented, but with the strength concentrated near the single–particle energy. This then leads to a well defined peak with a large width. The reason is that hole states far from the Fermi level occur in the same region as the 2h1p intermediate states, with which they mix due to the residual interaction. Hole states close to the Fermi energy  $\epsilon_F$ , on the other hand, have single–particle energies far enough away from the 2h1p and 2p1h energies. Especially in finite nuclei there is a gap between the Fermi energies of the particle and hole spectrum, which makes the quasi–particle picture a good approximation for some application.

The momentum distribution in Fig. 1.6 shows clearly an enhancement of the high momentum components due to correlations relative to the IPSM. The spectral function was originally computed for  $^{16}\text{O}$  [128] using the Bonn B potential, but renormalized for  $^{12}\text{C}$ . The quasi–hole part, which includes LRC, accounts for 88 % of the spectral function.

To compare different approaches and the effect of different N–N potentials one can compare the binding energy per nucleon as a function of the Fermi momentum (i.e. density) for nuclear matter. This curve is called saturation curve and can be considered as the equation of state (at zero temperature). The theoretical saturation point is the minimum of the saturation curve and can be compared to the experimental result, which is indicated as large square in Fig. 1.8. The size of the square represents the experimental error bars. The empirical values are  $E_{sat}/A \approx -16$  MeV and  $\rho_o \approx 0.17 \text{ fm}^3$  ( $k_F = 1.36 \text{ fm}^{-1}$ ). The theoretical results shown in Fig. 1.8 use the BHF approximation with the gap (circles) and continuous (stars) choice. The BHF result for different potentials and the gap choice lie all along a so called Coester band [44] and miss the empirical value. The BHF calculation with the continuous choice are grouped together and are closer to the experimental value. It should be noted that the BHF calculations do not include hh–contributions. A better treatment of SRC in a fully self–consistent Green’s function approach leads

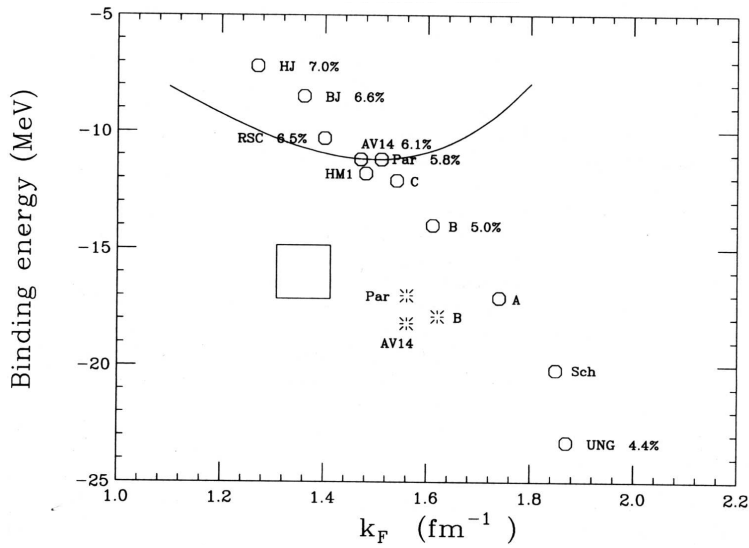


Figure 1.8: Saturation points calculated for different N–N interactions in the BHF approximation. The numbers indicate the probability of the D-state in the N–N potential. The full line represents the saturation curve for Argonne V14. The large square corresponds to the empirical value.

to better agreement [49].

All modern potentials used are realistic potentials, i.e. they fit the experimental phase shifts and deuteron properties, but this constraint is not sufficient for an unique determination of the scattering matrix  $T$  because of off-shell terms. The potentials are all based to some degree on the meson exchange theory. A schematic view of the central part of the N–N potential as a function of the nucleon–nucleon distance is shown in Fig. 1.9.

The location of the various results on the Coester band is related to the deuteron D–state probability predicted by the N–N potential, which is also indicated in Fig. 1.8. The D–state probability in the deuteron is directly connected to the strength of the tensor correlations. Interactions, in which most of the attractive part in the T–matrix comes from the bare potential (Born term), are called “soft”. The attractive terms of higher order in  $T$ , in particular the matrix elements of the kind  $\langle S|V|D \rangle$ , are less important in these potentials. When calculating the G–matrix the terms of higher order responsible for correlations are suppressed due to the Pauli operator. For a soft interaction the G–matrix contains still a large attractive part, which leads to large binding energies at large densities. In contrast, a “stiff” interaction produces more correlations, because more attraction resides in the higher

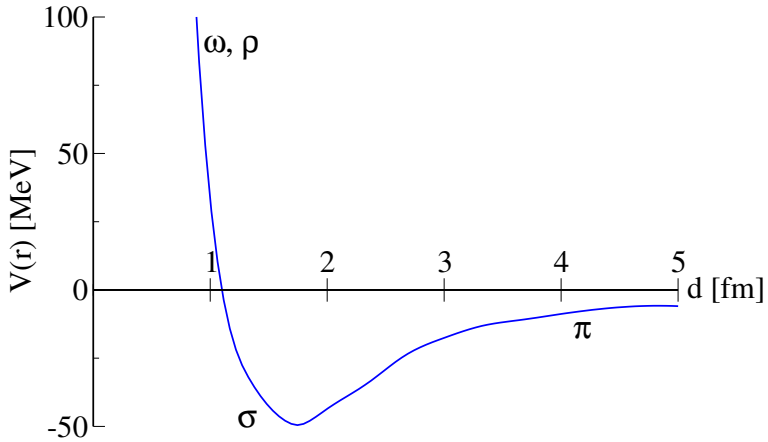


Figure 1.9: Central part of the N–N potential as a function of the distance between the nucleons. The long range part is provided by one-pion exchange as it is the lightest meson. The attractive part is produced by correlated two-pion exchange, which is usually represented as a  $\sigma$ -field. The short-range repulsion is due to the exchange of heavy mesons like the  $\omega$  and the  $\rho$ . The latter is responsible for the short-range tensor correlations.

order terms, which are quenched in the dressed potential  $G$ . The saturation point is therefore shifted to less binding energy and smaller densities for interactions containing a large D-state probability.

From the condition that the G-matrix acting on the uncorrelated wave function  $\Psi_{uc}$  has to give the same result as the bare interaction  $V$  acting on the correlated wave function  $\Psi_c$

$$G |\Psi_{uc}\rangle = V |\Psi_c\rangle \quad (1.20)$$

and from the BG equation 1.14 one can obtain the correlated wave function via

$$|\Psi_c\rangle = |\Psi_{uc}\rangle + \frac{Q}{E - Q H_o Q} G |\Psi_{uc}\rangle. \quad (1.21)$$

The second term on the right hand side is called the defect function and describes the difference between the correlated and the uncorrelated wave function. Because the matrix elements of  $G$  are real there exists no phase shift between the correlated and the uncorrelated wave function. Further for large distances the defect function vanishes, i.e. the correlated wave function heals to the uncorrelated one. For distances smaller than the hard core radius ( $\approx 0.4$  fm) the correlated wave function drops to zero, which is necessary to keep all integrals finite. Between  $\approx 0.7$  and  $1.7$  fm the correlated wave

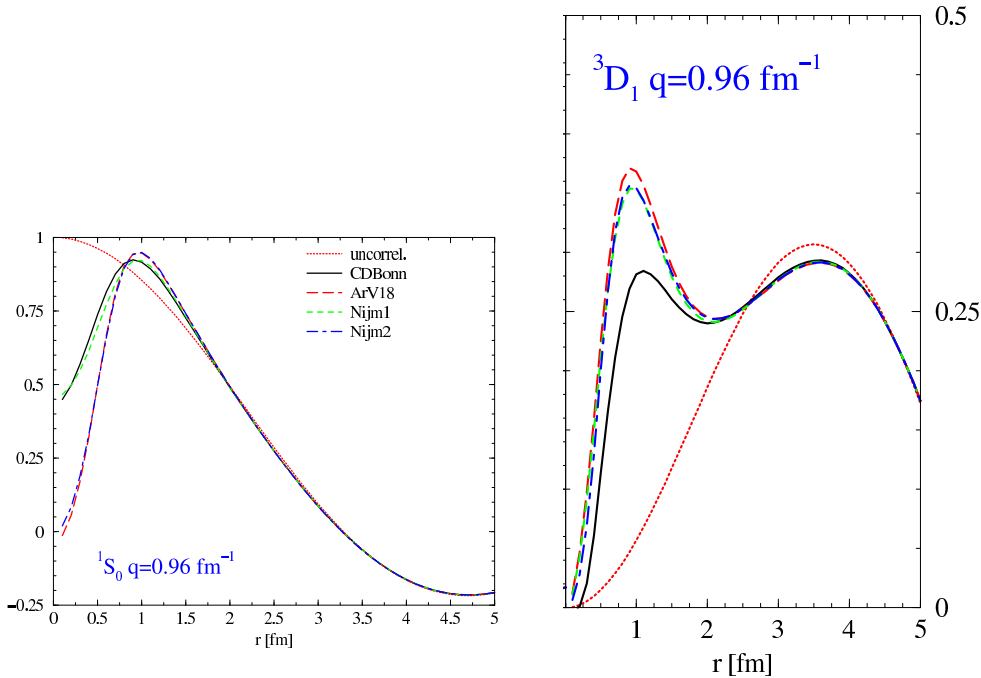


Figure 1.10: Correlated wave function for a pair of nucleons in the  $^1S_0$  (left) and  $^3D_1$  (right) state in nuclear matter at the empirical saturation density as a function of the relative distance between the two nucleons for different potentials as indicated. At large distance it merges with the uncorrelated wave function for momentum  $q = 0.96 \text{ fm}^{-1}$ , which corresponds to the chosen starting energy in the calculation.

function is enhanced as compared to the uncorrelated one due to attractive components in the interaction in this range.

The correlated wave functions for the  $^1S_0$  and the  $^3D_1$  partial waves in nuclear matter are shown for different potentials in Fig. 1.10 as a function of the relative distance between the two nucleons. It can be clearly seen that non-local interactions like the CD-Bonn and Nijmegen1 have a much softer core than local interactions. Comparing the correlated and the uncorrelated wave functions for the  $^3D_1$  state one sees a strong enhancement caused by tensor correlations, which couple the partial waves  $^3S_1$  and  $^3D_1$ . For the CD-Bonn potential the bump is less pronounced. Contrary to the other potentials it contains a relativistic, non-local pion-exchange contribution. The large increase of the correlated wave function compared to the uncorrelated one in the  $^3D_1$  state reflects the fact that isospin dependent tensor correlations are much more important than central correlations. The same conclusion can

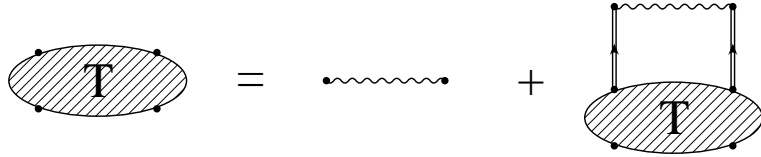


Figure 1.11: Graphical representation of the T-matrix used for the fully self-consistent calculation of the Green's function in the grand-canonical approach.

be drawn, when comparing the momentum distribution calculated in CBF theory with and without tensor correlations in Fig. 1.6. Therefore neutron–proton correlations are significantly stronger than pp or nn correlations.

### 1.2.6 Self-consistent Green's function for nuclear matter at finite temperature

Calculations for nuclear matter have the advantage that, due to simplifications arising from translational invariance, more sophisticated approaches can be pushed. Using the grand-canonical formulation of the Green's function it was possible for the first time to obtain a fully self-consistent Green's function not only at the level of the quasi-particle spectrum but also for the off-shell structure [68][69]. No approximation was made except for using the standard method of angle-averaging of the two-particle propagator. When summing up all ladder diagrams the free propagators are replaced by the full Green's functions, which is indicated by the double lines in the graphical representation of the T-matrix (Fig. 1.11). Due to the self-consistent evaluation of the Green's function the dressing of particle lines leads to the inclusion of diagrams, which contain also self energy insertions. The T-matrix represents an effective two-body interaction that contains all the ladder diagrams and accounts for short-range and tensor correlations. It reduces to the G-matrix in the BHF approximation.

In the grand-canonical approach the Green's function can only be calculated at finite temperature whereas the experimental conditions using ( $e, e' p$ ) scattering correspond to zero temperature. Below a critical temperature  $T_C$  the transition to a superfluid phase sets in, which can be understood as a superposition of N–N pairs with particles of opposite spin and momentum [69]. This phenomenon can not be described in terms of a propagator expansion and is referred to as pairing instability. In principle the results from the grand-canonical calculation can be extrapolated to zero temperature on the

level of the self energy, which is a rather smooth function of energy. On the other hand the occupation for nuclear matter becomes already temperature independent below 5 MeV. For  $T < 5$  MeV, finite-temperature calculation thus can be employed to describe  $T = 0$  systems. The occupation is 89 % at zero momentum.

To compare the result from this approach with the data of the present work (sec. 8.4) the spectral function was calculated for the lowest accessible temperature of 2 MeV at half of the saturation density, which corresponds to the average density for  $^{12}\text{C}$ . Because the spectral function is calculated for infinite nuclear matter a useful comparison can only be made in the correlated region at large momentum and energy, where effects of the shell structure are suppressed. In this region SRC play the dominant role compared to LRC and finite size effects which are not treated in the present state of the theory.

### 1.2.7 Correlated Basis Function theory for nuclear matter and finite nuclei

The calculation of the spectral function using the Correlated Basis Function theory (CBF) is quite complex and only practical for nuclear matter. For finite nuclei the spectral function can be obtained using the Local Density Approximation (LDA). In the following these methods will be briefly explained.

The CBF theory is based on the variational method, which is the zeroth order of the perturbative expansion used in CBF. Contrary to the approaches discussed above correlations are directly included in the wave function. The variational wave function  $\Psi_V$  is obtained from the uncorrelated one  $\Psi_{uc}$  (i.e. plane waves with occupation number  $n^{occ}(k < k_F) = 1$ ) via the pair-correlation operator  $F_{ij}$

$$\Psi_V = \left( S \prod_{i>j=1}^A F_{ij} \right) \Psi_{uc} \quad \text{with} \quad (1.22)$$

$$F_{ij} = \sum_p f^p(r_{ij}) O_{ij}^p \quad (1.23)$$

The product runs over all pairs i,j in the nucleus A and  $S$  takes care of the symmetrization. The operator  $O^p, p = 1 \dots 8$  contains the central (Jastrow), spin, tensor, isospin and spin-orbit correlations. The radial correlation functions  $f^p(r)$  are determined by minimizing the energy expectation value. The evaluation of the expectation value is quite elaborate and can be done most efficiently with the help of Fermi-hypernetted chain (FHNC) or Variational

Monte Carlo Method. The FHNC is an integral equation, which sums up the important diagrams in the cluster expansion. Comparing the contribution from the Jastrow correlation operator with and without the spin-orbit part, it turns out that the spin-orbit correlations are more important. In Fig. 1.5 one can note that the variational approach does not have the right behavior close to the Fermi momentum. The occupation probability increases first and drops to a small constant value 0.01 beyond the Fermi momentum. Therefore a correction of second order seems to be necessary. This is done in the correlated basis perturbation theory.

In CBF theory the ground state is constructed in analogy to Eq. 1.22 but now using n-hole–m-particle Fermi gas states with occupation number smaller than one. With the pair-correlation operator  $F_{ij}$ , which was determined using the variational method, this leads to the correlated basis. Initially the correlated states are not orthogonal to each other. They are orthogonalized by the Schmidt-Löwdin transformation. The lowest order approximation is identical to the variational method. At zeroth order SRC are already included and a substantial quenching of the quasi-particle states is observed (Fig. 1.5). In the following the correlated basis perturbation theory is restricted to second order ( $n = m = 2$ ). Then the ground state is restricted to 2h2p intermediate states. The 2h2p admixture to the ground state is the most important perturbative correction to the ground state [20]. It contributes to all momenta below and above the Fermi momentum. The main effect of the ground state correction is the quenching of the strength for  $k < k_F$  and consequently an increase for  $k > k_F$ . Further it leads to a shift of the single-particle energies for particles and holes, which is also experimentally observed (s. discussion in sec. 1.1). The 2h1p state contributes in lowest order to two-nucleon emission. It gives the main contribution to the background term for all momenta below and above the Fermi momentum, which is associated with multi-particle emission. The background contribution is continuous at  $k_F$  and  $\epsilon_F$  (s. also Fig. 1.4). In second order of the perturbative expansion the 2h1p states lead to broadening of the otherwise delta-shaped single-particle states due to the coupling with the hole states but does not affect the momentum distribution.

In Fig. 1.5 the occupation probability

$$n^{occ}(k) = \int_{\epsilon_S}^{\infty} 4\pi k^2 S_h(E, k) dE \quad (1.24)$$

as a function of the momentum is shown for the variational method as well as for the CBF approach with and without tensor correlations. The large effect of the second-order corrections included in the CBF theory is obvious, when comparing to the variational approach. Most important are the tensor

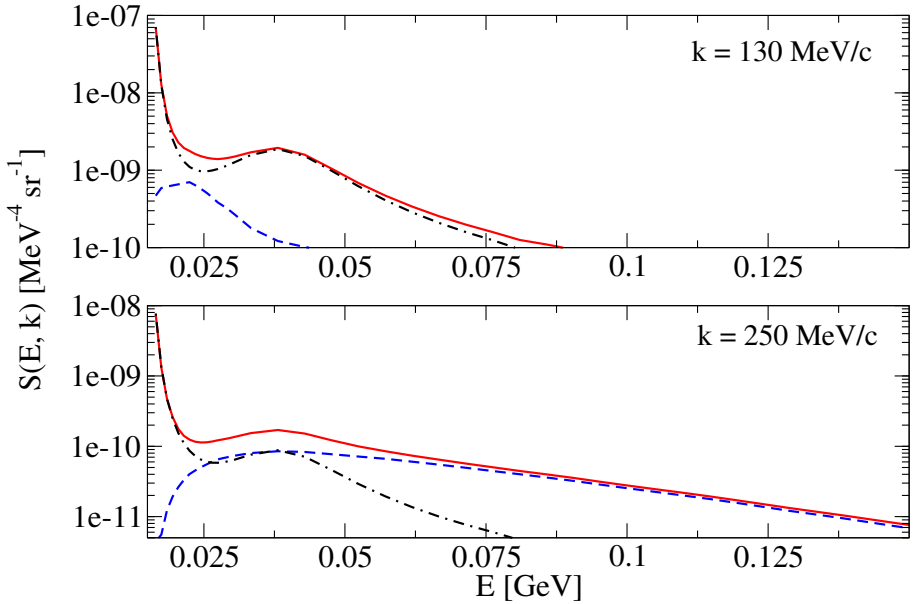


Figure 1.12: Decomposition of the spectral function for  $^{12}\text{C}$  from CBF theory into the single-particle (dot-dashed) and correlated part (dashed). The total spectral function is shown by the solid line.

correlations. Without tensor correlations the second-order CBF corrections are reduced by almost a factor of four [64]. For this calculation the Urbana V14 + TNI interaction was used.

The spectral function for nuclear matter can easily be separated into a background (also called correlated or continuous) part  $S_{corr}$  and the quasi-hole strength  $S_{qh}$ , which is obtained, when only one-hole intermediate states are included.

$$S = S_{qh} + S_{corr} \quad (1.25)$$

In Fig. 1.12 the two parts of the spectral function for  $^{12}\text{C}$  are shown for two momenta  $k = 130 \text{ MeV}/c$  and  $250 \text{ MeV}/c$ . Below the Fermi momentum the correlated part is negligible (dashed line) compared to the quasi-hole strength (dot-dashed). At the Fermi momentum the two parts have already equal strength at low energy, whereas at larger energy ( $> 50 \text{ MeV}$ ) the correlated spectral function dominates entirely. For even larger momenta the single-particle spectral function dies out in favor of the correlated one.

To get the spectral function for finite nuclei the quasi-hole part is replaced by the single-particle spectral function  $S_{sp}$  taken from IPSM or experimental data but normalized such that, together with the correlated part, the number of particles is conserved. The correlated part is obtained using the

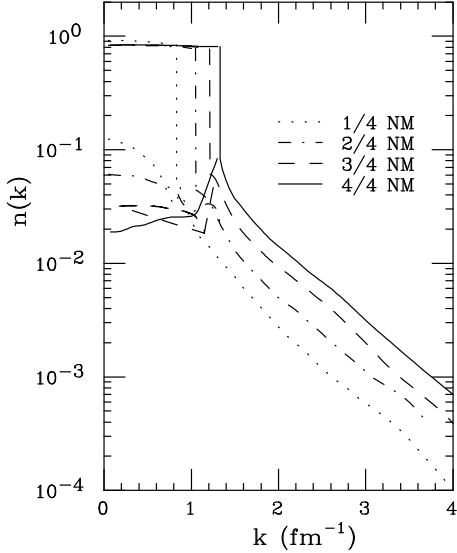


Figure 1.13: Momentum distribution of nuclear matter for different densities. The lower curves give the contribution to the correlated part [22].

Local Density Approximation (LDA). For this it is convenient to work in the coordinate representation. The r-space spectral function depends besides the energy on the positions of the two interacting nucleons or alternatively on the center-of-mass coordinate  $R$  and the relative interparticle distance  $r$ . The r-Fourier transformation

$$S(R, k, E) = \int dr e^{ikr} S(R, r, E) \quad (1.26)$$

gives the probability to find a nucleon with momentum  $k$  and energy  $E$  at the c.m. distance  $R$  in the nucleus. Integration over  $R$  gives the previously defined spectral function. In LDA the correlated spectral function  $S_{corr}^{LDA}$  for finite nuclei is obtained from the spectral function for nuclear matter via

$$S_{corr}^{LDA}(R, r, E) = \rho(R) S_{corr}^{NM}(\rho(R), r, E) \quad (1.27)$$

evaluated for different fractions of the density in nuclear matter  $\rho(R)$ . The approximation of using  $\rho(R)$  instead of  $\sqrt{\rho(r_1)\rho(r_1')}$  gives indistinguishable results [22].

In Fig. 1.13 the spectral function of nuclear matter is shown for different densities. With increasing density the strength at high momentum increases. For large density correlations are more pronounced due to the reduced average distance between the nucleons. The correlated part for finite nuclei is

obtained by integrating the spectral function  $S_{corr}^{LDA}(R, r, E)$  over the nuclear volume. The application of the LDA requires that the spectral function does only weakly depend on the center-of-mass coordinate. This should be the case because the interparticle distance is in particular for SRC much smaller than the surface thickness, where the density changes rapidly.

The strengths of the correlated part for carbon, iron, and gold are 0.220, 0.215, 0.207 respectively [23]. The single-particle spectral function was taken from IPSM (sec. 4.1.2), normalized and added to the correlated part. For carbon the momentum distribution is shown in Fig. 1.6 together with the one from IPSM and from the Green's function approach [128]. The CBF theory has more strength at the high momentum components compared to the Green's function approach.

To include approximately finite size effects the imaginary part of the CBF self energy was modified in such a way to reproduce the measured widths of the states close to the Fermi surface. This procedure is justified in the quasi-particle approximation (sec. 1.3.1). The  $E$ -dependence of the self energy was fitted using the empirical parametrization for the imaginary part of the self energy  $\text{Im}\Sigma = W_o(e - \epsilon_F)^2 = W_o E_x^2$ . The so obtained hole strength  $Z$  for Pb is shown in Fig. 1.4 as the long-dashed line. In comparison with the hole strength for nuclear matter a significant decrease of  $\approx 15\%$  is obtained at the Fermi surface. The result is in remarkable agreement with the data of [151]. This leads to the conclusion that the integrated strength measured at NIKHEF does not include the background contribution  $n_c$  but is a measure of the spectroscopic strength summed over a few fragments of the single-particle state rather than the occupation number. Shown in the same figure are the occupation probability and the background term  $n_c$  for nuclear matter. Because of the smallness of  $n_c$  it is augmented by a factor of three in the plot. It should be pointed out that the difference between the occupation probability and the integrated spectroscopic strength is due to the background term, which is spread over a wide energy range. This is the reason why the occupation number is extremely difficult to measure.

The list of theoretical approaches discussed above is certainly not complete. For a review of modern many-body theories see [15] and [130].

### 1.2.8 Conclusions

Correlations cause part of the strength of a state to be redistributed over a broad continuum, predominantly due to the coupling of the ground state to 2h1p configurations. Part of the strength is shifted to energies above  $\epsilon_F$  and can therefore be found in the particle spectral function. Similar to Eq. 1.24

the depletion in the hole states can be defined as

$$d(k) = 1 - n^{occ}(k) = \int_{\epsilon_S}^{\infty} 4\pi k^2 S_p(E, k) dE \quad (1.28)$$

The redistribution of strength results in a deviation of the spectroscopic factor from one and a spread of the strength to high energy and momentum. Since in the HF approximation the self energy does not contain any residual interaction besides the mean field, no fragmentation and reduction of the strength can occur. However, modern many-body theories predict an occupation of  $\approx 80\%$ , whereas in the experiment only 60 % of the strength is found for valence states (sec. 1.1). On one hand side this is due to the fact that these experiments measure rather spectroscopic factors than occupation numbers and thus the background term, which can not be attributed to a specific state via its momentum distribution, is not included. On the other hand this is ascribed to LRC, which couple the single-particle states to low-lying excitations like surface vibrations and the Gamow-Teller resonance. In most of the theories which treat SRC, this coupling is not included; if included, then in a crude approximation, where only 2p1h and 2h1p intermediate states are considered. On this level collective excitation of pp, ph or hh pairs are missing.

Comparison with experimental data [100] shows that the distribution of the fragmented strength can not be described by the theory yet. A better treatment of LRC can be achieved by including in addition correlations obtained in the Random Phase Approximation (RPA). A problem arising in RPA is the appearance of imaginary eigenvalues for some excitations due to the strong collective correlations. Therefore these solutions have to be disregarded. In a self-consistent RPA (Super RPA), where the Green's function formalism is used for a consistent summation of all ph, pp and hh excitations, such problems would disappear. Such an approach is especially needed for open-shell nuclei, where pairing correlations play a dominant role. The RPA reduces to the Tamm-Dancoff Approximation (TDA) when correlations in the ground state are neglected. Comparing both approaches with the experimental excitation spectrum obtained from  $^{48}\text{Ca}(\text{e},\text{e}'\text{p})^{47}\text{K}$  [100] shows that the fragmentation is overestimated in RPA and underestimated in TDA [50]. In this calculation the additional depletion from SRC was neglected. If one would account for 10–15 % depletion due to SRC then the spectroscopic factors could be well reproduced. An improved treatment of collective excitations was developed by [16], where three-body terms are treated by embedding the Faddeev equation into the self-consistent Green's function formalism.

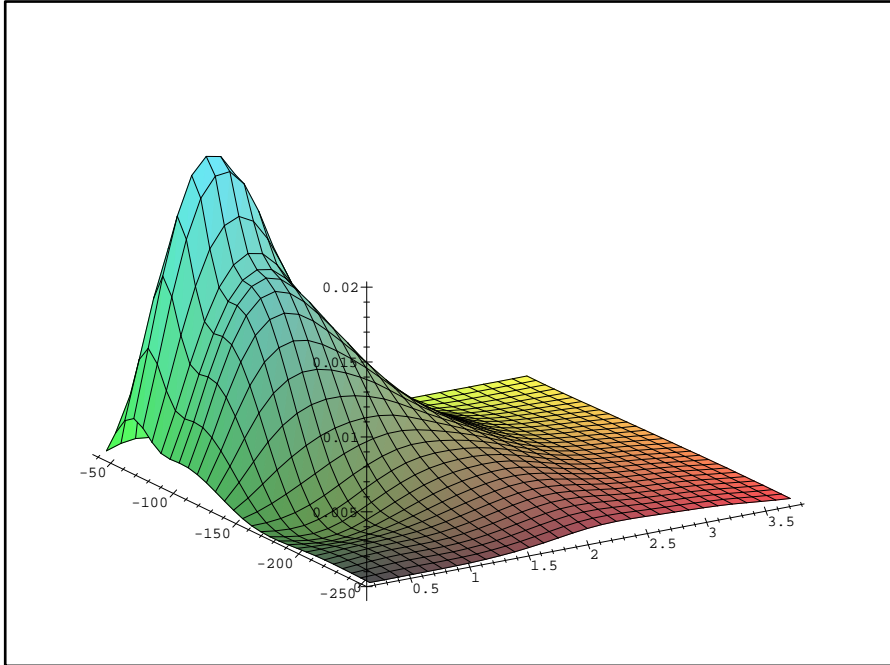


Figure 1.14: The correlated part of the spectral function for  $^{16}\text{O}$  weighted with  $4\pi k^2$  in units of fm/MeV as a function of energy [MeV] and momentum [fm].

The high-momentum components induced by SRC originate from the spectral function preferably at large missing energies and lead to configurations of the A-1 particle system at energies above the threshold of emission of an additional nucleon. In a simple view of SRC a virtual nucleon–nucleon pair is formed and due to the repulsive core of the N-N potential at short distance both nucleons are scattered to high momenta. If the incident electron interacts with one nucleon of such a pair then one nucleon will be knocked out as usual in a  $(e,e'p)$  reaction while the other leaves the nucleus with the opposite initial high momentum. The residual nucleus acts in this case as spectator. From energy conservation it follows that

$$E_x(A-1) + T_{A-1} = \frac{k^2}{2M}, \quad (1.29)$$

where  $T_{A-1}$  is the recoil energy of the A-1 system. With  $T_{A-1} \approx \frac{k^2}{2(A-1)M}$

one obtains for the excitation energy of the A–1 system

$$E_x(A-1) = \frac{A-2}{A-1} \frac{k^2}{2M} \quad (1.30)$$

The missing energy measured in the experiment for such a system would then consist of  $E_x(A-1)$  plus the threshold for two–nucleon knock–out  $E^{2N} = E_o^A - E_o^{A-2}$  of around 40 MeV<sup>6</sup>. At this energy the maximum of the spectral function is expected, leading to a ridge. The Green’s function approach and the CBF theory as presented in this section and most other theories agree with this prediction from the simple model. However, for the self–consistent solution of the Green’s function for nuclear matter (sec. 1.2.6) a shift of the maximum of the spectral function to lower energies is observed [69]. All three theoretical spectral functions will be compared to the experimental result for <sup>12</sup>C in sec. 8.4.

In Fig. 1.14 the correlated part of the spectral function from the Green’s function approach for <sup>16</sup>O is shown as a function of energy and momentum. For a better presentation the spectral function is weighted with  $4\pi k^2$  (spectral density) to make the high momentum components visible. The position of the ridge can be clearly seen at high momenta.

## 1.3 Occupation numbers

### 1.3.1 $n^{occ}$ from theory

In theory the occupation number can be obtained by integrating the hole spectral function over the total momentum range

$$n^{occ}(E) = \int_{\epsilon_S}^{\infty} 4\pi k^2 S_h(E, k) dk. \quad (1.31)$$

If the occupation number is divided by the number of protons in the nucleus, one obtains the occupation probability. In Fig. 1.4 the occupation probability calculated in CBF theory [21] is shown as a function of the energy relative to the Fermi energy. The background contribution  $n_c$  from the hole ( $e - \epsilon_F < 0$ ) and particle ( $e - \epsilon_F > 0$ ) spectral functions<sup>7</sup> is indicated by the dotted line. The discontinuity at the Fermi energy in nuclear matter

---

<sup>6</sup>This value is usually taken for nuclear matter. For <sup>12</sup>C a 2–N threshold of 22.34 MeV was measured [27].

<sup>7</sup>Because this is a calculation for nuclear matter the energy  $e$  is defined in analogue to the Fermi model. Due to the relation  $e = k^2/2M$  also the correlated part of the hole spectral function for momenta larger than  $k_F$  appears at  $e > \epsilon_F$  in Fig. 1.4.

separating the hole and the particle part can be related to the quasi-hole strength  $z$ ,

$$z(\epsilon_F) = n^{occ}(E-) - n^{occ}(E+) \quad (1.32)$$

where  $n^{occ}(E-)$  ( $n^{occ}(E+)$ ) is the occupation probability just below (above) the Fermi energy. The quasi-hole strength gives the probability that the (quasi-) particles reside in a well defined orbit as expected from the simple shell model.

$$n_i^{occ} = \frac{\langle i | a^+ a^- | i \rangle}{\langle i | i \rangle}, \quad (1.33)$$

Neglecting configuration mixing and LRC  $z$  corresponds approximately to the spectroscopic factor  $Z$  for valence shells (near the Fermi energy) in finite nuclei [142]. The spectroscopic factor is defined as the square of the overlap of the ground state of the nucleus A with the wave function of the final state  $\alpha$  in the nucleus A-1

$$Z_\alpha = | \langle \Psi^{A-1} | a_\alpha | \Psi_o^A \rangle |^2 \quad (1.34)$$

From Eq. 1.32 it becomes clear that the quenching of the single-particle contribution observed experimentally (sec. 1.1) is also due to partial occupation of the orbits in the residual nucleus A-1. The presence of correlations in the hole states is reflected by the deviation of  $z$  from unity as well as by an increase in the width of the valence states. These features appear most clearly in the quasi-particle approximation. It is obtained by expanding the self energy  $\Sigma(k, E)$  around the single-particle energy  $\epsilon(k)$ , which is a solution of Eq. 1.15. Then one obtains the following expression for the spectral function in the quasi-particle approximation<sup>8</sup>

$$S_{QP}(E, k) = \frac{1}{\pi} \frac{z^2(k) |W(k)|}{(E - \epsilon(k))^2 + (z(k)W(k))^2} \quad (1.35)$$

with  $W(k) = \text{Im } \Sigma(k, \epsilon(k))$  and

$$z(k) = \left[ 1 - \frac{d}{dE} \text{Re } \Sigma(k, E) \right]_{E=\epsilon(k)}^{-1} \quad (1.36)$$

According to Eq. 1.35 the shape of the spectral function in the quasi-particle approximation is a Lorentzian centered at the single-particle energy with a width  $\Gamma = 2z(k)|W(k)|$ . The width is related to the life time of the state  $\tau = 1/\Gamma$ . The quasi-hole strength is a measure of the total strength in the quasi-hole peak. The inverse of it is proportional to the E-mass/M used in the work of [112].

---

<sup>8</sup>In some works this is called Lorentzian approximation and the term "quasi-particle approximation" is used if the width  $\Gamma$ , i.e. the imaginary part of the self energy, is neglected.

### 1.3.2 $n^{occ}$ from experiment

From the previous remarks it becomes clear that occupation numbers are difficult to measure because the strength, which belongs to a shell, is spread over a large range of momentum and energy respectively. This is caused on one hand side by LRC, which leads to a strong fragmentation in energy and an increased width of the deep lying hole states. On the other hand SRC, which leads to high momentum components, are responsible. One should keep in mind that in the theoretical definitions of the occupation number in Eqs. 1.24 and 1.31 either the momentum is fixed and the integration is performed over the energy ( $\Rightarrow n^{occ}(k)$ ) or the energy is kept constant while performing the integration over the complete momentum range ( $\Rightarrow n^{occ}(\epsilon)$ ). For nuclear matter these definitions can be used equivalently but from the experimental point of view only the latter definition is useful. In [19] it was possible to sum up nearly all fragmented pieces of the deep-lying hole states in lead in a limited momentum range. The average depletion in the missing energy range from 30 to 60 MeV is  $0.8 \pm 0.06$  including statistical, systematic and model dependent error. This result is in good agreement with the prediction of the modern many-body theory for nuclear matter. Including the valence states (0 – 60 MeV) the average occupation is reduced to  $0.77 \pm 0.05$  due to LRC at the Fermi surface.

Another method to extract occupation numbers is the Combined Evaluation of Relative spectroscopic factors and Electron Scattering (CERES), which was applied to spectroscopic factors obtained from pick-up reactions [43] [82] as well as from (e,e'p) experiment [150]. The CERES method needs two ingredients. One is the z-value of the 3s orbit extracted from the absolute charge difference  $\rho(^{206}Pb) - \rho(^{205}Tl)$ , which was determined from elastic scattering. A value  $z = 0.64 \pm 0.06$  was found using a careful treatment of the core polarization effects [40] [162]. Core polarization effects lead to an additional change of the charge distribution induced by adding a nucleon to the core. In CERES it is assumed that the change in the charge difference of the  $3s_{1/2}$  state can be identified with the difference in occupation numbers  $n_{3s}^{occ}(^{206}Pb) - n_{3s}^{occ}(^{205}Tl)$ .

The other ingredient necessary to obtain occupation numbers is the ratio of the spectroscopic factors  $Z(^{206}Pb)/Z(^{208}Pb)$  and  $Z(^{205}Tl)/Z(^{208}Pb)$  for the  $3s_{1/2}$  orbit, which is best taken from (e,e'p)-experiments performed in the single-particle region. An advantage of this method is that only relative spectroscopic factors are needed, which reduces the sensitivity to the experimental details like resolution and integration range as well as systematic errors. To obtain the occupation one replaces the ratio of spectroscopic factors by the ratio of occupation numbers, which is valid, if the same fraction

of nucleons resides in the single-particle orbit (main fragment). As the  $3s_{1/2}$  state is a valence state, which is half filled in  $^{205}\text{Tl}$ , it will be more influenced by LRC, which is sensitive to the shell structure. On the other hand, when using neighboring nuclei the shell structure is quite similar. Taking the results from [151] for the relative spectroscopic factors one obtains the occupation number for  $^{206}\text{Pb}$  via

$$n^{occ}(^{206}\text{Pb}) = z / \left( \frac{Z(^{206}\text{Pb})}{Z(^{208}\text{Pb})} - \frac{Z(^{205}\text{Tl})}{Z(^{208}\text{Pb})} \right). \quad (1.37)$$

The result  $n^{occ}(^{206}\text{Pb}) = 0.76 \pm 0.07$  is in remarkable agreement with the one from [19] using the full missing energy range.

Using the same method occupation numbers of the  $2s_{1/2}$  state in  $^{30}\text{Si}$ ,  $^{31}\text{P}$ ,  $^{32}\text{S}$  were obtained [187]. For  $^{30}\text{Si}$  an occupation of  $\approx 0.25$  nucleons was found for the  $2s_{1/2}$  orbit, which is empty in the IPSM. The occupation of the  $2s_{1/2}$  orbit in  $^{32}\text{S}$  was determined to 1.35(19), which corresponds to around 70 % of the IPSM prediction. The influence of using different effective nucleon-nucleon interaction was investigated. It turns out that the result of the analysis for even-even nuclei is not very sensitive to the chosen interaction (finite or zero-range character).

## 1.4 Different approaches to search for SRC

Considerable effort was made in the past to look for an unique signature of SRC. Quite different approaches were tried. Different particles as probes like protons, electrons and photons were used. Recently polarization observables were exploited [76]. The investigated nuclei range from deuterium to gold. In addition different kinematics were chosen to optimize the condition, where SRC could be observed and would not be hidden by contributions from other reaction mechanisms like FSI and MEC. These processes make the unique identification of SRC very difficult. In the following some experiments and results will be reviewed, but the list will be rather incomplete.

At BNL the reaction  $^{12}\text{C}(\text{p},2\text{p}+\text{n})$  was studied at beam momenta 5.9 – 9.0 GeV/c leading to  $Q^2 > 4.8$  (GeV/c)<sup>2</sup> [168]. In a preceding experiment [116] it was shown that under the kinematical condition  $\theta_{cm} = 90^\circ$  the scattering process is quasi-elastic and PWIA can be applied. For p-p elastic scattering at  $\theta_{cm} = 90^\circ$  the cross section decreases like  $s^{-10}$ , where s is the c.m. energy. Therefore protons with large initial momentum in direction of the beam are selected. The scattered and knocked-out protons were detected in one spectrometer. In the backward hemisphere below the midplane of the spectrometer a segmented neutron detector was placed. The neutron

momentum was determined via TOF with a resolution of 30 MeV/c at the highest momentum of 600 MeV/c. A clear correlation between back-to-back scattered neutrons and protons with initial momentum  $k$  larger than the Fermi momentum were observed whereas no such correlation was found for neutrons with initial momentum less than  $k_F$ . This distribution is taken as evidence for short-range correlations. Further the reconstructed c.m. (longitudinal) momentum of the pn-pair in the nucleus is centered at zero. This supports the association of a correlated pair. Remarkable is the large fraction ( $\approx 50\%$ ) of (p,2p) events with  $k > k_F$ , where an additional neutron with momentum larger than  $k_F$  is emitted backward. The statistics of this experiment is low, as only 18 triple coincidence events were found. It should be noted that this fraction includes only pn-pairs. The advantage of N-N scattering is that radiative corrections are negligible as compared to electron scattering. Further the pp cross section is larger than the ep cross section due to the strong interaction. On the other hand it is a much more difficult task to get initial and final state interactions of all participating particles under control.

Already in the '50s it was discovered that photodisintegration on complex nuclei shows a similar angular distribution as found in the photodisintegration of the deuteron except that the angular correlation of the pn-pair was broadened due to the Fermi motion of the pair. Several experiments were performed using real photons to study the behavior of nucleon pairs at short distances. Because the reaction is purely transverse several reaction mechanisms like MEC, IC and  $\Delta$ -excitation are involved. These experiments are often used to study the reaction mechanism.

The experimental cross sections have been compared to the Valencia model for example, which gives a reasonable description of the  $(\gamma, \text{pn})$ -reaction but overestimates the  $(\gamma, \text{pp})$  cross section. In the reaction  $^{12}\text{C}(\gamma, \text{pn})$  significant excess in the pair momentum distribution for recoil momenta larger 400 MeV/c was found relative to a calculation without SRC. The prediction of [141] treating SRC could explain the trend of the data [178].

Other experiments with high resolution aim to determine the quantum numbers of the pn-pair absorbed in the reaction. This is possible using e.g.  $^{16}\text{O}$ , which has vanishing spin. Therefore the quantum numbers of the pair are identical to the one of the residual nucleus [74] [88]. This opens up the possibility to test predictions of the momentum distribution of the np-pairs in  $^{16}\text{O}$  dependent on the quantum numbers of the pair. Under certain conditions NN-correlations can contribute up to 50 % and affect also the shape of the cross section as a function of the angle of the second emitted nucleon [156]. Recently the three-nucleon mechanism was studied using  $^{12}\text{C}(\gamma, \text{ppn})$  [179].

Evidence for short-range correlations was found in inclusive electron scat-

tering data at high  $Q^2$  and  $x > 1$  [66], which corresponds to the low energy loss side of the quasi-elastic peak. Here the contribution from inelastic electron scattering and MEC is small but FSI is not negligible. For large  $x$  large missing momenta are sampled. Because the nucleon momentum distribution at large  $k$  is very similar for light and heavy nuclei, if caused by SRC, the ratio of cross sections measured for different nuclei should scale, i.e. be independent of  $Q^2$  and  $x$ . Scaling is indeed observed for  $Q^2 > 1.4$  (GeV/c) $^2$  and  $x > 1.5$  [61]. From the ratio of the cross section for heavy nuclei to deuterium the per-nucleon SRC probability can be derived, which saturates for  $A \geq 12$ . Approximately 5.5 times more correlated nucleons for  $A \geq 12$  are found as compared to deuterium and a factor of  $\approx 3.5$  more for  ${}^4\text{He}$ .

An (e,e'p)-experiment was performed for  ${}^{16}\text{O}$  at  $Q^2 = 0.8$  (GeV/c) $^2$  in Hall A at Jlab covering a region of  $E_m < 120$  MeV and  $p_m \leq 340$  MeV/c [106]. In all kinematics the angle between the final proton momentum and the momentum transfer was less than  $20^\circ$ . This experiment confirms the result of previous measurements at MIT [107][176][181][122] finding large transversal strength at high  $E_m$  and  $p_m > 200$  MeV/c. In this region the cross section becomes almost constant and many times bigger than the cross section expected due to SRC. Calculations of Ryckebusch [90], which include pion-exchange and isobar configuration as well as SRC could only account for half of the cross section.

A few experiments investigated the reaction (e,e'NN), but suffer from the extremely small cross sections ( $\approx$  attobarn =  $10^{-42}$  cm $^2$ ). In PWIA one can then access directly the two-nucleon spectral function  $F_{h_1 h_2}(E_m, p_m)$ , which gives the joint probability to find a pair of nucleons with  $p_m$  and  $E_m$ . In [28] data in the dip region on  ${}^{12}\text{C}$  were taken using the reaction (e,e'pp). The largest sensitivity to NN correlations was found in super-parallel kinematics, where the protons are emitted back-to-back and one proton along the momentum transfer. This suppresses effectively the  $\Delta$  contribution. Good agreement of the data was found with the Green's function approach of [51]. Different kinematics could be studied at once using an almost  $4\pi$ -detector. Similar data of the CLAS collaboration at higher  $Q^2$  are currently under analysis [182]. Calculations of the mutual interaction between the two outgoing protons (NN-FSI) were performed for several kinematics [158]. It was found that even in the super-parallel kinematics significant contribution from NN-FSI makes a PWIA analysis questionable. The authors conclude that a full three-body calculation is necessary to control NN-FSI in the experiment. The same result was found earlier in [97].

At  $Q^2$  between 0.5 and 1 (GeV/c) $^2$  the CLAS collaboration investigated the reaction  ${}^3\text{He}(\text{e},\text{e}'\text{NN})$  under the condition of a fast striking nucleon [138], which got most of the momentum transfer. Then the correlated specta-

tor NN-pair could be detected almost entirely back-to-back. Calculations showed that the PWIA cross section is reduced significantly by continuum state interaction of the outgoing NN-pair. The yield obtained from experiment and the full calculation of Laget is roughly in agreement.

In summer 2004 experiment E01-015 [191] in Hall A at Jlab is scheduled. It will take data at large  $Q^2$  and  $x > 1$  probing initial momenta in the range 250–600 MeV/c via the reaction  $^{12}\text{C}(\text{e},\text{e}')\text{p}+\text{N}$ . For this an array of scintillators will be placed behind the BigBite to measure simultaneously neutrons and protons back-to-back to the proton detected in one of the standard Hall A spectrometers. In this arrangement one can compare between the cross sections containing pn- and pp-pairs. Further the fraction of  $(\text{e},\text{e}')\text{p}$  events, which are associated with NN-SRC can be determined.

## 1.5 Design of the present experiment

The aim of experiment E97-006 is to measure the spectral function of the proton at high initial energy and momentum using the reaction  $(\text{e},\text{e}')\text{p}$  in order to get insight into short-range correlations. At the time of the proposal several  $(\text{e},\text{e}')\text{p}$ -experiments had been already carried out for the same purpose, performed at Bates, Saclay and Mainz. The region in momentum and energy covered is shown in Fig. 1.15. The abbreviations used for each experiment can be found in the figure caption. The experiments at Bates [107] [13] [181] [121] were all performed on  $^{12}\text{C}$ . At Mainz [27] a waterfall target was used as  $^{16}\text{O}$  target. At Saclay [80] [115] data were taken on  $^4\text{He}$  and  $^3\text{He}$ .

Experiments performed in the region of high missing energy and moderate initial momentum (less than  $k_F$ ) found cross sections much larger than predicted by PWIA. These experiments are marked with solid lines. At high missing energy and high momentum the experimental cross sections were comparable to PWIA within a factor of two (dashed lines). At moderate momentum the spectral function decreases rapidly with increasing energy whereas at high momentum the spectral function is widely distributed. Therefore experiments done at high  $E_m$  and  $p_m < k_F$  are affected considerably by 2-step processes as it was shown in a simulation performed for the proposal E97-006 [163]. In the 2-step process the  $(\text{e},\text{e}')\text{p}$ -reaction is followed by  $(\text{p},\text{p}'\text{N})$  in the same nucleus. This process is called rescattering (sec. 8.6). It was argued in the proposal that the 2-step process depends primarily on the spectral function relevant for the  $(\text{e},\text{e}')\text{p}$  process. If the same kinematical conditions for electrons and protons can be reached either in the  $(\text{e},\text{e}')\text{p}$  reaction or in the 2-step process the size of the spectral function decides whether

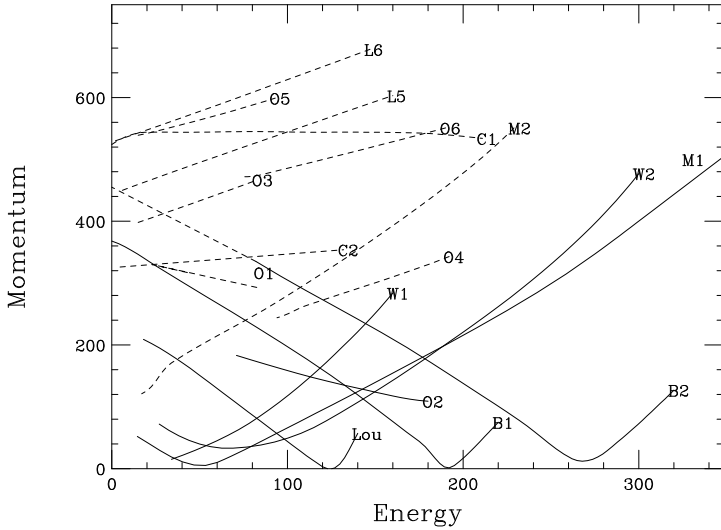


Figure 1.15: Kinematical coverage of first generation  $(e, e' p)$ -experiments indicated with *Lou* [107], *B1, B2* [13], *W1, W2* [181], *M1, M2* [121][122], *L1–L6* [80], *C1, C2* [115], *O1–O6* [27]. The dashed lines corresponds to kinematics, where the measured cross section is approximately in agreement with PWIA. Solid lines indicate the region, where the experimental cross section exceeds the PWIA prediction considerably.

the reaction one is searching for is overwhelmed by rescattering or not. The latter is the case for perpendicular kinematics, where the initial momentum is perpendicular to the momentum transfer  $q$ . Rescattering contributes less in parallel kinematics because of the high momentum of the knocked-out proton required by the kinematics. These basic findings are also confirmed by a calculation of the rescattering contribution for this experiment by C. Barbieri (sec. 8.6).

Further the region of high  $E_m$  and low  $p_m$  is fed from the single-particle region via the  $\Delta$ -excitation or higher resonances. Because the spectral function is orders of magnitude larger in the single-particle region this process can make significant contributions. Due to the decay of the resonance a pion is produced but not detected. Because of the pion mass of 140 MeV this strength reappears at  $E_m$  larger than 150 MeV. Due to the transversal character of the resonances as well as MEC and isobar configuration (IC) it is expected that the perpendicular kinematics is more affected.

| Label | Beam energy | Central electron momentum | Central electron angle | Central proton momentum | Central proton angle | Average $\theta_{qpi}$ |
|-------|-------------|---------------------------|------------------------|-------------------------|----------------------|------------------------|
|       | (GeV)       | (GeV/c)                   | degree                 | (GeV/c)                 | degree               | degree                 |
| kinp1 | 3.298       | 2.75                      | 12.5                   | 1.00                    | 73.0                 | 91                     |
| kinp2 | 3.298       | 2.75                      | 12.5                   | 0.85                    | 70.0                 | 92                     |
| kin3  | 3.298       | 2.05                      | 12.5                   | 1.70                    | 29.0                 | 36                     |
| kin4  | 3.298       | 2.40                      | 12.5                   | 1.50                    | 30.0                 | 21                     |
| kin5  | 3.123/3.120 | 2.50                      | 12.5                   | 1.25                    | 38.0                 | 25                     |

Table 1.1: Overview of the five kinematics used in experiment E97–006.

### 1.5.1 Kinematics

Because of the considerations discussed above the experiment was performed primarily in parallel kinematics (kin3, kin4, kin5). Two perpendicular kinematics (kinp1, kinp2) were included for comparison. The central kinematics are shown in Tab. 1.1. The  $Q^2$  is 0.3–0.4 (GeV/c)<sup>2</sup> for all kinematics. In parallel kinematics one is probing the high energy loss side of the quasi-elastic peak. Therefore large  $p_m$  leads to small Bjorken x, which is 0.1–0.3 for the present experiment.

It should be pointed out that the notation "perpendicular" and "parallel" refers to the angle  $\theta_{qpi}$  between the momentum transfer q and the initial momentum. In much of the literature the angle between q and the final proton momentum is taken as indication. This is by far not the same. The requirement of small angles  $\theta_{qpi}$  for parallel kinematics is much more restrictive and more difficult to fulfill. The term "perpendicular kinematics" in the sense it is used here is sometimes called transverse kinematics. The angle  $\theta_{qpi}$  are shown in Tab. 1.1 for the five kinematics. The resonance region appearing in the parallel kinematics was removed from the data according to sec. 8.7.4, which would otherwise result in a misleadingly large  $\theta_{qpi}$ .

The perpendicular kinematics should help to understand the reaction mechanism. Calculations done to correct the measured distorted spectral function can be tested (sec. 8.6). Further, data for four different targets <sup>12</sup>C, <sup>27</sup>Al, <sup>56</sup>Fe and <sup>197</sup>Au in the same kinematics were taken. These nuclei are approximately equally spaced in the mass number  $A^{1/3}$ , which is proportional to the size of the nucleus. The contribution of rescattering and absorption increases with the size of the nucleus.

In Fig. 1.16 the  $E_m p_m$ -region covered by the experiment is shown for perpendicular and parallel kinematics. A missing momentum of up to 800

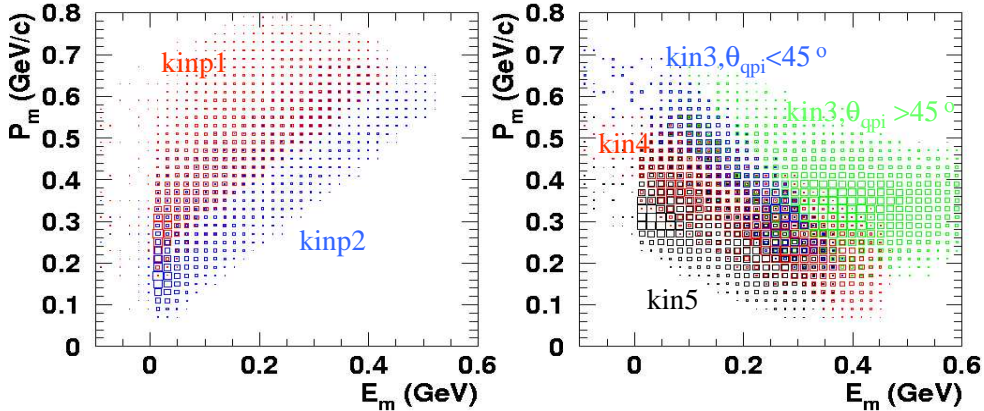


Figure 1.16:  $E_m p_m$ -region covered by the present experiment in perpendicular (left) and parallel (right) kinematics measured on  $^{12}\text{C}$ . Indicated are the labels of the different kinematics as introduced in Tab. 1.1. Kinematics kin3 is split into angles  $\theta_{qpi}$  smaller and larger than  $45^\circ$ .

(700) MeV/c is reached in perpendicular (parallel) kinematics in the useful acceptance of the spectrometer. The details of the analysis will be described in sec. 4 and 8. Due to the large acceptance of the spectrometer also data in near perpendicular kinematics are sampled, in particular in kin3, which is split into a region  $\theta_{qpi}$  less and larger than  $45^\circ$ . This region is dominated by pion-electroproduction as obvious by the strength in Fig. 1.16 (sec. 8.7).

The protons were detected in the magnetic spectrometer SOS in coincidence with the electrons in the HMS. The setup of the experiment will be described in sec. 2. For calibration and check of the setup data were also taken on hydrogen and carbon on top of the quasi-elastic peak, i.e. in the single-particle region. The kinematics were chosen such that the same outgoing momenta for electron and proton were used as for the production runs, but the angles were changed. The analysis of these data and the results will be described in sec. 6 and sec. 7.

## 2 Experimental Setup

The experiment described in this work was performed in Hall C of the Department of Energy's Thomas Jefferson National Accelerator Facility (abbreviated with Jlab in the following). Data were taken from mid of August to the beginning of October 1999 with a two week maintenance period in between. This section gives an overview of the experimental equipment used by the experiment. The electron accelerator and the beam line instrumentation in Hall C are described and in particular the measurement of the beam energy explained. Further the solid targets and the hydrogen cryo-target used by the experiment are introduced. The section closes with the design and features of both magnetic spectrometers in Hall C with their detector packages and the trigger logic.

### 2.1 Electron accelerator

The accelerator of the Continuous Electron Beam Accelerator Facility (CE-BAF) consists of 160 super-conducting niobium cavities operating at 2 K in a racetrack-shaped layout (Fig. 2.1), where two linacs are connected by arcs containing bending magnets. In the standard tune each linac contributes 400 MeV to each pass  $i$ . Due to the increasing energy of the electrons after each pass an increasing bending power in the arc is required. Therefore the way through the arc is different for each pass. A maximum of five passes is possible, which leads to available electron energies of  $(i * 800 + 45)$  MeV<sup>1</sup>. The 45 MeV are provided by the injector.

Polarized electrons are produced by using strained-layer GaAs-crystal; a polarization of up to 80 % at a current of  $\approx 100 \mu\text{A}$ <sup>2</sup> can be obtained. For each hall a separate laser system is installed. When polarization is not

---

<sup>1</sup>Nowadays it is possible to tune the machine to a final energy of 6 GeV.

<sup>2</sup>200  $\mu\text{A}$  are possible with a reduced cathode lifetime of 300 C (Half of the lifetime at currents less than 100  $\mu\text{A}$ ).

needed as for the present experiment, the wavelength is reduced ( $\approx 780$  nm instead of  $\approx 840$  nm) to take advantage of the higher quantum efficiency [3].

The accelerator can deliver beam to all three experimental halls quasi simultaneously through the Beam Switch Yard. For each hall a different beam energy has to be delivered except for the highest pass, which can be used by all halls at the same time. The electron beam is quasi-continuous, but contains a microstructure of short beam bursts (1.67 ps) at a frequency of 1497 MHz. Each third burst is delivered through an arc to Hall C, which leads to a 2 ns structure. The arc of Hall C serves also for the measurement of the beam energy (sec. 2.2.4).

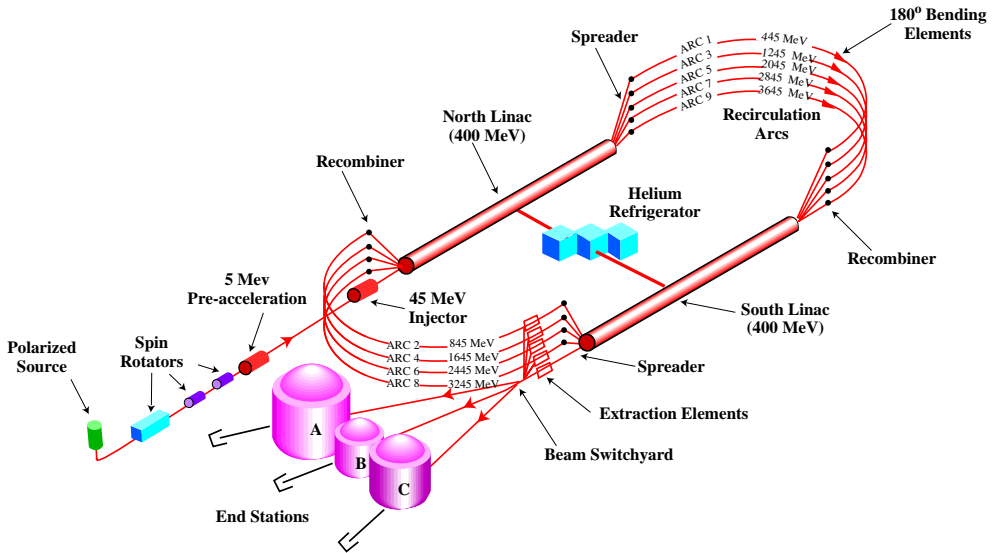


Figure 2.1: Schematic view of the Continuous Electron Beam Accelerator Facility.

## 2.2 Hall C beam line and instrumentation

The Hall C beam line consists of eight dipole and several quadrupole magnets to steer and focus the electron beam. The position and current is monitored by Beam Position and Beam Current Monitors (sec. 2.2.1 and sec. 2.2.2). The shape of the beam can be measured by so called Superharps [193][84]. They consist of three wires, one horizontal and two vertical, which can be remotely moved through the beam. The electrons hitting the wire produce a current of secondary electrons, which is recorded as a function of the position

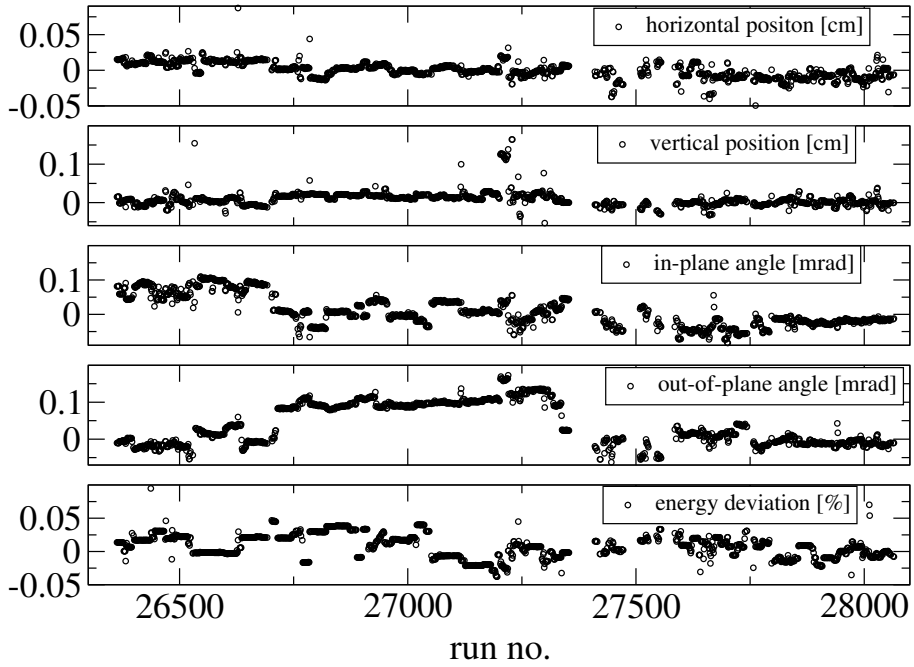


Figure 2.2: Averaged horizontal and vertical position and angle of the beam at the target for each run of this experiment. This information was taken from the ADC-values, which were calibrated against the EPICS-values. In the lower figure the deviation of energy from the nominal energy is shown, which was obtained from the BPM's in the arc.

of the wire. This procedure affects the beam quality and can not be used during the experiment. The beam has a typical beam size of  $100 \mu\text{m}$ . Due to this small size the beam has to be rastered to avoid overheating of the targets (sec. 2.2.3).

### 2.2.1 Beam Position Monitor

The beam position is measured by the Beam Position Monitors (BPM's) [98] and continuously recorded by the Data Acquisition System. The BPM is a cavity with four antennae rotated by  $45^\circ$  from the vertical and tuned to the fundamental frequency of the beam. The signals induced by the electron beam on each antenna are recorded. From two opposite antennae the beam position is calculated by the difference over the sum of the signals. This ratio guarantees that the measurement is independent of the beam current. The conversion factor from the analog signal to distance in cm is known from previously performed calibrations. The absolute beam position of the BPM's

in the arc is taken from the well surveyed Superharps. A deviation from the nominal beam position indicates a change in the beam energy (sec. 2.2.4). In the experimental hall three BPM values (H00A, H00B, H00C) are located at 3.27 m, 2.31 m, 1.36 m upstream of the target pivot. The nominal values were determined from the midplane symmetry in both spectrometers<sup>3</sup>. From a linear fit to these three BPM's the position and angles of the beam are obtained. During the beam time these values were quite stable (Fig. 2.2). They are taken into account in the reconstruction of the target quantities from the focal plane coordinates measured in the spectrometers (sec. 3.1.2). The accuracy of the beam position measurement is  $\pm 1$  mm.

### 2.2.2 Beam Current Monitor

There are three Beam Current Monitors (BCM's) and an Unser monitor in the beam line of Hall C. The BCM's are microwave cavities, which are tuned in resonance with the  $TM_{010}$  mode of the beam. In this mode the signal induced by the beam is relatively insensitive to the beam position, but proportional to the beam current. The proportionality factor depends mainly on the quality factor of the cavity, which is different for each cavity and in addition temperature dependent ( $\approx 0.25\%$ /degree). Therefore the BCM's have to be calibrated against the Unser, a parametric DC current transformer. When the beam passes the Unser it induces a magnetic field. Because the yoke is ferromagnetic, the hysteresis curve becomes unsymmetric. This is compensated by an additional current through the wire loop, which is used as the output of the device.

The Unser gain was calibrated in the maintenance period between the two beam times by sending a precisely measured current through the wire, which simulates the beam. Its gain is very stable, but the offset can have large drifts over short time periods. Therefore the following calibration procedure was chosen: The beam current was first increased and then decreased in steps of  $10\ \mu A$  up to  $60\ \mu A$ . Between each step the beam was turned off for a minute to measure the offset of the Unser. Then a linear fit to the Unser measurement and the BCM output was performed. Because the relation is not exactly linear, later on a correction was applied to this result. The overall accuracy on the charge is 1 %; for small currents ( $10\ \mu A$ ) it is 2 %, because of the uncertainty in the Unser offset of  $\approx 0.2\ \mu A$  [111]. For a detailed description of the BCM's and the calibration procedure see [6][135][29].

---

<sup>3</sup>(x,y) = (0,-0.1 cm) on H00A, (0, -0.15 cm) on H00C.

### 2.2.3 Beam Raster

Due to the small spot size of the beam ( $\approx 100 \mu\text{m}$ ) the solid targets can be damaged by overheating, or local boiling can occur in cryo targets. This is avoided by sweeping the beam spot over an area of a few millimeters squared. For this a pair of magnets 21 m upstream of the target is installed for sweeping the beam in horizontal and vertical direction by up to  $\pm 5 \text{ mm}$  (fast raster) [193]. The raster size used in this experiment was 2 mm times 1.2 mm. A smaller size in the vertical direction was chosen, because the reconstruction of the momentum in the spectrometer depends on the vertical beam position. This would lead to an artificially worsened momentum resolution. It will be shown in sec. 3.1.2 that this effect can be corrected.

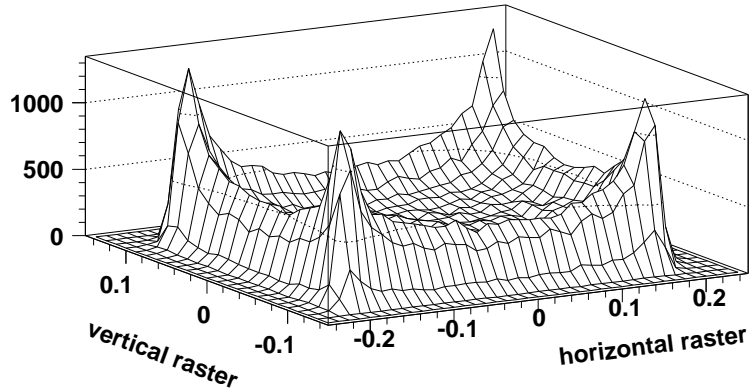


Figure 2.3: Beam intensity distribution as reconstructed from the currents at the fast raster magnets. It is strongly peaked at the corners of the 2 mm times 1.2 mm covered squared area.

To avoid a repetitive Lissajous pattern the ratio of the frequencies for the horizontal to vertical direction is chosen to be  $\sqrt{2}$  (24.2 kHz to 17 kHz). In Fig. 2.3 the beam intensity distribution is shown as calculated from the read-back of the currents from the fast raster magnets. The intensity is greatest at the corners of the distribution, because of the sinusoidal raster pattern. Recent development on the raster electronics provide a veto signal, which can be used to avoid offline or online the regions of high intensity [189]. This feature was not used in the analysis. It can be useful, when using a cryo-target and high currents to avoid the effects of local boiling.

There exists also a so called slow raster just upstream of the target to protect the beam dump. It would be required for beam currents above  $80 \mu\text{A}$ . The slow raster was not used in this experiment.

## 2.2.4 Beam energy measurement

The beam energy can be measured using the Hall C transport line (called arc) as a spectrometer. In this case the beam is transported in dispersive mode with all focusing elements (quadrupoles, sextupoles and beam correctors) turned off, using only the eight dipole magnets [83]. One of the dipole magnets has been field mapped, whereas for the other dipoles the same field map is assumed. Then the energy  $E$  and its spread can be determined from the field integral along the beam and the bending angle  $\theta_B$ :

$$E = \frac{ec}{\theta_B} \int B dl \quad (2.1)$$

The bending angle  $\theta_B$  is the opening angle between the incoming and outgoing beam. It is measured with the Superharps at the beginning and the end of the arc. The net bending angle ( $37.5^\circ$ ) of the arc had to be precisely surveyed. This allows an energy measurement with a relative uncertainty of  $\delta E/E \approx 2 \cdot 10^{-4}$ .

Initially there was a difference of the energy measured in Hall A and C of approximately 0.3 %. Even after correction of the field integral for the fringe field in Hall A the two energy measurements differed by 0.2 %. Therefore the dipole field in the Hall C arc was remapped and the field integral recalculated. This leads to the corrections shown in Fig. 2.4 as a function of the beam energy [111], which lowers the energy measured. For the energy used in the experiment a correction of  $\approx -0.2$  % has to be applied. In addition it was observed that the remanence field of the six focusing elements in the Hall C arc is not negligible, but has to be taken into account. This results in a small correction of  $+1.6 \cdot 10^{-4}/E(\text{GeV})$ . With these corrections the energy measurements of Hall A and C agree to better than 0.1 %. In addition the eP-method, also used in Hall A, agrees with the energy determined in the Hall A arc by better than 0.06 % [31]. The eP-method is based on elastic kinematics and measures the opening angle in the  $H(e,e')$  reaction.

An independent analysis was done by E. Christy using 35 different  $H(e,e')$  kinematics at a beam energy of 2.2, 3.1, 4.4, 5.5, 5.7 GeV, with the scattered electron detected in the HMS magnetic spectrometer. He fitted the invariant mass by adjusting the angle and momentum offset of the spectrometer (sec. 6.3) as well as an offset for each beam energy. His result is indicated by squares in Fig. 2.4 [42]. It agrees with the corrections given by D. Mack to within 0.1 %.

After the beam energy measurement the achromatic mode is restored in the arc. With the BPM's the beam position in the arc is monitored continuously during the experiment. A deviation from the nominal beam

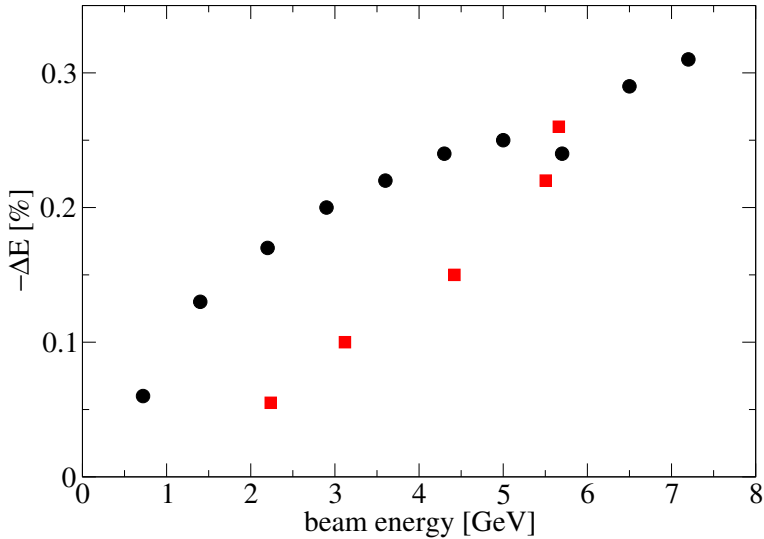


Figure 2.4: The correction for the beam energy in the Hall C due to remapping of the dipole field are indicated by circles. This analysis was done in September 2000 by D. Mack. A second analysis based on the redundancy in the elastic hydrogen kinematics leads to the results indicated by squares [42].

position corresponds to a change in the beam energy. The point of high dispersion in the middle of the arc is best suited for this purpose. The conversion from the beam position to an energy deviation was provided by P. Gueye. The change in energy during the run period was at most a few  $10^{-4}$ . This was taken into account in the analysis of the experiment. The spread in energy was less than  $1 \times 10^{-4}$ . Overall a relative uncertainty of  $5 \times 10^{-4}$  of the beam energy was assumed.

## 2.3 Targets

The vacuum scattering chamber on the target pivot contains two target ladders, one for solid targets and one for cryogenic targets. They are called the solid and cryogenic target ladder respectively, even the cryogenic target ladder contains in addition some solid targets. This experiment uses besides the solid targets carbon, aluminium, iron and gold the hydrogen cryo target as well as the optics target for checks. The optics target, which consists of a stack of several solid targets placed along the beam axis (s. below), and four solid targets are mounted together with three independent cryogenic loops on the cryogenic target ladder. Both target ladders can be remotely

moved in and out of beam as well as in vertical direction to put a selected target on beam height. In the following the solid and cryogenic targets will be described in so far as needed by the experiment. Details can be found in [10][56].

### 2.3.1 Solid targets

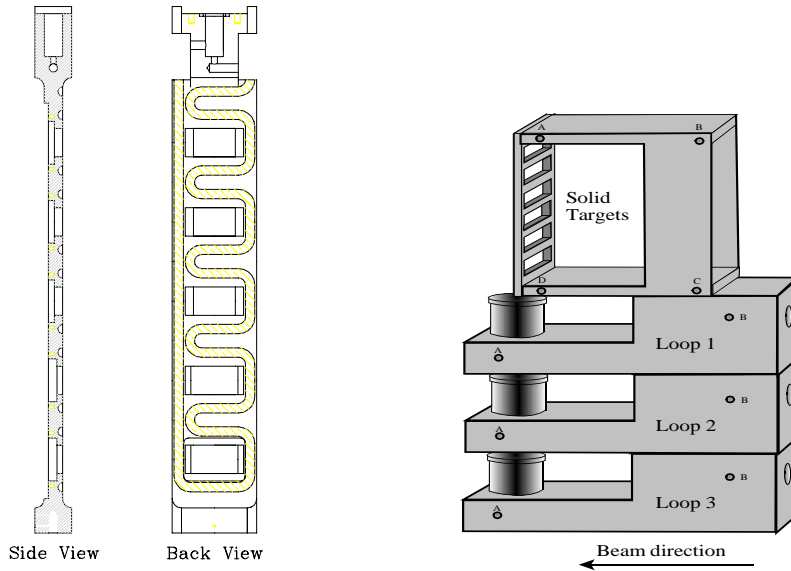


Figure 2.5: Left: Side and back view of the water cooled solid target ladder. Right: Stack with three cylindrically shaped cryo targets and a ladder containing four solid targets and the optics target.

The solid target ladder shown in Fig. 2.5 has space for three thin and two thick targets. The targets are water cooled from each side to dissipate the heat caused by the electron beam. Due to the decreasing thermal conductivity with increasing temperature the maximum beam current for iron was limited to  $40 \mu\text{A}$  to prevent the iron from melting. One carbon, one aluminium, two iron and one gold target found place on this target stack. Tab. 2.1 lists their thicknesses and radiation lengths. The thick iron and the aluminium target consist of two plates.

According to the procedure described in [110] the target thickness was determined as follows: With a microscope the edges of each target were measured relative to a reference point. The area of the target plate were then calculated assuming a rectangular shape [139]. The mass was measured

| target | thickness [g/cm <sup>2</sup> ] | radiation length [%] |
|--------|--------------------------------|----------------------|
| C      | 1.245                          | 2.52                 |
| Al     | 1.084                          | 4.50                 |
| Fe     | 0.488                          | 3.54                 |
| Au     | 0.476                          | 7.47                 |
| Fe     | 0.773                          | 5.64                 |

Table 2.1: Thickness (=areal density) and relative radiation length for the targets on the solid target ladder. The order corresponds to the arrangement of the targets on the target stack. Below the iron target resides a BeO screen.

using a balance with 1 mg precision. From the ratio of mass and area the areal density (also called thickness) is obtained. The accuracy of the length and weight measurement is estimated to 0.16 % and 0.13 % respectively. This leads to a relative uncertainty in the thickness of 0.24 % [139]. Here it is assumed that the target thickness is uniform. All targets consist of material with its natural isotopic abundance. The largest isotopic mixture occurs for iron with a fraction of 5.9 % <sup>54</sup>Fe.

Each target is 2.3 cm high and 3.8 cm wide. The visible area when clamped into the frame is 2 cm times 3 cm; thus the frame is not hit by the beam even with a rastered beam or small vertical beam offset. The ladder can also be rotated around its vertical axis by remote control to change the angle of the target relative to the beam. Depending on the angles of spectrometers this can reduce the amount of target material that the outgoing particles have to transverse. This in turn reduces also the correction due to energy loss in the target. The error on the target angle is approximately  $\pm 2^\circ$ . A target angle of 25 ° towards the SOS was used for the kinematics with proton angles above 70 °.

### 2.3.2 Cryo targets

The cryogenic target ladder was designed and first used in summer 1999. It contains besides the three separate cryogenic systems a ladder for six solid targets (Fig. 2.5). On this ladder the following targets were mounted: Al(0.549 g/cm<sup>2</sup>), Fe(0.384 g/cm<sup>2</sup>), Au(0.250 g/cm<sup>2</sup>), CH<sub>2</sub>(0.220 g/cm<sup>2</sup>), optics target. This target ladder is not cooled by water as is the solid target ladder. Therefore these solid targets were only spares and not used in the experiment except for the "Quintar" and the dummy target, which are part of the optics target. The Quintar target consists of five 1 mm thick aluminium and carbon targets horizontally spaced by  $\approx \pm 3$  cm along the beam line.

The five targets are shaped such that the targets can be placed in the beam in some combination or all together (= Quintar). For a few optics checks the Quintar and the so called z=0–carbon target were used. The ladder further contains the dummy target, which consists of two 1 mm thick aluminium plates at  $\pm$  2.25 cm simulating the walls of the cryo target cells. It is used for determining the contribution of the target walls (sec. 6.4). According to two surveys performed in July and September 1999 the cryo target ladder is displaced by 2.3 mm downstream. This is confirmed by the target position obtained from the vertex reconstruction of the spectrometer and was taken into account in the analysis.

The new design of the cryo target consists of an upright standing aluminium cylinder with diameter 40.238 mm and a wall thickness of 127  $\mu\text{m}$  (also called new tuna can or pillbox) [58]. This design has the advantage that the target material transversed by the particles is the same in each direction, which simplifies the calculation of the energy loss and external bremsstrahlung. The maximum target length changes for a horizontal beam offset of 2 mm by 0.5 %. In fact also the rastering of the beam leads to a small reduction of the effective target length.

In the experiment only the middle loop was used and filled with liquid hydrogen. It is cooled down to 19 K at a pressure of 165.5 kPa. In this state the boiling temperature of hydrogen is 22.8 K and the density 0.0723  $\pm$  0.00036 g/cm<sup>2</sup>. The uncertainty in the density of 0.5 % is mainly due to the uncertainty of the relative amounts of ortho and para hydrogen [57]. To avoid local boiling a fan operating at 60 Hz provides circulation of the hydrogen. A few runs with the hydrogen target were taken at the stand-by frequency of 20 Hz with beam currents up to 20  $\mu\text{A}$ . The runs were repeated with the correct fan frequency. No difference in the yield from those runs were observed. In addition no significant difference occurs for runs with a beam current of 10 and 50  $\mu\text{A}$ . Nevertheless a systematic error of 0.1 %/10  $\mu\text{A}$  for a possible small variation in the density due to local boiling is taken into account according to [10].

Samples of the hydrogen gas were analyzed by Atlantic Analytical Laboratories. Only an amount of nitrogen of 14 ppm could be detected, all other impurities tested like HD, D<sub>2</sub>, oxygen, argon, carbon and water were below the detection limit of a few ppm [159]. Therefore no correction is necessary.

## 2.4 Spectrometers

Two magnetic spectrometers, the High Momentum Spectrometer (HMS) and the Short Orbit Spectrometer (SOS) belong to the standard equipment of

Hall C. Both spectrometers were used during experiment E97–006. Most of the time protons were detected in the SOS and electrons in the HMS, but both spectrometers can be used as electron as well as proton detector. They contain nearly the same detector packages, which consist of two drift chambers, four scintillator planes, a Cerenkov and a lead–glass detector. On the other hand the two spectrometers differ in the design concept completely. The HMS consists of magnets with superconducting coils with a maximum central momentum of 7.4 GeV/c; the SOS has common iron yokes and reaches only 1.75 GeV/c. Both spectrometers and their detector package will be described in the following section.

#### 2.4.1 High Momentum Spectrometer

The HMS features a QQQD configuration, where the particles are bent  $25^\circ$  upward. In its standard tune it is operated in point-to-point mode<sup>4</sup> in both the dispersive and non-dispersive direction. This leads to a large momentum, solid angle and extended target acceptance (Tab. 2.2). In this tune, Q1 and Q3 serve as focusing elements in the dispersive plane and Q2 in the transverse direction. The fields of the dipole and quadrupoles are stable at the  $10^{-4}$  level and are continuously monitored by NMR probe or by their currents. In front of the first quadrupole a remotely controlled collimator stack is mounted, which contains a small and a large octagonal shaped collimator, a sieve slit (an array of small holes) for optics study and a blank space ("no collimator"). They are machined out of a tungsten composite (HEAVYMET) and are 6.35 cm thick (3.175 cm for the sieve slit). In this experiment the large collimator with a solid angle of 6.74 msr was used. Since '97<sup>5</sup> the collimator was moved back about 40 cm. This allows a minimal central angle of  $10.5^\circ$  instead of  $12.5^\circ$ . This configuration is called HMS–100 tune and was also used for this experiment.

#### 2.4.2 Short Orbit Spectrometer

The SOS uses water-cooled resistive magnets in a QDD configuration. The quadrupole focuses in the non-dispersive direction, the first dipole bends the particles up by  $33^\circ$ , whereas the second dipole bends them down by  $15^\circ$ . Focusing is also provided by the fringe fields of the curved shaped dipole magnets. This makes the optics especially sensitive to saturation effects of the magnets. This will be discussed in sec. 6.3. In the standard tune the SOS

---

<sup>4</sup>A point-to-point tune maps each distinct point at the target to a distinct point at the focal plane.

<sup>5</sup>for experiment E93–021 [177]

| Quantity                        | Unit  | HMS        | SOS        |
|---------------------------------|-------|------------|------------|
| Momentum range                  | GeV/c | 0.5–7.4    | 0.1–1.75   |
| Optical length                  | m     | 26.0       | 7.4        |
| Momentum acceptance             | %     | $\pm 10$   | $\pm 15$   |
| Momentum resolution             | %     | 0.07       | 0.1–0.15   |
| Solid angle                     | msr   | 6.74       | 7.55       |
| In-Plane angular acceptance     | mrad  | $\pm 27.5$ | $\pm 57.5$ |
| In-Plane angular resolution     | mrad  | 1.5        | 3.2        |
| Out-of-Plane angular acceptance | mrad  | $\pm 70$   | $\pm 37.5$ |
| Out-of-Plane angular resolution | mrad  | 2.3        | 0.5        |
| Extended target acceptance      | cm    | $\pm 7$    | $\pm 1.5$  |
| Vertex reconstruction accuracy  | mm    | 2          | 1          |

Table 2.2: Characteristics of HMS and SOS. For the HMS the specifications for the HMS-100 tune are given. The angular and the vertex resolutions were obtained from sieve slit runs (sec. 3.1.3). The momentum resolution is derived from  $H(e,e'p)$ -runs. Therefore these values are influenced by multiple scattering and have to be considered as upper limits.

is operated in a point-to-point mode in the non-dispersive direction. The special feature of the SOS is its short optical length of only 7.4 m. Therefore it is especially suited for detection of short lived particles. On the other hand it can only be used for momenta less than 1.75 GeV/c. A new design will be required, when the extension of the TJNAF accelerator to electron energies of up to 12 GeV is accepted [39]. The characteristics of the SOS are given in Tab. 2.2. Further details can be found in [46]. The collimator system of the SOS is similar to the one of the HMS.

### 2.4.3 Detector package

The detector packages in the HMS and SOS are very similar. Therefore they will be described in one section. A side view of the detectors in the SOS is shown in Fig. 2.6. They are mounted on slides placed in a meter thick concrete shielding. After transversing the magnetic elements the particle passes first through two drift chambers, a set of x-y hodoscopes, a Cerenkov detector, another set of x-y hodoscopes and a shower counter made out of lead-glass. The voltages of the detectors and other parameters are monitored and controlled remotely by the EPICS (Experimental & Physics Industrial Control System [63]) slow control system.

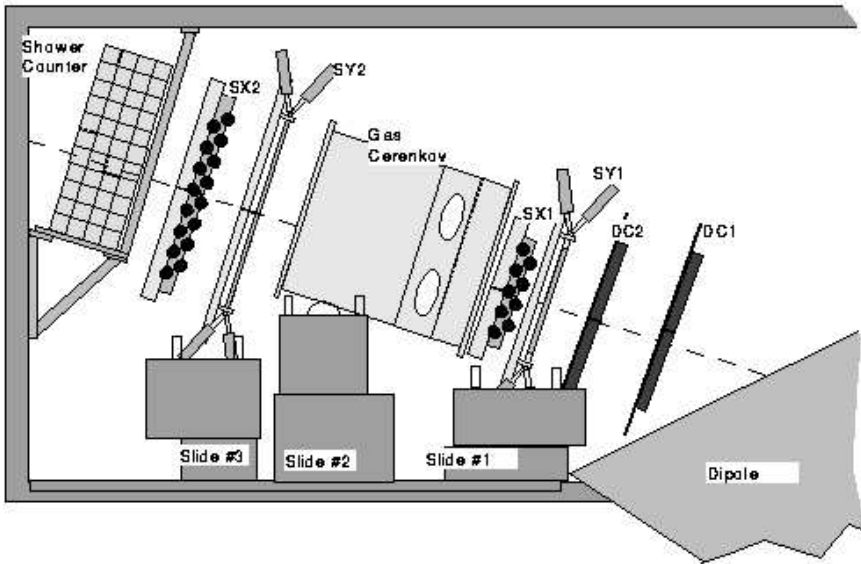


Figure 2.6: Side view of the SOS detector hut.

### Drift chambers

Both spectrometers have two drift chambers, which consist of six planes each. They provide information about the trajectory of the particle. The drift chambers contain 1 cm spaced sense (anode: 0 V) and field wires (cathode: negative voltage) and are filled with a mixture of argon-ethane of equal amount and 1 % isopropyl alcohol. When a charged particle is penetrating the drift chamber it ionizes the gas, and electrons are released. Due to the electrical field produced by the field wires the electrons drift to the sense wires. The time required is called drift time. It is measured as the time difference between the detection of the electrons in the drift chamber and in the hodoscopes corrected for the transit time of the electron from the drift chamber to the hodoscope. The conversion from drift time to drift distance is provided by field maps, which are obtained by a fitting procedure performed for each kinematics setting of the experiment. The field maps are determined by comparing the distribution of drift times in the chamber with the expected (flat) distribution within a cell. To resolve the side of the wire which the particle passes through the drift chamber (left-right ambiguity) the drift chamber have planes with differently oriented wires. In addition planes of the same type are offset by half a drift cell. The tracking algorithm is described in sec. 3.1.1.

In the HMS the six planes are arranged in the order X, Y, U, V, Y', X'. The X planes are orthogonal to the Y planes and measure the vertical track position. The U and V stereo planes are inclined  $\pm 15^\circ$  with respect to the X planes. Due to the small angle the U and V planes are X-like, which leads to a good redundancy in the vertical direction, but a poor one in the horizontal direction, especially when one of the Y planes is missing (sec. 3.1.1). A useful criterion for the performance of the wire chamber is the tracking position resolution per plane. It is obtained by fitting a straight line to the hit position of the remaining five planes and comparing it to the hit position measured by the plane of interest. The width of this (residual) spectrum is the sum of the square of the uncertainties in five planes [14]. Therefore the sigma value has to be divided by  $\sqrt{5}$  to get the resolution for this plane. Under the conditions of the current experiment a position resolution of  $\approx 130 \mu\text{m}$  per plane is achieved.

The planes in the SOS are ordered in the sequence U, U', X, X', V, V', where the U and V planes are rotated by  $\pm 60^\circ$  with respect to the X planes. The position resolution is typically  $100 \mu\text{m}$ .

## Hodoscopes

Each spectrometer contains four scintillator planes, where two are located in front and two in the back of the Cerenkov detector. Each set is called hodoscope and consists of scintillators segmented in the vertical and horizontal direction (s. e.g. [10]). The distance between the two hodoscopes is about 2 m. Therefore it is suitable for measuring the particle velocity using the time-of-flight method. This can be used for particle identification and is discussed in sec. 6.2. Corrections for the 'time walk' due to variations in the pulse height and offsets between the individual planes were done in an offline fitting procedure [9][7]. The scintillators are read out by a photomultiplier at each end. This makes possible a rough position determination of the hit, which can be compared to the position reconstructed using the information of the drift chambers. The main purpose of the hodoscope is to provide a trigger signal for the data acquisition system. Therefore the signals of all photomultipliers of one side of a scintillator are combined with an OR. The input used for the trigger logic is then the AND of the two signals of one plane, which are called S1X, S1Y, S2X, S2Y respectively. Furthermore the OR of the front and back plane is needed:  $S1 = S1X + S1Y$ . The trigger logic will be discussed in sec. 2.4.4.

### Cerenkov detector

The Cerenkov detector is used to discriminate between electrons and other charged particles. In the HMS it was filled with 40.4 kPa Perfluorobutane ( $\text{C}_4\text{F}_{10}$ ,  $n = 1.00143$  at 1 atm), which corresponds to a pion detection threshold of just above 4 GeV/c. The Cerenkov light is reflected by two parabolic mirrors into two photomultipliers. In average nine photoelectrons were detected and the detection efficiency was better than 99 % for a two-photoelectron cut. The Cerenkov efficiency is obtained by preselecting electrons with a hard cut in the lead glass detector and comparing it to the number of events obtained with the two-photoelectron cut in the Cerenkov. The largest pion contamination in the production runs was 10 % (kinematics kin3). Therefore the contribution of misidentified pions, which mostly produce a high energy electron in the material in front of the Cerenkov detector is negligible. In [10] a pion rejection of 500:1 is given under very similar conditions.

The Cerenkov detector in the SOS is only used for a few calibration runs (sec. 5), where electrons are detected. It is filled with 1 atmosphere of Freon-12 ( $\text{CCl}_2\text{F}_2$ ,  $n = 1.00108$ ), which corresponds to a pion threshold of 3 GeV/c. Details can be found in [186][10].

### Lead-glass shower counter

The lead-glass shower counter consists of four layers with 13 (11) lead-glass blocks of 10 cm x 10 cm x 70 cm in the HMS (SOS), which corresponds to nearly 16 radiation lengths. Electrons entering the lead-glass produce a shower of bremsstrahlung and charged particles, which in turn emit Cerenkov light. Whereas electrons deposit their entire energy in the lead-glass, pions lose typically 300 MeV independently of their momentum. Therefore the signal output of all photomultipliers is summed after gain matching and normalized to the electron momentum [119]. According to [10] the resolution of the shower counter is  $6.5\%/\sqrt{E}$  in the HMS and is  $5.6\%/\sqrt{E}$  in the SOS. Although the lead-glass detector can be used to discriminate between electrons and hadrons it is only used for determining the detection efficiency of the Cerenkov (sec. 2.4.3), because its efficiency is low ( $\lesssim 90\%$ ). Further it is in the trigger logic for preselecting electrons (sec. 2.4.4).

### 2.4.4 Trigger logic and Data Acquisition

The single-arm trigger logic is almost identical for HMS and SOS and shown in Fig. 2.7. With minimal modifications it serves as trigger for electrons,

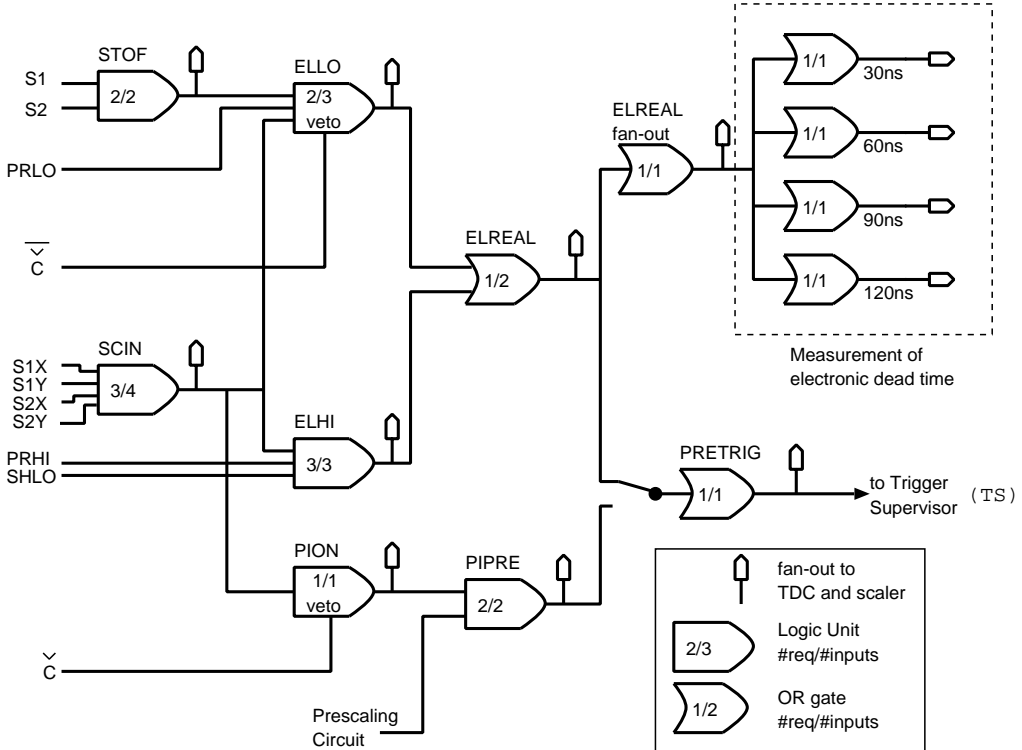


Figure 2.7: Electronic layout of the single-arm trigger logic in HMS and SOS for the case electron detection. The numbers e.g. 3/4 indicate that three out of four requirements have to be fulfilled (logical 1). The unit on the top right is used for the determination of the dead time and will be discussed in sec. 2.4.5.

protons and other particles.

We first discuss the electron trigger as it was used in the HMS. The pretrigger for electrons can be generated in two different ways called the low-level (ELLO) and high-level (ELHI) electron trigger. The low-level electron trigger requires that at least two conditions are true out of the following three: a valid TDC signal in at least one of the planes in each hodoscope (STOF), not less than three of the scintillator planes have fired (SCIN), the energy deposit in the first layer of the calorimeter exceeds a low threshold (PRLO). This signal is vetoed by the negated Cerenkov signal. The high-level electron trigger requires the threefold coincidence of a valid SCIN signal and a calorimeter signal, whose first layer summed up exceeds a high threshold and the signals of all layers are above a low threshold. This kind of trigger is also called '3 out of 4 + PID', where the first part is a reference

to the three of four required scintillator planes and PID is the abbreviation for Particle Identification referring to a valid Cerenkov or calorimeter signal. This trigger benefits from the high trigger efficiency of the scintillator planes ( $> 99.5\%$ ) and the good and efficient electron discrimination of the Cerenkov detector. For redundancy the full information of the calorimeter is used in the second trigger. In both cases a valid TDC signal of the back and front planes of the hodoscope is required for offline particle identification. For detecting protons the particle identification using Cerenkov and calorimeter is removed.

The pretrigger signals of HMS and SOS are fed into the trigger supervisor (TS) [91], which determines the type of signal (HMS or SOS singles, coincidence, pedestal), applies a possible prescale factor and provides the signals for reading out the TDC and ADC information. The TDC's are operating in sparsified mode, i.e. only channels, which received a stop after the common start, are read out. Further, only ADC-values above a certain threshold are recorded by the Data Acquisition (DAQ). The threshold is determined by taking 1000 pedestal events directly after starting a new run with sparsification disabled. In addition part of the data was recorded in buffered mode. In this mode the Fastbus modules can store up to sixteen events while the DAQ is busy. This helps to reduce the computer dead time (sec. 2.4.5) at high data rates.

The software of the data acquisition system CODA (Cebaf Online Data Acquisition) was developed at Jlab [1]. It provides an user interface for controlling the current run and reconstructs each event by merging the fragments from the VME crates and Readout Controllers (ROC's) together. The run is continuously written to disk. Later on the run is automatically backed up using the tape storage facility (Silo) at Jlab. A more detailed description of the trigger supervisor and CODA can be found in [136].

#### 2.4.5 Dead time

The fraction of events, which is missed because the trigger supervisor or the trigger logic is processing other data, is called computer and electronic dead time, respectively. Each event to be processed by the trigger supervisor takes a certain time  $\tau$ . During this time the trigger supervisor is in the busy state and pretriggers arriving at the trigger supervisor are lost. The computer dead time is obtained by the ratio of trigger (processed events) to pretrigger rate. The probability of  $n$  events occurring during this time at a rate  $R$  is given by the Poisson distribution, which for zero events within the time interval  $\tau$  is  $\exp(-R\tau)$ . This is equal to the life time, the complement to the dead time.

In the left of Fig. 2.8 the computer dead time versus the total event rate<sup>6</sup> is shown for data taken in buffered and unbuffered mode. The processing

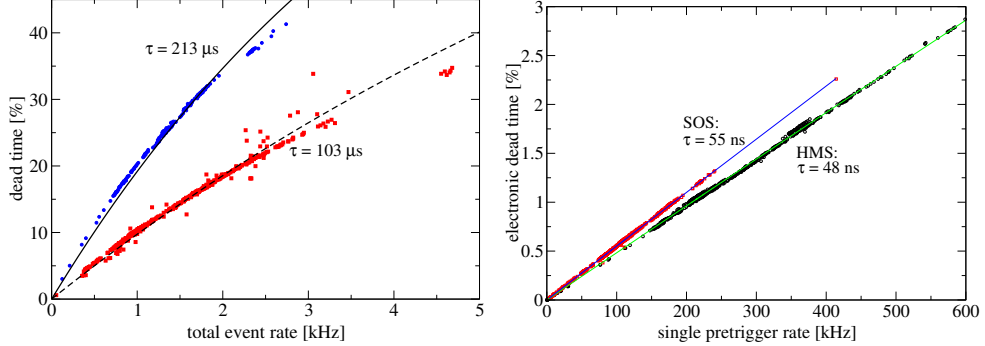


Figure 2.8: Left: Computer dead time versus the total event rate. The exponential fit gives a processing time per event of  $213\ \mu\text{s}$  for the unbuffered mode and  $103\ \mu\text{s}$  for the buffered mode. Right: Electronic dead time as a function of the single pretrigger rate for HMS and SOS. The numbers given result from a exponential fit and correspond to an effective gate time in the trigger electronics.

time in buffered mode of  $103\ \mu\text{s}$  is only half of the one in unbuffered mode<sup>7</sup> and obtained by fitting the dead time with an exponential in Fig. 2.8. It is mainly determined by the time needed to perform the FASTBUS conversion. Therefore it depends also on the multiplicity of TDC signals for each event.

After the conversion is done the FASTBUS is ready to accept new events, if operating in buffered mode. Otherwise the data acquisition is busy with the TDC readout. Especially for high rates the buffered mode significantly reduces the dead time. At event rates of about 3 kHz the dead time is less than 30 %. It was observed that access to the data disk by other processes than CODA leads to a large variation and an increase in the dead time. This mainly causes the scatter in the dead time in Fig. 2.8 at high rates. Further the amount of singles in the event rate reduces the dead time, because a coincidence event takes longer to be processed.

The electronic dead time shown in Fig. 2.8 on the right is small and always below 3 %. For determining the electronic dead time the rates measured with gate widths of 30, 60, 90, 120 ns were used (Fig. 2.7). With the

---

<sup>6</sup>The total event rate was obtained by taking the sum of prescaled single and coincidence events and correcting it for dead time.

<sup>7</sup>This is already an improvement compared to data taken in 1997 , where it took  $490\ \mu\text{s}$  for data processing in unbuffered mode [177].

approximation for small dead times  $\exp(-R\tau) \approx 1 - R\tau$  the electronic dead time can be obtained, if one knows the gate width relevant for the trigger logic. The largest gate width required is the one for combining all scintillator signal. It is 50 ns in the HMS and 60 ns for the SOS, which approximately agrees with the result of the exponential fit shown in Fig. 2.8. The fitted values are 48 ns for the HMS and 55 ns for the SOS.

# 3 Basics of the analysis

Here the basic features of the analysis are presented, which are common for all runs analyzed. Because the Monte Carlo Code SIMC of Hall C plays a major role in the analysis of the data it is explained in a separate section. Subsequently the analysis of the calibration runs in inelastic and quasi-elastic kinematics on hydrogen and carbon as well as the production runs are discussed. In this section an overview of the standard Hall C analysis code will be given with emphasis on the tracking algorithm, tracking efficiency and the event reconstruction. In this context optics checks with the runs using the sieve slit as collimator will be presented. In the second part of this section the particle identification and background subtraction using the coincidence spectrum will be discussed. Due to events with the wrong TDC information a correction on the experimental yield has to be applied.

## 3.1 Hall C analysis code

The standard analysis Code of Hall C is written in Fortran 77 and called 'Hall C Engine' or shortly 'replay'. It is used for online and offline analysis and converts the detector output into tracking information and physical quantities. Further, the hardware scalers are read out and stored in so called report files. They contain also software scalers (e.g. tracking efficiency), which are handled by the CEBAF Test Package (CTP) [190]. This code is written in C and can share common variables with the main analysis code. It makes it convenient for the user to change input parameters and add software scalers. The detector calibrations were done with separate analysis codes, but usually using the output of the replay in form of HBOOK files [37] or PAW ntuples [45]. The ntuples and report files were also used by a stand-alone Fortran code doing the physical analysis, which was specially written for this experiment.

### 3.1.1 Tracking algorithm

The tracking information in form of drift times and drift distances is provided by the two drift chambers in each spectrometer (sec. 2.4.3). The tracking algorithm identifies clusters of hits (space points) in each chamber. For each space point a track is fitted ('stub'). The left-right ambiguity is resolved by either choosing the stub with the lowest  $\chi^2$  out of all combination or by using the small angle approximation, which makes use of the fact that the wires of similar planes are offset by half the wire distance. This reduces the computer time needed to perform the tracking. Then each stub of the front and back chamber is linked to a track using user-defined criteria for reasonable combinations. Problems to find the right track can occur, if too few or too many hits are found in the chambers. Therefore the maximum number of hits is limited to 30 in each chamber.

In [78] it is noticed that for the SOS a minimum number of five planes in each chamber ('5 out of 6') is required for good tracking results. This condition was also tried out for the HMS. This however is not a good choice for the HMS, because in the second X-plane of the front chamber two wires were dead. One of them is located in the central region of the momentum acceptance. In Fig. 3.1 it is shown that this leads to a local inefficiency of up to 7 % in the electron momentum spectrum. Therefore only four planes of each chamber were required to fire ('4 out of 6'). In [184] the

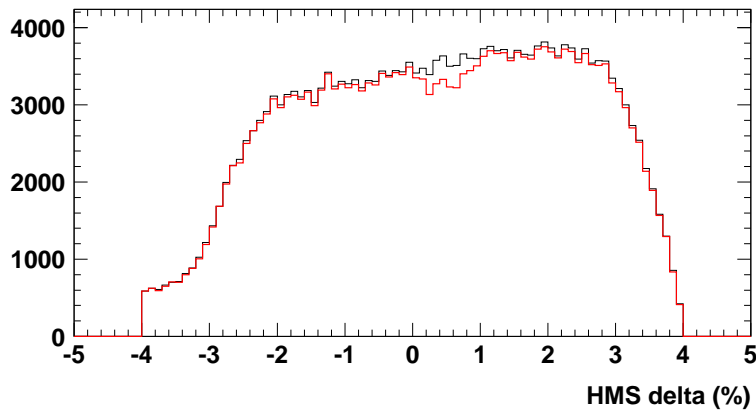


Figure 3.1: HMS momentum spectrum with two different conditions for reconstructing a track: '4 out of 6' (black thin line) and '5 out of 6' (red thick line).

resolutions obtained with both tracking conditions were compared. Possible errors introduced by a wrong left-right decision were examined due to the

fact that there are only two y-like planes in each chamber. It was found that the '4 out of 6' algorithm gives comparable results to the ones achieved with '5 out of 6'.

If multiple tracks are found the code chooses the one with the best  $\chi^2$ . For high single rates in the HMS this condition is not sufficient. For most of the events with more than three possible tracks the wrong track was chosen. This was examined with the software package 'Event Displayer' [185], which is able to visualize all hits in the drift chamber and the hodoscope. All tracks found are shown and the track finally chosen by the tracking algorithm is highlighted. Further conditions on reconstructed quantities or the number of tracks can be applied in the Event Displayer. After this examination the maximum number of tracks in the HMS and SOS was limited to three. Further loose cuts on the reconstructed variables had to be set to find a reasonable track (s. below).

### Tracking efficiency

The tracking efficiency is defined as the fraction of events with a valid track in a certain region (fiducial area) of the hodoscope with respect to all events. It is important to limit the region of the hodoscope to be tested, because otherwise noise and momenta outside the nominal acceptance will be included. Whereas for the HMS no dependence of the tracking efficiency on the chosen fiducial area could be observed within 0.5 %, the tracking efficiency of the SOS varies quite strongly, up to  $\pm 2$  %. This variation was greatly reduced, when requiring for the event preselection that all four hodoscope planes have fired. To have a cleaner ensemble coincidence events are selected and in the case of electrons the Cerenkov information is used. Usually the number of hits in at least one of the chambers is limited to 15, when calculating the tracking efficiency. It turned out that for high rates in the HMS this requirement had to be dropped.

The reliability of the tracking efficiency can be best tested for runs of the same setting<sup>1</sup>, but with different beam currents. This leads to a large range of different pretrigger rates in the spectrometer and therefore to different trigger efficiencies. The beam current varies from 10 to 45  $\mu\text{A}$ , which leads to pretrigger rates in the HMS between 100 and 500 kHz. The SOS pretrigger rate is always less than 60 kHz. In Fig. 3.2 the yield contains all corrections (sec. 3.3) and is normalized to the charge. Using the old definition of the tracking efficiency and the standard procedure for choosing the best track, which relies only on the lowest  $\chi^2$ , a strong dependence on the

---

<sup>1</sup>The runs for this test are taken in perpendicular kinematics (kinp1) on the iron target.

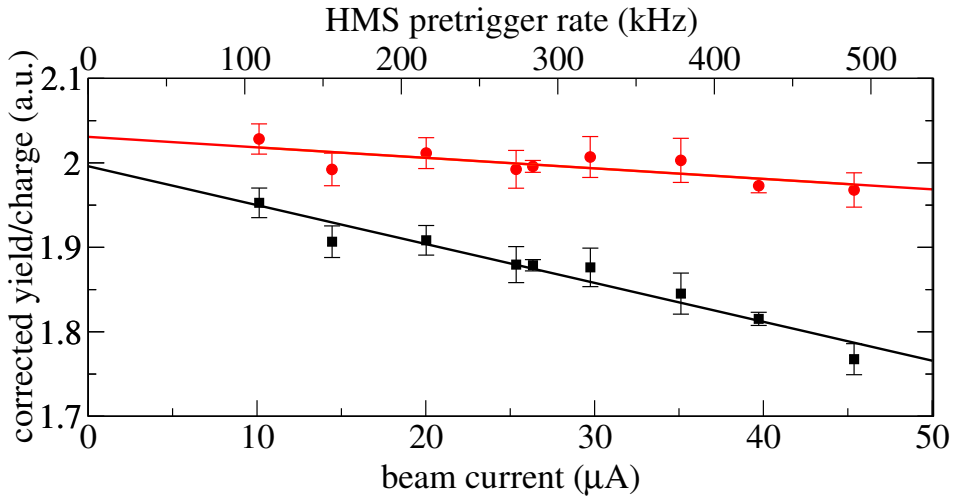


Figure 3.2: Dependence of the data yield per charge on the current and on the HMS pretrigger rate. The results indicated by squares use the standard procedure in the Hall C analysis program and show a strong dependence with the pretrigger rate of the HMS. The upper points (circles) were obtained with the modified algorithm explained in the text. The lines correspond to linear fits.

current respectively on the HMS pretrigger rate (upper x-axis) is observed. With the modified approach mentioned above a greatly reduced dependence is achieved (circles in Fig. 3.2). The maximum number of tracks found was limited to three, otherwise the event was discarded. Further it was found that the rate-current dependence shown in Fig. 3.2 gets worse, if the usual acceptance cuts were applied in the analysis. This is a consequence of the fact that the chance of choosing the wrong track increases with higher rates in the spectrometer. This leads to events with completely irrational values for the reconstructed quantities. Therefore loose cuts on reconstructed quantities were applied when choosing the particle track. The cuts made are summarized in Tab. 3.1. The small dependence still observed in the upper curve of Fig. 3.2 might come from event statistics or systematic errors in the current calibration. The fit extrapolated to zero pretrigger rate is approximately 1.5 % larger than the one obtained with the common procedure. This deviation can be accounted for by considering the uncertainty of the current measurement of 1–2 % (sec. 2.2.2) and of tracking efficiency of 0.5 % for each spectrometer. It is worth to mention that the modified procedure has no net effect on the runs taken on hydrogen (sec. 6). Here the pretrigger rates in the HMS were always less than 6 kHz.

| quantity     | HMS         | SOS         |
|--------------|-------------|-------------|
| y [cm]       | $\pm 10$    | $\pm 10$    |
| y' [rad]     | $\pm 0.045$ | $\pm 0.075$ |
| x' [rad]     | $\pm 0.08$  | $\pm 0.05$  |
| $\delta$ [%] | $\pm 20$    | $\pm 40$    |

Table 3.1: Summary of the cuts on the reconstructed quantities at the target used in the HMS and SOS for choosing the best track. For an large extended target y' has to be properly adjusted. Notation see sec. 3.1.2.

The modified procedure leads to a drop of the tracking efficiency of only  $\approx 2\%$  in the SOS and up to  $\approx 10\%$  in the HMS, which means a loss of partially good data. This is probably due to the fact that the HMS was affected by more noisy hits at extreme forward angles. The tracking efficiency for the HMS and SOS as a function of the pretrigger rate can be seen in Fig. 3.3.

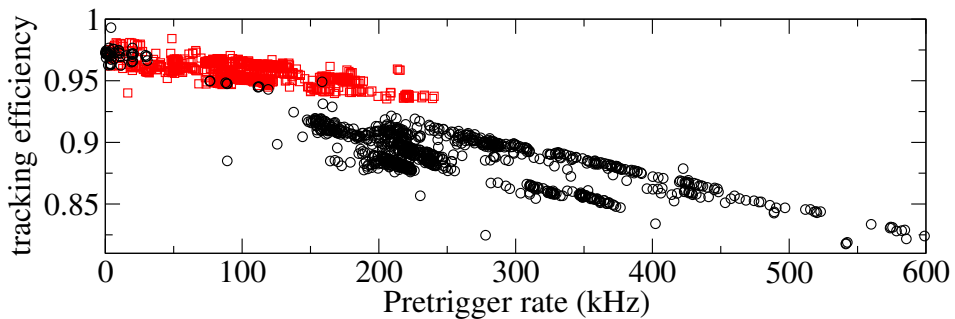


Figure 3.3: Tracking efficiency for the HMS (circles) and SOS (squares) as a function of the pretrigger rate.

### 3.1.2 Reconstruction of target quantities

After the particle track is found the intersection with the focal plane is determined. This leads to the focal plane coordinates  $x_{fp}$  (dispersive direction, downwards),  $y_{fp}$ ,  $x'_{fp}$ ,  $y'_{fp}$ . The two latter variables are the slopes  $dx_{fp}/dz$ ,  $dy_{fp}/dz$ . The z-direction is determined by the central ray. Strictly speaking the focal plane is the surface, where the rays coming from the target have their focus when covering the full angular acceptance. Usually this surface is tilted and not planar. Here as an approximation the focal plane is taken as a plane perpendicular to the central ray. The so called transfer matrix relates

the focal plane quantities to the vertex  $y$ , the slopes  $x'$ ,  $y'$  at the target and the particle momentum  $\delta = \Delta p/p_o$  relative to the central momentum of the spectrometer. The slopes  $y'$  and  $x'$  will be sometimes called in-plane and out-of-plane angle. The transfer matrix is based on a spectrometer model using COSY INFINITY [26] and has been refined by analyzing optics runs taken with the sieve slit under various conditions ( $\delta$  and  $y$  scans) [180]. Some transfer matrices provided by the Hall C collaboration were tried out and will be discussed in sec. 5.2. In sec. 3.1.3 a few spectra taken with the sieve slit in the SOS and HMS are shown.

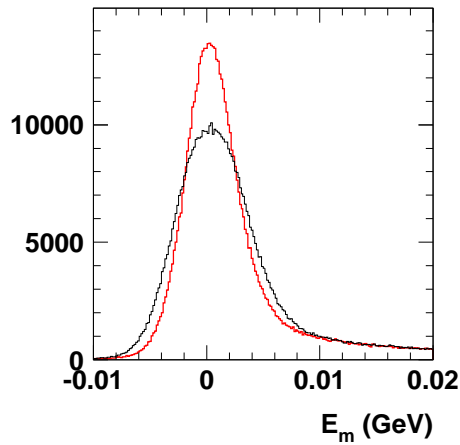


Figure 3.4: Spectrum of  $E_m$  without (black) and with inclusion (red) of the raster information in the reconstruction of the momentum. The data shown were taken via  $H(e,e'p)$ .

Because the focal plane coordinate  $x_{fp}$  in the dispersive direction is directly related to the relative particle momentum  $\delta$ , a vertical beam offset leads to a shift in  $\delta$ . For the HMS (SOS) a deviation of  $-1$  mm of the beam from the nominal position increases the momentum by  $0.07\%$  ( $0.03\%$ ). The same effect occurs due to rastering the beam in the vertical direction, which leads to a smearing of the momentum distribution, and an artificially worsening of the resolution. The actual vertical beam position is calculated from the current driving the magnets for beam rastering (Fig. 2.3). The vertical beam offset is obtained from the BPM by averaging over one run. Both effects are taken into account in the reconstruction of the target quantities. The effect on the missing energy  $E_m$  is shown in Fig. 3.4. The FWHM increases by  $2$  MeV to  $7.3$  MeV when neglecting the dependence of the reconstructed momentum on the vertical beam position. Further, both reconstructed angles are corrected for a possible tilt of the beam direction, which was in our case

very small (typical a few hundredth of a mrad).

### 3.1.3 Optics check

To check the angle and vertex reconstruction data with the sieve slit in front of the spectrometer were taken for a few kinematics. The data shown in the following were taken at central momenta of the spectrometers which correspond to the kinematics kin3 of the production data (2.05 GeV/c for the HMS, 1.7 GeV/c for the SOS). Both spectrometers detect electrons in single mode at an angle of 30°. Due to a large amount of pions in the data, which penetrate through the 3.175 cm thick sieve slit, restrictive cuts on the Cerenkov and the lead-glass detector are applied. The limits for the momentum acceptance evaluated in sec. 5 are used. Cuts on the angle acceptance were dropped as the sieve slit exceeds the dimensions of the large collimator (Fig. 3.5 and 3.6 for comparison of the dimensions of sieve slit and large collimator).

The sieve slit of the HMS is located at a distance of 168 cm from the pivot and consists of a regular pattern of holes with a diameter of 0.508 cm except for the middle hole, which is 0.254 cm wide and serves for determining the angular resolution. In the vertical (horizontal) direction the holes are spaced by 2.54 cm (1.524 cm). Two of the holes in the regular pattern are missing for checks of the orientation. In Fig. 3.5 the reconstructed vertical and horizontal position of the events at the sieve slit are given, where the orientation chosen corresponds to the front view of the collimator. In case of the HMS the positions  $sieve_{vert}$  and  $sieve_{hor}$  are obtained via

$$sieve_{vert} = -x' * d \quad (3.1)$$

$$sieve_{hor} = -y' * d - y \quad (3.2)$$

where  $d$  is the distance target–collimator. The reconstruction of the vertical position is slightly worse than in [177] even when the same transfer matrix was used. It might be due to the fact that the fast raster was not completely switched off during the sieve slit run but reduced in size to a square of 0.6 mm times 0.6 mm. The resolution is getting especially worse at large negative  $\delta$ . This feature also appears in the Monte Carlo using a transfer matrix based on the magnetic design parameter of the HMS. So it seems to be a general property of the HMS optics and not a lack in the experimentally obtained transfer matrix. Different available transfer matrices of fifth order were compared and no significant differences were observed. The resolutions of the in-plane and out-of-plane angle were obtained by fitting a gaussian to the distribution produced by the hole and taking half of the hole radius

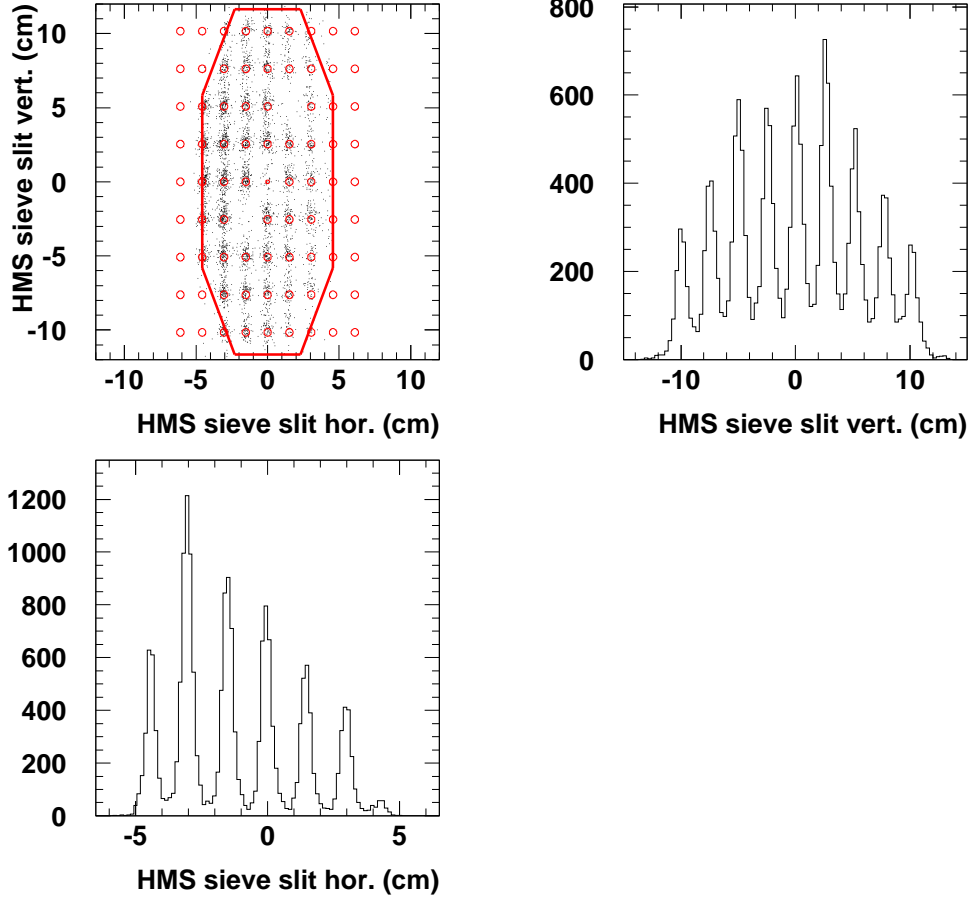


Figure 3.5: Reconstructed position at HMS–collimator using the sieve slit. The position of the holes in the sieve slit and the size of the large collimator are also shown for better comparison. The data shown are restricted to the central target as most of the runs in this work are taken with a solid target at central position.

as geometrical resolution into account. The angular and vertex resolutions are given in Tab. 2.2.

The sieve slit of the SOS at a distance of 127.8 cm from the target has holes 0.508 cm in diameter spaced by 1.542 cm in vertical direction and 2.540 cm in horizontal direction. The central three columns of holes are separated by 1.016 cm. The reconstructed positions at the collimator are shown in Fig. 3.6. Even the three central rows are spatially resolved. A transfer matrix expanded in sixth order was used. The angular and vertex resolutions obtained are summarized in Tab. 2.2.

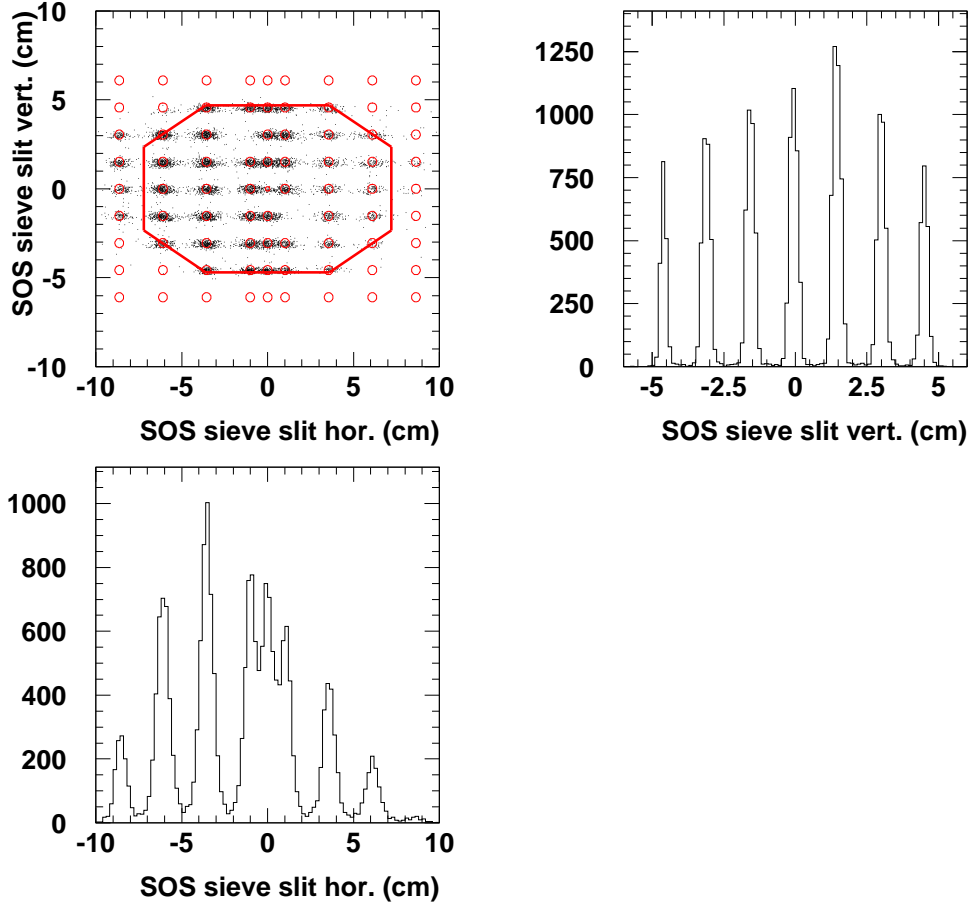


Figure 3.6: Reconstructed position at SOS–collimator using the sieve slit. The position of the holes in the sieve slit and the size of the large collimator are also shown for better comparison.

## 3.2 Particle Identification

In this experiment primarily the reaction  $(e,e'p)$  was examined. Electrons had to be separated from pions in the HMS and protons had to be identified in the SOS. Electrons can be easily separated from pions using the Cerenkov detector. Particles are defined as electrons when more than two photons in the Cerenkov detector were detected. Because the contribution of pions was always less than 10 % the lead–glass detector was only used for checking the efficiency of the Cerenkov detector (sec. 2.4.3). In the SOS protons are detected among other particles like pions, deuterons and heavier ions. They can be distinguished in the  $\beta$ -spectrum, which is obtained from the time-of-flight (TOF) between the hodoscopes (sec. 2.4.3). Because the  $\beta$ –

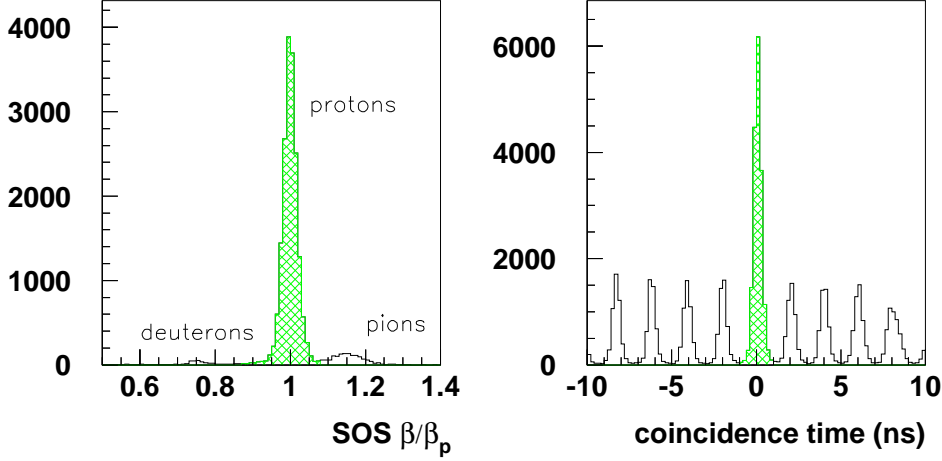


Figure 3.7: Left: Ratio of the measured  $\beta$  and the one calculated from the momentum in the SOS. Deuterons, protons and pions can be clearly distinguished. Right: Corrected coincidence time spectrum with accidental background left and right from the signal (shaded area).

distribution depends on the particle momentum it is convenient to divide  $\beta$  from TOF by  $\beta_p$  calculated from the momentum under the assumption that the particle is a proton. This is shown in Fig. 3.7, where the shaded area indicates protons distributed around unity. Protons are defined by  $0.85 < \beta/\beta_p < 1.08$ . The contribution of pions into that region is less than 1 % even for the highest central momentum of 1.7 GeV/c in the SOS shown in Fig. 3.7, when a cut on the coincidence time is applied (s. below). A correction of a few percent has to be applied due to events, where the  $\beta$  reconstruction failed (sec. 6.2).

Electrons and protons belonging to the same scattering process are selected in the coincidence time spectrum (shaded area in Fig. 3.7 right), which corresponds to the time at which the reaction in the target took place. All corrections due to different signal propagation, pulse height corrections and the path length in both spectrometers are taken into account (s. e.g. [186]). Then a FWHM of 0.5 ns in the coincidence time is achieved .The uncorrected coincidence time is called raw time and shown in Fig. 3.8. It is obtained from

$$\text{rawtime}(\text{SOS}) = \tau_{\text{protonarm}} - \tau_{\text{electronarm}} - \text{TDC}_{\text{SOS}}, \quad (3.3)$$

if the SOS starts the coincidence  $\text{TDC}_{\text{SOS}}$  and the HMS stops it. Because both spectrometers can start and stop the coincidence TDC there are two raw times. The analogous the rawtime of the HMS is

$$\text{rawtime}(\text{HMS}) = \tau_{\text{electronarm}} - \tau_{\text{protonarm}} - \text{TDC}_{\text{HMS}}. \quad (3.4)$$

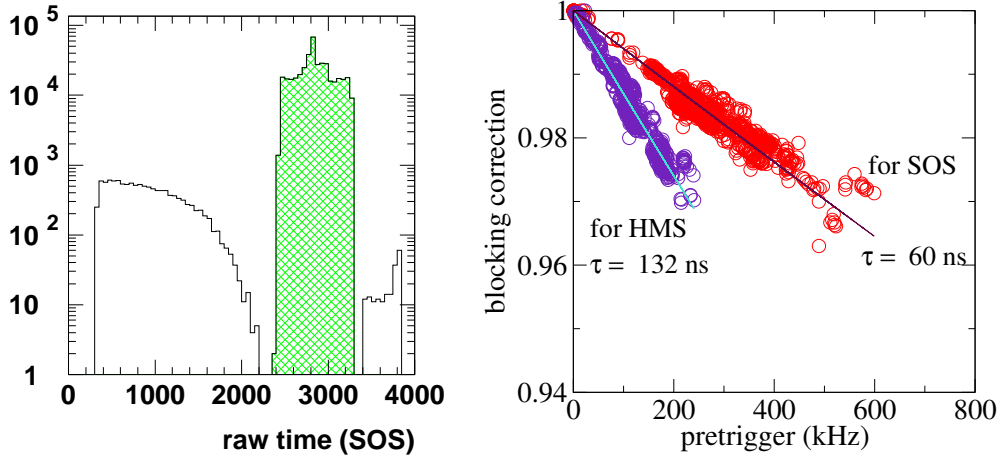


Figure 3.8: Left: SOS raw time spectrum as a function of TDC channel. Left and right from the coincidence window (shaded area) are events, which suffer from coincidence blocking and retiming. Right: Correction due to coincidence blocking in the HMS and SOS as a function of the pretrigger rate in the opposite spectrometer. The values are obtained by a fit and determine the coincidence window in the spectrometer.

The single-arm times  $\tau_{electronarm}$  and  $\tau_{protonarm}$  are measured between the front and the back hodoscopes (sec. 2.4.3). Failures occurring in the coincidence TDC and their correction are discussed in sec. 3.2.1. The random background left and right of the signal in Fig. 3.7 shows the microstructure of the electron beam of 2 ns (sec. 2.1). It is averaged and subtracted from the coincidence events (sec. 8.1). The coincidence events are defined by a cut  $\pm 1$  ns around the central peak in the coincidence time spectrum.

### 3.2.1 Blocking correction

In a few cases the timing information recorded by the HMS or SOS is incorrect and one has to correct for this inefficiency. It can be caused by blocked coincidences, self-timing events or loss of synchronization between the spectrometers. A coincidence is blocked by a single random event, which arrives before the corresponding coincidence event. This event is recorded as coincidence event, but with a raw time out of the coincidence window in one or both spectrometers. These events can be seen in Fig. 3.8 left and right of the shaded area in the SOS raw time spectrum. Here events with a raw time smaller than the coincidence window are caused by an early stop due to a HMS random trigger whereas the events above the shaded area occur due to an early start due to a SOS single event. The latter kind of events have also

a too short HMS raw time and occur also in the raw time spectrum of the HMS, but this time with a smaller time than the coincidence window. This can be seen in the two-dimensional plot of the raw times (Fig. 3.9 left). To avoid double counting the blocking correction is obtained by the fraction of events with too short raw time only. The blocking correction for the HMS and SOS in Fig. 3.8 is shown as a function of the pretrigger rate from its counterpart, which determines the rate of singles of possible blocking events. The exponential fit gives approximately the width of the coincidence window. According to that the coincidence window in the HMS electronics is 60 ns and 132 ns for the SOS. The large coincidence window in the SOS is probably due to the fact that a conversion factor of 50 ps per TDC channel was accidentally chosen instead of 25 ps/channel<sup>2</sup>. An uncertainty of 1 % for the entire blocking correction was applied, which reflects both the scatter in the blocking correction in Fig. 3.8 and a small dependence on the conditions applied in the algorithm of the tracking (sec. 3.1.1). A larger fraction of the events which were blocked are removed by cuts or by the tracking. This is probably due to mixed-up ADC-values of the drift chambers, which belong both to the coincidence event and the random single blocking the coincidence.

The rightmost peak in the SOS raw time spectrum is due to selftiming. It occurs when the SOS is started and stopped by the HMS, which results in a fixed time. These events appear also as blocked coincidences in the HMS raw time spectrum.

The HMS and SOS coincidence time are related to each other for events inside the coincidence window, which can be clearly seen in Fig. 3.9. A late HMS trigger corresponds to a large SOS raw time and a small HMS raw time, and vice versa. Therefore the sum of the SOS and HMS raw times (= 'checksum') is a constant within the resolution of the timing. In a few runs, which were taken in buffered mode, synchronization between the spectrometers was lost due to problems in a Fastbus TDC. This means that a coincidence event in the SOS is assigned to the wrong HMS event. Its effect on the two-dimensional raw time spectra of HMS and SOS is shown in the Fig. 3.9 on the right. Normally synchronization is checked and restored after flushing the buffer of the Fastbus, but in a few runs this process failed. The affected parts of the runs were removed from the database.

---

<sup>2</sup>This is a relict from experiment E93–026 performed a year before and was discovered during the present experiment.

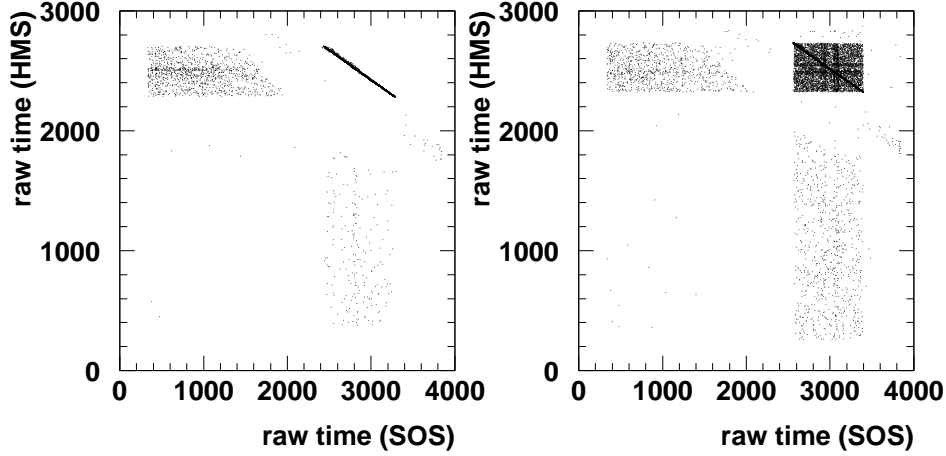


Figure 3.9: HMS raw time versus SOS raw time. Whereas in the left picture the raw times are directly related to each other, in the right picture this relation is lost due to a synchronisation problem.

### 3.3 Experimental yield

The experimental yield  $Y_{exp}$ , which is used for comparing with the Monte Carlo simulation and to evaluate cross sections, is obtained from the number of events  $N_{exp}$  in a bin or within the nominal cuts by

$$Y_{exp} = \frac{N_{exp}}{\epsilon L} \quad (3.5)$$

All corrections, which have to be applied to the data like dead time, efficiencies, are condensed in  $\epsilon$  and evaluated on a run-per-run basis. The yield is usually normalized to the luminosity, which contains the accumulated charge  $Q$  during data taking times the target thickness  $t$ .

$$L = \frac{Q}{e} t \frac{N_A}{A} \quad (3.6)$$

Here  $N_A$  is the Avogadro constant and  $A$  the mass number of the target nucleus.

# 4 The Monte Carlo Simulation

The Monte Carlo Simulation of Hall C ('SIMC') is a major ingredient for the analysis of the present work and it was also used extensively in several previous experiments. It can be used for single and double arm experiments not only for the reaction  $(e,e'p)$  but also for kaon and pion production. The reaction mechanism is based on PWIA, but in addition energy loss, multiple scattering, Coulomb and radiative corrections are taken into account. The optical properties of the spectrometer HMS and SOS<sup>1</sup> are modeled as well. Its quality can be best demonstrated by comparing the Monte Carlo spectra to the data in the reaction  $H(e,e'p)$  (sec. 6.4). In this section the main features of SIMC will be described as far as needed for the  $(e,e'p)$  analysis. Further details can be found in e.g. [59].

## 4.1 Basic structure of SIMC

The simulation of an event starts with the random generation of position, angle and energy of the incoming electron. The limits and options like raster size, beam offset and multiple scattering in the target material are set by the user via an input sheet. The nominal beam energy is influenced by energy loss in the target material and by bremsstrahlung (sec. 4.1.3) as well as Coulomb distortions (sec. 4.1.5). The location of the scattering vertex is chosen within the target dimension. Then the momenta and angles of the scattered electron and proton are randomly generated in a range, which exceeds the spectrometer acceptances. In case where the kinematics constrains the momenta and angles as in  $H(e,e'p)$  only a part of the trajectories are generated and the remaining are calculated. From the quantities at the vertex the cross section is calculated and the spectral function at  $(E_m,p_m)$  is determined according to a look-up table. Both contribute to the weight of

---

<sup>1</sup>In the release of 2001 also a model for the High Resolution spectrometer of Hall A exists.

the event (s. below). Unphysical events or events outside the spectrometer acceptances get weight zero. Before the particles enter the spectrometer corrections in the momenta due to bremsstrahlung and ionization in the target material and Coulomb distortion are applied. Further the angles are smeared out by multiple scattering. The particles are then transported through the magnetic sections in several steps by a COSY generated forward transfer matrix. At certain points the particles' position is checked against the aperture of the spectrometer. The intersection of the track at the focal plane is determined using resolutions, which were adjusted by means of  $H(e,e'p)$  data (sec. 6.4). The target quantities are obtained with a backward COSY matrix in the same manner as described in sec. 3.1.2. The vertical beam position determined by the raster can be taken into account in the reconstruction. Further Coulomb corrections can be applied and the amount of energy lost in the target added. Using these ingredients spectra of physical quantities are obtained and later on compared to the data.

All relevant kinematical quantities are written to a PAW ntuple together with their weight. The weight consists of the already mentioned cross section and the spectral function, a weight due to radiation  $W_{rad}$  and a generation weight  $W_{gen}$ .  $W_{rad}$  is determined by the energy and angular distribution of the bremsstrahlung. The generation weight is coming from the dynamical limits set, in which the quantities for each event are generated. The limits depend on the detector acceptances, but are redefined using kinematical relations and further user-defined cuts on the reconstructed  $E_m$  and  $p_m$ . This speeds up the time needed for the event generation. To compare with the data the events in SIMC have to be multiplied with the experimental luminosity and a normalization factor, which contains the ratio of generated events to the number of generation attempts. In the following the models used for the cross sections, the spectral function and the radiative processes will be described. Furthermore Coulomb corrections, energy loss due to ionization and multiple scattering will be addressed.

#### 4.1.1 The cross section

For the reaction  $H(e,e'p)$  the well known Rosenbluth cross section was taken, which contains besides the purely kinematical terms the electromagnetic structure of the proton. As form factor parametrization the fit of [118] is used, which is based on a dispersion-theoretical analysis. Different fits were tried, but differ by less than 1 %. Some are compared in Fig. 6.11.

When the proton is bound in a nucleus the kinematics is not so clear anymore. The relation between mass, momentum and energy known from relativity is not fulfilled as the proton is off-shell. No unique and exact

description of the current operator exists up to now. Constructing an off-shell operator similar to the one used for the on-shell case does not help due to the unknown off-shell electromagnetic structure of the nucleon. In particular more than two form factors appear, which in the on-shell case cancel due to gauge invariance [132]. The form factors for an off-shell nucleon can depend on other scalar variables like the invariant mass of the nucleon in addition to  $Q^2$  [148]. Due to a lack of theory to calculate the off-shell form factors, which can not be accessed experimentally, one has to take the free current operator and usually some modifications are applied.

First the modifications made by deForest [65] will be described. deForest starts from two expressions for the current

$$J_1^\mu = e\bar{u}(\vec{p}') \left\{ [F_1(q^2) + F_2(q^2)]\gamma^\mu - F_2(q^2)\frac{(p + p')^\mu}{2M} \right\} u(\vec{p}), \quad (4.1)$$

and

$$J_2^\mu = e\bar{u}(\vec{p}') \left\{ F_1(q^2)\gamma^\mu + F_2(q^2)\frac{i\sigma^{\mu\nu}q_\nu}{2M} \right\} u(\vec{p}), \quad (4.2)$$

which are equivalent on-shell, because the current operators  $\Gamma_1$  and  $\Gamma_2$  in the braces can be transformed into each other using the Gordon decomposition. The form factors are the free Dirac and Pauli form factors  $F_1$  and  $F_2$ . For the wave function of the final and initial nucleon both the free Dirac spinors  $\bar{u}(\vec{p}')$  and  $u(\vec{p})$  are used. The use of a free on-shell spinor requires the on-shell energy

$$E_{on} = \sqrt{\vec{p}_m^2 + M^2} \quad (4.3)$$

for the initial nucleon in the current operator. The on-shell energy differs from the energy of the initial bound nucleon  $E'_p - \omega$ . For consistency in the kinematics the energy transfer  $\omega$  has to be replaced by  $\bar{\omega} = E'_p - E_{on}$ , which breaks gauge invariance, i.e. conservation of the electromagnetic current at the hadronic vertex is not fulfilled. Note, that in the second choice of the current (Eq. 4.2) the energy of the initial nucleon does not appear explicitly. The deviation from the free scattering kinematics is given by  $\Delta\omega = \omega - \bar{\omega}$ , which is called off-shellness [132]. The off-shellness is high for large  $p_m$  and  $E_m$ . If the current would be conserved, the continuity equation would be satisfied:

$$qJ = \omega J_o - \vec{q}\vec{J} = 0 \quad (4.4)$$

To restore current conservation on the one-body level after the above modifications deForest replaces the longitudinal component  $J_q$ , which is parallel to  $\vec{q}$ , by the charge density  $J_o$  using Eq. 4.4:

$$J_q = \frac{\omega J_0}{|\vec{q}|} \quad (4.5)$$

Using this recipe deForest obtains two cross sections, called  $\sigma_{cc1a}$  and  $\sigma_{cc2a}$  in the following, which use the current operator in Eq. 4.1 and 4.2 respectively. The reason to keep the charge density instead of the vector current is suggested by the Siegert theorem.

In [132] it is doubted that this argument is applicable for the one-body current. In this paper the authors found a different behavior of shape and magnitude of the cross section, when eliminating the charge density and replacing instead

$$J_o = \frac{\vec{q}\vec{J}}{\omega}. \quad (4.6)$$

The resulting expression for the cross section called  $\sigma_{cc1b}$  [23] is given in appendix A for the current operator  $\Gamma_1$ . In [148] it is shown that the different ways to restore current conservation can be seen as a choice of gauge. Accordingly the choice of deForest Eq. 4.5 is equivalent to working in the Coulomb gauge; using Eq. 4.6 corresponds to the Weyl gauge.

One can also consider not to restore current conservation, which is equivalent to replace the current by

$$\bar{J}^\mu = J - \frac{\vec{J}\vec{q}}{q^2}q^\mu, \quad (4.7)$$

because the last term vanishes when multiplied by the lepton tensor. This choice was used by Mougey [126] and corresponds to the Landau gauge. The equation for the cross section  $\sigma_{cc2c}$  of Mougey based on the current operator  $\Gamma_2$  was taken from [65] Eq. 25. The expression using  $\Gamma_1$  will be given in appendix A. It is denoted by  $\sigma_{cc1c}$ . The cross section was criticized because Eq. 4.7 diverges in the photon limit. For the kinematics of this experiment this does not matter.

Another cross section is obtained when one does not use the on-shell energy but leaves the kinematics as required by energy conservation. Then the momentum transfer  $\vec{q}$  is NOT replaced by  $\vec{q}$  and the on-shell energy  $E_{on}$  is not used for the energy of the bound nucleon. But the problem remains that one uses an on-shell current operator for off-shell kinematics. This is especially serious for the current operator  $\Gamma_1$ , which contains the four-vector of the bound nucleon explicitly. Further, to get the cross section the matrix element is calculated from the contraction of the lepton and hadron tensor. Both tensors are obtained from the spin sum over the Dirac spinors sandwiched by the current operator. Using the completeness relation of the Dirac spinors the spin sums collapses to traces, which finally are evaluated using trace theorems. The point is that the completeness relation is not valid anymore. To solve this inconsistency the Lorentz-products of the kind  $[p,p']$

(4–vector  $\mathbf{p}$ ,  $\mathbf{p}'$  of the initial and final proton) are evaluated using the on–shell condition. The result is called  $\sigma_{cc}^2$  and is based on the current operator  $\Gamma_1$ . It is interesting to note that no on–shell condition is necessary when using  $\Gamma_2$ . The result is numerically very close to  $\sigma_{cc}$ . All cross sections above, which are derived from  $\Gamma_1$ , will reduce to  $\sigma_{cc}$  when omitting the replacement suggested by deForest [23]. The influence on the extracted spectral function in parallel and perpendicular kinematics will be examined in sec. 8.2.5.

One can ask the question, which of the cross sections one should prefer. In [132] it was realized that  $\sigma_{cc2}$  does fulfill the half off–shell Ward–Takahashi identity at least at the photon point  $q^2 = 0$ , which is not the case for  $\sigma_{cc1}$ . Here half off–shell means that the initial nucleon is taken off–shell whereas the final nucleon is on–shell. In addition due to the structure of the current operator in Eq. 4.2 there is no need to use the expression for the on–shell energy explicitly in  $\sigma_{cc2}$ .

#### 4.1.2 Models of the spectral function and its implementation

One has to distinguish between the spectral functions for the single–particle region, the theoretical spectral functions of [22] and [128] and the spectral functions extracted from the data by means of an iterative procedure (sec. 8.1). Spectral functions for carbon, iron and gold were already implemented in SIMC for its use in the single–particle region. They are the same as for the experiments NE–18 [114][133] and E91–013 [59][186]<sup>3</sup>. These are derived in the framework of IPSM (sec. 1.2.2) and based on the assumption that the spectral function can be decomposed into its momentum and energy distribution  $n(\vec{p}_m)$  and  $\epsilon(E_m)$  for each orbit. The momentum distributions were calculated using the program DWEEPY<sup>4</sup> [79], which solves the Schrödinger equation for an optical potential. The optical potential was chosen as the sum of a Wood–Saxon and Coulomb potential. The parameters of the Wood–Saxon potential for <sup>12</sup>C were taken from data measured at Saclay [125]. This reference provides also <sup>56</sup>Ni(e,e'p) parameters, which were slightly modified to fix the potential for <sup>56</sup>Fe [114]. In a similar way the <sup>208</sup>Pb(e,e'p) data of [151] were used for deriving the momentum distribution for <sup>197</sup>Au. The re-

---

<sup>2</sup>To obtain the cross section from the expressions given in [65] the sum of the energies in the initial state  $(E + E_{on})^2$  in the structure functions  $w_C$  and  $w_I$  has to be replaced by  $(E_{on} - \bar{\omega}/\bar{q}^2(E_{on}\bar{\omega} - \bar{q}\bar{p}))^2$ .

<sup>3</sup>With the exception that the width of the 1p<sub>3/2</sub>–state was changed from 5 to 1 MeV, which seems to be more reasonable and fits the data better.

<sup>4</sup>DWEEPY stands for Distorted Wave eep and is usually used for calculating Coulomb corrections.

removal energy distribution is described by a Lorentzian with a width  $\Gamma$  around a central energy eigenvalue  $\epsilon$ . The width is related to the life time  $\tau$  of the nucleon in the shell by  $\Gamma = 1/\tau$ .  $\epsilon$  and  $\Gamma$  were either taken from fits to data or from the equation of [35].

The theoretical spectral functions of Benhar [22] for carbon, iron and gold contain initially only the continuum part caused by SRC (sec. 1.2.7). The normalization obtained by integrating the correlated part of the spectral function over  $E_m$  and  $p_m$  is 0.220 for  $^{12}\text{C}$ , 0.215 for  $^{56}\text{Fe}$  and 0.217 for  $^{197}\text{Au}$ . Therefore the single-particle spectral function mentioned above was normalized in such a way that it adds to one together with the part provided by Benhar. The result was implemented in SIMC via a look-up table with a spacing of 20 MeV/c in  $p_m$  and 0.5 to 5 MeV in  $E_m$  to account for the detailed shell structure. In a similar way the spectral function of Müther et al. [128] is used. This spectral function was originally calculated for  $^{16}\text{O}$ , but renormalized for  $^{12}\text{C}$ . The strength of the quasi-particle part is 0.88 and contains in addition long-range correlations, which lead to a fragmentation of the single-particle states (sec. 1.2.5).

The spectral function from the data is extracted by an iterative process. An iterative procedure is needed due to the influence of radiative processes on  $E_m$  and  $p_m$  (sec. 4.1.3), the contribution of which depends on the kinematical distribution of the data and thus on the spectral function. In practice this means that one starts e.g. with a theoretical spectral function as input for SIMC. Then the spectral function obtained from the experiment is written to a look-up table and used by the next Monte Carlo simulation. This procedure is explained in more detail in 8.1.

It should be noted that each kinematics in the experiment can only cover a part of the  $(E_m, p_m)$ -region due to the limited detector acceptance. On the other hand some events originating from outside of the experimental phase space are scattered into the detector acceptance due to radiative processes. Therefore the spectral function needs to be known in a larger region. This is possible by combining the results from the three parallel (two perpendicular) kinematics. The spectral function evaluated in IPSM is reduced by a factor of 0.8. For  $^{27}\text{Al}$  the momentum distribution of  $^{56}\text{Fe}$  was taken and the shells not occupied in  $^{27}\text{Al}$  were removed. The width and the central binding energy were taken from [131] and adjusted to a run taken on the Al-dummy target in quasi-elastic kinematics<sup>5</sup>.

---

<sup>5</sup>This run serves normally for subtracting the amount of background due to the target windows of the hydrogen cell (sec. 6.4).

### 4.1.3 Radiative corrections

The cross sections considered so far do not involve the process of radiating additional photons at the scattering vertex. Charged particles in the electric field of a nucleus can emit real photons. This process is called bremsstrahlung. The nucleus can be directly involved in the scattering process (internal radiation) or belong to material penetrated by the charged particle (external radiation). The scattering vertex can be modified by further virtual photons. The leading Feynman graphs are referred as vertex correction, self-energy, vacuum polarization, box and crossed-box diagram. The corresponding scattering amplitudes are called elastic whereas the one involving real photons are named inelastic.

The effect on the experimental data is twofold. First, especially electrons can loose a large amount of energy and thus fall outside the momentum acceptance of the spectrometer<sup>6</sup>. As a rule of thumb this leads to a reduction in the yield of 20–30 %. Second, the reconstructed quantities  $E_m$  and  $p_m$  important for the present work will be changed due to photons radiated by the incoming and outgoing electrons and the knocked-out proton. Combined this leads to a modification  $\vec{p}_m + \vec{p}_\gamma$  and  $E_m + E_\gamma$ , when  $p_\gamma$  and  $E_\gamma$  is the sum of the momenta and energies of all emitted photons in the reaction. Because bremsstrahlung in direction of the particle momentum is by far the dominant process the relation  $|p_\gamma| = E_\gamma$  is valid. For high photon energies this leads to a tail in  $(E_m, p_m)$  with  $E_m \approx p_m \approx E_\gamma$ . This tail can be clearly seen in the  $p_m$ – $E_m$  distribution in elastic kinematics for hydrogen (Fig. 6.12). As consequence events will be radiated in and out of a given  $(E_m, p_m)$  bin. Therefore the radiative process has to be included in the kinematics of SIMC and it is not sufficient to correct for it only by a global factor as it was done in former times. This requires an angular and energy distribution of the radiated photons.

The approach incorporated in SIMC follows the work of Makins [114][62], which is based on the treatment of radiative processes by Mo and Tsai [120], but extended to the case of coincidence experiments  $(e, e' p)$ . Here one has also to take into account the radiative effect from the proton alone as well as an interference term between the proton and electron radiation. Furthermore, integration over all final states as used in the  $(e, e')$  reaction can not be performed.

Two models are realized in SIMC to serve for comparison and estimating the accuracy of the treatment of radiative processes. They are called peaking and multiphoton technique according to their treatment of the angular

---

<sup>6</sup>Depending on the kinematics it is also possible to gain events originally with higher momentum.

distribution of the photons [62]. Both models are based on the Soft Photon Approximation (SPA), where the assumption is made that the energy of the radiated photon is much less than the momenta of the initial and final particles participating in the primary scattering reaction. Due to the limited momentum acceptance of the spectrometer this assumption is well fulfilled. Using SPA the basic scattering cross section factorizes from the amplitudes of the bremsstrahlung. The total cross section for the reaction  $(e, e' p)$  including *one* photon radiation with energy less than  $\Delta E$  can be written to first order in  $\alpha$  as

$$\frac{d\sigma}{d\Omega_e}(E_\gamma < \Delta E) = \frac{d\sigma}{d\Omega_e} |_{ep} (1 - \delta_{soft}(\Delta E) - \delta_{hard}) \quad (4.8)$$

Here  $\frac{d\sigma}{d\Omega_e} |_{ep}$  is the usual PWIA cross section for the reaction  $(e, e' p)$ . This cross section has to be evaluated at the energy of the initial electron after radiation. The contributions from the radiative process are divided into  $\delta_{soft}$ , which accounts for the emission of one real photon (Bremsstrahlung), and  $\delta_{hard}$  coming from the second order virtual photon diagrams. Some of these diagrams depend on the off-shell proton current. To avoid ambiguities such terms are dropped in  $\delta_{hard}$  except for the infrared divergent terms, which cancel with those from the Bremsstrahlung part. This is the same approach as used in [120]. Note, that  $\delta_{hard}$  is negative and leads to an increase of the measured cross section. Its contribution less than 10 % even at high  $Q^2$ . Eq. 4.8 is divergent for  $\Delta E \rightarrow 0$ . In the regime of small photon energies multiple photon emission dominates. It was shown by [194] that the soft-photon diagrams can be summed up to all orders by exponentiation

$$\frac{d\sigma}{d\Omega_e}(E_\gamma^i < \Delta E) = \frac{d\sigma}{d\Omega_e} |_{ep} e^{-\delta_{soft}(\Delta E)} (1 - \delta_{hard}), \quad (4.9)$$

which corresponds the cross section for emitting any number of photons, each with energy less than  $\Delta E$ . It is up to order  $\alpha^2$  identical with the cross section of emitting a number of photons with the total energy less than  $\Delta E$ . The differential cross section for emitting any number of photons of total energy  $E_\gamma$  is

$$\frac{d\sigma}{d\Omega_e dE_\gamma}(E_\gamma) = \frac{d\sigma}{d\Omega_e} |_{ep} (-\delta'_{soft}) e^{-\delta_{soft}(E_\gamma)} (1 - \delta_{hard}), \quad (4.10)$$

where  $\delta'_{soft}$  is the derivative of  $\delta_{soft}$  with respect to  $E_\gamma$ . This expression together with the pure peaking approximation is used in the peaking technique. The pure peaking approximation allows photon radiation only in the direction of one particle. In fact this means that the incoming, outgoing electron *or* proton can emit photons in their flight direction. The strength is distributed according to the integrated angular distribution in the three directions  $(\lambda_e, \lambda'_e, \lambda'_p)$ . Terms caused by an interference between proton-electron

and electron–electron are taken into account in the 'extended peaking' approximation. The total strength is preserved in the ultrarelativistic limit ( $Q^2, k, k', p' \ll m_e, M_p$ ) and distributed among the radiation tail of the initial and final electron.

In the multiphoton technique all three particles can emit photons at the same time but only along the particles' direction. The total momentum of the radiated photons is then the vector sum of all photons along the three possible directions. It is assumed that photons, which are emitted along the flight path of one of the outgoing particles, can be treated as emitted by the corresponding particle. The energy distribution has the form of Eq. 4.10, but the soft–photon part factorizes into three independent terms for the radiation tails of both electrons and proton. It is calculated in the ultrarelativistic limit. For completeness the result is given (s. [114] for derivation):

$$\frac{d\sigma}{d\Omega_e dE_e dE_{e'} dE_{p'}} = \frac{d\sigma}{d\Omega_e} |_{ep} (1 - \delta_{hard}) \frac{\lambda_e}{E_\gamma} \left( \frac{E_\gamma}{\sqrt{|kk'|}} \right)^{\lambda_e} \frac{\lambda_{e'}}{E_\gamma} \left( \frac{E_\gamma}{\sqrt{|kk'|}} \right)^{\lambda_{e'}} \times \frac{\lambda_{p'}}{E_\gamma} \left( \frac{E_\gamma}{\sqrt{|ME_{p'}|}} \right)^{\lambda_{p'}} \quad (4.11)$$

These two approaches should help to give an estimate of the error introduced by an oversimplified angular distribution (peaking technique) and an energy distribution only valid in the ultrarelativistic limit (multiphoton technique). The first approach uses the best available equations for the energy distribution whereas the second approach improves the angular distribution significantly. The ultrarelativistic limit is certainly not fulfilled on the proton side for the kinematics under consideration. In addition, the peaking approximation for the proton will fail as the angular distribution is only peaked for highly relativistic particles (s. Fig. 4 in [62]). On the other hand the direct contribution of the proton to the radiative tail is small (< 2 %) at low  $Q^2$ . The interference term proton–electron is about twice the size. The two techniques will be compared in sec. 8.2.4, when extracting the spectral function from the data.

In [62] a third technique, the modified equivalent radiator method (MERM), is studied. It treats the internal radiation like the external one using an equivalent radiator thickness. Here the close relation between internal and external radiation in the energy distribution is exploited. Its result is in agreement with the other two techniques.

In [117] the work of Mo and Tsai [120] was improved by a refinement of the mathematical treatment and the contribution of real soft photon emission by the electron and proton is calculated exactly (without SPA). In particular,

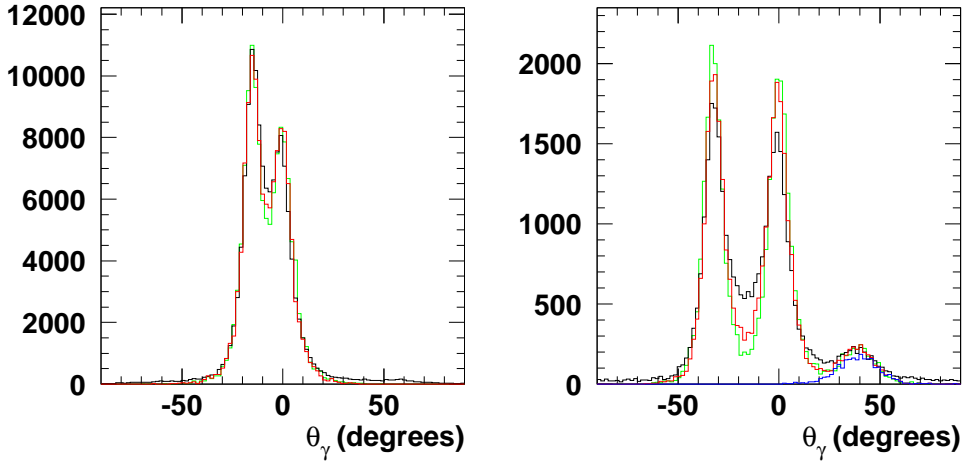


Figure 4.1: Angular distribution of radiated events for the reaction  $H(e,e'p)$  for  $Q^2 = 0.6$  ( $\text{GeV}/c^2$ ) (left) and  $2.0$  ( $\text{GeV}/c^2$ ) (right). The data in black are compared to the Monte Carlo using the peaking (green) and multiphoton (red) technique for radiating events. The blue curve shows the contribution from events, which lost energy by penetrating through the collimator material (sec. 6.5). Kinematics for left (right) figure:  $E_e = 3.12$  GeV,  $E'_e = 2.75$  ( $2.05$ ) GeV,  $p'_p = 0.85$  ( $1.7$ )  $\text{GeV}/c$ ,  $\theta_e = 15.3^\circ$  ( $32.5^\circ$ ),  $\theta_p = 59.5^\circ$  ( $38.5^\circ$ ). As cut of  $E_m > 30$  MeV is applied to reduce the sensitivity to the finite resolution.

the finite size of the nucleon is included by using the current of Eq. 4.2. It turns out that these refinements lead to a difference of 2 % compared to [120] only at very high  $Q^2 > 10$  ( $\text{GeV}/c^2$ ). For the  $Q^2$ -range relevant for the present experiment the difference is negligible.

A rigorous test of the radiation technique can be made by reconstructing the experimental angular distribution of the photons in the reaction  $H(e,e'p)$  and comparing it to the Monte Carlo prediction. It exploits the fact that energy loss due to radiation suffered by a participating particle will lead to a non-zero  $p_m$  in the direction of the sum of the emitted photon momenta. The angle  $\theta_\gamma = \text{atan}(p_m^y/p_m^z)$  is then the angle of the summed-up photon momenta with respect to the electron beam direction in the horizontal plane.

In Fig. 4.1 the two dominant peaks belong to the direction of the incoming and outgoing electron. At low  $Q^2$  photon emission along the proton flight path is suppressed. The bump around  $40^\circ$  in Fig. 4.1 on the right is predominantly caused by fast protons, which are penetrating through the collimator of the SOS and thus lose a significant amount of energy (sec. 6.5). This

process is included in SIMC and these events are shown by the blue curve. From the comparison of the data with SIMC one can conclude that a small fraction of events is coming from photon emission in direction of the proton, which disappear when switching off the proton radiation in the Monte Carlo. In [32] this was also observed and reported as first evidence for virtual Compton scattering from the proton. In Fig. 4.1 the Monte Carlo simulation was done with the peaking (green) and multiphoton (red) technique. The second method can describe the data better in the region of coherent interference between the two major peaks. The deviation seems to increase at high  $Q^2$ . It might be that the close vicinity of the scattered to initial electron at low  $Q^2$  leads to better agreement. Further the width of the two dominant peaks seems to be too small in the Monte Carlo. This might be due to the detector resolution not perfectly matched to the experimental conditions, even though an effort was made to get optimal agreement of the kinematical spectra (sec. 6.4).

In ref. [62] the multiphoton technique seems to fit better the data. It might be also an indication of the failure of the peaking approximation. A treatment, which allows multiple photon emission in any direction, would lead to a broadening of the two peaks in Fig. 4.1 and to a fill-in of the region between the two peaks. Such a treatment is in progress [183] and preliminary results show considerable improvement. Aside from this the difference in the total yield found exceeds not 1 % compared to the peaking approximation. The fraction of data shown in Fig. 4.1 is  $\approx 15 \%$ , because a cut  $E_m > 30$  MeV is applied to reduce the sensitivity to the finite detector resolution, which is matched by SIMC only approximately. Further to exclude the  $\Delta$ -resonance  $E_m < 0.12$  GeV is required.

External bremsstrahlung due to the finite target thickness is included as well. An analytical expression based on Early's numerical work [60] was obtained by [172] [173]. Accordingly the probability to find an electron with initial energy  $E$  in the energy interval  $E'$  and  $E' + dE$  after transversing a material with thickness  $t$  (in radiation lengths) is given by

$$I(E, E', t) dE = \frac{bt}{\Gamma(1+bt)} \frac{1}{E - E'} \left( \frac{E - E'}{E} \right)^{bt} \phi\left(\frac{E - E'}{E}\right) dE. \quad (4.12)$$

where  $b$  depends on the nuclear charge and is approximately  $4/3$ . The function  $\phi$  describes the shape of the bremsstrahlung spectrum in the complete screening limit. Complete screening of the nucleus due to the surrounding electrons is reached for small photon energy. Then  $\phi$  simplifies to

$$\phi(v) = 1 - v + \frac{3}{4}v^2 \quad (4.13)$$

This equation is accurate to within 0.5 % for  $t=0.1$  and improves for thinner targets. As can be seen from Tab. 2.1 thicker targets are not used in this experiment. It should be mentioned that external bremsstrahlung from the proton is suppressed by  $1/M_p^2$ . This factor does not appear explicitly in Eq. 4.12 but is hidden in the radiation length. Comparing the expressions for internal and external radiation (Eq. 4.11 and Eq. 4.12) their dependence on the photon energy is the same in the leading terms, if one exchanges  $bt$  by  $\lambda$ . This is also the starting point of MERM mentioned above. Therefore the external radiation can be included in the equation for the internal radiation in a consistent way.

Friedrich [70] proposed a modification of Eq. 4.12 with a exponential function

$$I(E, E', t) dE = \frac{bt}{E - E'} \left( \frac{E - E'}{E} \right)^{bt} \phi(v) e^{[t(b-0.5) - bv + v^2/2]} dE \quad (4.14)$$

with  $v = \frac{E-E'}{E}$ . The exponential factor should account for multiphoton emission. The function  $\phi$  is modified using  $1/b$  instead of  $3/4$ .

The two equations will be compared using data taken with different target thicknesses, but in the same kinematics and with the same target material (sec. 8.2.4).

Combining external and internal bremsstrahlung the energy dependence is mainly determined by  $E^{g-1}$  with  $g=bt + \lambda$ . In order to use it as generation function  $G$  for the energies of the emitted photons it has to be integrated between the limits of the smallest and largest photon energy  $E_{min}^g$  and  $E_{max}^g$  possible and then normalized to one. These limits are determined by kinematics, detector acceptance and the largest accepted  $E_m$ . The generation function

$$G = \frac{g E^{g-1}}{E_{max}^g - E_{min}^g} \quad (4.15)$$

is used to generate photons with the correct energy shape. The radiation weight  $W_{rad}$  is the product of the probability of emitting internal and external bremsstrahlung as well as virtual photons. It is given by the product of the energy distributions for internal and external bremsstrahlung, e.g. Eq. 4.11 and Eq. 4.14, divided by the generation function at the photon energy generated ([59] [186]).

#### 4.1.4 Energy loss and multiple scattering

The second major process, which leads to energy loss of the charged particle when transversing material, is caused by inelastic collisions with the atomic

electrons of the material. These collisions are divided into two groups: soft collisions, which result only in excitations, and hard collisions, which lead to ionization. At large energy transfers secondary ionization can occur ( $\delta$ -rays). The energy spectrum of the  $\delta$ -electrons has a much shorter tail than for bremsstrahlung ( $1/\epsilon^2$  versus  $1/\epsilon$ ). Further, for electrons passing through material the energy loss due to external bremsstrahlung will always dominate over the ionization at the particle energies of interest here. Therefore it is sufficient to take only the most probable energy loss into account. The equation used is described in [140] [149] and valid for high-energy electrons and thin targets. For protons the mean energy loss is calculated using the Bethe–Bloch equation [109]. Energy straggling is approximated by a gaussian distribution and the Landau tail is neglected.

In addition to inelastic collisions charged particles also experience elastic Coulomb scattering, which leads to a random zigzag path through the medium. Most of the deflections are small and can be approximated by a gaussian distribution [145]. Multiple scattering is taken into account for the in-plane and out-of-plane angle in all materials around the target and in the spectrometer. It deteriorates the angular resolution achievable with the spectrometer.

#### 4.1.5 Coulomb corrections

A further correction to PWIA is the distortion of the electron and proton wave function due to the charge of the nucleus involved in the reaction. The effect of the Coulomb potential on the electron wave function in first order leads to an acceleration (deceleration) of the incoming (outgoing) electrons. Higher orders increase the electron flux on the target nucleus (focusing) and distort the plane waves. The size of these corrections depends on the kinematics. The distorted wave function for the electron can be obtained by solving the Dirac equation for a spherically symmetric Coulomb potential, which is usually derived from the experimental nuclear charge distribution. Because of the long-range character of the Coulomb potential a large number of partial waves have to be included, which leads to a considerable numerical effort. Therefore often the effective momentum approximation (EMA) is applied in the analysis of experimental data. The EMA is the first order approximation in  $Z\alpha$  of the exact solution. In EMA the initial and final momentum of the electron are replaced by

$$\vec{k}^{EMA} = \vec{k} + V_c \frac{\vec{k}}{k} \quad (4.16)$$

Thereby  $\vec{k}$  represents the nominal beam momentum or alternatively the momentum measured in the detector. The  $r$ -dependent Coulomb potential is replaced by a mean potential  $\bar{V}_c$ . Its value will be discussed below. In this approximation the energy transfer remains unchanged and the 3-momentum transfer is given by

$$\vec{q}^{EMA} = \vec{q} + \frac{\bar{V}_c}{E}(\vec{q} - \omega \hat{k}_f) \quad (4.17)$$

The wave functions of the incoming and outgoing electron have to be renormalized

$$e^{ik\vec{r}} \implies \frac{k^{EMA}}{k} e^{i\vec{k}^{EMA}\vec{r}} \quad (4.18)$$

This leads to a modification in the off-shell cross section

$$\sigma_{cc}^{EMA} = \left( \frac{k_i^{EMA}}{k_i} \right)^2 \sigma_{cc}. \quad (4.19)$$

The corresponding factor for the outgoing electron cancels with the same factor from the density of states [92]. It should be noted that the factor  $k_i^{EMA}$  in Eq. 4.19 cancels in the Mott cross section. Together with the remaining part one can obtain the same result, if one lets the Mott cross section unchanged. Whereas the electron kinematics is changed according to the recipe described above, the proton kinematical variables remain unchanged, i.e. the asymptotic ones. However, the form factors of the proton are now evaluated at  $q^{EMA}$  instead of  $q$  [92].

From the above equations it is clear that for electron momenta, which are large compared to the modification induced by the Coulomb potential in Eq. 4.16, the correction will be small and EMA is applicable. On the other hand kinematics as used at Saclay and NIKHEF to measure spectroscopic factors (sec. 1.1) can have sizeable Coulomb corrections for heavy nuclei, which can not be fully accounted for by EMA. This will be demonstrated on an example for a kinetic energy of the outgoing proton ( $T_p = 100$  MeV) and an incoming electron energy of  $E_e = 412$  MeV. In Fig. 4.2 the reduced cross section for the  $3S_{1/2}$ -state in  $^{208}\text{Pb}$  was calculated by Udias et al. [174] in PWIA, full DWIA (proton and electron distortion) and EMA for parallel and perpendicular kinematics. In parallel kinematics the Coulomb distortions lead to a shift of the reduced cross section to higher  $p_m$ , which can be well accounted for by the EMA. This is quite an improvement compared to pure PWIA. On the other hand the filling of the minimum can not be accounted for by EMA or PWIA. In addition DWIA predicts a 8 % (14 %) higher amplitude for the first (second) maxima compared to PWIA<sup>7</sup>. This is due to the focusing

---

<sup>7</sup>As can be seen from Fig. 4.2 the amplitudes predicted using PWIA and EMA are quite the same in parallel kinematics.

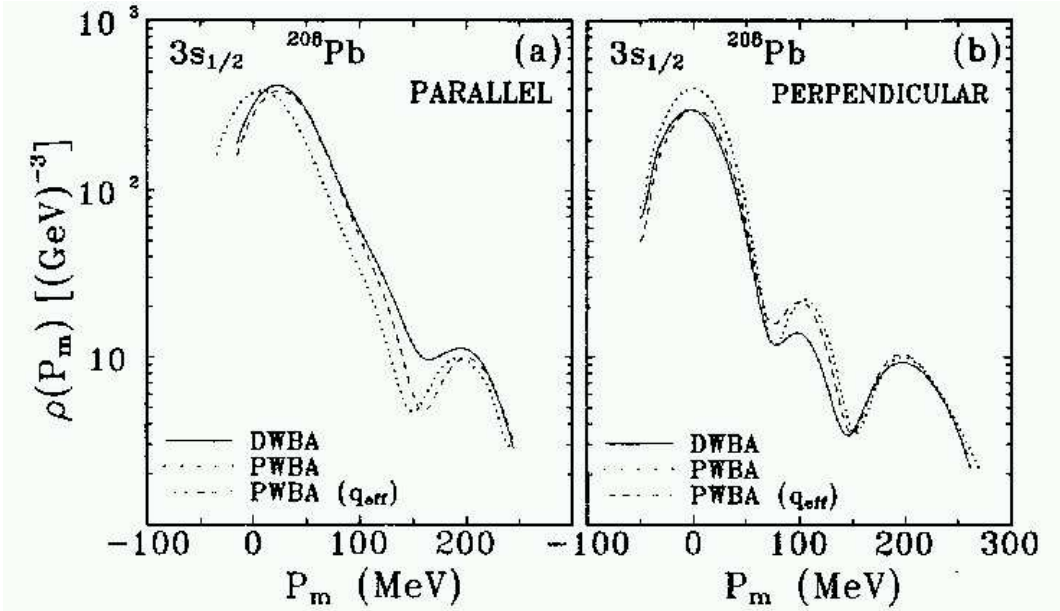


Figure 4.2: Effect of Coulomb distortion on the reduced cross section in parallel and perpendicular kinematics [174].

effect, which is not accounted for by the EMA. In perpendicular kinematics no shift in  $p_m$  is observed, but a reduction in the cross section at  $p_m \approx 0$ . This is a kinematical effect and caused by the fact that the maximum of the bound nucleon wave function is not reached with the modified kinematics. The reduction of the cross section is well reproduced by the EMA at least for the first maximum. The size of the corrections and the effects are confirmed by [92] [93].

For the kinematics of this work with momenta in the GeV-region the effect of the Coulomb distortion is small in general. In addition, forward electron scattering angles help to reduce the size of the Coulomb correction. To check this assumption calculations by [12] were performed in an eikonal approximation, which has the advantage that it provides an analytic expression for the wave functions. Because an IPSM wave function seems not appropriate for kinematics probing the region of high missing energy and momentum, a wave function with a high momentum tail was reconstructed from one hundred single-particle model wave functions each containing significant strength in the high momentum region. The so obtained cross sections for gold, where the Coulomb corrections are largest, show good agreement with the EMA corrections for the kinematics used in this work. The size of the

Coulomb correction is  $\approx 1.2\%$ , which is of the order of the focusing factor. Different choices of the momentum distribution had negligible influence on the result. The deviation of the Coulomb correction from EMA is typically 20–30 % of the size of the Coulomb correction, which in our case leads to a small error of  $\approx 0.3$ – $0.4\%$

In the Monte Carlo as well as in the experimental analysis Coulomb corrections are included on the EMA level. For the static Coulomb potential the following expression is used:

$$\bar{V}_c = 1.2 \frac{Z\alpha\hbar c}{R_c} \approx 1.34 \frac{Z}{\langle r^2 \rangle^{1/2}} \quad \text{in MeV fm} \quad (4.20)$$

Here  $R_c$  is the radius of a charged sphere equivalent to the nuclear charge distribution. It is connected to the rms-radius  $\langle r^2 \rangle^{1/2}$  of the nucleus via  $R_c = \sqrt{5/3} \langle r^2 \rangle^{1/2}$ . For a Wood–Saxon potential  $R_c$  is  $\approx 1.18A^{1/3}$ . The factor 1.2 arises from averaging the potential of a homogeneously charged sphere

$$V(r) = \frac{Z\alpha}{R_c} \left( \frac{3}{2} - \frac{1}{2} \frac{r^2}{R_c^2} \right). \quad (4.21)$$

In most of the literature the potential at the origin of the sphere is taken. This assumption does not agree with a cross section measurement using electrons and positrons as projectiles under otherwise identical conditions [85]. Because the Coulomb correction for electrons and positrons changes sign the total response function for positrons at an incident energy  $E_{e+}$  and for electrons at  $E_{e-} - 2V_c$  has to be the same, if EMA is valid. At least it allows to extract a value for  $V_c$  to be used in EMA. The result [85] is

$$V_c = \frac{(1.27 \pm 0.10)(\text{MeV fm})}{\langle r^2 \rangle^{1/2}} Z, \quad (4.22)$$

which agrees with the expression used in SIMC (Eq. 4.20).

# 5 Correction to the tracking efficiency

As described in sec. 3.1.1 the tracking efficiency is determined by using a large region of the focal plane. Therefore variations in the efficiency over the focal plane are averaged out. The correction to the tracking efficiency will be called shortly “focal plane” efficiency. In principle the tracking efficiency can depend on each quantity measured in the spectrometer. In this section the correction is determined as a function of the relative particle momentum  $\delta = \Delta p/p_o$  for each spectrometer.

## 5.1 Idea and method

To determine the “focal plane” efficiency inclusive data ( $e,e'$ ) on carbon were taken in the inelastic region ( $x_{Bj} = 0.15 - 0.38$ ) with both spectrometers positioned at an angle of  $20^\circ$ . In the SOS six kinematics with central momentum  $p_o = 1.35, 1.45, 1.5, 1.55, 1.6, 1.65, 1.7$  GeV/c were used. The central momentum of the HMS varied from 1.45 to 2.05 GeV/c in steps of 0.1. In this region the cross section shows only small and smooth variations with the energy of the scattered electron. Due to the spectrometer momentum acceptance of several percents a part of the data taken in different kinematical settings corresponds to the same momentum of the electron, but different relative momentum  $\delta$ . One then exploits the fact that the cross section does not depend on the relative momentum. A dependence on  $\delta$  is due to local variations of the detector efficiency and will be corrected by the “focal plane” efficiency. In addition there also exists a kinematical overlap of the data measured with HMS and SOS. Therefore both cross sections can be directly compared as a function of the electron momentum. The cross section does, however, have a dependence on the scattering angle (2–3 % for  $0.1^\circ$ ). To correct for this the angular dependence was fitted for a region close to

the central momentum (SOS: $\pm 5\%$ ,HMS: $\pm 4\%$ ) and used as a weight for each event relative to the central angle of  $20^\circ$ <sup>1</sup>. The angular dependence makes the comparison between the cross sections obtained with the HMS and SOS also sensitive to the offset applied to the central angle of the spectrometer (sec. 6.3). This fact helped finally to favor the spectrometer offsets obtained for an initial electron energy reduced by 0.1 %. This choice is in agreement with the analysis of E. Christy [42] using H(e,e'p) data in several kinematics.

## 5.2 Inelastic cross section

To extract the cross section from the data the phase space is generated by the Monte Carlo simulation for the HMS and SOS. The generated phase space is sensitive to the transfer matrices used, which connect focal plane coordinates with the quantities of the scattering reaction and vice versa. The transfer matrices for the HMS-100 tune in 1999 as well as for the SOS are provided by D. Potterveld. The limits of the momentum and angular acceptance,

---

<sup>1</sup>Alternatively one can restrict the angular acceptance of the HMS and SOS in such a way that they match each other. This was used as a check.

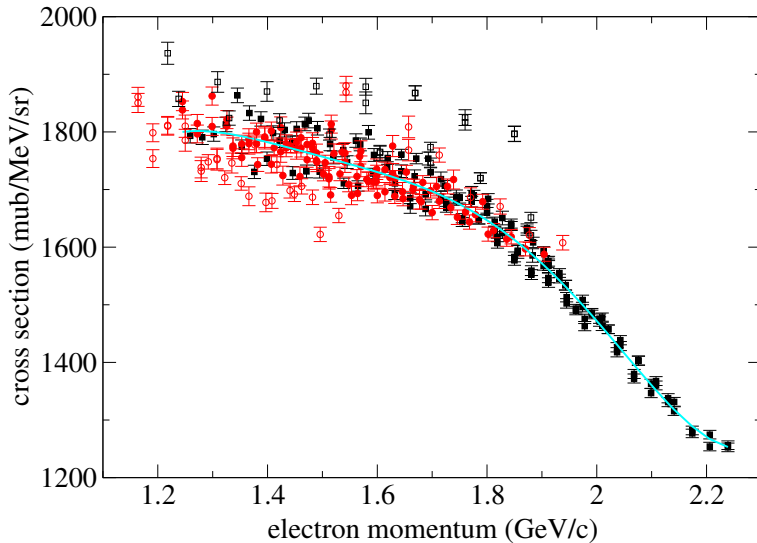


Figure 5.1: Cross section as a function of the electron momentum covering the inelastic region. Data are taken with the SOS (circles) and with the HMS (squares). The line is a fit to both data sets with reduced momentum acceptance (full symbols). No “focal plane” efficiency correction is applied.

which can be safely used in the data analysis, are mainly determined by the quality of these matrices. In the HMS this limits the useful momentum acceptance to  $\delta > -9\%$ . For smaller values the out-of-plane angle gets an asymmetric smearing compared to the initially generated value in the Monte Carlo before tracking. This leads to a shift of events from the central to the outer region and therefore to a cut dependence. Further the dependence of the out-of-plane angle from the momentum bin  $\delta$  differs in the simulated and experimental data in the outer region of the acceptance. To match this dependence cuts are applied<sup>2</sup>. For the SOS the angular acceptance is well reproduced by the Monte Carlo simulation.

The cross section as a function of the electron momentum is shown for data obtained with the SOS (circles) and the HMS (squares) in Fig. 5.1. These results are corrected for the angular dependence as described above and correspond to an scattering angle of  $20^\circ$ , but no radiative corrections are applied. Full symbols indicate data within a momentum acceptance of  $-9\% < \delta < 13\%$  for the SOS and  $-7.2\% < \delta < 10.4\%$  for the HMS. These data were used for the fit also shown in Fig. 5.1. It is assumed, that this fit represents a good average of the cross section. The data indicated by the hollow symbols belong to momentum bins from  $-15\%$  to  $-9\%$  and  $13\%-15\%$  for the SOS as well as  $-10.4\%$  to  $-7.2\%$  for the HMS. These results show a larger deviation from the fit and thus require a larger correction. This correction is obtained by calculating the deviation from the fit as a function of the relative momentum  $\delta$  for the SOS and HMS. The resulting “focal plane”

---

<sup>2</sup>(25\*hsxptar -9.5 < hsdelta < 875 \* hsxptar + 63.75) and (hsxptar > -0.065)

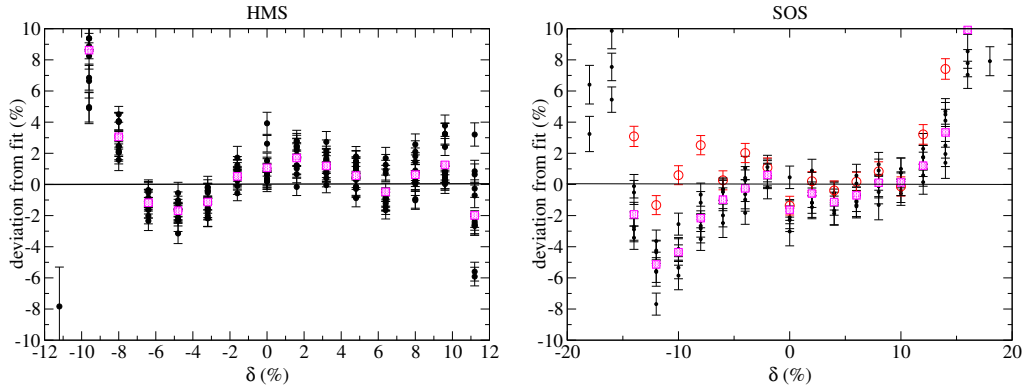


Figure 5.2: Deviation of the rate from the fit in fig.5.1 as a function of  $\delta$  for the HMS (left) and the SOS (right). The squares indicate the weighted average.

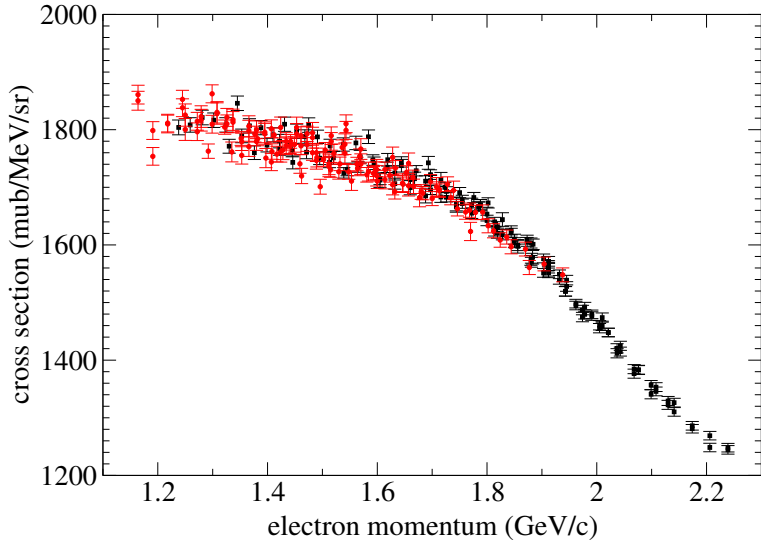


Figure 5.3: Cross section corrected with the “focal plane” efficiency as function of the electron momentum for data taken with the SOS (circles) and HMS (squares).

efficiencies are shown in Fig. 5.2, where positive deviation leads to a reduction of the cross section. The average of the “focal plane” efficiency is obtained by weighting each data point with its statistical error. It is represented by the squares in the same figure. The scatter of the results for different runs and kinematical settings is 1–2 %. This variation is also observed for the production runs taken at one kinematical setting (see Fig. 8.1). The scatter can also reflect the dependence on the remaining kinematical variables. In addition, the “focal plane” efficiency seems to be dependent on the central momentum  $p_o$  of the SOS. Close to the magnetic saturation of the SOS the correction near  $\delta = -12\%$  increases. Especially for small central momentum  $p_o = 1.35 \text{ GeV}/c$  no correction is necessary. Therefore the “focal plane” efficiency is only applied for data taken at momenta larger than 1.36 GeV/c in the SOS.

In Fig. 5.3 the rate is corrected with the “focal plane” efficiency. In the SOS a momentum acceptance of  $\pm 15\%$  is used, whereas the momentum acceptance of the HMS is limited from  $-8.8$  to  $10.4\%$ . Within these acceptances reliable cross sections can be obtained. In the following analysis the cut  $-8.5 < \delta < 10\%$  is applied for the HMS. Comparing the uncorrected cross section in Fig. 5.1 with the corrected ones in Fig. 5.3 the spread of the data points is improved by a factor of 2. Further, the data taken with

SOS (circles) and HMS (squares) are in good agreement. From the variation of the “focal plane” efficiency obtained for runs of different momenta and kinematical constraints (cuts) an uncertainty of 0.5 %(1 %) for the “focal plane” efficiency is applied for the HMS (SOS).

# 6 H(e,e'p) analysis

During the experiment E97-006 runs in 16 different kinematical settings using the reaction H(e,e'p) were taken, where the electrons were detected in the HMS in coincidence with the protons in the SOS. All runs belong to the same beam energy<sup>1</sup>. The kinematics were chosen such, that the central momenta  $p_o$  of the SOS correspond to the one used in the production runs ( $p_o = 0.85, 1.0, 1.25, 1.5, 1.7 \text{ GeV}/c$ ). Further a so called focal plane scan was performed in the SOS, where the location of the proton peak was varied over the momentum acceptance ( $\pm 15\%$ ) of the SOS. This allows us to examine a dependence of the missing energy and the cross section on the peak position in the focal plane. Further, the transmission of the protons from the target to the hodoscope in the spectrometer will be extracted from the data and compared to calculated values. Because the reaction H(e,e'p) is kinematically overdetermined, spectrometer offsets to the central angle and the momentum are obtained. The histograms of several kinematical variables will be compared to the one obtained from the Monte Carlo simulation.

## 6.1 Proton transmission

On the way from the scattering vertex taking place in the target to the hodoscope of the spectrometer the proton has to pass several materials. Some of the protons will undergo a nuclear interaction in these materials and will be absorbed or scattered out of the spectrometer acceptance. Therefore protons are lost and the yield of protons measured in the spectrometer has to be corrected. The proton transmission can be obtained with H(e,e'p) data, because each elastically scattered electron requires a proton of known

---

<sup>1</sup>One run was taken after a maintenance period, where the beam energy was 3.3 MeV lower.

kinematics. Therefore the proton transmission  $T$  can be obtained from

$$T = \frac{N_e^{coin}}{ps1 * N_e^{single} + N_e^{coin}} \quad (6.1)$$

where  $N_e^{coin}$  and  $N_e^{single}$  are the electron yield with coincidence and single trigger<sup>2</sup>. Due to high single rates the single events in the HMS were usually reduced by the prescale factor ps1, which varies between 1 and 100 for the data under consideration. Care has to be taken to select electrons in elastic kinematics on hydrogen, where the corresponding proton is definitely within the spectrometer acceptance of the SOS. Therefore strong constraints on the angular acceptance and the kinematical relation between the scattering angle and the momentum of the electron were applied, which vary for each kinematics. Further a hard cut is made on the reconstruction of the reaction vertex to exclude contributions from the target windows. This contribution is largest for the kinematics with small proton momentum and therefore small electron scattering angles, but does not change the proton transmission by more than 0.4 % when varying the cut.

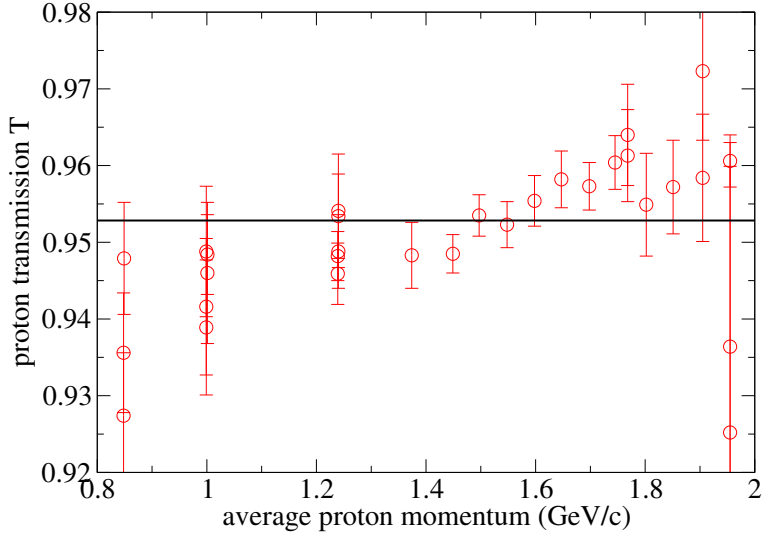


Figure 6.1: Proton transmission as a function of the average momentum of the protons in the SOS. The line is an error weighted fit to the data points.

The result for the proton transmission as a function of the proton momentum is shown in Fig. 6.1. A straight fit weighted with the statistical

---

<sup>2</sup>Note that  $N_e^{coin}$  is independent of the tracking efficiency for protons in the SOS, because a valid trigger does not require a valid track.

| target | X [g/cm <sup>2</sup> ] | $\lambda$ [10 <sup>-3</sup> g/cm <sup>2</sup> ] | $\theta_p$ [°] | $\theta_T$ [°] | 1-T [%] |
|--------|------------------------|---|----------------|----------------|---------|
| C      | 1.24                   | 86.3  | 30             | 0              | 0.83    |
|        |                        |   | 70             | 25             | 1.0     |
| Al     | 1.08                   | 106.4   | 30             | 0              | 0.6     |
|        |                        |   | 70             | 25             | 0.72    |
| Fe     | 0.49                   | 131.9   | 30             | 0              | 0.21    |
|        |                        |   | 70             | 25             | 0.26    |
|        | 0.77                   |   | 30             | 0              | 0.34    |
|        |                        |   | 70             | 25             | 0.41    |
| Au     | 0.48                   | 190   | 30             | 0              | 0.15    |
|        |                        |   | 70             | 25             | 0.18    |

Table 6.1: Absorption of protons in solid targets C, Al, Fe, Au for two different target angles  $\theta_p$ .

error of the data leads to  $0.953 \pm 0.011$ . There seems to be a tendency to smaller values for small proton momenta and a larger variation of the results for runs of the same kinematics. Background contribution alone can not explain this, because it is small. The shared acceptance for coincidence events in the electron spectrometer is very small for these kinematics. This induces larger statistical errors as well as the contribution of real single event electrons scattered into the chosen region. Then the resolution of the electron angles becomes important. Due to the large prescale factor of 100 chosen for the two lowest momenta single events accidentally counted enhance the denominator in Eq. 6.1 considerably. Further the loss of events due to multiple scattering is more pronounced at small proton momenta.

The proton transmission can be calculated from the mean free path  $\lambda_j$  between nuclear collisions and the areal density  $X_j$  of the specified material j:

$$T = e^{-\sum_j X_j / \lambda_j} \quad (6.2)$$

The nuclear interaction consists of an elastic and an inelastic part, where the angular distribution of the elastic reaction is strongly forward peaked. Therefore the proton transmission will be calculated as average  $\bar{\lambda}$  from the total and inelastic interaction length  $\lambda_T$  and  $\lambda_I$  as well as for the inelastic part alone. The interaction lengths are taken from [145] and are related to the cross section by  $\lambda = A/(N_A \sigma)$ . The cross sections were measured for protons with momenta larger than 60 GeV/c, where no energy dependence could be observed [38]. For the energy range of interest ( $T_p = 0.35 - 1.0$  GeV) the inelastic cross section shows a minimum at around 300 MeV and increases

then slightly with energy [171, 155]. This behavior is contrary to the one observed in Fig. 6.1. The areal densities of the materials in the SOS are listed in [59][186]. This leads to a proton transmission of 0.943 using  $\bar{\lambda}$  and 0.951 for the inelastic interaction only. Both results are in fair agreement with the one obtained from the data, even the one using  $\lambda_I$  is closer to the experimental result. This might be an indication that most of the events affected by elastic collisions do not get lost, because they experience only a small change in angle due to the strongly forward peaked cross section.

In the following the data yield for the reaction H(e,e'p) will be corrected by  $1/T$ , where the experimentally obtained value is used. The hydrogen target itself makes a contribution of 0.5 % to the proton transmission. For the solid targets the contributions are summarized in Tab. 6.1. As effective areal density half of the target thickness is taken, which is weighted by  $1/\cos(\theta_p - \theta_T)$ . Here  $\theta_p$  is the scattering angle of the proton and  $\theta_T$  the target angle.

## 6.2 Efficiency of the $\beta$ -cut

The identification of protons relies on the relative particle velocity  $\beta = v/c$ , which is calculated from the time of flight difference between two hodoscopes. Because  $\beta$  is related to the mass  $M$  and the momentum  $p$  of the particle ( $\beta = 1/\sqrt{1 + M^2/p^2}$ ), other particles like deuterons, positrons and pions can be rejected by a cut in the beta spectrum. This cut is chosen as  $0.85 < \beta/\beta_p < 1.08$ , where  $\beta_p$  is calculated from the momentum of the proton according to the above equation. The upper cut had to be tight to separate protons and pions at high momentum (Fig. 3.7). The cut in the  $\beta$ -spectrum of the electrons is chosen to be  $|\beta - 1| < 0.15$ . These cuts will be referred as  $\beta$ -cuts in the following. Due to large tails in the  $\beta$ -distribution and a few failures in the reconstruction of  $\beta$  good protons and electrons will be lost. Failures in the reconstruction of  $\beta$  can occur, if multiple hits in the hodoscope are found. The inefficiency of this cut can be obtained by comparing the yield of protons and electrons, which fulfill both the elastic angle-energy relation, with and without applying the  $\beta$ -cut. With these hard conditions one can be sure, that the elastic H(e,e'p) reaction is selected.

The fraction of particles lost in the HMS and SOS is shown in Fig. 6.2 as a function of the particle momentum. The events can be lost due to a failure of the TOF measurement (circles), i.e.  $\beta = 0$ , or due to the  $\beta$ -cut applied (squares), which excludes in addition events with  $\beta = 0$ . Due to the cut applied in the  $\beta$ -spectrum the loss of events is related to the resolution obtained for  $\beta$ , which was determined by means of a gaussian fit to  $\sigma=0.015\text{--}0.02$  in  $\beta/\beta_p$ . This is about the same as in the HMS, but in the SOS the

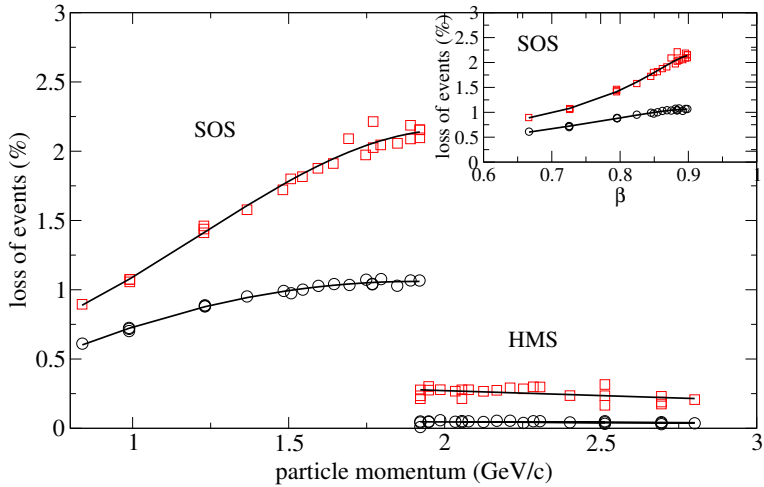


Figure 6.2: Loss of electrons (HMS) and protons (SOS) due to the  $\beta$ -cut as a function of the particle momentum (squares). The contribution, which is caused by a failure of the  $\beta$ -reconstruction ( $\beta=0$ ) is indicated by circles. In the insert graph the loss of events in the SOS is displayed as a function of  $\beta$ .

left tail in the  $\beta$ -distribution increases with momentum. This leads to a dependence of the number of lost events on the particle momentum, contrary to the behavior in the HMS. Further the failure in the reconstruction of  $\beta$  increases slightly with particle momentum as indicated by the circles in Fig. 6.2. This inefficiency depends on the velocity of the particle in a linear way, which is shown in the insert graph of Fig. 6.2. For electrons in the HMS  $\beta$  is equal to one independently of the momentum. Only a very small fraction of electrons is lost.

Electrons and protons for elastic scattering  $H(e,e'p)$  can be clearly identified and no  $\beta$ -cut is needed. For the  $(e,e'p)$  reactions on nuclei the  $\beta$ -cut has to be applied and the yield is corrected according to the results shown in Fig. 6.2. An uncertainty of 0.5 % for the  $\beta$ -cut used in both detector arms will be applied. No  $\beta$ -cut was used for electrons detected in the SOS (sec. 5), because the identification of electrons with the Cerenkov is sufficient. Comparison of the yield in the inelastic reaction measured with the SOS and HMS using a cut of  $|\beta - 1| < 0.25$  would lead to  $\approx 3\text{--}4\%$  correction on the cross section obtained from the data in the SOS. This value can also be obtained, if one extrapolates the fraction of lost particles to  $\beta = 1$  in the insert graph of Fig. 6.2.

## 6.3 Determination of the spectrometer offsets

Even though the central angle of the spectrometers are surveyed and the magnetic field is measured by means of NMR, small offsets in these quantities can not be excluded. These offsets are called spectrometer offsets. In addition the measurement of the electron beam energy is sensitive to systematic errors (see discussion in sec. 2.2.4) and has to be checked. The determination of the spectral function depends on a reliable measurement of the missing energy  $E_m$  and the missing momentum  $p_m$ , which are directly affected by the spectrometer offsets. The reaction  $H(e,e'p)$  is ideal for the determination of the spectrometer offsets, because it is kinematically overdetermined. Each of the following quantities, the initial electron energy  $E$ , the scattering angle  $\theta$  and the energy of the scattered electron  $E'_e$  can be uniquely determined by the remaining two. On the other hand, the offset to the beam energy can not be determined by the  $H(e,e'p)$  data of this experiment alone, because all  $H(e,e'p)$  runs were taken at one beam energy  $E_e = 3.1233 \text{ GeV}$ <sup>3</sup>. However, E. Christy analyzed [42] several inclusive kinematics at five different beam energies taken with the HMS in 1999 and 2000. From the fit, which varies the offsets of  $E_e$ ,  $E'_e$  and  $\theta_e$  to minimize the deviation of the invariant mass  $W$  from the proton mass, an offset of  $-0.1\%$  is obtained for third pass energy. From a recent remeasurement of the magnetic field in the arc beam line to Hall C, D. Mack calculates a correction of  $-0.2\%$  [111] (sec. 2.2.4). Therefore for both beam energies a set of spectrometer offsets will be determined. It can be later used for studies of systematic errors.

For exclusive elastic data the kinematical quantities measured with different spectrometers can be checked against each other. This is needed for the SOS, because the momentum offset is known to be affected by the saturation of the iron yokes and therefore varies for central momenta larger than  $\approx 1.5 \text{ GeV}/c$  (s. below). Further, the smallest central angle of the SOS used is  $35^\circ$ . Therefore the kinematics is quite insensitive to angle offsets in the SOS.

The following procedure for determining the spectrometer offsets was applied: It was found, that the quantity  $\Delta p$ , which is the difference between the momentum  $p_{calc}$  calculated from the electron scattering angle  $\theta_e$  and  $E_e$  and the electron momentum  $p_{meas}$  reconstructed in the spectrometer, is quite sensitive to angle and momentum offsets. A deviation of  $\Delta p$  from a straight line at small angles indicates an angle offset. On the other hand the deviation is small for a variation of  $\pm 0.6 \text{ mrad}$  with respect to other effects (Fig. 6.3),

---

<sup>3</sup>Except for one run, which was taken at  $E_e = 3.1200 \text{ GeV}$ , because the beam energy shifted slightly after a maintenance period.

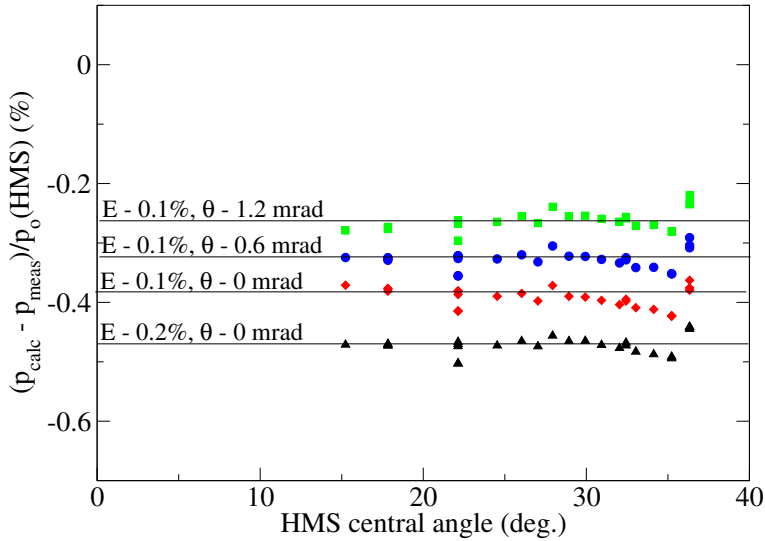


Figure 6.3: Difference between the electron momentum, which is calculated from the scattering angle and the beam energy, and the momentum measured in the HMS as a function of the central angle of the HMS. Results for different energy and angle offsets are shown.

which seems to affect the measurement at large angles. For a beam energy offset of  $-0.1\%$  an angle offset of  $-0.6$  mrad to the central angle of the HMS is obtained. Within the uncertainty of  $0.6$  mrad this is in agreement with the result of  $\Delta\theta = -1.2$  mrad obtained by E. Christy. For the beam energy  $E-0.2\%$  no angle offset is needed. After adjusting the momentum offset of the HMS ( $\Delta p(\text{HMS}) = -0.34\%$  for  $E-0.1\%$  and  $\Delta p(\text{HMS}) = -0.47\%$  for  $E-0.2\%$ ) the angle offsets for the SOS are calculated from the beam energy and the corrected electron scattering angle measured in the HMS. The angular distributions are fitted by a gaussian. The angle offset for the SOS is not constant, but varies between  $0$  and  $1.4$  mrad (Fig. 6.4 left). This is due to the fact, that the SOS angle had to be read from a monitor in the counting room, which was connected to a TV camera mounted on the SOS. The orientation of the TV camera varies slightly with the angle position of the SOS. On the other hand it is known that the angle readback displayed by the GUI (Graphical Unit Interface) contains an offset, which can vary if the direction of the spectrometer rotation is changed. If one uses the value of the angle displayed by the GUI for consecutively taken data sets without changing the orientation of the spectrometer rotation, the angle offset obtained in the analysis described above is essentially constant. On the other hand the

setting of the SOS angle via TV camera can be reproduced to better than 0.1 mrad. Because some of the production runs use SOS angles of less than  $35^\circ$ , where no  $H(e,e'p)$  runs were taken, the uncertainty in the SOS angle offset is estimated to  $\pm 0.7$  mrad.

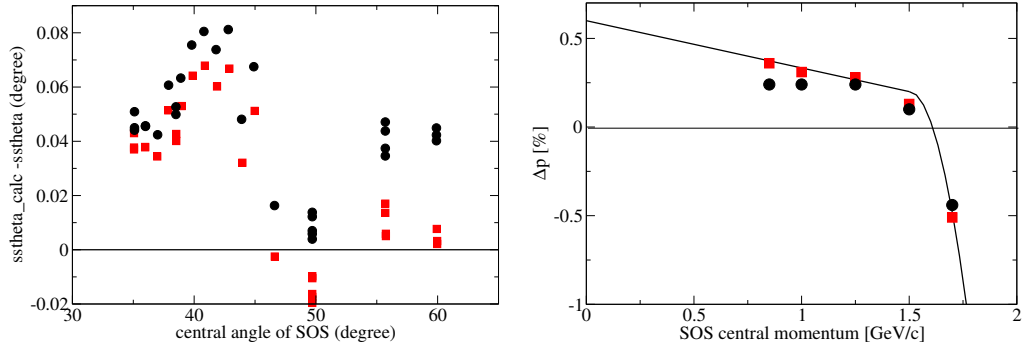


Figure 6.4: Left: Difference between the proton angle calculated from kinematics and the one measured in the SOS as a function of the central angle of the SOS. Right: Momentum offset for the SOS as a function of the central momentum. The curve is taken from [177]. Circles (squares) belong to a beam energy offset of  $-0.1\%$  ( $-0.2\%$ ).

The correction to be applied to the central momentum of the SOS was also calculated from the electron scattering angle. The result can be seen in Fig. 6.4 as a function of the central momentum of the SOS. The values for a beam energy offset of  $-0.2\%$  (squares) are very close to a fit obtained by J. Volmer [177] using  $H(e,e'p)$  data from experiment E93-021 and E91-003. Above  $p_o = 1.5$  GeV/c the momentum offset for the SOS can be parametrized by  $\Delta p = a + b(p_o - 1.5)^2$ , with  $a = 0.002$  and  $b = 0.17$ . Below 1.5 GeV/c,  $\Delta p$  depends linearly on  $p_o$ , with  $\Delta p(p_o=0) = 0.006$  and  $\Delta p(p_o=1.5) = 0.002$ . For a beam energy offset of  $-0.1\%$  the momentum correction is constant for  $p_o$  less than 1.5 GeV/c. The strong dependence of the correction on the central momentum of the SOS for  $p_o > 1.5$  GeV/c can be explained by magnetic saturation of the iron yokes in the SOS. In saturation, the magnetic field is smaller than expected from the linear dependence between current and magnetic field.

Magnetic saturation affects not only the central momentum, but also the relative momentum  $\delta$  along the focal plane. To study this effect elastic data on hydrogen were used with the momentum of the proton located at different relative momenta ranging from  $-15\%$  to  $+15\%$  at fixed central momentum (“focal plane scan”). Two sets of inclusive data at  $p_o = 1.0$  and 1.5 GeV/c

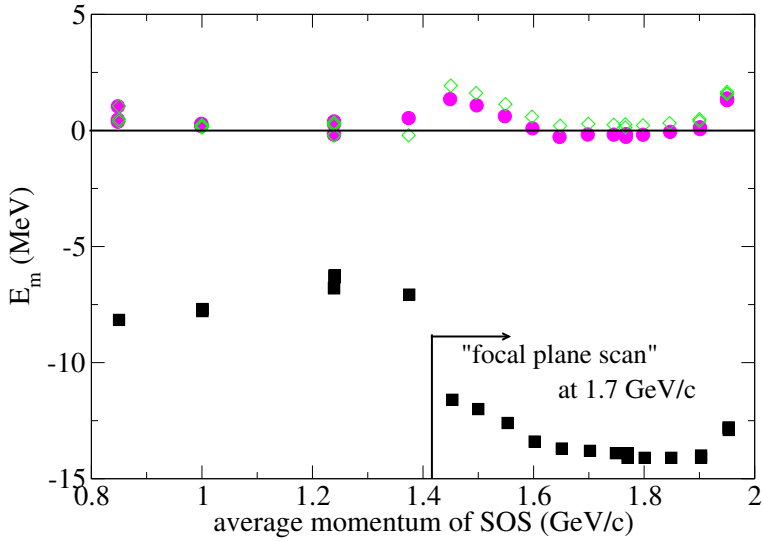


Figure 6.5: Missing energy  $E_m$  as a function of the average proton momentum. Squares:  $E-0.1\%$ , no corrections. Circles (diamonds): corrected values for  $E-0.1\%$  ( $E-0.2\%$ ).

as well as exclusive data at 1.7 GeV/c were taken. From these data the invariant mass or the missing energy were reconstructed as a function of  $\delta$ . No dependence on  $\delta$  was observed for the data at 1.0 GeV/c. The invariant mass extracted from the data at  $p_o = 1.5$  GeV/c decreases linearly with increasing  $\delta$ , which is a clear sign of magnetic saturation. It can be corrected by a fit (Tab. 6.2). A stronger influence of magnetic field distortion appears at  $p_o = 1.7$  GeV/c, which can be seen in Fig. 6.5. Here the missing energy  $E_m$  as a function of the averaged proton momentum is shown without (squares) and with corrections applied using a beam energy offset of  $-0.1\%$  (circles) and  $-0.2\%$  (diamonds). The data belonging to the focal plane scan at  $p_o = 1.7$  GeV/c are best corrected by applying a vertical offset of  $\approx 0.4$  mm to the focal plane<sup>4</sup>. An offset of 0.1 mm corresponds to  $\approx 0.1\%$  correction in  $\delta$ . This leads to a rather symmetric shape of  $E_m$  obtained from data along the focal plane. The uncertainty in the momentum offset is estimated to  $\pm 0.1\%$ .

It should be noted, that an additional offset of  $-0.025\%$  had to be applied to the momentum of the HMS to take the energy loss due to bremsstrahlung into account. Otherwise a shift in  $E_m$  between the Monte Carlo, which

---

<sup>4</sup>In the standard analysis program of Hall C this corresponds to the variable s\_det\_offset\_x.

includes radiation, and the experiment would be observed. This correction is not applied when calculating the remaining offsets for the SOS.

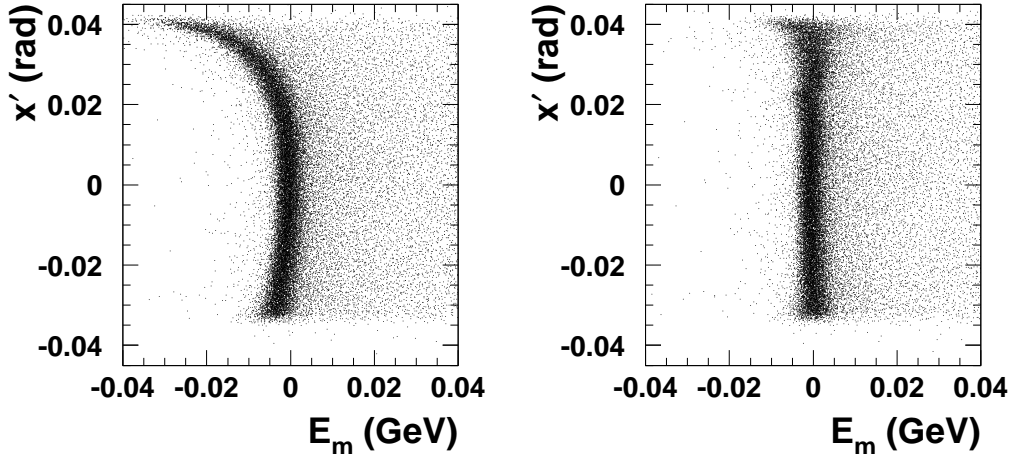


Figure 6.6: Before (left) and after (right) applying the saturation correction to the momentum  $\delta$ . The spectra show the dependence of the missing energy  $E_m$  on the out-of-plane angle  $x'$  at  $p_o = 1.7 \text{ GeV}/c$ .

Due to changes in the fringe field of the SOS for different magnetic settings the reconstructed momentum becomes dependent on the out-of-plane angle. This effect is especially pronounced at the highest central momentum  $p_o = 1.7 \text{ GeV}/c$  of the SOS, which leads to a “banana” shape in the correlation between the missing energy  $E_m$  and the out-of-plane angle  $x'$  (Fig. 6.6). The correction  $\delta_{corr}$  to  $\delta$  depends on  $x'$  (respectively on the focal plane coordinate  $x'_{fp}$ ) and the central momentum  $p_o$ .

$$\delta_{corr} = 0.013x'_{fp} + [0.47 - 1.37p_o + 1.81p_o^2 - 0.76p_o^3](x'_{fp})^2 \quad (6.3)$$

For  $p_o < 1.0 \text{ GeV}/c$  the expression in squared brackets reduces to 0.15. Additional corrections are needed for  $p_o = 1.5$  and  $1.7 \text{ GeV}/c$  at large  $x'$ . For  $p_o = 1.5 \text{ GeV}/c$  and  $x' \geq 0.036 \text{ rad}$  an offset to  $\delta_{corr}$  of  $-0.12\%$  is applied. At higher momentum this correction becomes dependent on the focal plane position. For  $x' \geq 0.02 \text{ rad}$  the following correction to Eq. 6.3 is added:

$$\delta\delta_{corr} = \{-0.46[(x')^2 - 0.02^2]\}/\{0.21 - \delta\} \quad (6.4)$$

For  $x' > 0.032 \text{ rad}$  a linear term  $-0.6x' + 0.021$  is used together with Eq. 6.3 and 6.4. These corrections combined lead to the Fig. 6.6 on the right.

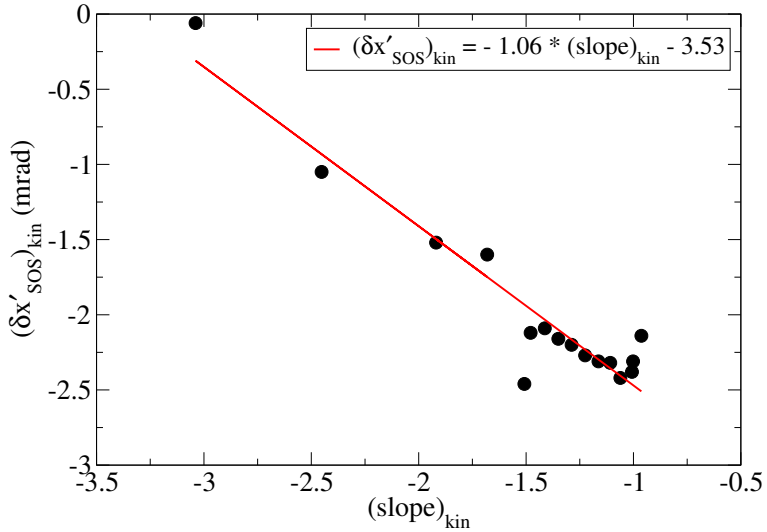


Figure 6.7: Fit according to Eq. 6.7 to the fit results obtained from Eq. 6.5 for evaluating the spectrometer offsets  $\delta x'_{HMS}$  and  $\delta x'_{SOS}$ .

To determine the offsets  $\delta x'$  to the out-of-plane angle  $x'$  the linear relation between  $x'_{SOS}$  and  $x'_{HMS}$  in hydrogen kinematics is exploited. First the function

$$x'_{SOS} = x'_{HMS} * \text{slope}_{\text{kin}} + (\delta x'_{SOS})_{\text{kin}} \quad (6.5)$$

is fitted to the 2-dimensional spectra  $x'_{SOS}$  versus  $x'_{HMS}$  for all hydrogen kinematics. The subscript “kin” indicates, that its value varies with the hydrogen kinematics. The slope and the offset  $\delta x'_{SOS}$  are used as fit parameters. Eq. 6.5 can be rewritten as<sup>5</sup>

$$x'_{SOS} = (x'_{HMS} + \delta x'_{HMS}) * \text{slope}_{\text{kin}} - \delta x'_{SOS} \quad (6.6)$$

with spectrometer offsets  $\delta x'_{HMS}$  and  $\delta x'_{SOS}$  independent of kinematics. Comparing Eq. 6.5 and 6.6  $\delta x'_{SOS}$  can be identified as

$$(\delta x'_{SOS})_{\text{kin}} = \delta x'_{HMS} * \text{slope}_{\text{kin}} - \delta x'_{SOS} \quad (6.7)$$

This function is fitted to the fit results from Eq. 6.5 in Fig. 6.7, which leads to the spectrometer offsets  $\delta x'_{HMS} = -1.06$  mrad and  $\delta x'_{SOS} = 3.53$  mrad. Using these values together with the corrections mentioned above the out-of-plane component of the missing momentum  $p_{oop}$  is centered around zero (sec 6.4). This quantity is most sensitive to the out-of-plane angle.

---

<sup>5</sup>Because  $x'$  is not equal to the physical out-of-plane angle  $\phi$  the slope depends on the kinematics.

| spectrometer | quantity                   | $E_e - 0.1 \%$   | $E_e - 0.2 \%$   |
|--------------|----------------------------|------------------|------------------|
| HMS          | $\theta$                   | -0.6 mrad        | 0 mrad           |
|              | $x'$                       | -1.06 mrad       | -1.06 mrad       |
|              | $p_o$                      | -0.34 - 0.025 %  | -0.47 - 0.025 %  |
| SOS          | $\theta$                   | s. Fig. 6.4      | s. Fig. 6.4      |
|              | $x'$                       | 3.53 mrad        | 3.53 mrad        |
|              | $p_o = 0.85 \text{ GeV}/c$ | 0.24 %           | 0.35 %           |
|              | $p_o = 1.00 \text{ GeV}/c$ | 0.24 %           | 0.32 %           |
|              | $p_o = 1.25 \text{ GeV}/c$ | 0.24 %           | 0.27 %           |
|              | $p_o = 1.5 \text{ GeV}/c$  | 0.10 %           | 0.10 %           |
|              | correction:                | -0.38 % $\delta$ | -0.65 % $\delta$ |
|              | $p_o = 1.7 \text{ GeV}/c$  | -0.0036          | -0.0040          |

Table 6.2: Corrections for the quantities reconstructed in the HMS and SOS using beam energy offsets of -0.1 % and -0.2 %. For  $p_o = 1.7 \text{ GeV}/c$  the vertical offset at the focal plane is given (s\_det\_offset\_x).

A summary of all offsets and corrections can be found in Tab. 6.2. The offset to the central angle of the SOS was implemented as a look-up table using the results of Fig. 6.4 and interpolating them if needed.

## 6.4 Comparison to Monte Carlo simulation

Because of the simple and unique kinematics elastic scattering on hydrogen is suitable for testing the Monte Carlo simulation as well as the efficiencies and corrections applied to the data. The spectrometer acceptance predicted in SIMC can be tested by comparing the spectra of reconstructed quantities with the one obtained in the experiment. These spectra are quite sensitive to the transfer matrix and especially to the geometric arrangement of the magnetic elements in the spectrometer. The angular and momentum resolutions of SIMC are adjusted to the data with the help of sieve slit runs.

In Fig. 6.8 the spectra for the relative momentum  $\delta$ , in-plane and out-of-plane angle  $y'$  and  $x'$ , which are reconstructed from the measured focal plane observables, are shown in black on the left for HMS and on the right for the SOS. The spectra in red are obtained from the Monte Carlo simulation for the same kinematics and cuts. The kinematics for the chosen  $H(e,e'p)$  run are  $p_o(\text{HMS}) = 2.05 \text{ GeV}/c$ ,  $\theta_e = 32.5^\circ$ ,  $p_o(\text{SOS}) = 1.7 \text{ GeV}/c$ ,  $\theta_p = 38.5^\circ$ . The comparison shows that, even at the highest possible momentum in the SOS, the agreement between the spectra are quite good except for the

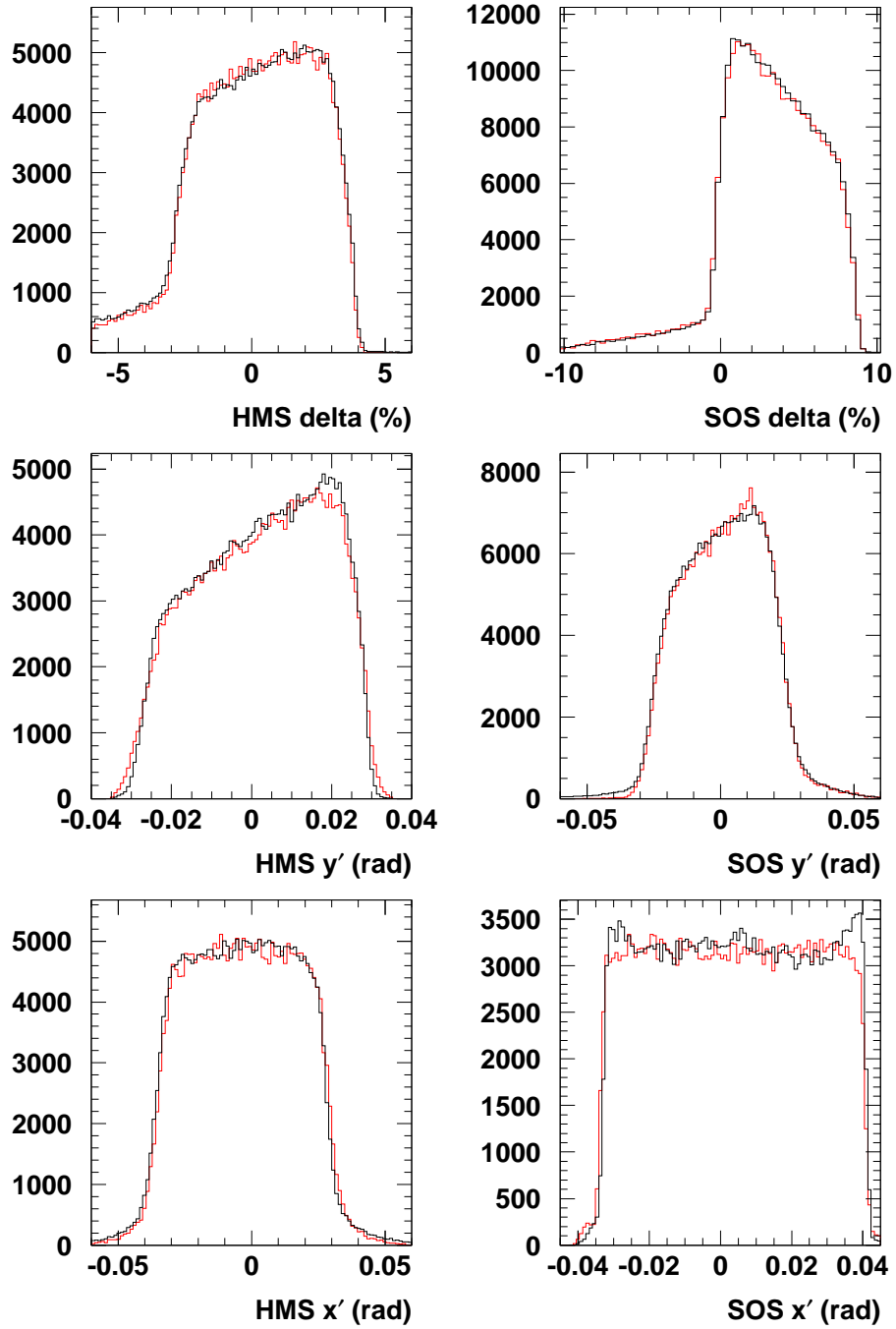


Figure 6.8: Relative momentum, in-plane and out-of-plane angle as reconstructed in the HMS (left) and SOS (right) for a  $H(e,e'p)$  run at  $p_o(\text{SOS})=1.7 \text{ GeV}/c$ . The experimental spectra (black) are compared to the result of the Monte Carlo in red.

SOS  $x'$ -spectrum. Here the data show a peak at the extremes, which appears already at low central momentum  $p_o(\text{SOS}) = 0.85 \text{ GeV}/c^6$ . Cuts were applied on the Cerenkov to identify the electron. A cut on the coincidence time between the detected electron and proton is in fact not necessary due to negligible background from accidental events. To suppress the beginning of the  $\Delta$ -resonance the relative momentum  $\delta$  in the HMS was restricted to  $> -6\%$ . Wrongly reconstructed events at large negative  $\delta$  were excluded by requiring  $x_{fp}(\text{SOS}) > -20$ . Because the agreement of the phase space between experiment and Monte Carlo gets worse for extended targets, a cut was applied at  $|y(\text{SOS})| < 1.5 \text{ cm}$ , where  $y$  is the projected target length seen by the spectrometer (Fig. 6.9). A closer look to the reconstructed target position reveals, that the central position of the hydrogen target cell is shifted by about 0.23 cm downstream. This value is in agreement with a survey of the target position, which was carried out in the maintenance period during the experiment (sec. 2.3.2).

All spectra shown in Fig. 6.8 and 6.10 are corrected for contributions originating from the walls of the hydrogen target. For this runs at the same kinematics were taken with a dummy target, which consists only of two thin aluminium plates spaced by a distance corresponding to the length of the hydrogen target. The events from these runs are properly scaled to match the charge of the corresponding hydrogen run and the target wall thickness (factor 7.8). This contribution is shown in Fig. 6.9 as shaded area compared to the events from the  $H(e,e'p)$  reaction. This contribution is typically 0.5 % and does not exceed 2 %.

Physical quantities shown in Fig. 6.10 are compared to the Monte Carlo simulation. Because the main experiment emphasizes the missing energy  $E_m$  and missing momentum  $p_m$  these quantities were chosen for comparison. The resolutions for the reconstructed quantities  $x'$ ,  $y'$  and  $\delta$  in the Monte Carlo were adjusted to the experimental results such that the distributions shown in Fig. 6.10 as well as the invariant masses obtained from the SOS and HMS separately are best matched for all kinematics used in this experiment. In addition the raster widths are adjusted to experimental conditions. To achieve the best resolution in the experiment the vertical beam displacement due to the rastering of the beam were taken into account in the reconstruction of the target from the focal plane quantities (sec. 2.2.3). The physical quantities were calculated using the offset set corresponding to a beam energy of  $E_e - 0.1\%$ . Cuts mentioned above were used.

To check all corrections, which have to be applied to obtain the cross

---

<sup>6</sup>It can only be seen, if the in-plane angle is restricted to the central region of the octogonal shaped collimator.

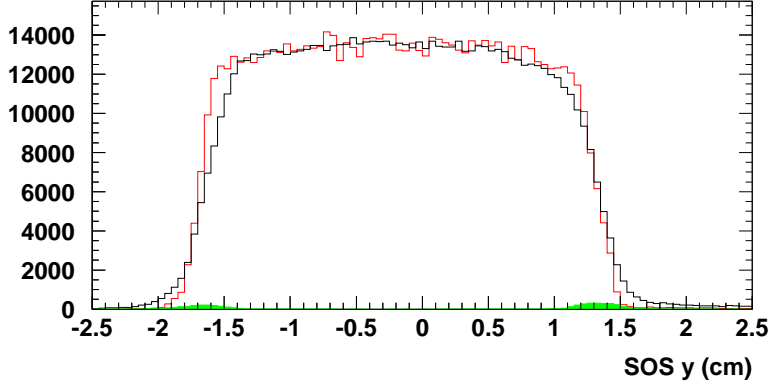


Figure 6.9: Vertex position obtained from the SOS at a scattering angle of  $49.4^\circ$  for the 4 cm long hydrogen target (black: data, red: Monte Carlo). The (green) shaded area is the contribution of the target walls taken from a run with a dummy target.

section, the ratio of the yield from the data and the Monte Carlo simulation is calculated. These corrections include detector and tracking efficiencies (sec. 3.1.1), “focal plane” efficiency (sec. 5.2), dead time corrections (sec. 2.4.5), coincidence blocking correction (sec. 3.2.1), proton transmission (sec. 6.1) for the yield as well as the current calibration (sec. 2.2.2) for the luminosity. All kinematics were modeled by the Monte Carlo, which takes into account multiple scattering and radiative effects for both the electron and the proton using the formalism of [62].

In the Monte Carlo the yield is weighted by the cross section calculated from the Rosenbluth equation. The magnetic and electric form factor of the proton are taken from the dispersion theoretical analysis of [118]. The ratio of the simulated yield to the data is shown in Fig. 6.11 as a function of the 4-momentum transfer  $Q^2$  in the range of 0.6 to 2.2  $(\text{GeV}/c)^2$ . The dashed line in Fig. 6.11 is an improved fit of [86] compared to [118]. The dotted line corresponds to a fit that includes the time-like region. The shaded area represents the world data with their uncertainty. The dashed-dotted fit takes into account the recent result of the double polarization experiment in Hall A [77], which indicates, that the electric form factor of the proton for  $Q^2$  larger than 1  $(\text{GeV}/c)^2$  is suppressed as compared to the dipole parametrization. Results of the present experiment shown as circles (squares) refer to a beam energy of  $E_e - 0.1\% (-0.2\%)$ . To demonstrate the effect of the “focal plane” efficiency on the yield the analysis was also performed without correcting for the “focal plane” efficiency obtained in sec. 5.2. This result is indicated by

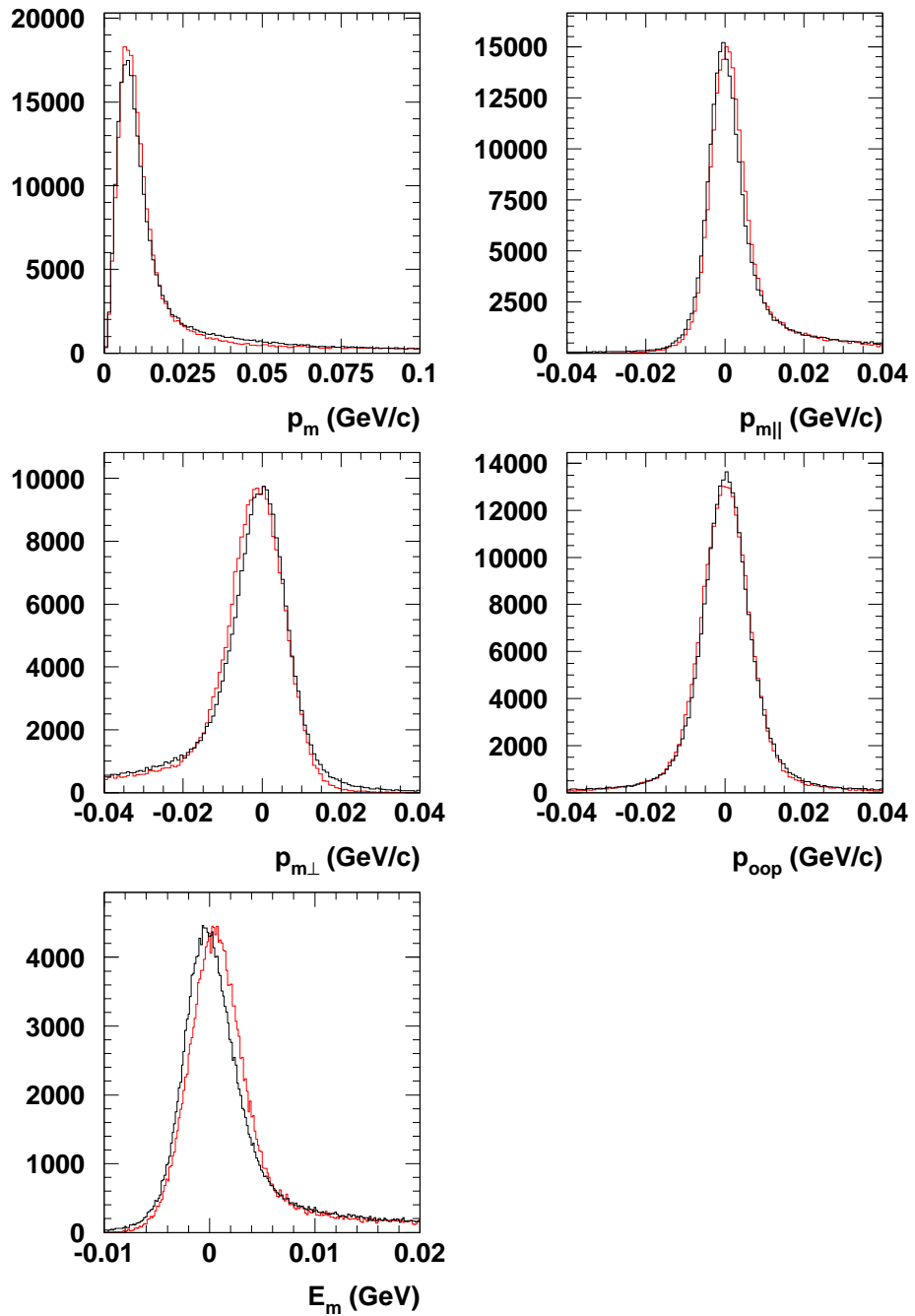


Figure 6.10: Physical quantities derived from the reconstructed spectrometer quantities: Missing momentum  $p_m$ ,  $p_{m||}$  (parallel to  $q$ ),  $p_{m\perp}$  (perpendicular to  $q$ ),  $p_{oop}$  (out-of-plane component) and the missing energy  $E_m$ . Experimental spectra in black are compared to the results of the Monte Carlo simulation in red.

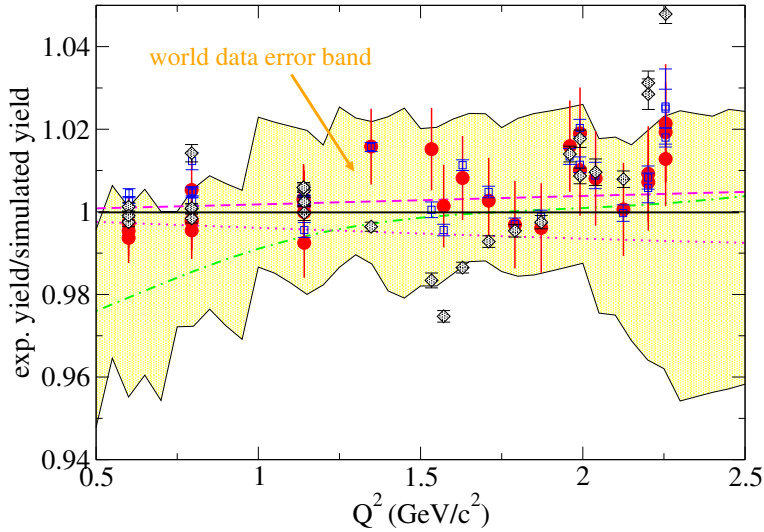


Figure 6.11: Ratio of the experimental to simulated yield for the reaction  $H(e,e'p)$ , which uses the form factor parametrization of [118]. Circles (squares) indicate the analysis using an offset to the beam energy of  $-0.1\%$  ( $-0.2\%$ ). The results indicated by the diamonds are not corrected for the “focal plane” efficiency. The shaded area represents the world data band without the recent measurements of Hall A [77], whereas the fit of [11] (dotted–dashed line) includes these data. The fit indicated by the dotted line considers also the form factors in the time–like region [86] and the dashed line is an improved version of [118].

diamonds in Fig. 6.11, which has to be compared to the circles. In the outer regions of the momentum acceptance the difference amounts to  $\approx 3\%$ .

The error bars of the square symbols include only the statistical error, which is of the order of  $0.5\%$ . The systematic error from kinematic uncertainties only is quadratically added to the statistical error and shown together with the data points indicated by circles. For this an uncertainty of  $0.6$  mrad in the electron angle (sec. 6.3) and of  $0.5\%$  in the beam energy (sec. 2.2.4) are taken into account. Other sources of systematic uncertainties are summarized in Tab. 6.3.

Some of the stated uncertainties depend on the current used in the  $H(e,e'p)$  measurement. In this experiment data at currents between  $8.6$  and  $59\ \mu\text{A}$  were taken. For small currents the uncertainty is  $2\%$  due to the Unser offset of  $0.2\ \mu\text{A}$  (sec. 2.2.2). A possible dependence of the result on the current can be caused by errors in the charge measurement, density variations due to local boiling in the hydrogen target, but also due to inefficiencies in the

| source  | uncertainty          | reference           |
|---|----------------------|---------------------|
| H <sub>2</sub> target thickness<br>due to local boiling | 0.5 %<br>0.1 %/10 μA | 2.3.2<br>2.3.2 [10] |
| charge measurement                                      | 1 – 2 %              | 2.2.2               |
| run stability   | 0.5 %                |                     |
| background contribution (wall)                          | 0.1 – 0.5 %          |                     |
| tracking efficiency(HMS/SOS)                            | 0.5/0.5 %            | 3.1.1               |
| “focal plane” efficiency(HMS/SOS)                       | 0.5/1 %              | 5.2                 |
| dead time   | 0.5 %                | 2.4.5               |
| proton transmission                                     | 1.1 %                | 6.1                 |
| radiative correction                                    | 1 %                  | 4.1.3               |
| phase space (M.C.)                                      | 2 %                  | 4.1                 |
| kinematics  | ≈1 %                 | Fig. 6.11           |

Table 6.3: Systematic uncertainties in the determination of the H(e,e'p) cross section.

tracking algorithm at large event rates (sec. 3.1.1). During the H(e,e'p) measurements the rates in both spectrometers were moderate (a few kHz). At  $Q^2$  of 1.14 (GeV/c)<sup>2</sup> three runs were taken at currents of 10, 30 ,50 μA. The results agree within 1 % and no rate dependence could be observed.

Different runs at the same kinematics and conditions agree within 0.5 %. Even though the background contribution from the target wall is small, an uncertainty of 0.5 % is applied for those runs belonging to the focal plane scan at  $p_o(\text{SOS}) = 1.7 \text{ GeV}/c$ . Here only one dummy run was taken for the kinematics at  $Q^2 = 2 \text{ (GeV}/c)^2$ , but also used to correct the yield obtained in similar kinematics at  $p_o(\text{SOS}) = 1.7 \text{ GeV}/c$ . The radiative corrections for the H(e,e'p) reaction are relative small (≈ 15 %). Further the agreement of the experimental and simulated spectra is quite good. Therefore only an additional uncertainty of 1 % is assumed. The uncertainty in the phase space is a measure how well the Monte Carlo simulation can describe the data. This can be probed by varying the cuts applied to the kinematical variables. As can be seen from Fig. 6.8 and 6.10 the largest difference occurs in the out-of-plane angle  $x'$  in the SOS. Here the largest effect in the ratio of the experimental and simulated yield is expected. The two cuts  $|x'| < 0.045 \text{ rad}$  and  $|x'| < 0.035 \text{ rad}$  were tested (s. also sec. 6.5 for the reason of the latter cut). The yield ratio for the second cut is 0.5 to 1 % lower. From Tab. 6.3 a systematic error of 3.3–3.7 % in total is obtained. No uncertainty for the blocking correction is applied, because for the small rates during the data

| $p_o$ [GeV/c] | $\delta E_m$ [MeV] | $\delta p_m$ [MeV/c] |
|---------------|--------------------|----------------------|
| 0.85          | 4.5                | 9.6                  |
| 1.0           | 4.6                | 9.5                  |
| 1.25          | 5.1                | 9.3                  |
| 1.5           | 5.3                | 9.5                  |
| 1.7           | 5.4                | 8.8                  |

Table 6.4: Experimental resolutions (FWHM)  $\delta E_m$  and  $\delta p_m$  in  $E_m$  and  $p_m$  for the five momentum settings of the SOS.

taking with hydrogen this correction is negligible.

#### 6.4.1 Experimental resolution in $E_m$ and $p_m$

Because the main experiment focuses on the determination of the missing energy and missing momentum, the experimental resolutions have to be known. The  $E_m$ -distribution was fitted with a gaussian distribution for each kinematics. The FWHM varies between 4.5 and 5.4 MeV and increases with the central momentum of the proton (Tab. 6.4). Fluctuations in the energy loss suffered by the particles when passing through e.g. the target material have a negligible effect (less than 0.2 MeV).

The  $p_m$ -distribution shows a large tail from radiative effects and can be barely fitted with a gaussian distribution. To suppress this tail the distribution  $y(p_m)$  is squared

$$y^2(p_m) \propto \left[ \exp\left(-\frac{p_m^2}{2\sigma_p^2}\right) \right]^2 \quad (6.8)$$

$$= \exp\left(-\frac{p_m^2}{2(\sigma_p/\sqrt{2})^2}\right) \quad (6.9)$$

and then fitted with a gaussian according to Eq. 6.9. Its standard deviation has to be multiplied by  $\sqrt{2}$  for the  $p_m$ -distribution (Tab. 6.4). The FWHM of the  $p_m$ -distribution is  $\approx 9.5$  MeV/c. The influence of radiative effects in the experimental resolution was tested with the Monte Carlo simulation by comparing the spectra with and without radiation. From this one gets a smearing caused by radiation of less than 0.2 MeV in  $E_m$  and  $< 0.7$  MeV/c in  $p_m$ .

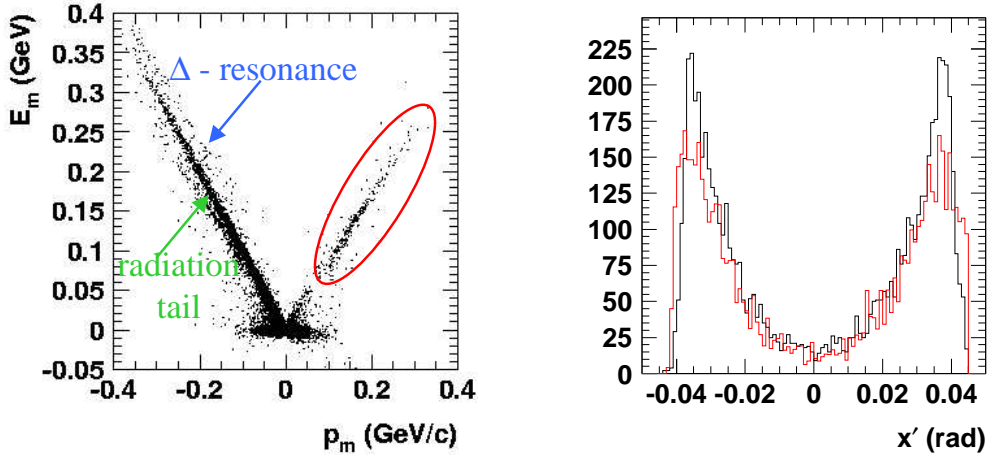


Figure 6.12: Left: Two-dimensional plot of  $E_m$  and  $p_m$  for a hydrogen run at  $p_o(\text{SOS}) = 1.7 \text{ GeV}/c$ . Indicated are the radiation tail, part of the  $\Delta$ -resonance and events corresponding to protons, which penetrate through the collimator material (ellipse). Right: The out-of-plane distribution for events corresponding to protons, which penetrate the collimator (black: experiment, red: Monte-Carlo).

## 6.5 Penetration of protons through the collimator

The collimator of the SOS consists of tungsten with a thickness of 2.5 inch and a conical shape. With the Bethe–Bloch equation [109] the energy lost by particles, when passing through material, can be calculated. The mean energy loss  $\Delta E$  for protons of momentum  $1.7 \text{ GeV}/c$  ( $1.5 \text{ GeV}/c$ ) passing through 2.5 inch tungsten is 150 MeV (170 MeV). Because of the large momentum acceptance of the SOS ( $\pm 15\%$  of the central momentum) protons can be still detected in the spectrometer after passing through the collimator material. A contribution of such events is expected for central momenta larger than  $1 \text{ GeV}/c$ . Due to multiple scattering of the protons in the collimator a portion will not reach the focal plane of the SOS. Further a large fraction of protons will be absorbed in the collimator material, which can be estimated via Eq. 6.2. With a nuclear interaction length of  $\lambda_i = 185 \text{ g/cm}^2$  for tungsten this leads to a proton transmission  $T$  of 0.52. Those protons, which made it through the collimator, are indicated by the ellipse in the two-dimensional plot of  $E_m$  and  $p_m$  (Fig. 6.12). In fact these events appear also

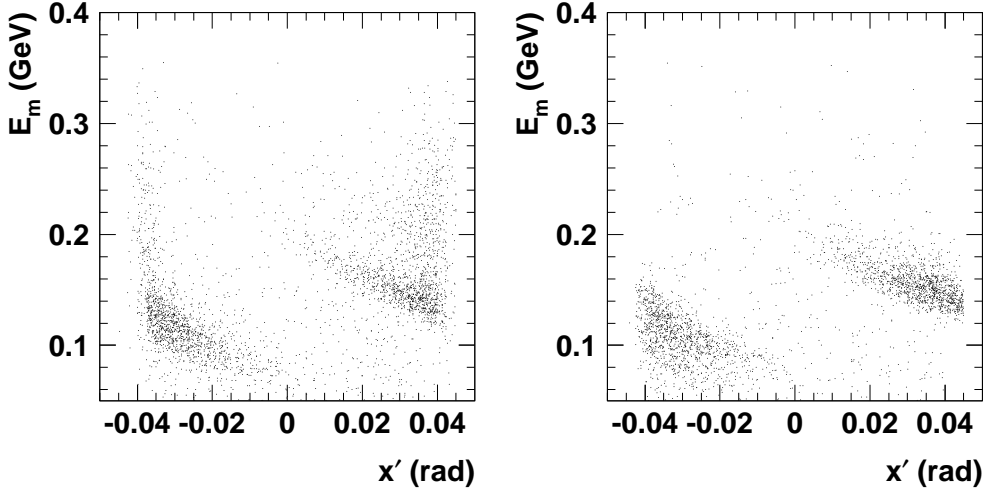


Figure 6.13: Two-dimensional plot of  $E_m$  and the out-of-plane angle in the SOS showing protons, which pass through the collimator material. Left: experiment, right: Monte-Carlo.

for negative  $p_m$ <sup>7</sup>, but there they are hidden by the large radiation tail and can barely be seen in Fig. 6.12. In addition the beginning of the  $\Delta$ -resonance at the pion mass ( $m_\pi = 145$  MeV) can be seen in Fig. 6.12 as a small band. The events corresponding to penetration through the collimator can be singled out for both negative and positive  $p_m$ . For this one selects first "good" electrons by cutting on the momentum-angle relation. Protons penetrating through the collimator have a momentum below the momentum-angle relation of the proton due to additional energy loss. The  $E_m$ -distribution of these events ranges between 50 and 300 MeV. Their contribution is less than 3 %.

The out-of-plane distribution in the SOS of the protons, which reside inside the ellipse of Fig. 6.12, is shown on the right. Large angles are enhanced, which confirms, that these protons took a peculiar path in the spectrometer. In the same picture the result of the Monte-Carlo simulation is shown in red. The simulation allows protons to penetrate through the collimator material taking energy loss and multiple scattering of such particles into account. To get approximately the same number of events detected in the experiment and simulated in the Monte-Carlo a reduction of a factor of two had to be applied. This is completely in agreement with the transmission

---

<sup>7</sup>Positive and negative  $p_m$  indicates the quadrant of  $p_m$  with respect to the momentum transfer  $q$ .

factor of the protons through the collimator calculated above. Further the two-dimensional spectra of  $E_m$  versus the out-of-plane angle  $x'$  of the SOS are compared in Fig. 6.13. The shape of the spectra are quite similar except that in the experiment the  $E_m$ -distribution shows a large tail for extreme  $x'$ . This can not be simulated, because the distribution of the energy loss suffered by charged particles penetrating thick absorbers is a gaussian shape. It might be possible, that some particles penetrate parts of the iron yoke or vacuum tube in the spectrometer and loose additional energy.

# 7 Single-particle region

In the first three weeks of beam time no  $H(e,e'p)$  data could be taken, because of a failure of the hydrogen target. Instead, runs in quasi-elastic kinematics covering the single-particle region of  $p_m < 300$  MeV/c were taken for each of the central momenta of the SOS used in the production runs. The position of the first peak, the  $p_{3/2}$  state of  $^{12}\text{C}$ , serves as a check of the beam energy and spectrometer offsets used, which is described in sec. 7.1. The histograms for  $E_m$  and  $p_m$  obtained from the data and Monte Carlo simulation are compared. Further, the nuclear transparency can be extracted for five different kinetic energies of the proton and compared with previous results.

## 7.1 Comparison with Monte Carlo simulation

In the ground state of  $^{12}\text{C}$  two shells are occupied: The  $s_{1/2}$  state contains nominally two protons and is located at  $E_B = 38.1$  MeV with a width of around 20 MeV. The remaining nominally four protons reside in the  $p_{3/2}$  state at 16.2 MeV. This shell has a width  $\Gamma$  of less than 1 MeV and is therefore suitable for an accurate determination of the peak position. Due to bremsstrahlung and the tail of the  $s_{1/2}$  state the position of the  $p_{3/2}$  shell is shifted by about 1.1 to 1.2 MeV according to the Monte Carlo simulation. Any further shift reflects a drift in the beam energy.

We find that the shifts in the beam energy over an 11 day period do not exceed 1 MeV. This is within the error of the beam energy measurement. Furthermore the width of the  $p$ -state is well reproduced by the Monte Carlo simulation (Tab. 6.4), which has a FWHM of around 7 MeV, i.e. larger than for the  $H(e,e'p)$ -runs. This is caused by the worse resolution at the border of the useful momentum acceptance. This region is not covered by the  $H(e,e'p)$ -runs. In the IPSM spectral function a width of 1 MeV was used contrary to previous analyses [186][59] (sec. 4.1.2).

In Fig. 7.1 experimental  $E_m$  and  $p_m$  spectra in black are compared to the

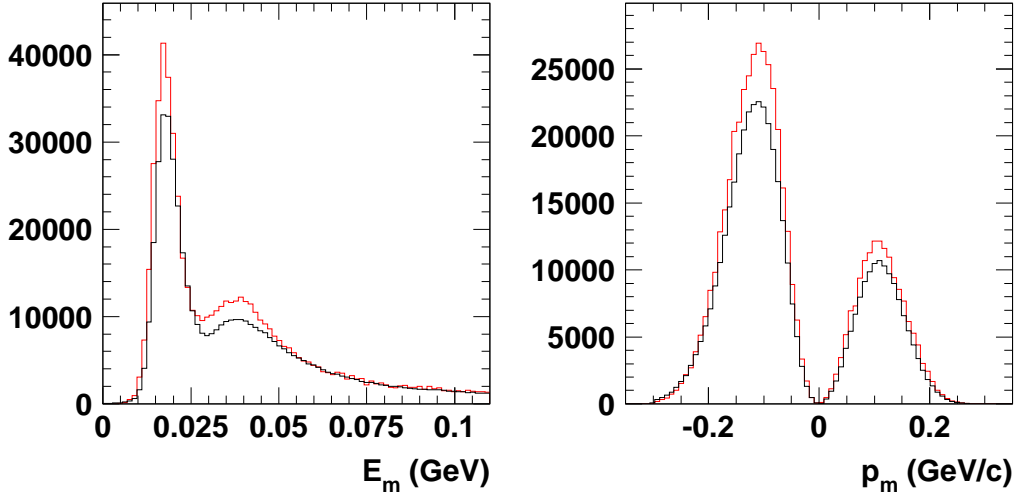


Figure 7.1: Comparison of the experimental  $E_m$  and  $p_m$  spectra (black) in the single-particle region and the Monte Carlo simulation (red).

one obtained from the Monte Carlo simulation in red<sup>1</sup>. In the  $p_m$ -distribution a cut of  $E_m \leq 0.08$  GeV is applied. To account for the absorption the yield in the Monte Carlo was multiplied with a nuclear transmission factor of 0.6 (sec. 7.2). The IPSM can describe the data well for small  $E_m$ , apart of an overall factor, which will be discussed in sec. 7.2. For larger  $E_m$  and  $p_m$  the experimental yield starts to exceed the IPSM prediction.

In Fig. 7.2 the  $E_m$ -distribution is shown for a slice of  $p_m = 250 \pm 50$  MeV/c. The data in black are compared to the results of the Monte Carlo simulation using the spectral function from IPSM (green) and from [22] (red). The latter accounts for SRC (sec. 1.2.7) [22]. As can be seen in Fig. 7.2 the distribution using the IPSM spectral function shows a deficiency between 50 and 100 MeV missing energy compared to the data. On the other hand the theory of [22], which contains  $\approx 25\%$  of correlated strength, agree well with the data in this  $E_m$ - $p_m$ -region. SRC are expected to become important already at the Fermi momentum near 250 MeV/c, which is covered by the quasi-elastic data.

The data as well as the Monte Carlo simulation with and without taking SRC into account show a large bump starting at  $E_m = 0.1$  GeV. For the kinematics shown in Fig. 7.2 the average energy loss due to radiation is around 200 MeV, which increases with larger  $p_m$ . As a rule of thumb the bump

---

<sup>1</sup> $p_m < 0$  corresponds to angles of the proton momenta being larger than that of the momentum transfer  $q$ .

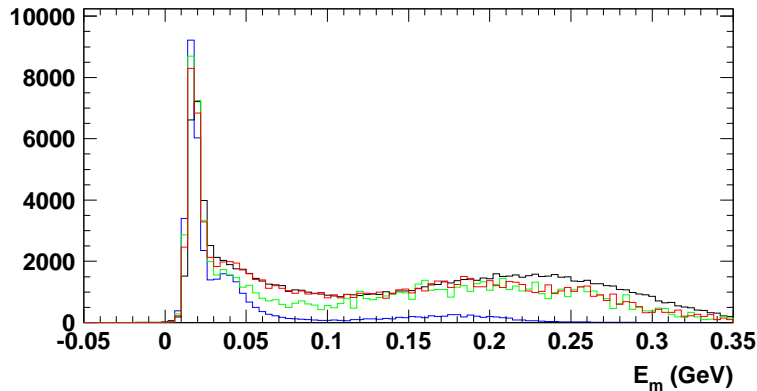


Figure 7.2:  $E_m$  spectrum for a slice in  $p_m$  of  $250 \pm 50$  MeV/c in quasi-elastic kinematics. Data are in black, the other curves are simulated using the IPSM model with (green) and without (blue) radiative effects. For the distribution in red the spectral function of [22] is used as input for the Monte Carlo.

in  $E_m$  appears roughly at an energy, which is slightly smaller ( $\approx 30$  MeV) than the corresponding central value of the  $p_m$  slice. In sec. 4.1.3 it was argued that  $E_m \approx p_m \approx E_\gamma$ , which is here confirmed within the approximation. For comparison the distribution in blue is obtained without taking into account radiative effects. The bump is almost removed. The small contribution left at large missing energies originates from protons penetrating the material of the collimator (sec. 6.5), which leads also to additional energy loss. The spectra shown in Fig. 7.2 are taken at a central SOS momentum of 1.5 GeV/c. Protons of these momenta can still be detected after passing through the collimator material (sec. 6.5).

## 7.2 Nuclear transparency

When a proton bound in a nucleus is hit by an electron, the proton has first to penetrate through the nuclear medium, before it can leave the nucleus. On its way several nucleon–nucleon interactions can occur. As a consequence the proton can be absorbed or deflected, so that the flux of protons detected is reduced. The reduction factor is called nuclear transparency  $T_A$ . The free N–N cross section shows a minimum at a proton kinetic energy of  $\approx 300$  MeV and reaches a plateau of 40–50 mbarn for proton energies larger than  $\approx 1$  GeV. The N–N cross section in medium has a similar dependence on the proton kinetic energy, but is reduced in strength by about 30 % [75]. The

nuclear transparency reflects this dependence at small proton energies. At very high proton energies  $T_A$  is expected to increase, because the interaction of hadrons with the nuclear medium is reduced according to PQCD [25] [34]. This effect is called color transparency, but no clear evidence for it was found so far. Further the nuclear transparency for different nuclei scales approximately with  $A^{-1/3}$ , because the probability for collisions increases with the distance the proton has to pass in the nucleus. Empirical fits of the form  $T_A = c A^{\alpha(Q^2)}$  to the experimental data results in values of  $c$  consistent with unity and  $\alpha = -0.24$  for  $Q^2 \geq 1.8$  (GeV/c)<sup>2</sup> [75].

A common method to measure the transparency exploits electron scattering in quasi-elastic kinematics. The knocked-out proton and the scattered electron are detected. Then  $T_A$  can be extracted from the measured yield  $N^{exp}$  in the single-particle region compared to the yield  $N^{IPSM}$  simulated by Monte Carlo using the IPSM spectral function:

$$T_A = \frac{\int_V d\vec{p}_m dE_m N^{exp}(E_m, p_m)}{\int_V d\vec{p}_m dE_m N^{IPSM}(E_m, p_m) / \epsilon^{SRC}} \quad (7.1)$$

The integration volume has to be restricted to the single-particle region. In former analyses the region  $E_m \leq 0.08$  GeV and  $p_m \leq 0.3$  GeV/c was chosen [2] [75], which will also be used below for consistency. A source of uncertainty in Eq. 7.1 is the factor  $\epsilon^{SRC}$ , which accounts for the depletion of the single-particle states due to SRC. A factor of  $1.11 \pm 0.03$  for carbon was used in previous analyses. For heavier nuclei like gold the correction is taken much larger ( $\epsilon^{SRC} = 1.28 \pm 0.1$ ), even though the correlated spectral functions of ref. [22] do not show such a dependence (sec. 1.2.7 and 4.1.2). The large uncertainties reflect the errors in the theoretical model and deviations in different theories as it was stated in [114] and [133]. In fact one can at best only measure the product of the nuclear transparency and the spectroscopic factor summed over some fragments (see also the discussion in [104]). More complicated FSI processes are ignored in the analysis as they would not allow a factorization of the cross section into spectral function and off-shell cross section.

### 7.2.1 Discussion of the results

The results for the nuclear transparency extracted via Eq. 7.1 are shown in Fig. 7.3 and indicated by the solid triangles. They are compared to previous measurements performed at SLAC [134] (circles) and at Jlab [2][75] (squares and diamonds). Data for carbon are in black and results for iron (red) and gold (orange) are also shown for later use. The error bars shown contain only

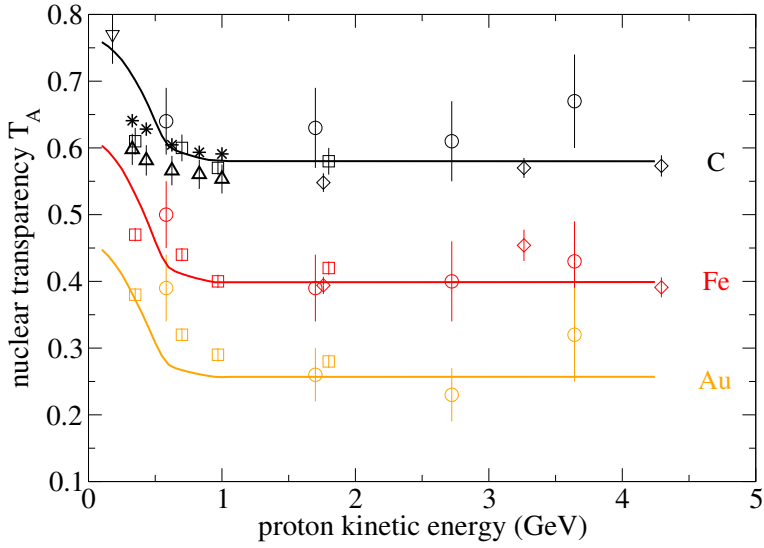


Figure 7.3: Nuclear transparency  $T_A$  for C, Fe and Au as a function of the proton kinetic energy compared to Glauber calculations of [24] (solid lines). The data indicated by circles are from the NE18-experiment at SLAC [134], squares and diamonds are Jlab data of [2] and [75]. The solid triangles are from the present work analyzed with the IPSM, whereas the result indicated by stars (without error bars) is obtained with the correlated spectral function of [22].

statistical and systematic uncertainties from the experiment (see below and Tab. 7.1). The model-dependent uncertainties, which are largest, are not presented in this plot. This is justified, because all experiments are analyzed with the same ingredients and therefore are consistent with each other.

The solid lines in Fig. 7.3 correspond correlated Glauber calculations of [24] treating NN scattering in the medium by accounting for Pauli blocking and dispersive effects. This model describes the transparency for carbon well, at least for  $Q^2 > 1$   $(\text{GeV}/c)^2$ . It was obtained using the local density approximation for the nuclear pair distribution function and including single and double rescattering contributions. The assumption made, that the struck nucleon will not be deflected on its path through the nuclear medium (eikonal approximation) might break down for small proton kinetic energies. This seems to be the case for kinetic energies less than 0.5 GeV. In particular the prediction for gold underestimate the experimental data. A similar trend is observed in the DWIA calculations of [96]. This latter model uses an optical potential with parameters determined by an effective empirical interaction

derived from fits to inelastic proton scattering data.

However, Frankfurt et al. [67] suggested that the experimental results for C, Fe, Au should be renormalized by a factor of 1.02, 0.896 and 0.83 respectively. They realized that the  $(e, e' p)$  cross section in quasi-elastic (transverse) kinematics depends on  $\int S(\vec{k}, E) / k d^3 \vec{k} dE$  rather than  $\int S(\vec{k}, E) d^3 \vec{k} dE$ , reducing the contribution of high-momentum components. This integral was calculated in a Hartree–Fock Skyrme model as well as for the IPSM spectral functions used by all the experimental analyses of the transparency factor. From the deviation of the two results the renormalization factors mentioned above are derived. This would bring the Glauber calculations for heavier nuclei in better agreement with the data.

| source                            | uncertainty | reference |
|-----------------------------------|-------------|-----------|
| solid target thickness            | 0.3 %       | 2.3.1     |
| charge measurement                | 1 %         | 2.2.2     |
| run stability                     | 0.5 %       |           |
| tracking efficiency(HMS/SOS)      | 0.5/0.5 %   | 3.1.1     |
| “focal plane” efficiency(HMS/SOS) | 0.5/1 %     | 5.2       |
| $\beta$ -cut inefficiency         | 0.5 %       | 6.2       |
| blocking correction               | 1/1 %       | 3.2.1     |
| dead time                         | 0.5 %       | 2.4.5     |
| proton transmission               | 1.1 %       | 6.1       |
| Cut stability                     | 2 %         |           |
| phase space                       | 2 %         |           |
| kinematics                        | 0.5 %       |           |
| total                             | 3.9 %       |           |

Table 7.1: Systematic uncertainties for the extraction of the nuclear transparency.

Most of the systematic uncertainties are the same as for the  $H(e, e' p)$  analysis and were already discussed in sec. 6.4. No error is applied to the background contribution, which is less than 0.2 % and therefore negligible. The extracted transparency is most sensitive to cuts in the missing energy and to a lesser extent to the missing momentum. In addition to the integration volume of  $p_m \leq 300$  MeV/c,  $E_m \leq 80$  MeV a region of  $p_m \leq 200$  MeV/c and  $E_m \leq 50$  MeV was chosen. Especially for  $T_A$  at the lowest proton kinetic energy this reduces the result of about 2.5 %. From the  $E_m$ -spectra one realizes that for  $E_m > 50$  MeV and for larger  $p_m$  the experimental data already exceed the IPSM prediction. This was already observed earlier (e.g. [108]).

It might be a hint on the presence of additional reaction mechanisms such as two-nucleon emission (SRC) and meson exchange. Further it is important, that the position of the  $p_{3/2}$ -state in the data and the Monte Carlo agrees. Shifts of less than 1 MeV were corrected for. The uncertainty due to cut constraints is estimated to 2 %.

The data were also analyzed for an offset of -0.2 % applied to the beam energy and the corresponding spectrometer offsets (sec. 6.3). This changes the results by less than 0.5 %. Concerning the run stability for each kinematics 3 to 4 runs were taken. The differences of  $T_A$  from run to run are small and compatible with the statistical errors. In total the systematic uncertainties summed quadratically amount to 3.9 % (Tab. 7.1).

| source                 | uncertainty | reference |
|------------------------|-------------|-----------|
| $\sigma_{ep}$          | 2 %         |           |
| IPSM spectral function | 2 %         | 1.2.2     |
| Correlation correction | 3 %         |           |
| radiative correction   |             | 4.1.3     |
| internal               | 2 %         |           |
| external               | 1 %         |           |
| total                  | 4.7 %       |           |

Table 7.2: Model-dependent uncertainties for the extraction of the nuclear transparency.

The model-dependent errors are summarized in Tab. 7.2 and amount to 4.7 %. The dependence on the chosen off-shell cross section was examined by taking the  $\sigma_{cc2a}$  and the  $\sigma_{cc}$  description instead of the  $\sigma_{cc1a}$ , which is commonly used. The influence on  $T_A$  is about 1.5 % for  $\sigma_{cc2a}$  and even smaller for  $\sigma_{cc}$ . Therefore an uncertainty of 2 % is applied. The error induced by the choice of the IPSM spectral function was estimated to 2 % in [114]. In [59][186] a larger uncertainty of 4.5 % was used. In [186] a spectral function for iron with a wider missing energy and momentum distribution was examined. The extracted transparency is quite sensitive to missing energy and momentum distribution, because events are shifted out or into the region of interest. On the other hand the agreement between the experimental and simulated  $E_m$  and  $p_m$ -spectra in Fig. 7.3 is so good, that the smaller uncertainty seems to be more realistic. Alternatively to the IPSM spectral function plus correlation correction the spectral function of Benhar (sec. 1.2.7) was used. It consists of the IPSM spectral function reduced by a factor of 0.78 and a correlated part calculated by Benhar in CBF theory

[22]. This leads to an approximately 6 % larger transparency as shown by the stars in Fig. 7.3. These values are in even better agreement with the Glauber calculation of [24] shown by the solid lines. Half of this discrepancy is taken as  $\sigma$ -uncertainty for the correction factor  $\epsilon^{SRC}$ .

The contribution of bremsstrahlung to the single-particle region of interest amounts to  $\approx 33\%$ . This is twice the amount compared to H(e,e'p)-kinematics. Further the radiative processes in the liquid hydrogen target used are dominated by internal bremsstrahlung rather than external radiation. In [114] C- and Fe-targets of different radiation lengths were compared. From this an uncertainty of 2 % for the external radiation is derived. A similar test is described in sec. 8.2.4 using data in the continuum region. The difference found between two different models of external bremsstrahlung was negligible. Therefore an uncertainty of 1 % will be applied.

According to the method of effective momentum approximation (sec. 4.1.5) Coulomb corrections were taken into account in the data as well as in the Monte Carlo simulation. Comparing the yield of the Monte Carlo simulation with and without Coulomb correction leads to a difference of less than 1 % for carbon. Therefore no additional uncertainty due to Coulomb correction is applied.

| $T_p$ (GeV) | $Q^2$ (GeV/c $^2$ ) | Transparency      |
|-------------|---------------------|-------------------|
| 0.328       | 0.59                | $0.598 \pm 0.023$ |
| 0.433       | 0.80                | $0.581 \pm 0.023$ |
| 0.625       | 1.13                | $0.566 \pm 0.022$ |
| 0.830       | 1.53                | $0.561 \pm 0.022$ |
| 1.00        | 1.85                | $0.553 \pm 0.022$ |

Table 7.3: Nuclear transparency for carbon using the IPSM spectral function. The error given is the quadratic sum of statistical and systematic uncertainty (Tab. 7.1). No model-dependent error is taken into account.

The results obtained for the nuclear transparency of carbon in the present work are summarized in Tab. 7.3 as function of  $Q^2$  and the proton kinetic energy. The error contains the negligible statistical error as well as the systematic one from Tab. 7.1. The model-dependent error (Tab. 7.2), which is the same for all analyses done so far, is not taken into account.

In [186] the transparency was analyzed for the  $s_{1/2}$  ( $0.03 \leq E_m \leq 0.05$  GeV) and  $p_{3/2}$  ( $E_m \leq 0.03$  GeV) state separately. There a difference in  $T_A$  of about 20 % was determined for carbon. A similar behavior using the same cuts was also observed for iron and gold. In case of carbon this was attributed to the

angular momentum of the  $p_{3/2}$ -state, which causes the protons to occupy in favor the nuclear surface. Contrary to this, the  $s_{1/2}$ -state occupies preferably the nuclear interior. The data of the present experiment were also analyzed to look for such a dependence. Within  $\pm 3\%$  the transparencies for the s- and p-state agree with each other. The only difference between this analysis and previous ones is the width of the  $p_{3/2}$ -state of 1 MeV instead of 5 MeV in the IPSM spectral function. This choice is closer to the expected value [34] and agrees with the data. Further it was observed that such an analysis is quite sensitive to the accurate description of the shape and width of the shells. The above mentioned  $\pm 3\%$  difference of  $T_A$  for the two shells is likely coming from small deviations of the  $E_m$ -spectra in experiment and Monte Carlo.

# 8 Analysis of the production runs

In this section the data taken in five kinematics, two perpendicular and three parallel (Tab. 1.1), on C, Al, Fe and Au will be analyzed with the help of the Monte Carlo simulation to obtain the distorted spectral function. Its sensitivity to internal and external radiative corrections, kinematical offsets, Coulomb corrections and the choice of the off-shell cross section will be examined. The distorted spectral function obtained for different nuclei as well as for the parallel and perpendicular kinematics are compared. Further the momentum distribution and the strength in the correlated region (with the  $\Delta$ -region and the single-particle region excluded) are obtained. The results for carbon are also compared to predictions from the CBF theory [22] and the Green's function approach [128]. Further the contribution from rescattering calculated for the kinematics used in this experiment [17] will be presented and compared to the data. Using a simulation based on the DMT-model of [94] the  $\Delta$ -resonance appearing at large  $\theta_{qpi}$  can be identified.

## 8.1 Extraction of the spectral function

Directly from experiment only the distorted spectral function can be obtained. Corrections, which come from reaction mechanisms beyond PWIA like rescattering (sec. 8.6), have to be applied subsequently. The analysis is based on Eq. 1.6, which is complemented by the transparency factor  $T_A$  (sec. 7.2) to take absorption of the proton inside the nucleus into account. Then the equation reads

$$\frac{d^6\sigma^{exp}}{d\Omega_e dE'_e d\Omega_p dE'_p} = p'E'_p \sigma_{ep} S(E, |\vec{k}|) T_A \quad (8.1)$$

As one can see from Fig. 7.3 the transparency factor varies a bit for small kinetic energy of the proton, which affects in particular the perpendicular

| nucleus | $T_A$ | relative error |
|---------|-------|----------------|
| C       | 0.6   | 10 %           |
| Al      | 0.5   | 15 %           |
| Fe      | 0.4   | 15 %           |
| Au      | 0.3   | 20 %           |

Table 8.1: Nuclear transparency for C, Al, Fe and Au as used for extraction of the spectral function. In the third row the estimated relative error of the transparency factor is given.

kinematics. The variation is largest for Au according to the experimental results ( $T_A = 0.38$  for  $T_p = 0.35$  GeV,  $T_A = 0.28$  for  $T_p = 1.8$  GeV). Given the systematic uncertainties of  $T_A$  a constant transparency factor is assumed for all kinematics. This does not affect the rescattering calculation in sec. 8.6. In Tab. 8.1 the used  $T_A$  for C, Al, Fe and Au are shown; they are in good agreement with the experimental values in Fig. 7.3 and the Glauber calculation of [18], which gives  $T_A = 0.63$  for carbon and 0.29 for gold for  $T_p = 1.8$  GeV. In the third row of Tab. 8.1 the relative error of  $T_A$  is estimated, which via Eq. 8.1 directly propagates as systematic error into the distorted spectral function.

To obtain the spectral function as a function of  $E_m$  and  $p_m$  the data yield is binned in both variables. The bin size in  $p_m$  is chosen as 40 MeV/c. Depending on the statistics in each  $p_m$ -bin the bin size in  $E_m$  varies between 10 and 50 MeV. Two different  $E_m$  step sizes can be chosen for the same  $p_m$ -bin. For the parallel kinematics one step size for each  $p_m$ -bin is sufficient. The data yield is corrected for background in the coincidence spectra (Fig. 3.7) and the cuts are applied. The accidental yield is averaged symmetrically left and right of the coincidence peak over three peaks (from |3| ns to |9| ns). All correction factors described in the previous sections in detail are taken into account (s. also Eq. 3.5). In addition Coulomb corrections via EMA are applied (sec. 4.1.5). Two methods, called Phasespace- and Yield-Analysis, were used to obtain the spectral function from the data. They will be described in the following.

### 8.1.1 Phasespace–Analysis

In the Phasespace–Analysis the phase space is taken from the Monte Carlo simulation performed without taking into account bremsstrahlung. From the experimental cross section the spectral function is extracted according to Eq. 8.1. All kinematical variables in each  $E_m$ – and  $p_m$ –bin are averaged over the

acceptance given by the cuts. The resulting  $S^{rad}(E_m, p_m)$  is still distorted by radiation, which tends to shift  $E_m$  and  $p_m$  to larger values. To correct for radiation effects a Monte Carlo simulation is performed, which accounts for bremsstrahlung. Then the corrected spectral function is obtained by multiplying  $S^{rad}(E_m, p_m)$  by the ratio of the simulated yield with and without bremsstrahlung bin per bin:

$$S^{derad}(\bar{E}_m, \bar{p}_m)_{ij} = S^{rad}(\bar{E}_m, \bar{p}_m)_{ij} \frac{N_{ij}^{norad}}{N_{ij}^{rad}} \quad (8.2)$$

To perform the Monte Carlo simulations a spectral function has to be provided, which is taken from a fit to the spectral function obtained from the data. Mainly due to radiation the spectral function has to be extended in  $E_m p_m$ -regions, where no data were taken in this experiment. For the single-particle region the spectral function is taken from the IPSM (sec. 4.1.2) multiplied by a normalization factor of 0.85. The contribution from the region outside of the one accessible in the experiment is small for the correlated region, i.e. the region not covered by nucleon excitation in pion-electroproduction (sec. 8.7). The procedure described above is an iterative process, which usually converges fast except for regions, where the spectral function is changing rapidly, as is the case for the single-particle states. Due to the modest missing energy resolution of  $\approx 7$  MeV in the experiment, which is reproduced by the Monte Carlo, the spectral function used as input for the Monte Carlo has to contain information, which goes beyond the detector resolution. Therefore for valence states at moderate  $p_m$  the obtained spectral function is of limited use.

The averaging of the kinematical variables over a large region is problematic in this approach. The cross section evaluated at the averaged kinematic variables can deviate from the average cross section in this region<sup>1</sup>. To avoid this problem a correction factor was calculated for each bin. The correction factor was obtained by comparing the spectral function used in the Monte Carlo and the one extracted from the Monte Carlo simulation. The correction is usually of the order of 5 % and serves also for a check of the procedure.

### 8.1.2 Yield–Analysis

As a cross check a second method was implemented in the analysis code. It is based on comparing directly the corrected experimental yield with the

---

<sup>1</sup>The method of calculating the off-shell cross section for each event separately was not used, because of the presence of non-valid events (background), resolution effects and occasional wrong reconstruction of the kinematical variables.

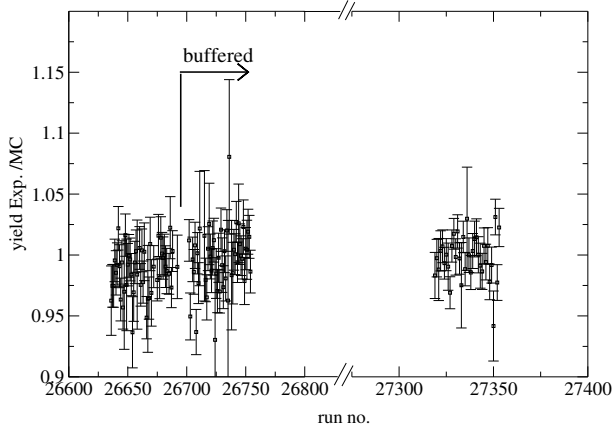


Figure 8.1: Ratio of the corrected yield obtained in kinematics kin4 for Au to the Monte Carlo simulation as a function of the run number. The first part of runs was taken in unbuffered data acquisition mode.

yield obtained in the Monte Carlo, which is appropriate weighted and normalized to the experimental luminosity (sec. 4.1). A deviation of the ratio from one is taken to correct the actual spectral function used in the simulation. This method is simple and can be directly checked by comparing the missing energy spectra for each  $p_m$ -bin. Further, only one Monte Carlo with bremsstrahlung included is required instead of two for the Phasespace–Analysis, which reduces the effort. In addition the statistical error from the events generated in the simulation is reduced. The results from the two methods are in fact undistinguishable. Therefore the Yield–Analysis is preferred.

Using this method also the ratio of the experimental to simulated yield was monitored on a run per run basis. This helps to find problems in a run, which occur usually due to loss of synchronization between the spectrometers (sec. 3.2.1) or due to a large inefficiency of one of the detectors because of HV problems. In Fig. 8.1 the yield stability per run is demonstrated for kinematics kin4 of Au. The first part of data was taken in unbuffered mode (sec. 2.4.5). Because of the large rate the data acquisition was switched to buffered mode, which reduces the dead time considerably. No change in the yield ratio is observed. Furthermore the third part of the data set, which was taken 11 days later, is in perfect agreement with the previous ones. This is also true for the other data sets taken in parallel kinematics. For perpendicular kinematics the yield ratio of the second data set is 1-2 % higher than the first one taken a few days earlier. We assign this to the fact that the target had to be tilted to  $25^\circ$ . The reproducibility of the target

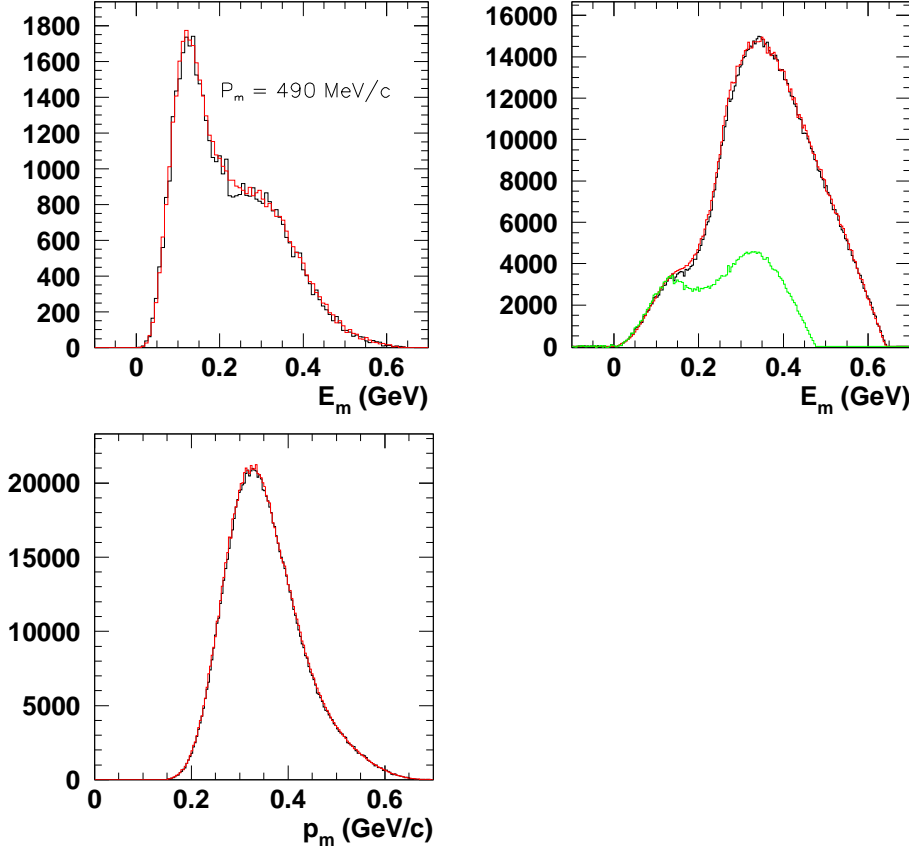


Figure 8.2: Comparison of missing energy for a  $p_m$ -bin of 490 MeV/c  $\pm$  20 MeV/c (left) and without cut in the  $p_m$ -distribution (right) shown below. Experimental spectra in black are compared to the results of the Monte Carlo simulation in red. The green curve in the  $E_m$ -spectrum is produced with additional cuts (sec. 8.7.4).

angle is  $\pm 2^\circ$ , which leads to an error in the target thickness of  $\pm 1.6\%$ .

In the analysis the  $E_m$ -spectra for all  $p_m$ -bins were carefully checked to ensure that the data and the simulation agreed after the iteration process. Convergence on the 5 % level between input and output spectral function is reached. This does not mean that the experimental spectral function gets an uncertainty of 5 % due to this mismatch. Because of the smoothness of the spectral function the size of the radiative corrections does not depend heavily on the input spectral function except in the region close to narrow valence states.

As example the  $E_m$ -spectrum for the  $p_m$ -bin = (490  $\pm$  20) MeV/c is shown in Fig. 8.2 for kinematics kin3 and Al. The data corrected for back-

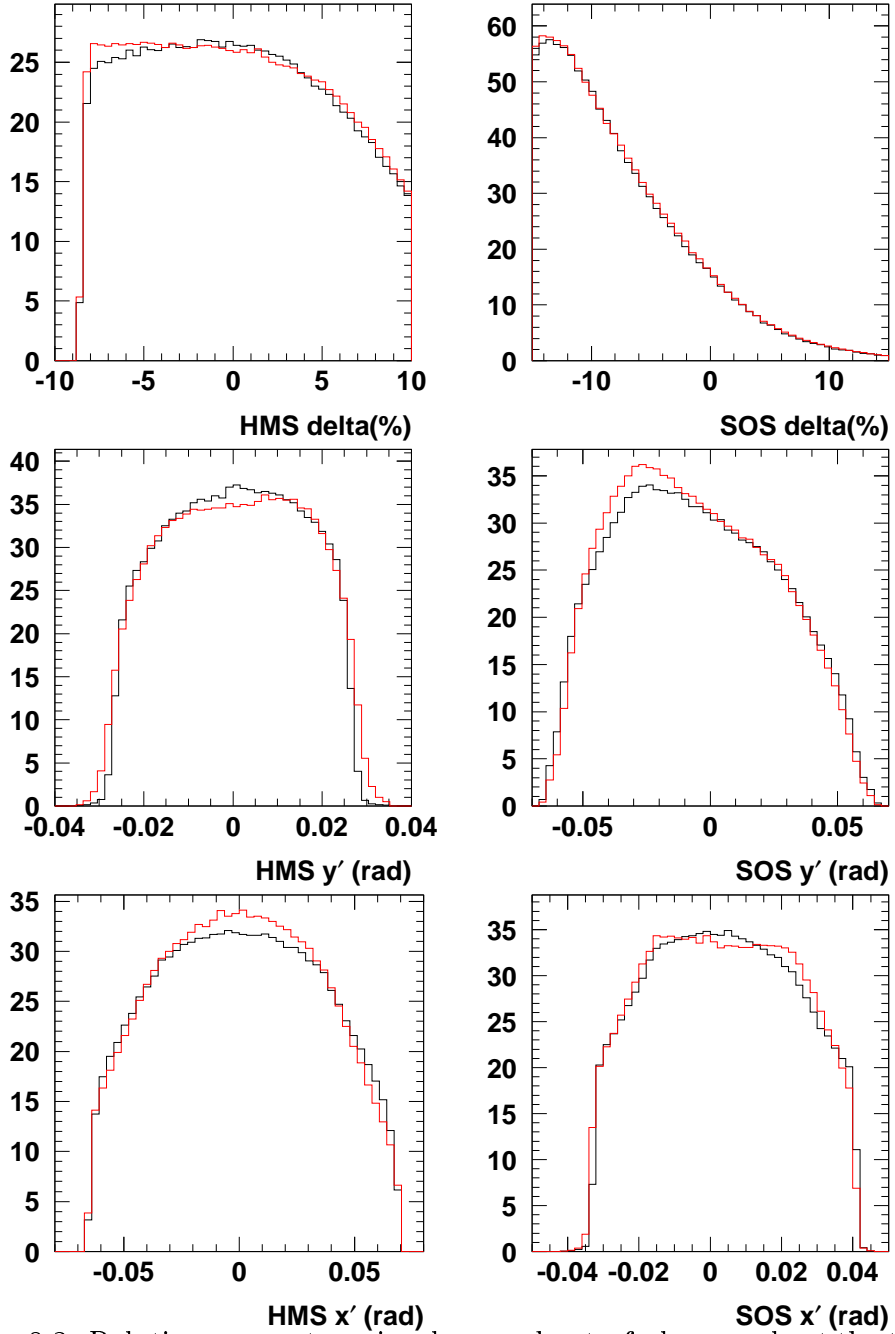


Figure 8.3: Relative momentum, in-plane and out-of-plane angle at the target in the HMS (left) and SOS (right) for kinematics kin3 of Al after completing the iteration procedure described in the text. The experimental spectra (black) are compared to the result of the Monte Carlo in red. The y-scale of the histograms is divided by 1000.

ground are shown in black compared to the simulation in red. Further the accepted  $E_m$ -distribution in this kinematics is shown. The large bump at high  $E_m$  is due to the higher resonances. The contribution of the resonance region was already obvious in Fig. 1.16. Due to its preferred transversal character appears at large angle between initial momentum and momentum transfer, but also at relatively small momenta of the scattered electron and proton due to the production of a pion. Therefore the appearance of the resonances gets suppressed at high  $p_m$  due to the kinematical acceptance as can be seen in Fig. 8.2 for  $p_m = 490$  MeV/c. The increasing contribution at low momenta is apparent in Fig. 8.3. Using cuts<sup>2</sup> a significant reduction of the resonance contribution is achieved (green curve) (sec. 8.7.4). It should be noted that these cuts have no influence on the extracted spectral function as long as the model used can describe the data. The model is based on Eq. 8.1 and it is clear that processes like the  $\Delta$ -excitation or rescattering can only approximately be described because their momentum and angle dependence is different. An amplitude factor, which depends only on  $E_m$  and  $p_m$  is used to parameterize the contribution from other reaction mechanism. This factor, however, does not have the meaning of a spectral function. The success of this model can be qualitatively evaluated, when comparing the angle and momentum distributions of data and simulation. Some shortcomings of the model can be seen in Fig. 8.3 in particular at small electron momenta and small proton scattering angles. The agreement of the spectra is improved, when applying additional cuts to reduce the resonance contribution. Even without additional cuts the agreement between data and simulation is good enough to achieve a result, which is stable against cuts.

## 8.2 Model and analysis dependence of the result

Before presenting the results the sensitivity of the spectral function on various ingredients is examined.

### 8.2.1 Sensitivity to kinematical offsets

Usually the analysis was performed with the spectrometer offsets corresponding to a correction of the beam energy of 0.1 % (Tab. 6.2). To examine the sensitivity of the result on the spectrometer offsets the second offset set for

---

<sup>2</sup>Cuts to reduce resonance contribution:  $-6\% < \text{ssdelta} < 15\%$ ,  $-7\% < \text{hsdelta} < 10\%$ .

$E_e - 0.2\%$  shown in Tab. 6.2 was used. The change in the spectral function was less than 1 % in the average. The reason for the small effect is that both sets were adjusted using  $H(e,e'p)$  to keep the  $E_m$ - and  $p_m$ -distribution at the same position. The spectral function is most sensitive to shifts in  $E_m$  and  $p_m$ , which do not occur in this case. The cross section is less sensitive to a slightly modified kinematics as can be also seen in Fig. 6.11 for the reaction  $H(e,e'p)$ .

The situation changes, if there would be an unknown shift of the beam energy occurring during the experiment. Usually, without changes in the setup of the accelerator the beam energy shows variations of the order of  $2 \times 10^{-4}$  as can be seen from Fig. 2.2. These shifts are taken into account in the analysis. Further the beam spread is less than  $1 \times 10^{-4}$ . Nevertheless, we checked the effect of a shift in the beam energy of  $10^{-3}$ . For this a simulation was performed at a 0.1 % higher (corrected) beam energy. Then both data and simulation were analyzed with the usual beam energy and the corresponding spectrometer offsets. The main effect is a shift in the  $E_m$ -distribution between data and simulation. Therefore in particular the first and also the second  $E_m$ -bin for each  $p_m$ -bin is dramatically affected depending on the bin size. The effect is amplified, if sharp structures from the single-particle region are present. Due to the modest  $E_m$ -resolution the spectral function obtained at very small energies should be taken with care. The increase of the total yield in case of using the wrong beam energy is 1.4 % for kin5. Overall the effect is small.

### 8.2.2 Check of the $p_m$ -binning

Using 40 MeV/c bins for  $p_m$  the spectral function decreases from bin to bin approximately by a factor of two. It then becomes questionable whether a linear interpolation of the spectral function between two bins is justified. As a test the  $p_m$ -grid was shifted by 20 MeV/c and the data reanalyzed. The result was compared to the linearly interpolated spectral function using the result of the analysis with the standard  $p_m$ -bins. The change is smaller than the statistical error bars. This means that the grid used is fine enough and the shape of the spectral function smooth enough to obtain reliable results.

### 8.2.3 Dependence on Coulomb corrections

The kinematics most sensitive to Coulomb corrections is kin3, because it has the lowest energy of the scattered electron (Tab. 1.1) and reaches to the highest  $p_m$ . Further, Coulomb corrections in parallel kinematics lead to a shift of the  $p_m$ -distribution (sec. 4.1.5). Therefore this kinematics was

chosen to determine the sensitivity of the result to Coulomb corrections. The shift for this kinematics on Au, the heaviest nucleus used in this experiment, is 3–4 MeV/c. Even for such a small shift the spectral function is especially affected at the lowest and highest  $p_m$ -bins. The effect depends on the shape of the  $p_m$ -distribution in the experiment. On the other hand, the size of the shift is quite well established and it is also confirmed by exact calculation that EMA can account for this shift. The reduction of the cross section averaged over the acceptance of the kinematics is 1.5 % compared to a simulation without Coulomb corrections applied. This comes mainly from the factor modifying the cross section in Eq. 4.19. From this and the discussion in sec. 4.1.5 we deduce a contribution to the systematic error of 2 %.

### 8.2.4 Sensitivity to radiative corrections

Radiative corrections depend on the model implemented. Therefore the data are analyzed with two different models and the results are compared. The effect of internal and external bremsstrahlung is separately examined.

In sec. 4.1.3 two methods to treat internal radiation were presented, the peaking and the multiphoton technique. By default the second technique is used in the data analysis. The contribution of radiative corrections can be large. At small  $E_m$  the yield is reduced due to bremsstrahlung whereas for large  $E_m$  and especially in perpendicular kinematics  $\approx 50$  % of the cross section originates from regions of small  $E_m$ , but radiated in regions of large  $E_m$ . Even though radiation has a large effect on the spectral function, the result analyzed with the peaking technique deviates by only  $\approx 1$  %. To be conservative a systematic error of  $\pm 2$  % will be applied for the accuracy of internal radiation.

To get a handle on the effect of external bremsstrahlung data were taken for two iron targets with different thicknesses in kinematics kinp2. The two iron targets had radiation lengths of 3.54 % and 5.64 % (Tab. 2.1) and were tilted by  $25^\circ$ . The amount of data taken with the thick target is a tenth of the luminosity with the thin target. Data taken with the thick target were analyzed with two models of external bremsstrahlung, which are described in Eqs. 4.12, 4.13, 4.14. The two methods give nearly identical results ( $\pm 0.2$  %). The contribution of external bremsstrahlung to the result is 10 % averaged over the acceptance of the kinematics, but can be as large as 30 % for large  $p_m$ . This was checked with a simulation using a very thin target of 0.1 % radiation length. The spectral functions obtained from the data taken with the two targets were compared. No difference could be found within the statistical error. A systematic error of 1 % accounts for the uncertainty in the external bremsstrahlung.

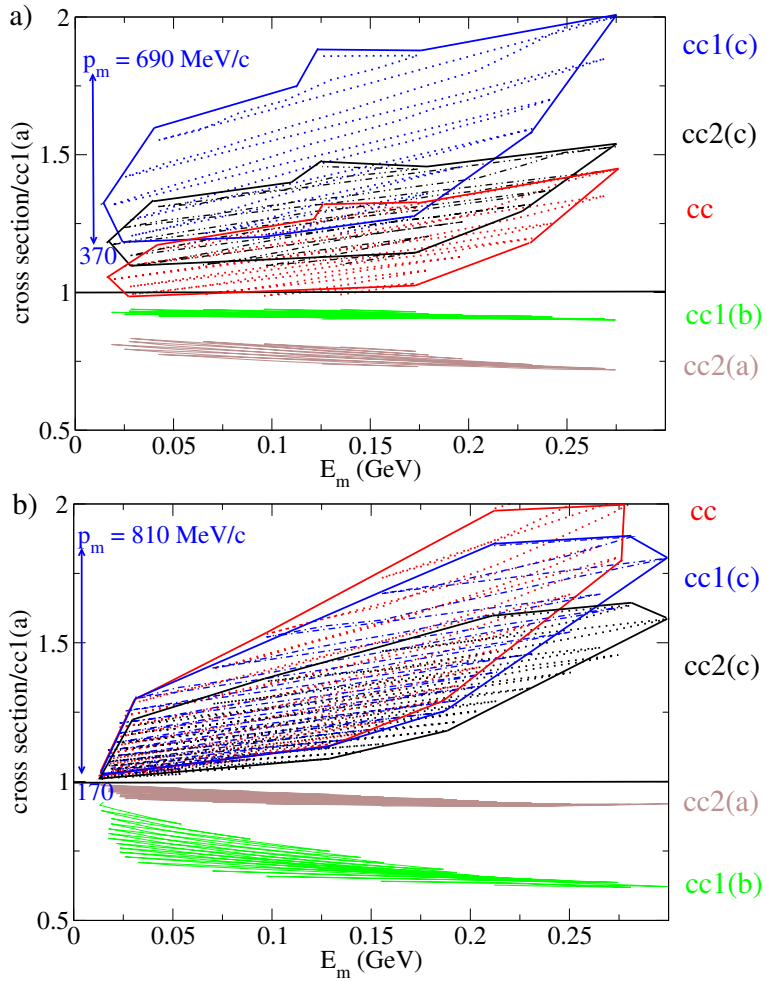


Figure 8.4: Behavior of the different off-shell cross sections relative to  $\sigma_{cc1a}$  as a function of  $E_m$  for parallel (a) and perpendicular (b) kinematics in the correlated region and in the range of  $p_m$  as indicated. Note that the scales and the color index of the pictures are the same.

To obtain the spectral function for kinematics kinp2 and Fe the results of the two data sets were averaged according to their statistical error.

### 8.2.5 Choice of the off-shell cross section

Because the spectral function is extracted according to Eq. 8.1 a change in the off-shell cross section will directly change the spectral function. In sec. 4.1.1 several choices of the off-shell cross section, which is not uniquely

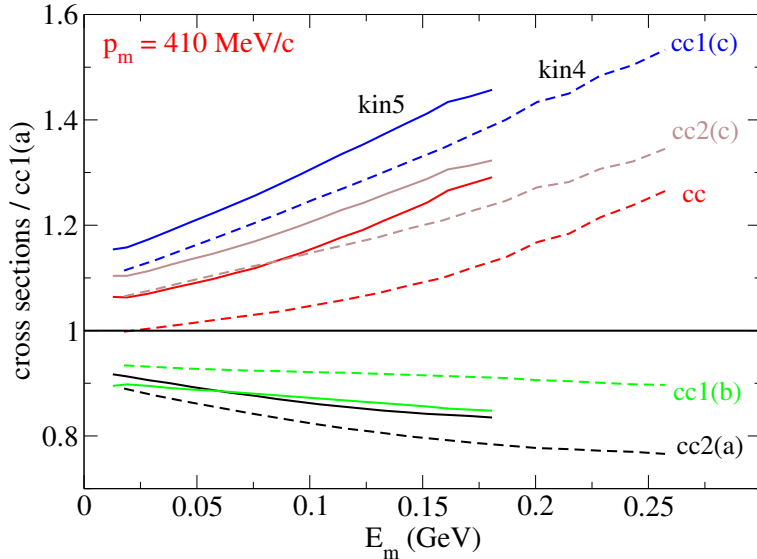


Figure 8.5: Ratio of the cross sections indicated in the figure with respect to  $\sigma_{cc1a}$  for the kinematics kin4 (dashed) and kin5 (solid) for a  $p_m$ -bin of 410 MeV/c.

determined, were discussed. In Fig. 8.4 several off-shell cross sections are shown relative to  $\sigma_{cc1a}$ , which is often chosen. The upper figure covers the correlated region of the parallel kinematics kin3, where  $p_m$  ranges from 370 – 690 MeV/c. The lower figure belongs to kinp1 with a  $p_m$ - range of 170 – 810 MeV/c restricted to the correlated region. The scales and the color index of the figures are the same. One can see that the behavior of the cross section ratios are quite different in parallel and perpendicular kinematics even for the same  $(E_m, p_m)$ . But there are also differences as a function of  $E_m$  within one set of kinematics. In extreme cases the variation can be between a factor 0.6 and 2 relative to  $\sigma_{cc1a}$ . The cross sections  $\sigma_{cc1b}$  and  $\sigma_{cc2a}$  are smaller than  $\sigma_{cc1a}$  and show approximately the same dependence on the missing momentum as  $\sigma_{cc1a}$ . This might be due to the similar technique used to restore the current conservation. In parallel kinematics  $\sigma_{cc2a}$  is 20–30 % smaller but deviates only 10 % in perpendicular kinematics with the opposite behavior for  $\sigma_{cc1b}$ . On the other hand  $\sigma_{cc}$  is much larger than  $\sigma_{cc1a}$  in perpendicular kinematics but the cross sections show only a moderate difference in parallel kinematics. For small  $E_m$  and  $p_m$  all cross sections tend to agree as they should.

The behavior of the cross sections is not only different for parallel and perpendicular kinematics but also within two parallel kinematics kin5 and kin4. Their cross sections relative to  $\sigma_{cc1a}$  as a function of  $E_m$  for a  $p_m$ -bin of

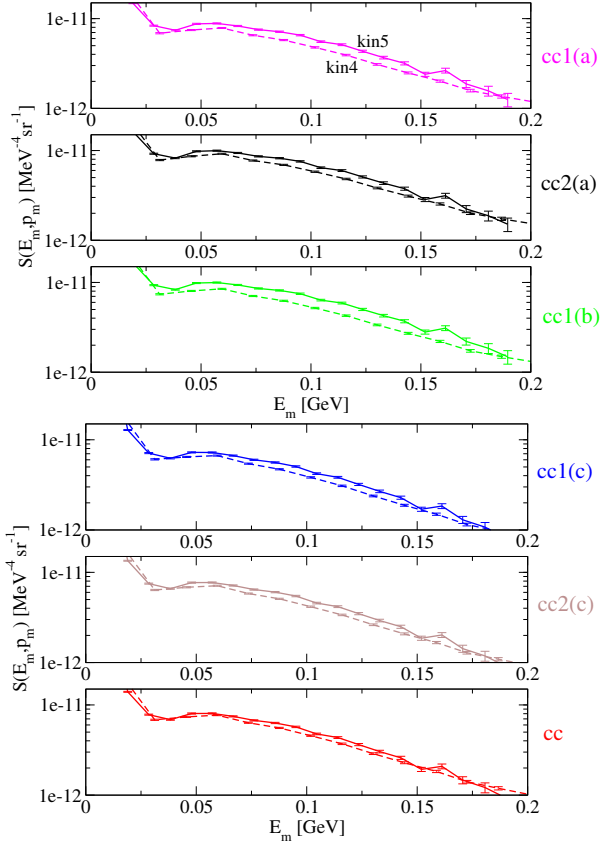


Figure 8.6: Spectral function of  $^{12}\text{C}$  for a  $p_m$ -bin of 410 MeV/c extracted from two parallel kinematics kin4 and kin5 using different versions for the e–p off–shell cross section. The upper curve belongs always to kin5.

410 MeV/c is shown in Fig. 8.5 by the solid and dashed line. The behavior of the cross section ratio with respect to its magnitude is the same as shown in Fig. 8.4a for kin3. But the ratio for the two kinematics can deviate for the same  $E_m$  and  $p_m$ -bin by nearly 15 %, although the two kinematics are quite similar (Tab. 1.1). This has direct consequences on the agreement or disagreement of the spectral functions extracted from different data sets in parallel kinematics. It should be noted that for kin3 and kin4 the deviation of the cross section ratio is not larger than 5 % and therefore not visible within the errors.

In Fig. 8.6 the spectral function of  $^{12}\text{C}$  for a  $p_m$ -bin of 410 MeV/c is obtained using different e–p off–shell cross sections. The two spectral functions are extracted from the data taken in the parallel kinematics kin4 and kin5. The higher curve in Fig. 8.6 belongs always to kin5. The deviation

between the two spectral functions is  $\approx 15\%$  using  $\sigma_{cc1a}$  and even increases for  $\sigma_{cc2a}$ . A better agreement is obtained with the two cross sections using the restoration of the current conservation according to Mougey. The best agreement is reached with the cross section  $\sigma_{cc}$ . It is remarkable that the shape of the spectral function does not depend on the choice of the cross section. Further it should be noted that the spectral function measured in the remaining parallel kinematics kin3 is within the errors always in agreement with the one from kin4 independently of the cross section employed. In the following the full accessible range of the spectral function in parallel kinematics obtained with the cross section  $\sigma_{cc1a}$  and  $\sigma_{cc}$  will be compared.

### 8.3 Results for $^{12}\text{C}$

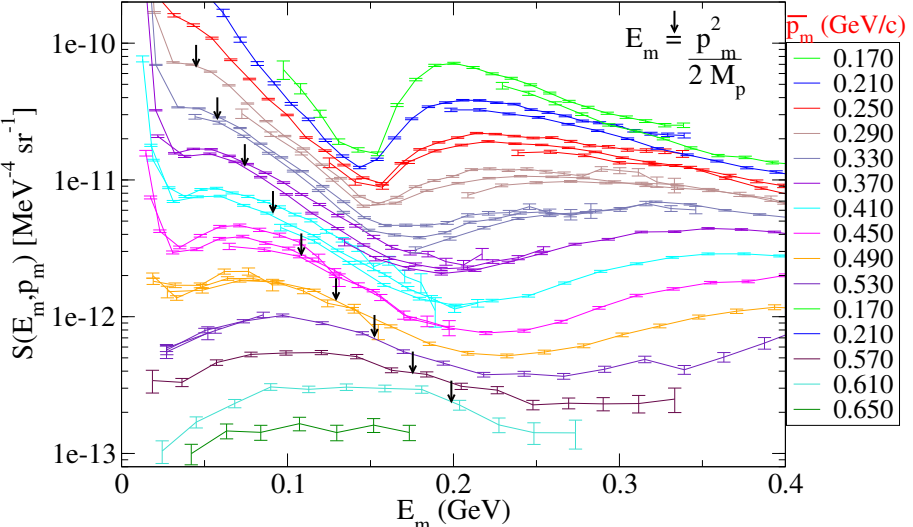


Figure 8.7: The distorted spectral function measured in parallel kinematics for  $^{12}\text{C}$  as a function of  $E_m$  for different  $p_m$ -bins as indicated by colors. In the analysis  $\sigma_{cc1a}$  was used.

In Fig. 8.7 the distorted spectral function obtained from parallel kinematics kin3, kin4, kin5 is shown as a function of  $E_m$  for  $p_m$ -bins from 170 to 650 MeV/c. For this analysis the off-shell cross section  $\sigma_{cc1a}$  was used. As mentioned in the last section the distorted spectral function from kin5 is always higher than from the other two kinematics. This deviation increases with increasing  $E_m$  and  $p_m$ . The correlated region is separated from the resonance region by a minimum (dip) in the distorted spectral function, which

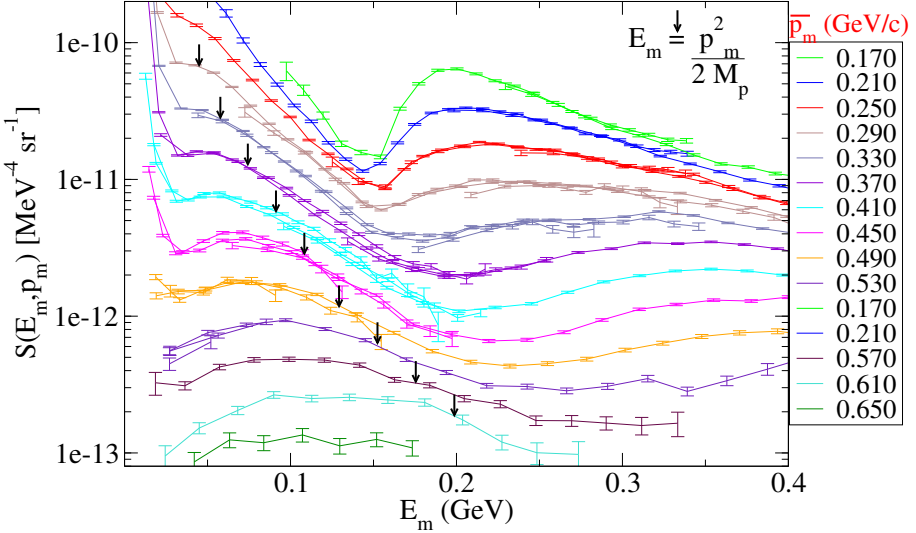


Figure 8.8: Same data as in Fig. 8.7 but analyzed with the cross section  $\sigma_{cc}$ .

appears at around  $E_m = 200$  MeV. The arrows in the figure indicate, where the maximum is expected according to the simple picture of SRC explained in sec. 1.2.8. The positions of the arrows follow the relation  $E_m = p_m^2 / (2 M_p)$ , which corresponds to the kinetic energy of the second undetected nucleon participating in the hard scattering induced by SRC. Note, that including the energy necessary for two-nucleon knock-out of 22 MeV measured for  $^{16}\text{O}$  in ref. [27] would shift the positions of the arrows to larger  $E_m$  about this amount. Comparing the maximum of the experimental distorted spectral function with the positions of the arrows one finds that the deviation increases with increasing  $p_m$ . The behavior disagrees also with the theories of [22] and [128], which show the maximum of the spectral function at larger  $E_m$ . This feature will be further discussed in sec. 8.4.

In Fig. 8.8 the same data are shown as in Fig. 8.7, but now using the cross section  $\sigma_{cc}$  instead of  $\sigma_{cc1a}$ . The scale and the color index of the pictures are the same. As one can see the agreement of the distorted spectral functions obtained from the three parallel kinematics is now much better even in the resonance region ( $E_m > \approx 200$  MeV), where it is not expected. As compared to the analysis using  $\sigma_{cc1a}$  the amplitude of the distorted spectral function changes 10 % or less except for the one from kin5. The shape of the distorted spectral function does not change.

The shape of the spectral function exhibits some interesting features. The contribution from the single-particle state  $p_{3/2}$  seems to die out around  $p_m$  of 500 MeV/c. For moderate  $E_m$  the distorted spectral function shows a bump,

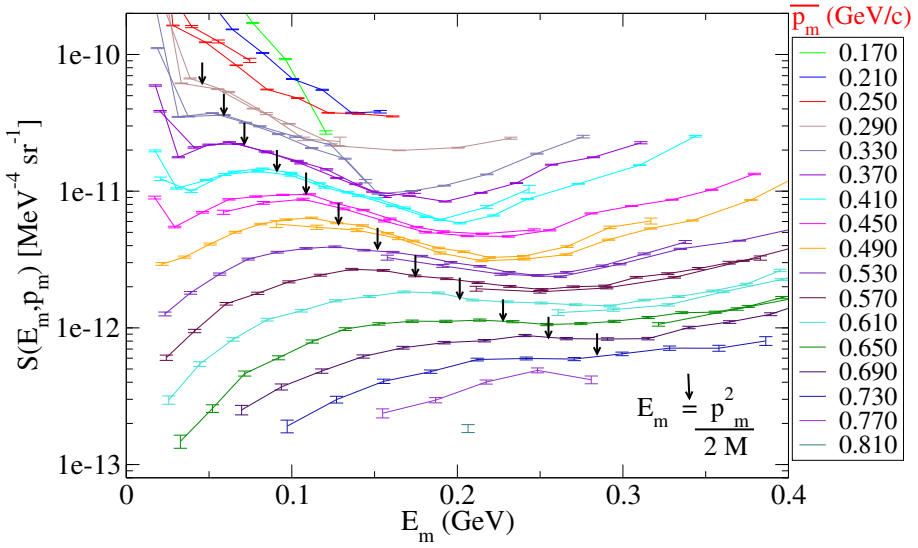


Figure 8.9: Distorted spectral function measured in perpendicular kinematics analyzed with the cross section  $\sigma_{cc}$ . Scale and color index of the figure are the same as for the distorted spectral function obtained in parallel kinematics.

whose maximum is located around 50 MeV for  $p_m \leq 410$  MeV/c. It shows up already for  $p_m = 250$  MeV/c. For smaller  $p_m$  the experimental acceptance does not cover this  $E_m$ -region. The location of the bump suggests that it comes from the deeper lying  $s_{1/2}$  state in  $^{12}\text{C}$ . A similar behavior appears in the distorted spectral function for  $^{56}\text{Fe}$ , where a small bump at 29 MeV can be seen up to  $p_m = 370$  MeV/c. The decrease of the distorted spectral function after the bump is steep for small  $p_m$ ; the slope becomes small at larger  $p_m$  probably due to the  $\Delta$ -contribution and higher resonances. The bump gets also broader for large  $p_m$  and its maximum is shifted to larger  $E_m$  of around 100 MeV. This feature can be also seen for the heavier nuclei. Therefore this shape seems to be independent of the single-particle structure. On the other hand all nuclei have there deepest lying hole state at 40–50 MeV with a large width of 20 MeV.

One should be aware that due to the spectrometer acceptance the data are getting increasingly non-parallel for large  $E_m$  and  $p_m$ . For example the angle  $\theta_{qpi}$  between the momentum transfer and the reconstructed initial momentum is larger than  $40^\circ$  for  $E_m > 120$  MeV and  $p_m = 570$  MeV/c. This can also be responsible for the shift of the maximum of the distorted spectral function to larger  $E_m$ .

In Fig. 8.9 the distorted spectral function obtained from the two perpen-

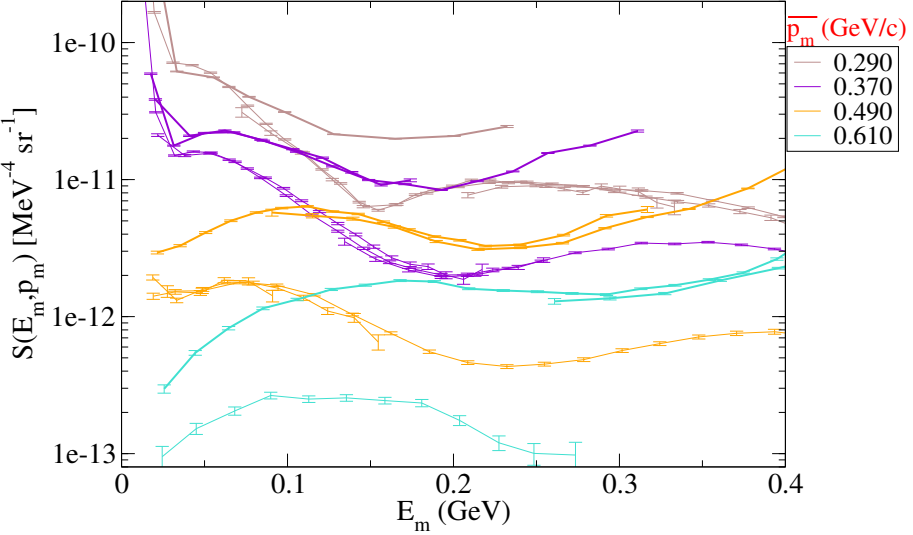


Figure 8.10: Direct comparison of the distorted spectral function measured in perpendicular (thick lines) and parallel kinematics for a few  $p_m$ -bins. As cross section  $\sigma_{cc}$  was used.

dicular kinematics kinp1 and kinp2 is shown. Here the cross section  $\sigma_{cc}$  is used. The agreement in the shape of the distorted spectral function between the two kinematics does not depend on the choice of the cross section, but the amplitude does. It is  $\approx 30\%$  smaller than the amplitude found using  $\sigma_{cc1a}$ . At large  $p_m$  the shape of the distorted spectral function in perpendicular kinematics is quite different from the one in parallel kinematics. The maximum of the bump is shifted to larger  $E_m$  and its position is close to the one indicated by the arrows. But this should not be taken as a signature of SRC, because any 2-body process can simulate such a peak. This will be confirmed by the rescattering calculations of [18] discussed below in sec. 8.6.2. The large amplitude of the distorted spectral function in perpendicular kinematics compared to the result in parallel kinematics is a clear indication that other reaction mechanisms are contributing. The deviation increases with increasing  $p_m$ .

In Fig. 8.10 a direct comparison of the distorted spectral functions measured in parallel and perpendicular kinematics is made for a few  $p_m$ -bins. For small  $E_m$ , less than 60 MeV, and  $p_m < 290$  MeV/c agreement between the two distorted spectral functions is good, which gives some confidence in the analysis. Moreover it will be shown in sec. 8.4 that this part of the distorted spectral function agrees also with IPSM. At larger  $E_m$  the dip region gets considerably filled compared to the parallel kinematics. For this rea-

son, the maximum of the distorted spectral function is shifted to larger  $E_m$  and misleadingly agrees with the expected signature of SRC. The disagreement increases up to an order of magnitude with increasing  $p_m$ . Due to the transversal character of IC, MEC and the  $\Delta$ -resonance the cross section in perpendicular kinematics is dominated by contributions from these reaction mechanisms. In addition rescattering plays an important role ( s. sec. 8.6).

### 8.3.1 Systematic uncertainties

| source                            | uncertainty | reference    |
|-----------------------------------|-------------|--------------|
| solid target thickness            | 0.3 %       | 2.3.1        |
| for tilted target                 | 1.6 %       | 8.1.2        |
| charge measurement                | 2 %         | 2.2.2        |
| run stability                     | 0.5 %       |              |
| tracking efficiency(HMS/SOS)      | 0.5/0.5 %   | 3.1.1        |
| “focal plane” efficiency(HMS/SOS) | 0.5/1 %     | 5.2          |
| $\beta$ -cut inefficiency         | 0.5 %       | 6.2          |
| blocking correction               | 1/1 %       | 3.2.1        |
| dead time                         | 0.5 %       | 2.4.5        |
| proton transmission               | 1.1 %       | 6.1          |
| Cut stability                     | 2 %         |              |
| kinematics                        | 1.5 %       | 8.2.1        |
| phase space                       | 2 %         |              |
| mismatch s.f. in MC and exp.      | 2 %         | 8.1.2        |
| Coulomb correction                | 2 %         | 8.2.3        |
| radiative correction              |             | 4.1.3, 8.2.4 |
| internal                          | 2 %         |              |
| external                          | 1 %         |              |
| background                        | 2 %         |              |
| total                             | 6.1 (6.3) % |              |

Table 8.2: Systematic uncertainties for the extraction of the distorted spectral function. The model-dependent uncertainties due to the choice of the off-shell cross section and the transparency factor are not included.

In Tab. 8.2 a summary of the systematic uncertainties for the distorted spectral function are given. Most of the uncertainties were already discussed in previous sections (sec. 7.2.1 and 6.4) and are the same as for the analysis of the hydrogen and quasi-elastic data. The remaining errors were discussed

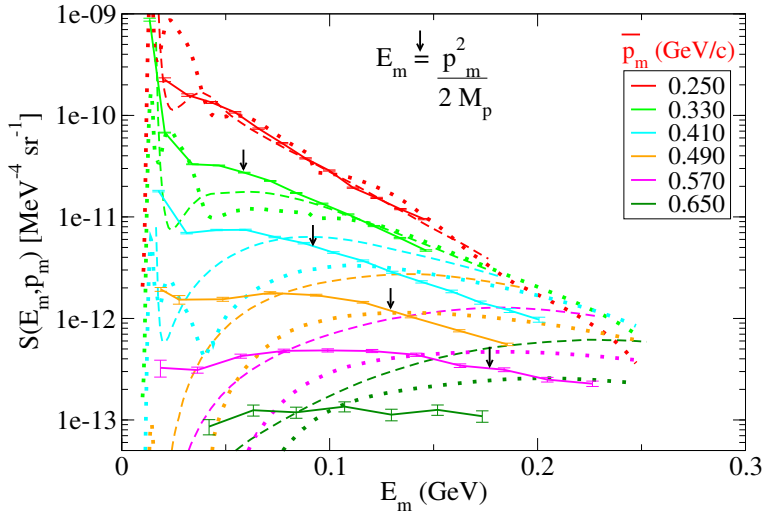


Figure 8.11: Comparison of the experimental distorted spectral function in parallel kinematics for  $^{12}\text{C}$  with the theoretical predictions of the CBF [22] (dashed) and the Green's function approach [128].

and estimated in sec. 8.2. For the background contribution an uncertainty of 2 % is taken into account. At high  $p_m$  the background contribution can be quite large. The negligible amount of events with  $E_m < 0$  after background subtraction serves as an indication that the background subtraction is done properly. Because a large amount of data were taken with currents less than 20  $\mu\text{A}$  an uncertainty of 2 % is added (sec. 2.2.2). The total systematic uncertainty is 6.1 %, and 6.3 % for the data in perpendicular kinematics taken with tilted target. The model-dependent uncertainties due to the choice of the off-shell cross section (sec. 8.2.5) and the transparency factor (Tab. 8.1) are not included. In the figures presenting the distorted spectral function only the statistical error of the data and the simulation is shown.

## 8.4 Comparison with theory

In Fig. 8.11 the distorted spectral function for  $^{12}\text{C}$  in the correlated region obtained from parallel kinematics (solid line) is compared to the predictions of the CBF theory [22] (dashed line) and the Green's function approach [128] (dotted line). For small  $p_m$ , around 250 MeV/c, both theories agree with the experimental result except for small  $E_m$ . Here the single-particle levels dominate. In particular the spectral function of the Green's function approach deviates significantly for small  $E_m$ . This effect is probably enhanced

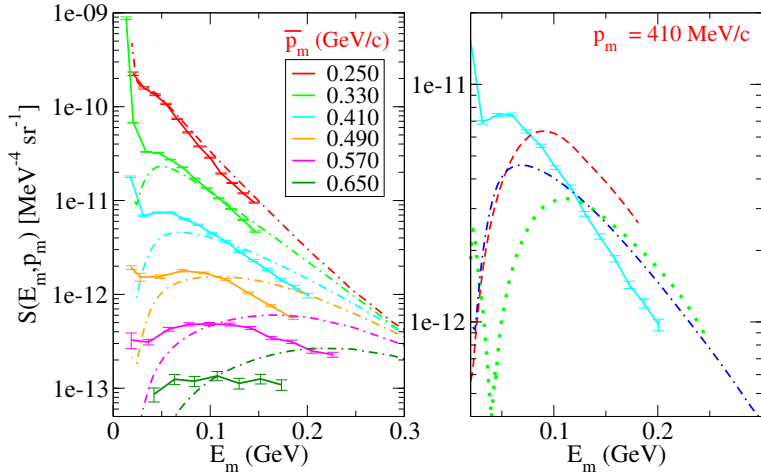


Figure 8.12: Similar picture as in Fig. 8.11. Here the self-consistent spectral function at a temperature of 2 MeV and for half of the saturation density of nuclear matter (dashed-dotted) [69] is compared to the distorted spectral function from the experiment for  $^{12}\text{C}$ . On the right the three theories of ref. [22] (dashed), [128] (dotted) and [69] (dashed-dotted) are shown together with the data for a momentum bin of 410 MeV.

due to the fact that it was originally derived for  $^{16}\text{O}$ . At small  $E_m$  LRC are expected to contribute. For larger  $p_m$  and moderate  $E_m$ , between 50 and 100 MeV, strength is missing in the theoretical predictions. In addition the maximum of the theoretical spectral function is shifted to large  $E_m$ . At large  $E_m > 150$  MeV both theories exceed the distorted spectral function from the experiment. For high  $p_m$  the spectral function from the Green's function approach seems to better fit the experimental result.

On the left hand side of Fig. 8.12 the self-consistent spectral function for nuclear matter of [69] for a temperature of 2 MeV and half of the saturation density of nuclear matter is compared to the data. Even though calculated for nuclear matter, neglecting finite size effects and LRC, the agreement with the experimental result is improved compared to the theories shown in Fig. 8.11. In particular for  $p_m$  around 400 MeV/c considerable strength is gained at moderate  $E_m$  compared to the Green's function approach of [128]. This can be seen most clearly on the right hand side of the figure, which shows all three theories and the data for a momentum bin of 410 MeV/c. In addition the slope at high energies is closer to the experimental result. This might be a hint that the fully self-consistent treatment with the dressing of the propagating particles, which leads to the inclusion of diagrams with

self energy insertions, is important. At smaller  $p_m$  the theoretical spectral function agrees with the data as well.

In Fig. 8.13 the average missing energy  $\bar{E}_m$  calculated from the measured distorted spectral function in parallel kinematics (triangles) and the theoretical prediction is shown as a function of  $p_m$ . It was obtained by integrating the spectral function over the correlated region according to

$$\bar{E}_m = \frac{\int E_m S(E_m, p_m) dE_m}{\int S(E_m, p_m) dE_m} \quad (8.3)$$

The integration region was chosen such as to be insensitive to single-particle states and to reduce the influence of the resonance region. Therefore the lower limit was set to 40 MeV and the higher limit was chosen to be in the minimum between the correlated region and the pion-electroproduction (Fig. 8.8). As can be seen from Fig. 8.13 the theoretical  $\bar{E}_m$  always exceeds the experimental result and the deviation increases with increasing  $p_m$ . At  $p_m = 610$  MeV/c the deviation amounts to 25 MeV. The result depends of course on the chosen integration region, but does not depend on the off-shell cross section used in the analysis.

Using the same integration region an effective experimental momentum distribution is obtained from the distorted spectral function using  $\sigma_{cc1a}$  (thin line) and  $\sigma_{cc}$  (solid line in Fig. 8.14) for parallel and perpendicular kinematics. It is compared to the corresponding result from the CBF theory and Green's function approach. Note that the integration regions differ slightly for parallel and perpendicular kinematics and therefore the theoretical momentum distributions in the left and right part of Fig. 8.14 are not identical. In parallel kinematics the experimental momentum distribution is in between the theoretical predictions. For  $p_m < 400$  MeV/s good agreement is achieved

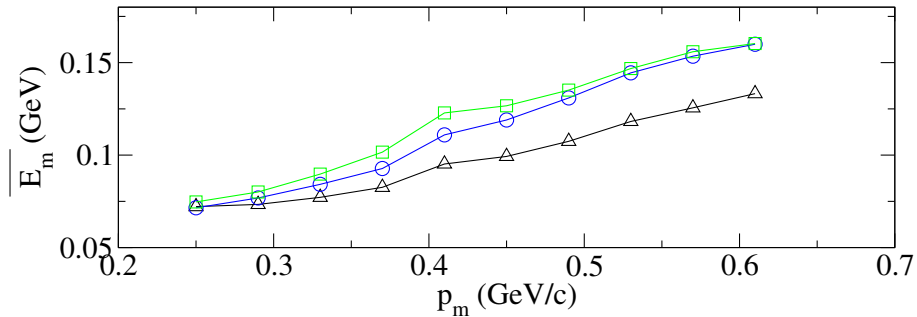


Figure 8.13: Missing energy averaged over the correlated region for each  $p_m$ . Triangles: data, circles: CBF, squares: Green's function approach.

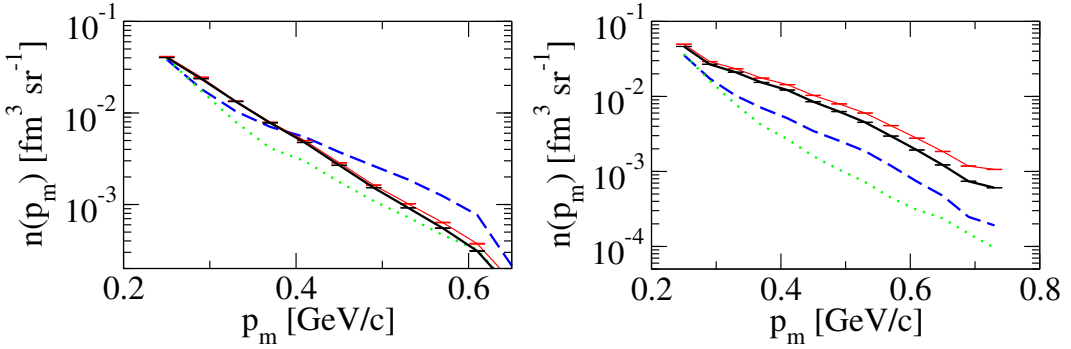


Figure 8.14: Experimental momentum distribution (thick solid line obtained using  $\sigma_{cc}$ , thin line using  $\sigma_{cc1a}$ ) compared to CBF theory (dashed) and Green's function approach (dotted) in the same  $E_m$ -region. Left: parallel kinematics. Right: perpendicular kinematics.

with the CBF theory, but at the highest  $p_m$  the experimental result is a factor of three smaller. Here it agrees better with the Green's function approach. The change of the experimental result is small, when using  $\sigma_{cc}$  instead of  $\sigma_{cc1a}$ . This would be not the case when using  $\sigma_{cc1c}$  for example as can be seen in Fig. 8.4.

In perpendicular kinematics the cross section  $\sigma_{cc}$  leads to a  $\approx 30\%$  reduction at large  $p_m$  compared to  $\sigma_{cc1a}$ . Still, the effective experimental momentum distribution is at least a factor of 2-3 too high for all  $p_m$ , when comparing to the CBF theory. The deviation even increases if one compares with the Green's function approach. A detailed picture is shown in Fig. 8.15, where the ratio of the experimental to the theoretical momentum distribution is calculated for parallel (open symbols) and perpendicular (filled symbols) kinematics. The large deviation from unity for the perpendicular kinematics is obvious.

Overall reasonable agreement between theory and experiment is obtained for parallel kinematics. However, one should be aware that due to the different shape of the theoretical and experimental distorted spectral function as seen in Fig. 8.11 the comparison depends on the chosen integration limits.

If one integrates the momentum distribution  $n(p_m)$  over the momentum one obtains the effective strength  $Z_C$  in the correlated region according to

$$Z_C = 4\pi \int_{230 \text{ MeV}/c}^{670 \text{ MeV}/c} dp_m p_m^2 n(p_m). \quad (8.4)$$

The result obtained for parallel and perpendicular kinematics is listed in Tab. 8.3. The number of protons found in the experiment is 0.64, which

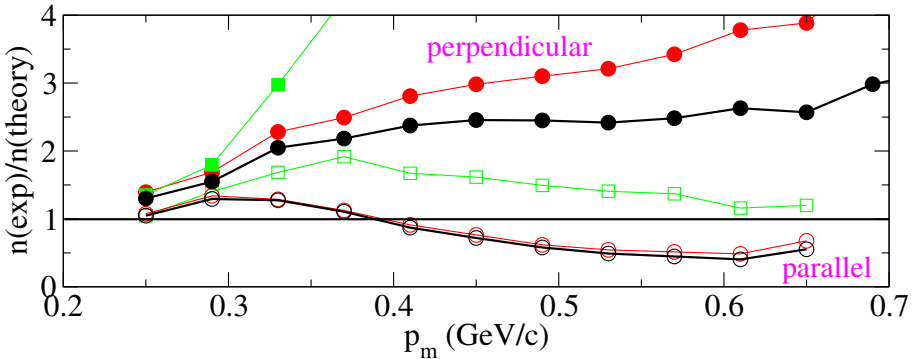


Figure 8.15: Ratio of the experimental and theoretical effective momentum distribution for parallel (open symbols) and perpendicular (filled symbols) kinematics. The thick black lines indicate the use of the  $\sigma_{cc}$  in the data analysis. Circles: CBF, squares: Green's function approach.

| kinematics    | experiment  | CBF theory | Green's function approach |
|---------------|-------------|------------|---------------------------|
| parallel      | 0.64 (0.61) | 0.64       | 0.46                      |
| perpendicular | 1.5 (1.25)  | 0.63       | 0.45                      |

Table 8.3: Strength in selected  $E_m p_m$ -region found in parallel and perpendicular kinematics compared to theoretical predictions. The numbers in brackets are obtained with  $\sigma_{cc}$ .

has to be compared to the value 0.64 for the CBF theory and 0.45 for the Green's function approach. The use of the cross section  $\sigma_{cc}$  leads to a slightly smaller result. Both theoretical predictions agree well with the data taken in parallel kinematics. One should keep in mind that this result depends on the integration limit chosen, due to the different shape of the experimental and theoretical spectral function. The strength found in perpendicular kinematics is a factor of 2–3 larger. The choice of the cross section  $\sigma_{cc}$  leads to a 20 % smaller result. The theoretical results for both kinematics differ slightly, because the integration region is different. The statistical error of the result is negligible.

The number of 0.64 protons in the correlated region, which corresponds to 10 % of the protons in  $^{12}\text{C}$  seems to be small at first sight. The reason: not the full  $E_m p_m$ -region is covered by the experiment. The distribution of the strength in the CBF spectral function as a function of  $E_m$  and  $p_m$  is shown in Fig. 8.16. 80 % of the strength is found in the single-particle region as it was already discussed in sec. 1. The strength induced by SRC is spread over

Figure 8.16: Distribution of the strength in the  $E_m p_m$ -region for the spectral function from the CBF theory. The numbers are the relative contribution of strength in the different regions. The pink area roughly indicates the integration region used to obtain the effective momentum distribution and the effective correlated strength.

a wide range in  $p_m$  and  $E_m$ , but most of it can be found at large  $p_m$ . The pink region indicates the area used in the integral of Eq. 8.4. It contains half of the strength in the full correlated region. From Fig. 8.16 it becomes also clear that the region of moderate  $p_m$  and large  $E_m$  is not suitable to search for SRC. Here only 1.5 % of the strength can be found.

From the discussion above it becomes obvious that the data in perpendicular kinematics are quite different from the one in parallel kinematics and contain much more strength, particularly at large  $p_m$ . However, at low  $p_m$  the distorted spectral functions from parallel and perpendicular kinematics agree well.

Because in perpendicular kinematics a significant amount of data was taken at small  $E_m$  this opens up the opportunity to compare these data to the IPSM prediction. Due to the moderate  $E_m$ -resolution it makes no sense to compare the experiment with the input theoretical spectral function directly. Because the Monte Carlo simulation was adjusted to reproduce the experimental resolution, the  $E_m$ -spectra of Monte Carlo and experiment can be compared. In Fig. 8.17 the experimental  $E_m$ -spectra in black are shown

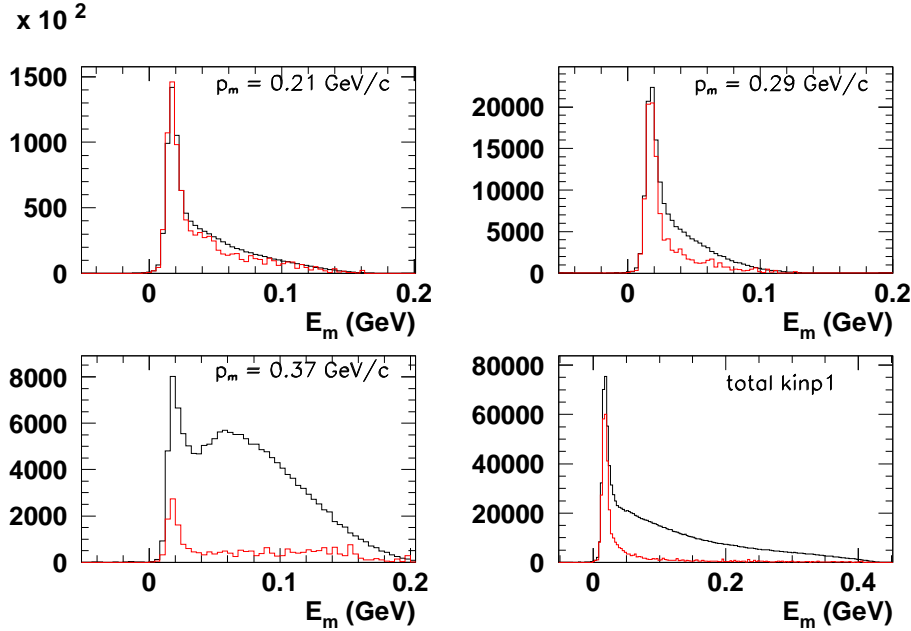


Figure 8.17:  $E_m$ -spectra for the  $^{12}\text{C}$  data (black) in perpendicular kinematics compared to the simulation using the spectral function from IPSM (red curve).

for three  $p_m$ -bins 210, 290 and 370 MeV/c. For the simulation (red) the pure IPSM spectral function for  $^{12}\text{C}$  (sec. 4.1.2) was taken, where no reduction factor accounting for SRC was applied. Further a transparency factor of 0.6 was used. Keeping this in mind the  $p_{3/2}$ -state predicted by the IPSM tends to be smaller than the data, but the overall agreement around the Fermi edge is reasonable. At  $p_m = 370$  MeV/c a large yield appears under the  $p_{3/2}$ -state, which can not be described by the IPSM. The same is true in the  $E_m$ -spectrum covering the total acceptance of kinematics kinp1 from 170 to 800 MeV/c.

## 8.5 Results for $^{27}\text{Al}$ , $^{56}\text{Fe}$ and $^{197}\text{Au}$

The distorted spectral functions obtained for the heavier nuclei Al, Fe and Au are shown in Fig. 8.18 to 8.23 for parallel and perpendicular kinematics. For the extraction of the distorted spectral function the off-shell cross section  $\sigma_{cc}$  was used. One can see that the agreement between the distorted spectral functions from the different data sets gets worse with increasing mass number. In particular for Au this becomes apparent. This is an indication that the contribution from other reaction mechanisms, whose strength depends

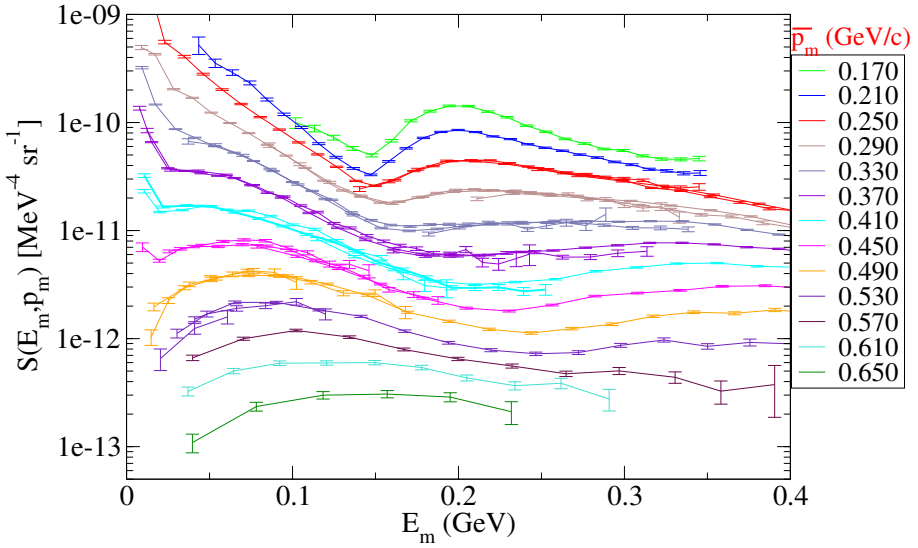


Figure 8.18: Distorted spectral function in parallel kinematics for  $^{27}\text{Al}$  obtained using  $\sigma_{cc}$ .

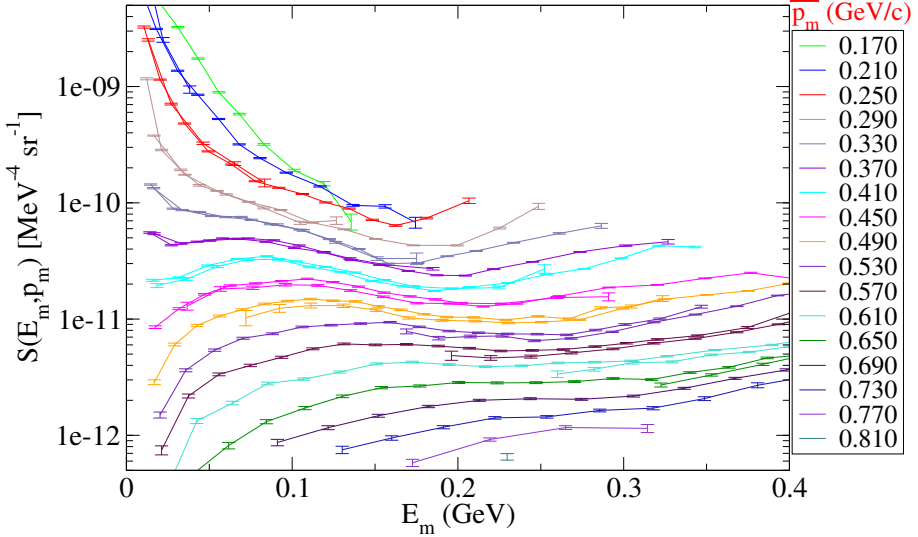


Figure 8.19: Distorted spectral function in perpendicular kinematics for  $^{27}\text{Al}$  obtained using  $\sigma_{cc}$ .

on the kinematical setting, increases. In addition the dip region between the correlated and the resonance region gets filled in, which is particularly apparent for the result for Au, but can be also observed for Fe. For Au the maximum of the distorted spectral function is shifted to larger  $E_m$ -values.

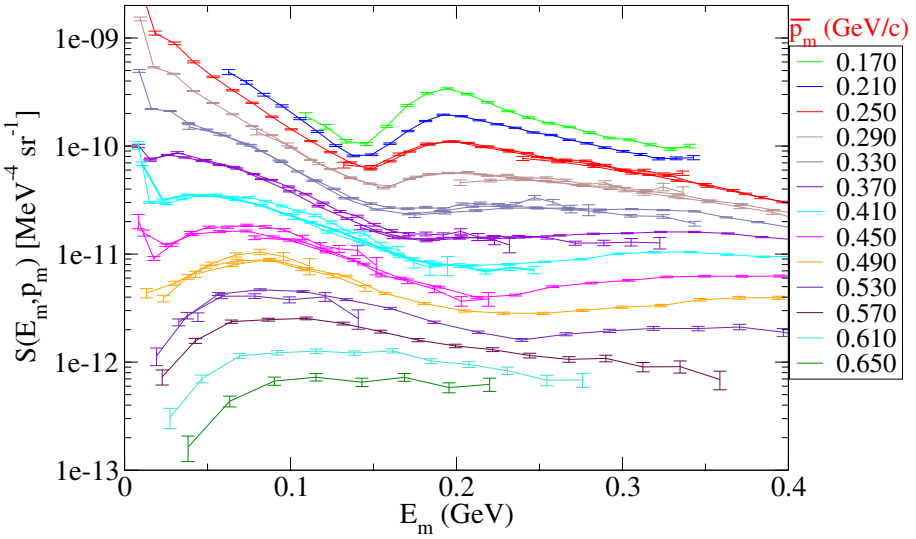


Figure 8.20: Distorted spectral function in parallel kinematics for  $^{56}\text{Fe}$  obtained using  $\sigma_{cc}$ .

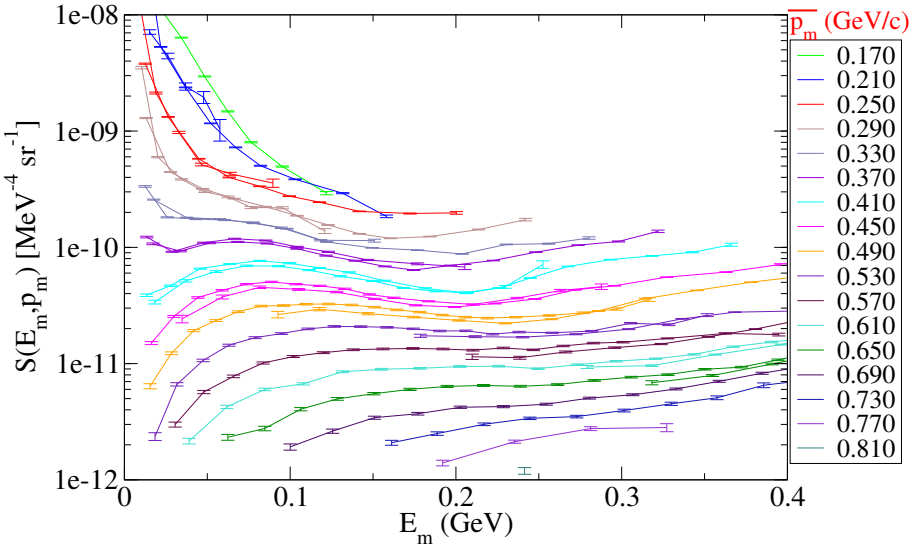


Figure 8.21: Distorted spectral function in perpendicular kinematics for  $^{56}\text{Fe}$  obtained using  $\sigma_{cc}$ .

This can explain the shift to large  $E_m$  of the maximum of the distorted spectral function measured in perpendicular kinematics. Apart from the filling of the dip region the shapes of the distorted spectral function obtained for the various nuclei are quite similar for the same kinematics.

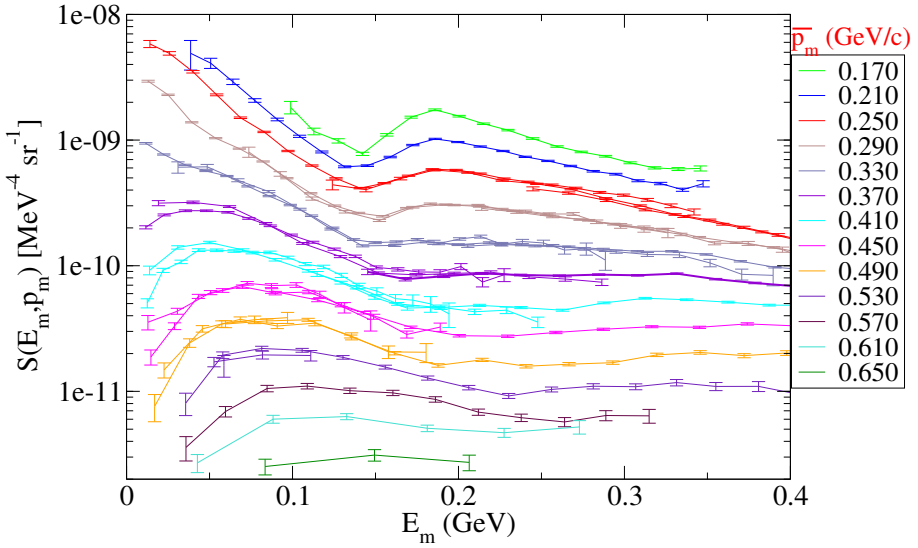


Figure 8.22: Distorted spectral function in parallel kinematics for  $^{197}\text{Au}$  obtained using  $\sigma_{cc}$ .

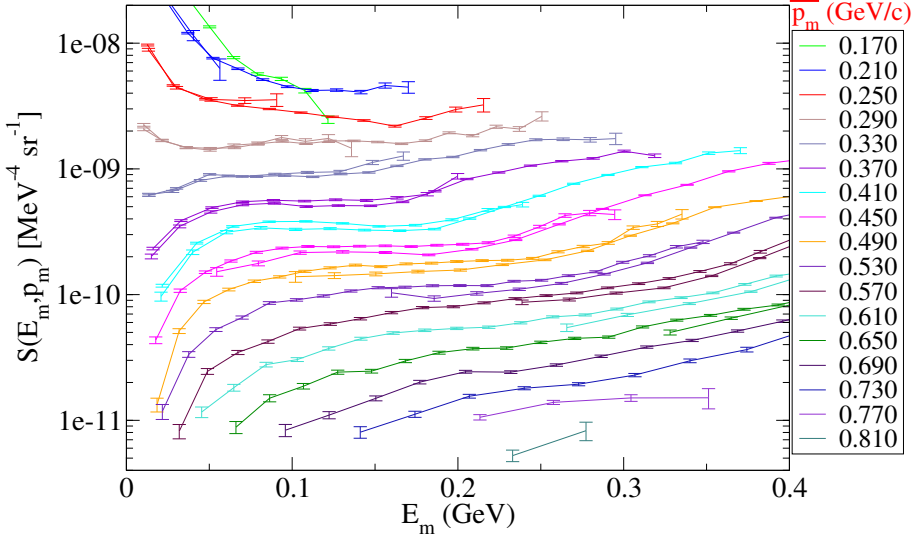


Figure 8.23: Distorted spectral function in perpendicular kinematics for  $^{197}\text{Au}$  obtained using  $\sigma_{cc}$ .

To compare the magnitude of the distorted spectral functions the results are divided by the number of protons in the nucleus. In Fig. 8.24 and 8.25 the normalized distorted spectral functions are shown for parallel and perpendicular kinematics and a few  $p_m$ -bins from 250 to 650 MeV/c. The

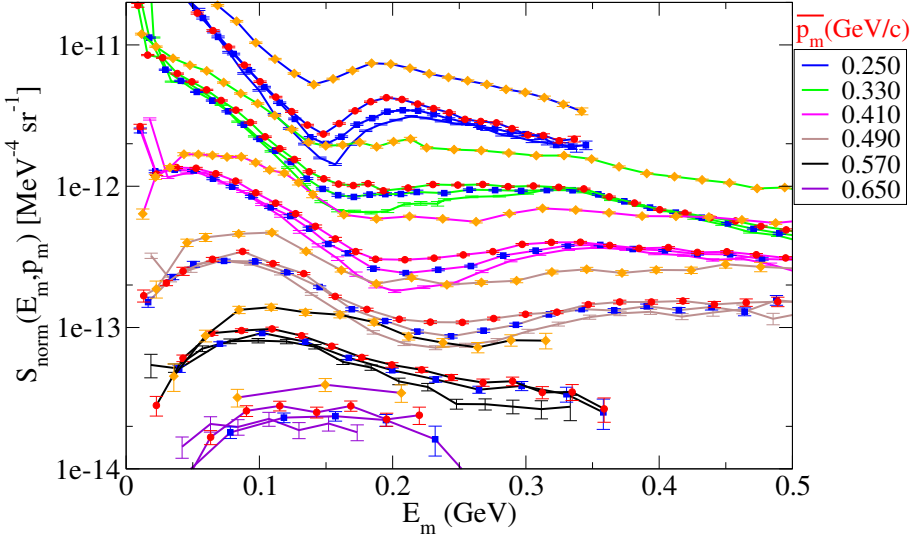


Figure 8.24: Comparison of the distorted spectral functions in parallel kinematics for C (solid line), Al (squares), Fe (circles), Au (diamonds). The spectral function is normalized to one proton.

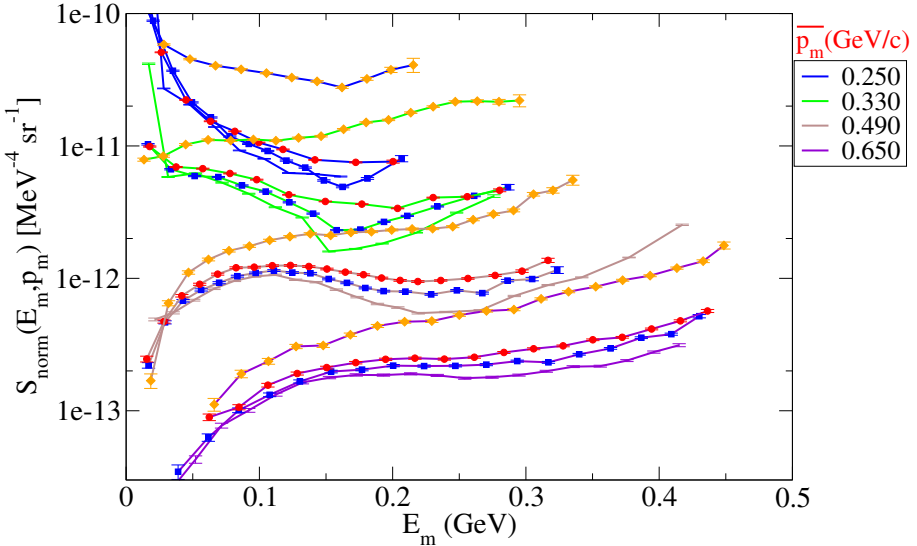


Figure 8.25: Similar figure as in 8.24 but for perpendicular kinematics.

solid line belongs to C, the symbols square, circle and diamond indicate Al, Fe and Au respectively. It is noteworthy that the results for C, Al and Fe agree quite well in the correlated region at moderate  $E_m$ . This is true for parallel as well as for perpendicular kinematics. The distorted spectral

function for Au shows a different behavior. In particular for moderate  $p_m$ , around 330 MeV, the magnitude of the distorted spectral function is much larger and the dip region is completely filled in perpendicular kinematics.

A better comparison of the magnitude of the distorted spectral function can be made via the correlated strength  $Z_C$  (Eq. 8.4) normalized to the number of protons in the nucleus. For all four nuclei the same integration region was chosen as described in sec. 8.4. The result were divided by the strength found for C in parallel and perpendicular kinematics, respectively. The result is shown in Fig. 8.26 and called spectral ratio. Circles (squares) indicate the result for parallel (perpendicular) kinematics. The spectral ratio is increasing with mass number in a linear way except for the Au-data in perpendicular kinematics, which seem to be affected strongly by the  $\Delta$  and higher resonances. The excess found in the heavier nuclei compared to C is approximately the same for parallel and perpendicular kinematics. This is surprising, because the rescattering is more pronounced in perpendicular kinematics and the correlated strength for carbon is three times larger than in parallel kinematics. One should keep in mind that these results were already corrected by the transparency factor to account for absorption. On the other hand the transparency factor does not take into account details of the kinematics. According to calculations of [17] (sec. 8.6) contributions from single-particle states, i.e. the mean field part of the spectral function, influences the correlated region due to rescattering for the heavier nuclei. In addition, it is also possible that due to the increasing number of pn-pairs in neutron rich heavy nuclei the contribution from tensor correlations is significantly enhanced. Further one should keep in mind that the equation of state for symmetric nuclear matter is quite different for pure neutron matter [4], which does not exhibit a minimum. In order to identify the effect for  $N > Z$ , one will need a calculation of the spectral function.

## 8.6 Rescattering contribution

The leading term of the final state interaction is due to rescattering, where the primary  $(e,e'N_1)$  process is followed by a second reaction  $N_2(N_1,pN_2')$  on a nucleon  $N_2$  in the same nucleus. Such a process can not be distinguished from the pure  $(e,e'p)$ -reaction in the experiment and leads to a misleading reconstruction of  $E_m$  and  $p_m$ . The distorted spectral function has to be corrected for this contribution by a theoretical calculation. Such a calculation was done by C. Barbieri in a semiclassical model, which is based on the work of [19]. In the following section the basic idea of the calculation of the rescattering contribution is given. The results obtained for the kinematics of

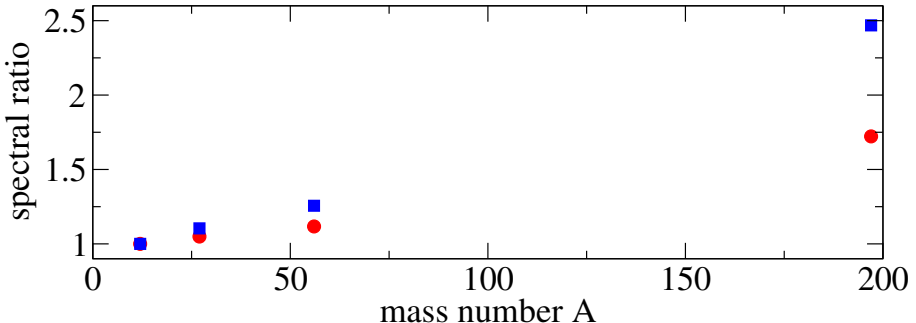


Figure 8.26: Ratio of the correlated strength for the four nuclei normalized to the result for C. The squares (circles) belong to perpendicular (parallel) kinematics.

the present experiment are presented and discussed with respect to the data.

### 8.6.1 Framework of the rescattering calculation

This approach considers a two-step process and uses Glauber theory to account for the interaction of the propagating nucleons in the nuclear medium. For free p-p and p-n scattering cross section is shown in Fig. 8.27. At proton momenta larger than 1 GeV/c the inelastic channel opens up and finally dominates for increasing momenta. In the nuclear medium the N-N cross section gets modified due to Pauli blocking and the velocity dependence of the nuclear mean field (dispersion effect). Pauli principle requires that both of the reaction partners need a momentum larger than the Fermi momentum to leave the nucleus. This modifies the cross section for momenta less than 500 MeV/c. The in-medium cross section for N-N scattering  $(\sigma_{pp} + \sigma_{pn})/2$  was calculated by [143] and is shown in Fig. 8.28 (lower blue curve). It is compared to the free N-N cross section. For large energies the cross section is damped by  $\approx 20\%$ . The behavior of the cross section is in agreement with the one for p-N scattering extracted from the measurement of the transparency factors [75], where after a steep increase a nearly constant cross section of around 31 mb is found for kinetic energies larger than 0.7 GeV.

In the present approach a fully relativistic calculation following [160] was performed to obtain the in-medium cross section. In this approach a vector and scalar Dirac potential  $U_V$  and  $U_S$  is used to account for the interaction with the medium. This is equivalent to the approach using an effective mass [143] as it has been discussed by ref. [89]. It was checked that the result for low momenta agrees with [143]. At higher momenta as needed

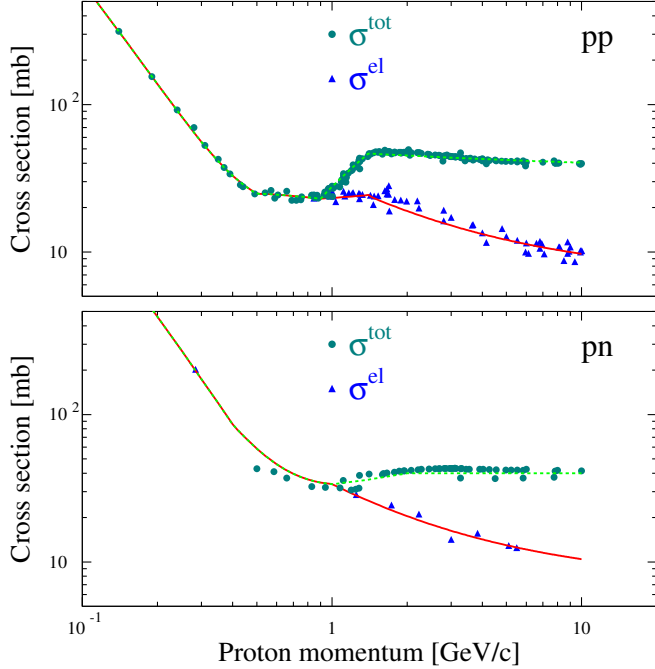


Figure 8.27: Free total p–p and p–n cross section as a function of the proton momentum. The data points are taken from [145] and the curve is a fit of [157]. The lower curve corresponds to the elastic cross section.

for this experiment the behavior of the scalar and vector potential  $U_S$  and  $U_V$  is not known. Because with increasing energy of the outgoing proton the surrounding nuclear medium becomes less important,  $U_S$  and  $U_V$  were neglected. The Pauli blocking is kept when calculating the in–medium cross section. The spectral distribution of the hit nucleon  $N_2$  is assumed to be the one for a free Fermi gas. The in–medium cross section is then obtained from the on–shell values for the scattering amplitude, which were extracted from the free scattering cross section generated from SAID.

The two–step process is schematically shown in Fig. 8.29. So far no excitation of one of the nucleons is considered here, so that the intermediate particle  $N_1$  with momentum  $p_{N_1}$  is either a neutron or a proton. The cross section for the two–step process can be written as

$$\frac{d^6 \sigma_{res}}{dE'_e d\Omega_e dE'_p d\Omega_{p'_f}} = \int_V d\vec{r}_1 \int_V d\vec{r}_2 \int_0^\omega dT_{N_1} \rho_{N_2}(\vec{r}_1) \frac{K S(E, k) \sigma_{cc1}}{A (\vec{r}_1 - \vec{r}_2)^2} g_{N_1 N'_2}(\vec{r}_1, \vec{r}_2)$$

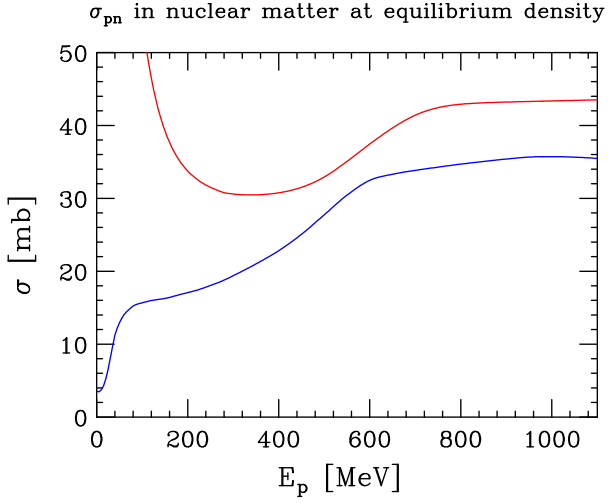


Figure 8.28: Total in–medium N–N cross section  $(\sigma_{pp} + \sigma_{pn})/2$  as obtained by [143] compared to the free N–N cross section (upper curve).

$$\times P_T(p_{N_1}, \vec{r}_1, \vec{r}_2) \rho_{N'_2}(\vec{r}_2) \frac{d^3 \sigma_{N'_2 N'_2}}{dE_f d\Omega_{\hat{p}_f}} P_T(p'_f, \vec{r}_2, \infty) \quad (8.5)$$

Here  $(E'_p, p'_f)$  is the energy and momentum of the detected proton. In the calculation the cross section  $\sigma_{cc1}$  is used and the primary  $(e, e' N_1)$  process is described by the factorized ansatz valid in PWIA (Eq. 1.6). After this the intermediate nucleon  $N_1$  propagates with probability  $P_T(p_{N_1}, \vec{r}_1, \vec{r}_2)$  from  $\vec{r}_1$  to  $\vec{r}_2$ , where it hits another nucleon  $N_2$ . The probability to find two nucleons at  $\vec{r}_1$  respectively  $\vec{r}_2$  is given by the pair distribution function  $g_{N_1 N'_2}(\vec{r}_1, \vec{r}_2)$ . The density distribution of the nucleons is given by  $\rho_N$ . After the second scattering process  $N_2(N_1, p_f N'_2)$  the final proton has to leave the nucleus with a propagation probability  $P_T(p_f, \vec{r}_2, \infty)$ . For this scattering process the in–medium cross section discussed above is used.

Note that for the rescattering calculation the differential in–medium cross section is needed whereas the propagation probability is obtained from the total in–medium cross section as a function of density. The propagation probability was calculated up to  $T_p = 300$  MeV using correlated Glauber theory by ref. [143] with an in–medium cross section. It was extended to higher energies by accounting for pion emission in the cross section. But the cross section is systematically too low, because it does not account for the full inelasticity. The propagation probability is directly related to the nuclear

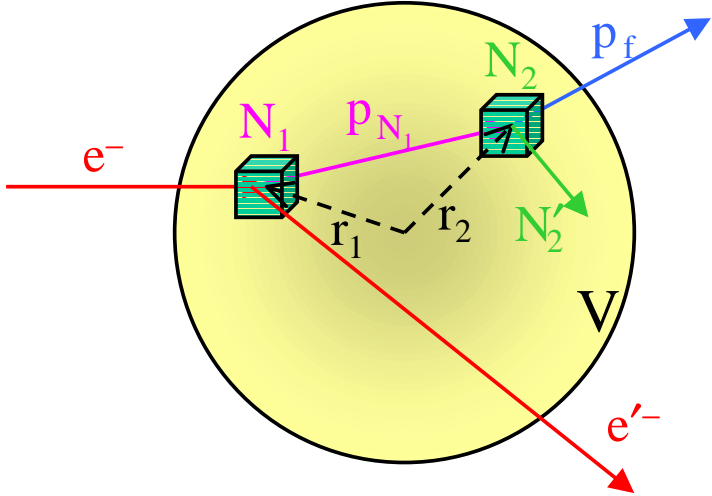


Figure 8.29: Schematic view of the two-step rescattering process. The momentum  $p_2$  of the second scattering partner  $N_2$  is not shown.

transparency by

$$T_A = \frac{1}{Z} \int d\vec{r} P_T(p, \vec{r}, \infty). \quad (8.6)$$

For protons with  $T_p \approx 1.8$  GeV a nuclear transparency of 0.63 for  $^{12}\text{C}$  and 0.29 for  $^{197}\text{Au}$  is obtained, which is in reasonable agreement with the experimental results (s. e.g. Fig. 7.3).

The integration in Eq. 8.5 is performed over the volume  $V$  of the nucleus for both nucleons as well as over the kinetic energy  $T_{N_1}$  of the first struck nucleon  $N_1$ . This is done by Monte Carlo techniques. To calculate the cross section according to Eq. 8.5 a spectral function as input is needed. For this the spectral function was split into a mean field and a correlated part. For  $^{12}\text{C}$  the normalization for the two single-particle states was taken from the mean of several experiments summarized in [104]. The correlated part for  $p_m \geq 200$  MeV/c was taken from a fit to the result of the present experiment measured in parallel kinematics on  $^{12}\text{C}$ . For this the spectral function was fitted with the function

$$S_{corr}(E_m, p_m) = \frac{C e^{-\alpha p_m}}{[E_m - e(p_m)]^2 + [\Gamma(p_m)/2]} \quad (8.7)$$

where  $e(p_m)$  and  $\Gamma(p_m)$  are smooth functions of  $p_m$ . The fit region was restricted to the correlated region and the region of pion-electroproduction was disregarded. The resulting spectral function for  $^{12}\text{C}$ , which enters the calculation, is shown as solid line in Fig. 8.30.

To calculate the rescattering contribution for data taken with the Au-target the correlated part obtained via Eq. 8.7 for  $^{12}\text{C}$  is scaled according to the number of protons in these nuclei. The mean field part is taken from a measurement at NIKHEF [151] [19] on  $^{208}\text{Pb}$ , which reaches missing energies up to 110 MeV and so also includes some of the background strength from SRC.

### 8.6.2 Results and comparison with experiment

To compare the theoretical result to the data it is divided by  $|p'_p E'_p| T_A \sigma_{cc1a}$  and then added to the input spectral function. The so obtained distorted spectral function  $S_{resc}(E_m, p_m)$  (dashed line) is shown together with the experimental data points in Fig. 8.30 for parallel kinematics and  $^{12}\text{C}$ . In the correlated region for moderate  $E_m$  the input spectral function (solid line) is nearly indistinguishable from the distorted one. Only for very large  $E_m$  and  $p_m$  the rescattering contribution becomes non-negligible. This confirms that rescattering does not play a major role in parallel kinematics.

The same calculation, but now for perpendicular kinematics, is shown in Fig. 8.31. Here a much larger influence of rescattering even at small  $E_m$  is observed, which was already expected from kinematical considerations discussed in the proposal of this experiment [163]. The shape of the experimental result can be approximately explained with the filling of the dip region due to rescattering, but the contribution from rescattering alone can not explain the large strength found in the data. This might be a hint on other reaction mechanisms not yet included in the calculation, like isobar configurations and the  $\Delta$ -resonance excitation in combination with rescattering and MEC. In Fig. 8.32 the calculated distorted spectral function for parallel and perpendicular kinematics is directly compared for  $^{12}\text{C}$ . The different influence due to rescattering is obvious.

Fig. 8.33 and 8.34 show the calculation performed for  $^{197}\text{Au}$  in parallel and perpendicular kinematics. For this calculation the same input spectral function as for  $^{12}\text{C}$  was used for the correlated part except for a scale factor accounting for the number of protons in  $^{197}\text{Au}$ . The rescattering contribution found in parallel kinematics is negligible in the correlated region and increases for large  $E_m$  with respect to the calculation performed for  $^{12}\text{C}$  (s. also Fig. 8.35). Rescattering alone can not explain the increase of the effective correlated strength by a factor of 1.7 seen for  $^{197}\text{Au}$  compared to  $^{12}\text{C}$  (Fig. 8.26). Other effects have to be accounted for. The treatment of MEC is not included in the theory yet. However, calculations of Laget performed for  $^4\text{He}$  for the kinematics of E97-111, which are comparable to the one in the present work, show that the contribution of MEC to the data in parallel

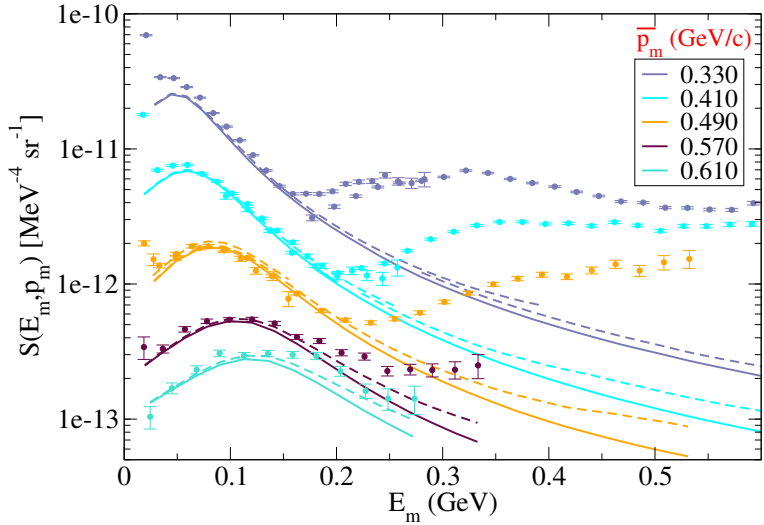


Figure 8.30: Distorted spectral function  $^{12}\text{C}$  in parallel kinematics (dots) compared to rescattering calculation (dashed line) for a few  $p_m$ -bins. The solid line is the spectral function used as input for Eq. 8.5.

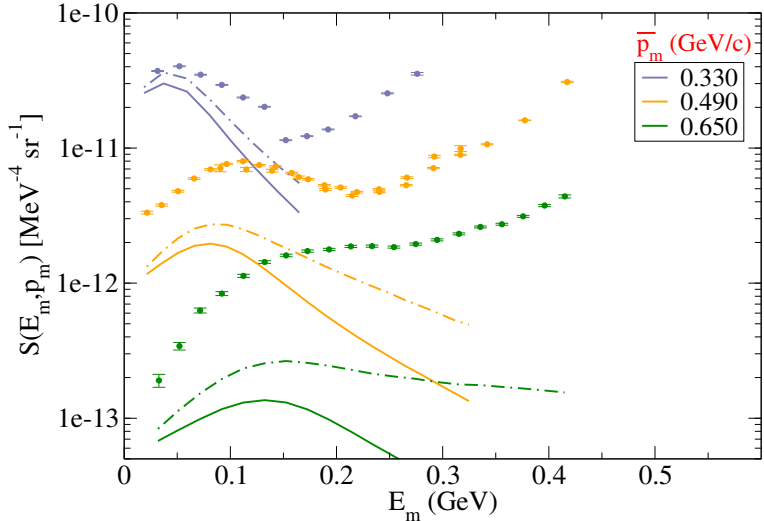


Figure 8.31: Similar to Fig. 8.30 but for perpendicular kinematics. The result of the rescattering calculation is indicated by the dashed-dotted line.

kinematics is negligible [154]. In contrast, there is considerable contribution due to MEC and IC in non-parallel kinematics. This might be due to the transversal character of the MEC contribution.

Another effect which could increase the strength of the spectral function

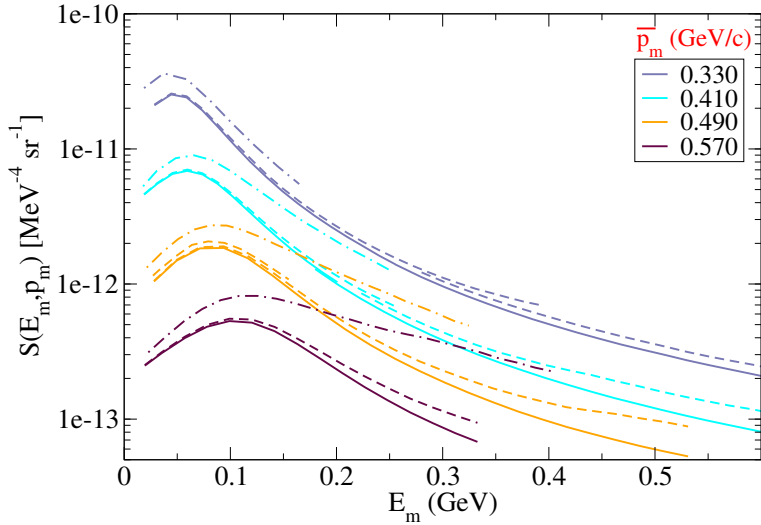


Figure 8.32: Direct comparison of the spectral function for  $^{12}\text{C}$  from the rescattering calculation for parallel (dashed) and perpendicular kinematics (dashed-dotted).

in  $^{197}\text{Au}$  compared to  $^{12}\text{C}$  is the increase of the neutron to proton ratio in heavy nuclei. Due to the strong tensor force between neutrons and protons more strength could be shifted to large  $E_m$  and  $p_m$ . The many-body theories of [128] and [20] treating short-range and tensor correlations are considering only symmetric nuclei and nuclear matter, respectively.

As can be seen from Fig. 8.36 the contribution from rescattering in perpendicular kinematics for  $^{197}\text{Au}$  is much larger than in parallel kinematics and exceeds also the one in perpendicular kinematics for  $^{12}\text{C}$ . As for the case of  $^{12}\text{C}$  the data still exceed the result of the rescattering calculation. At the highest  $p_m$ -bin shown in Fig. 8.34 for  $^{197}\text{Au}$  the dip region is completely filled by more than an order of magnitude due to rescattering. This is the mechanism, which shifts the maximum of the distorted spectral function to higher  $E_m$ .

It should be noted that in contrast to  $^{12}\text{C}$  the rescattering calculation for  $^{197}\text{Au}$  is sensitive to the mean field part of the spectral function. The reason is that for  $^{197}\text{Au}$  the mean field part shows strength up to  $E_m = 100$  MeV. It was found that strength between  $E_m = 40$  Mev and 100 MeV contributes to the correlated region up to  $p_m = 450$  MeV/c via rescattering. In  $^{12}\text{C}$  most of the strength in the IPSM region is located below 40 MeV and therefore its contribution is small. This was tested with a calculation, which sets the mean field part to zero.

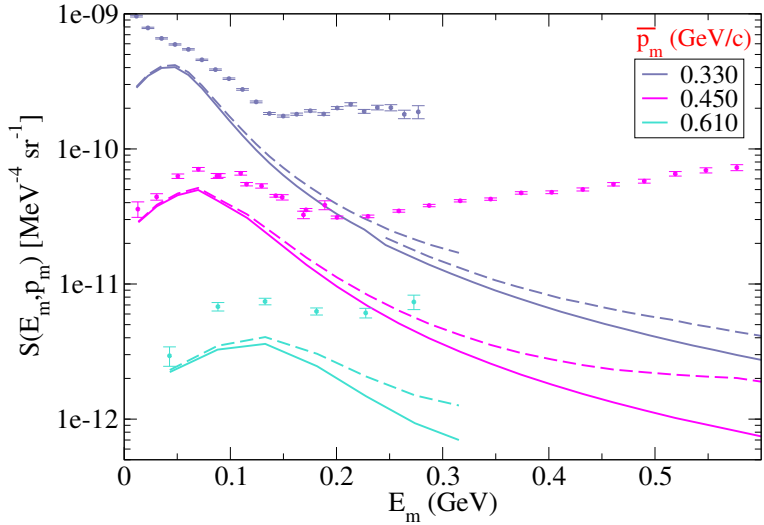


Figure 8.33: Similar to Fig. 8.30 but for  $^{197}\text{Au}$ .

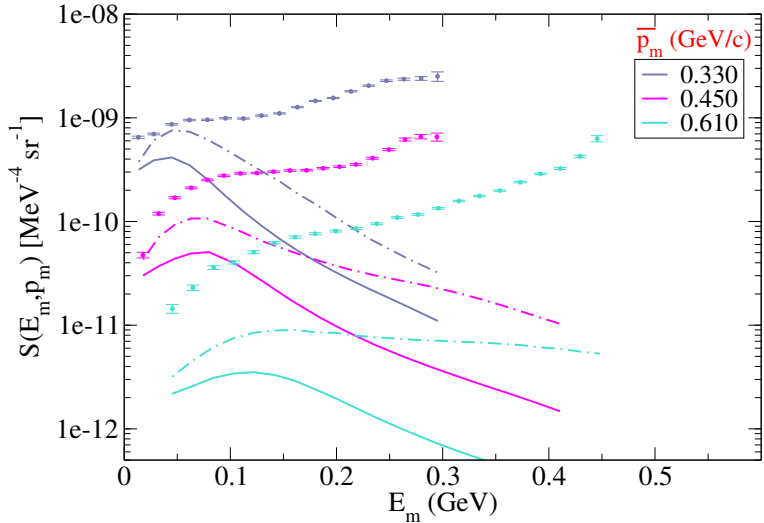


Figure 8.34: Similar to Fig. 8.33 but for perpendicular kinematics.

### 8.6.3 Discussion of possible multi-step processes

While the rescattering calculation is quite successful in general, it does not work well for perpendicular kinematics. The failure of the rescattering calculation in perpendicular kinematics is not new. Ref. [167] tried to explain the data for  $^{12}\text{C}$  measured in the single-particle region [107] by two-body rescattering. It was found that the contribution from two-step processes is very

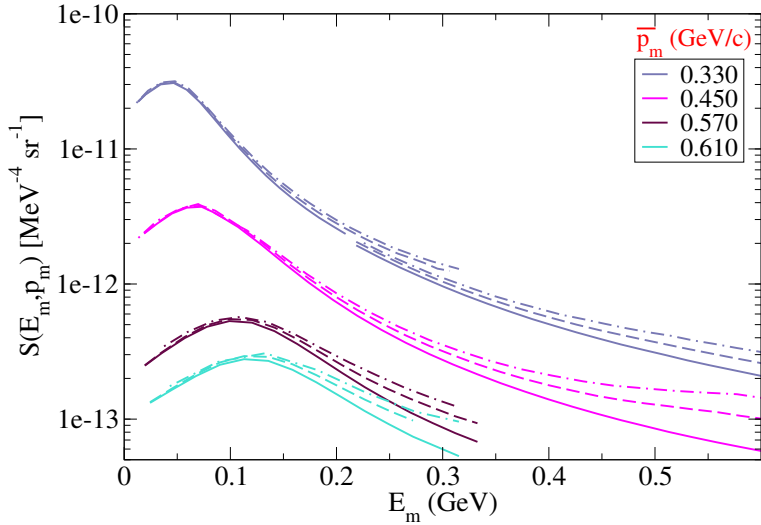


Figure 8.35: Comparison of the spectral functions with the calculated rescattering contribution for  $^{12}\text{C}$  (dashed) and  $^{197}\text{Au}$  (dashed-dotted) in parallel kinematics.

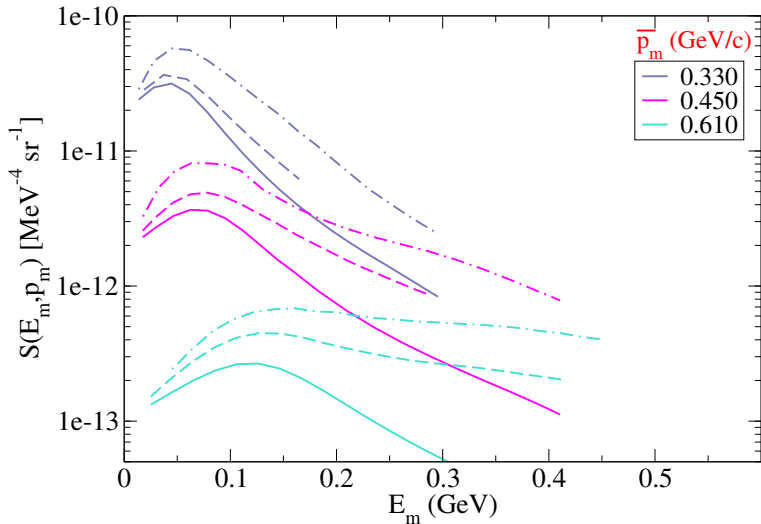


Figure 8.36: Similar to Fig. 8.35 but for perpendicular kinematics.

small (8 %) compared to the data. Many-body mechanisms were suggested to solve the discrepancy. It was found from kinematical considerations that three-body processes should contribute.

In ref. [48] important contributions from two- and three-step processes to  $^{40}\text{Ca}(e,e'p)$  data [125] are found. The increasing importance of two-, three-

and four-step processes with increasing angle  $(\vec{q}, \vec{p}_p)$  is nicely demonstrated. Calculations were performed for kinematics with small kinetic energy of the outgoing proton (around 100 MeV), where FSI are expected to be more important. On the other hand one should not forget that although proton kinetic energy  $T_p$  in the perpendicular kinematics of the present experiment is higher ( $T_p = 0.3$  and  $0.4$  GeV), it is much lower than in parallel kinematics ( $T_p = 0.6 \dots 1$  GeV).

In ref. [137] a Glauber calculation for multiple-step processes was performed. For  $^{12}\text{C}$  the average number of rescattering  $\nu$  is only 0.5 whereas for lead it increases to 2. These results were recently confirmed by an extended relativistic Glauber theory [157]. Further it was observed that higher-order terms in the nuclear interior contribute with the opposite sign and therefore suppress FSI. This would be an explanation for the overestimation of the distortion due to the two-step process alone in  $^{197}\text{Au}$ .

In the work of [123] this observation is confirmed by a Glauber multiple scattering approach for  $^4\text{He}(\text{e},\text{e}'\text{p})$  using realistic four-body variational wave functions. Here the contribution from double rescattering amounts to  $-14\%$  of the leading order term. Further it was found that due to the inclusion of ground state correlations the role of FSI is considerably suppressed. The effect of FSI in parallel kinematics ( $T_p \approx 1$  GeV) on the momentum distribution was found to lead to a reduction of about  $20\%$  with respect to PWIA for low and high momentum components. For medium momenta  $k$  around 300 MeV/c the momentum distribution affected by FSI exceeds slightly the one from PWIA according to their calculation. For antiparallel kinematics the influence of FSI is similar but larger. In particular for large momenta a reduction of a factor of two is predicted. In perpendicular kinematics the momentum distribution for  $k > 400$  MeV/c, influenced by FSI, exceeds the PWIA calculation by a factor 3 to 4. These results, even though calculated for  $^4\text{He}$ , are qualitatively in agreement with the findings of the present work.

## 8.7 The resonance region

Due to the higher energy transfer in parallel kinematics (Tab. 1.1) and the large momentum acceptance of the spectrometers the resonance region is included in the data. The invariant mass  $W$  reaches from 1.2 to 2 GeV and thus covers the first, the second and the third resonances, which decay mainly to a nucleon plus one or more light mesons. Experiments investigating the resonance region usually detect the outgoing mesons. For  $(\text{e},\text{e}'\text{p})$  and hydrogen as target one can reconstruct the kinematics of the non-detected meson in an unique way. In the present work the detected proton is knocked-

out from a nucleus. Therefore the resonance excitation, which starts at  $E_m$  larger than the pion mass ( $\approx 150$  MeV), can not be separated from the tail of the quasi-elastic peak at high  $E_m$ . No explicit information on the resonance region can be gained from these data, but existing models can be tested. The resonance region was simulated with a modified version of the HallC Code SIMC assuming single-pion production, although above the  $\Delta$ -resonance two-pion production becomes more important for increasing invariant mass and  $E_m > 300$  MeV.

The cross section for single-pion production is obtained from the unitary isobar model MAID [55][54][113]. This model gives a good description of pion-photoproduction on hydrogen. For electroproduction a  $Q^2$  dependence of the photon coupling parameters has to be introduced. Because of the scarce data set some amplitudes have large uncertainties (50 %). For pion production on the neutron the situation is even worse. Further, for nuclei final state interaction and medium effects can become important. Keeping this in mind it is not expected to get a perfect agreement between data and MAID.

In the following the formalism for the electroproduction of pions on nuclei and the MAID-model will be described. Then the results will be presented in terms of its contribution to the  $E_m$ - and  $p_m$ -distributions, which are most relevant for the extraction of the spectral function. Finally cuts to reduce or partly eliminate the resonance region from the data set are discussed.

### 8.7.1 Formalism for pion-electroproduction

Because the formalism was originally developed for photoproduction on hydrogen in the  $\gamma$ -proton center of mass (cms) system it has to be modified for electroproduction. To keep the analogy to the case of real photons the cross section for the reaction

$$e + p = e' + p' + \pi \quad (8.8)$$

is usually written as (Hand convention [87])

$$\frac{d\sigma}{d\Omega_e dE'_e d\Omega_\pi^*} = \Gamma_v \frac{d\sigma_v}{d\Omega_\pi^*}, \quad (8.9)$$

where the factor

$$\Gamma_v = \frac{\alpha}{2\pi^2} \frac{E'_e}{E_e} \frac{K_{eq}}{Q^2} \frac{1}{1-\epsilon} \quad (8.10)$$

can be interpreted as the flux of virtual photons. Here  $K_{eq}$  is the so called equivalent photon energy, i.e. the energy, which is required to excite a nucleon

to (invariant) mass  $W$  using real photons. Its definition will be given below. The quantity  $\epsilon$  is a measure for the transverse polarization and defined as

$$\epsilon = \left[ 1 + 2 \frac{|\vec{q}|^2}{Q^2} \tan^2 \frac{\theta}{2} \right]^{-1}. \quad (8.11)$$

The star in Eq. 8.9 denotes the  $\gamma$ -p cm-system and  $d\sigma_v/d\Omega_\pi^*$  is the virtual photon cross section in the cm-system. For bound nucleons the momentum of the pion  $p_\pi$  is not fixed by kinematical constraints and the 5-fold differential cross section in Eq. 8.9 is replaced by a 6-fold cross section. In order to use the cross section in the Monte Carlo simulation it has to be transformed from the  $\gamma$ -p center of mass system to the lab frame, where the nucleus is at rest. As the bound nucleon is moving in the nucleus with momentum  $k$  its energy is not uniquely defined (off-shell). One can consider two definitions of the energy for the nucleon

$$E_N(1) = \sqrt{M_N^2 + k^2} \quad (8.12)$$

$$E_N(2) = M_T - \sqrt{M_{rec}^2 + k^2}. \quad (8.13)$$

In the first equation the off-shell nucleon is put on-shell. This resembles the case of scattering on a free nucleon, for which the cross section  $d\sigma_v/d\Omega_\pi^*$  obtained from MAID is valid. The second choice is the kinematically correct version. The mass of the recoil system accounts also for the missing energy and is obtained from

$$M_{rec} = M_T + E_m - M_N. \quad (8.14)$$

Here  $M_T$  and  $M_N$  are the mass of the target nucleus and the struck nucleon respectively. The effect of both definitions on the result will be investigated.

The kinematics is determined from the energy and momentum conservation

$$E_e + M_T = E'_e + E'_p + E'_\pi + E_R \quad (8.15)$$

$$\vec{k}_e = \vec{k}'_e + \vec{p}'_p + \vec{p}'_\pi + \vec{p}_R. \quad (8.16)$$

The momentum  $\vec{p}_R$  of the recoil system with mass  $M_{rec}$  is set to the opposite of the initial momentum of the nucleon. Initial momentum  $k$  and energy  $E$  are distributed according to the correlated spectral function of Benhar with a properly weighted single-particle part (sec. 1.2.7). Except for a small tail  $k$  is less than 300 MeV/c and  $E$  less than 80 MeV, i.e. most nucleons are from the single-particle region and the simulation is hardly sensitive to the correlated part of the spectral function.

When transforming the kinematics calculated via Eq. 8.15 into the  $\gamma$ -p cm-system, one assumes that the reaction occurred on a free moving nucleon. This leads to momenta of the proton and pion in the cm-system, which are not exactly opposite to each other. The difference in the momenta of  $\approx 500$  MeV is around 10 MeV and the angle mismatch about  $1^\circ$ . Because the cross section is a smooth function of the angle, the error introduced is negligible compared to the model dependent uncertainties.

The cross section  $d\sigma_v/d\Omega_\pi^*$  is decomposed into the longitudinal and transverse response function

$$\frac{d\sigma_v}{d\Omega_\pi^*} = \frac{p_\pi^*}{K_{eq}^*} [R_T + \epsilon R_L + [2\epsilon(1+\epsilon)]^{1/2} R_{LT} \cos \phi_\pi^* + \epsilon R_{TT} \cos 2\phi_\pi^*] \quad (8.17)$$

The factor in front of the squared brackets is the phase space factor in the cm-system after the Hand convention [87]. Note, that here the longitudinal polarization  $\epsilon_L = Q^2/(\omega^*)^2\epsilon$  is not written in front of the longitudinal and longitudinal-transverse term but included in the response functions to be consistent with the convention used in MAID. The longitudinal-transversal and transversal-transversal part of the cross section depend on the out-of-plane angle  $\phi_\pi^*$  of the pion in the cm-system. The equivalent photon energy  $K_{eq}$  corresponds to the photon energy  $\omega$  at  $Q^2 = 0$  for a given invariant mass  $W$ . For a hydrogen target the following relation is valid

$$K_{eq} = \frac{W^2 - M_N^2}{2M_N} = \frac{W}{M_N} K_{eq}^*. \quad (8.18)$$

If the nucleon is bound, it moves with momentum  $k$  and an (off-shell) mass  $M_N^* = \sqrt{E_N^2 - k^2}$ . One then obtains

$$K_{eq} = \frac{W^2 - (M_N^*)^2}{2(E_N - k \cos \theta_{kq})} = \frac{W}{E_N - k \cos \theta_{kq}} K_{eq}^*. \quad (8.19)$$

Using Eq. 8.17 only the ratio  $K_{eq}/K_{eq}^*$  appears in the cross section of Eq. 8.9. The factor  $1/(E_N - k \cos \theta_{kq})$  plays the role of the correction to the flux factor due to the moving reaction partner.

The response functions needed in Eq. 8.17 are reconstructed from the CGLN-amplitudes<sup>3</sup> [41], which are taken from the MAID Webpage as a function of  $W$  for a grid in  $Q^2$  and  $\theta_{cm}$ . Here  $\theta_{cm}$  is the scattering angle of the pion in the cm-system. The CGLN-amplitudes are interpolated in  $W$ ,  $Q^2$  and  $\theta_{cm}$  from a look-up table.

---

<sup>3</sup>More precisely the response functions in the simulation are obtained from the helicity amplitudes, which are calculated from the CGLN-amplitudes. These can be decomposed into the electromagnetic multipoles [54][55].

It is important to note that the CGLN-amplitudes for two elementary processes are contributing to the resonance region. Pion production can take place on a proton or neutron in the nucleus

$$e + p = e' + p' + \pi^0 \quad (8.20)$$

$$e + n = e' + p' + \pi^- . \quad (8.21)$$

In both cases a proton will be detected. Both processes were simulated separately and then added.

### 8.7.2 The MAID-model

In the unitary isobar model MAID pion production is decomposed into a non-resonant (B) and a resonant (R) term. These terms are separately unitarized. The non-resonant contribution (background) is calculated from Born terms in the s, t, and u-channel, the contact term as well as Feynman diagrams containing  $\omega$  and  $\rho$  exchange in the t-channel. For the Born terms an energy dependent superposition of pseudovector (PV) and pseudoscalar (PS)  $\pi NN$ -coupling (hybrid model) is used. In the threshold region the PV-coupling is preferred, because it is consistent with the low energy theorem and chiral perturbation theory. At higher energies the PS-coupling leads to better results. The Born term contribution dominates over the one from the  $\omega$  and  $\rho$  exchange diagrams. The coupling constants and cut-off parameters for the  $\omega$  and  $\rho$  exchange are taken as free parameters. The free parameters and the parametrization of the  $\pi NN$ -coupling are fixed by non-resonant multipole data. The background part is unitarized in the K-matrix approach using the phase shifts  $\delta_{\pi N}$  from  $\pi N$  scattering. To account for inelastic contributions the inelasticity  $\eta$  is introduced. The parameter  $\delta_{\pi N}$  and  $\eta$  are taken from the VPI-analysis (SAID program) [8]. Contrary to the dynamical (DMT) model off-shell rescattering contributions are not included in MAID [95].

The bare resonances are parametrized as Breit-Wigner shapes with a phase  $\phi(w)$ , which is adjusted such that the phase of the total multipole (resonance plus background) is equal to the corresponding  $\pi N$  phase shift. For the higher resonances, where reliable information about the scattering phases is missing, the phase is taken as constant and is fitted at the position of the resonance. This is required by the Fermi-Watson theorem under the assumption that the inelastic channels are negligible. The total width  $\Gamma_{tot}$  of each resonance is assumed to be the sum of the widths from the  $\pi N$  and  $2\pi N$  channel. In MAID2000 the strength of the resonances is given by amplitude factors  $A^R(Q^2)$  taken at the mass of the resonances. They are called the electric, magnetic and longitudinal multipole photon couplings,

respectively. Except for the two lowest resonances the longitudinal part is neglected in MAID2000. In the kinematics of interest here the longitudinal coupling is small. In the MAID2003 the strength of the resonance is directly proportional to helicity photon couplings  $A_{1/2}$ ,  $A_{3/2}$  and  $S_{1/2}$ , which are defined at the resonance position  $W = M_R$ . They can be written as linear combinations of the multipole photon couplings. The amplitudes  $A_{1/2}$  and  $A_{3/2}$  describe the excitation of nucleons into resonant states with  $J_z = 1/2$  and  $3/2$  respectively via the absorption of a transverse photon whereas  $S_{1/2}$  requires longitudinal photons. Using recent data from Mainz, Bonn, Bates and Jlab for the reaction  $(p,p \pi^0)$  a first attempt was made to extract the amplitudes for all four-star resonances below  $W = 2$  GeV [169]. These are  $P_{33}(1232)$ ,  $P_{11}(1440)$ ,  $D_{13}(1520)$ ,  $S_{11}(1535)$ ,  $S_{31}(1620)$ ,  $S_{11}(1650)$ , [ $D_{15}(1675)$ ],  $F_{15}(1680)$ ,  $D_{33}(1700)$ , [ $P_{13}(1720)$ ], [ $F_{35}(1905)$ ], [ $P_{31}(1910)$ ], [ $F_{37-}(1950)$ ]. They are classified according to the spectroscopic notation  $l_{2I2J}(W)$ , where  $l$  is the orbital angular momentum of the pion decay channel,  $J = l \pm 1/2$  the total spin,  $I$  the isospin of the resonance. The resonances written in parentheses were not included in MAID2000. They are weak as compared to the  $P_{33}(1232)$ ,  $D_{13}(1520)$  and  $F_{15}(1680)$ , which dominate the first, second, and third resonance region. The database for the reaction  $(n,p \pi^-)$  is much smaller and contains no recent data. On the other hand due to isospin symmetry only the resonances with  $I = 1/2$  for the neutron have to be determined.

For pion–electroproduction a  $Q^2$ –dependence of the helicity amplitudes and the photon couplings is required. In general the magnitude of the resonance peaks decreases with increasing  $Q^2$ . This can be interpreted as a form factor effect in analogy to the form factors of the nucleons probed in quasi–elastic scattering. In MAID2000 the  $Q^2$  dependence of the magnetic multipole photon coupling for the  $\Delta$ –resonance is fitted to data of the magnetic form factor of the  $\Delta$ . The same  $Q^2$  behavior is assumed for the electric and longitudinal photon coupling of the same resonance. The  $Q^2$ –dependence of the Roper resonance  $P_{11}(1440)$  is taken from [105] assuming it is a hybrid state with explicit gluonic degrees of freedom. For the second and third resonances the  $Q^2$ –dependence is parameterized in terms of the electric and magnetic quark multipoles. Neutron and proton amplitudes are treated in the same way.

In MAID2003 the three helicity amplitudes are parameterized as

$$A(Q^2) = A(0) \frac{1 + c_1 Q^2}{(1 + c_2 Q^2)^n} \quad (8.22)$$

with  $n \geq 2$ . Whereas  $A(0)$  is the helicity amplitude taken from photoproduction data, the parameters  $c_1$  and  $c_2$  are obtained from a fit to electro-

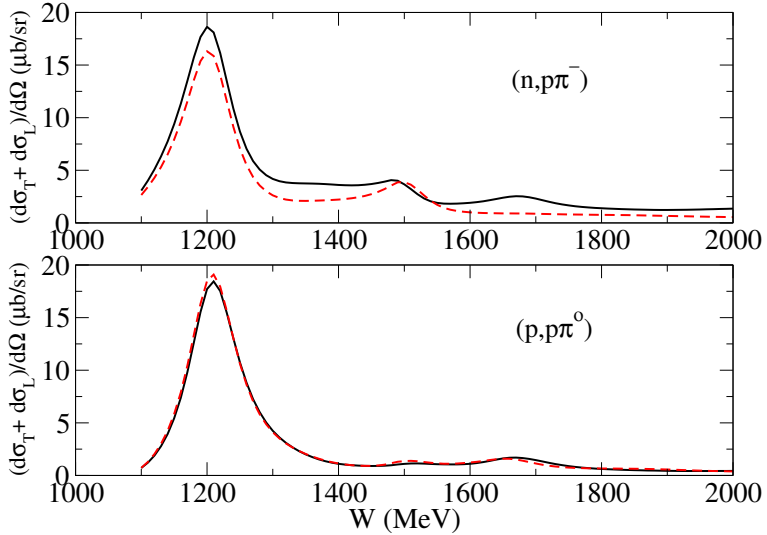


Figure 8.37: Comparison of the cross section  $(d\sigma_T + d\sigma_L)/d\Omega^*$  from MAID2000 (black solid line) and MAID2003 (red dashed line) for  $Q^2 = 0.3$   $(\text{GeV}/c)^2$  and a pion angle of  $\theta_{cm} = 150^\circ$  as a function of  $W$  for  $(n,p\pi^-)$  (upper picture) and  $(p,p\pi^0)$ . The three resonance regions can be distinguished.

production data. For the channel  $(p,p\pi^0)$  sufficient data are available, so that the  $Q^2$  dependence of the helicity amplitudes for the four resonances  $P_{11}(1440)$ ,  $D_{13}(1520)$ ,  $S_{11}(1535)$  and  $F_{15}(1680)$  plus the  $\Delta$ -resonance can be determined with sufficient accuracy; however the model uncertainty for  $S_{1/2}$  could be as large as 50 % for  $D_{13}(1520)$  and  $F_{15}(1680)$ . For the remaining, weaker resonances precise data are missing and the uncertainties are even larger. For the reaction  $(n,p\pi^-)$  the situation is worse. This is a problem in particular, because this channel dominates the reaction  $(p,p\pi^0)$  above the  $\Delta$  resonance in the present experiment as can be seen from Fig. 8.37.

The cross section  $(d\sigma_T + d\sigma_L)/d\Omega^*$  obtained from MAID2000 (black solid line) and MAID2003 (red dashed line) is shown in Fig. 8.37 for  $Q^2 = 0.3$   $(\text{GeV}/c)^2$  and pion angle  $\theta_{cm} = 150^\circ$  for both reaction channels. Because  $\epsilon$  is close to one in this experiment, the transversal and longitudinal part of the cross section is summed, but the longitudinal part is negligible at backward pion angles. The contributions of the mixed terms are also small. Whereas for the reaction  $(p,p\pi^0)$  no significant difference is observed, large deviations in the cross section for the second and third resonance region occur. In general the new fit MAID2003 describes the experimental data better, but no data are available in or around the kinematical region shown in Fig. 8.37. The largest

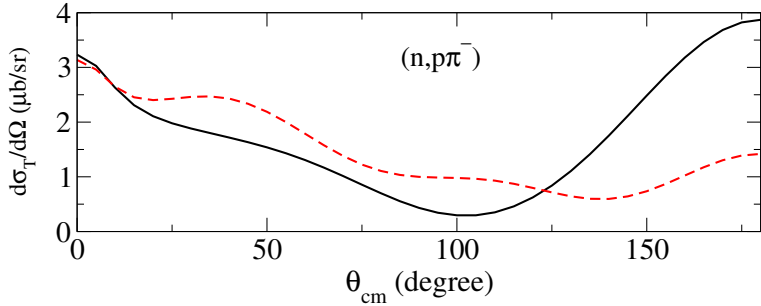


Figure 8.38: Comparison of the transverse cross section  $d\sigma_T/d\Omega$  from MAID2000 (black solid line) and MAID2003 (red dashed line) for  $Q^2 = 0.3$  (GeV/c) $^2$  and  $W = 1670$  MeV as a function of  $\theta_{cm}$  for  $(n,p \pi^-)$ . The longitudinal cross section is negligible at large pion angles.

pion angle in the database for  $(n,p \pi^-)$  is  $\theta_{cm} = 120^\circ$  for photoproduction and  $84^\circ$  for electroproduction [170]. For the kinematics shown in Fig. 8.37 the cross section from MAID2003 is much smaller around the Roper resonance and the third resonance region is missing for  $(n,p \pi^-)$  but not for  $(p,p\pi^0)$ . In Fig. 8.38 the cross section is shown for  $W = 1670$  MeV as a function of  $\theta_{cm}$ . Clearly the largest difference between the two models occurs at angles larger than  $120^\circ$ , where no constraints from data exist. Unfortunately this is the region the present experiment is most sensitive to.

### 8.7.3 Comparison to experimental data

Initially we hoped that a simulation of the resonance region would allow a determination of the spectral function at very high missing energy. Due to the ambiguities in the kinematics mentioned above as well as the uncertainty in the model itself this turned out to be unrealistic. Simulation of the resonance contribution can however, be used to determine where the spectral function can be extracted without being affected by the resonance region. For this the experimental spectral function shown in Fig. 8.8 was extrapolated into the region of  $E_m > 150$  MeV using a shape similar to the spectral function of Benhar at large  $E_m$  (Fig. 8.11). This modified spectral function was used in the Monte Carlo simulation. It turns out that more than half of the strength in the tail underlying the resonance region comes from bremsstrahlung. The total simulated strength under the resonance region amounts to around 20 % as can be seen in the  $E_m$ -spectra shown in Fig. 8.39 for the parallel kinematics. Therefore the uncertainties from extrapolating the spectral function become less important. In Fig. 8.39 the red curve represents the simulated

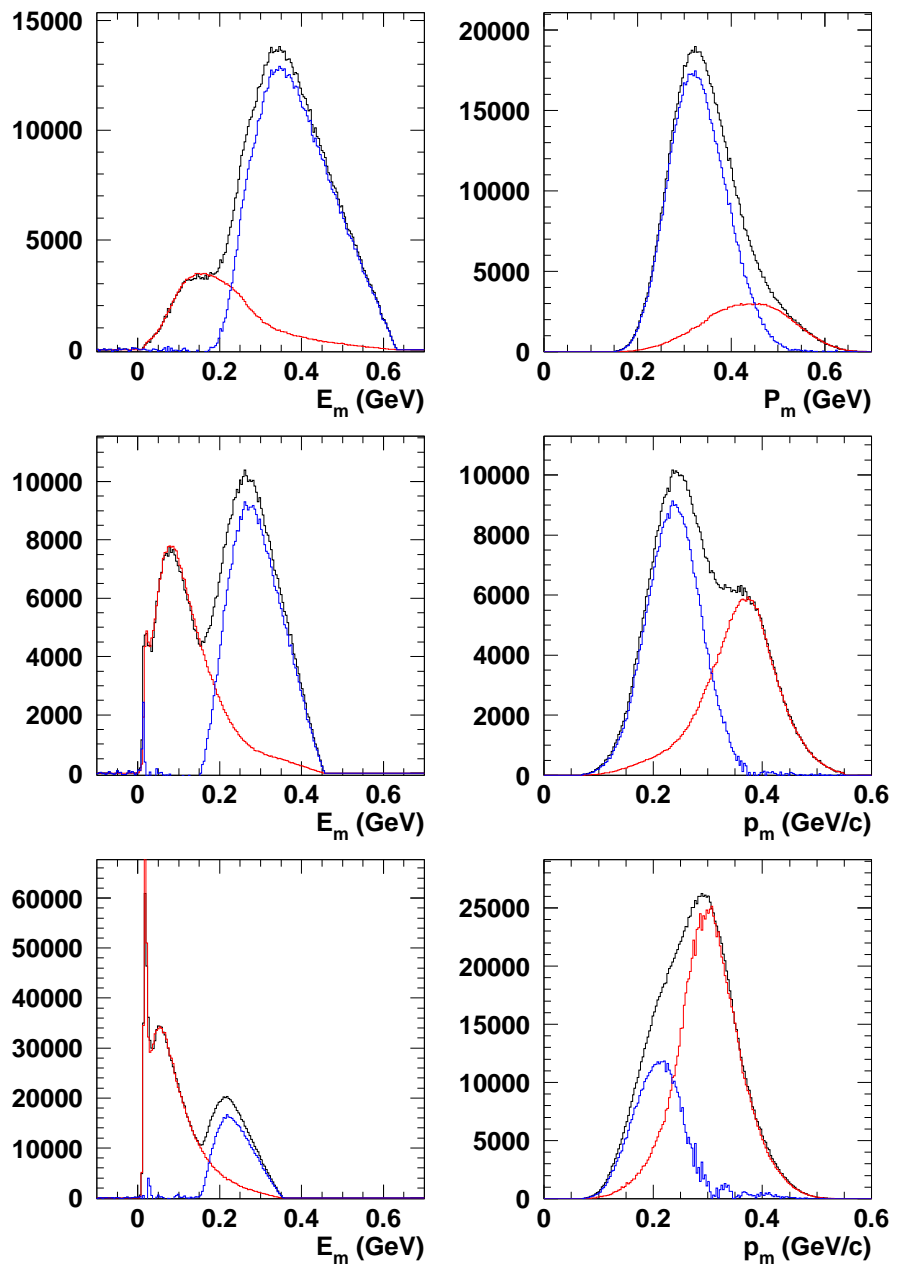


Figure 8.39:  $E_m$ - and  $p_m$ -spectra for the three parallel kinematics kin3 to kin5 from top to bottom. The data (black) are shown together with the simulated spectra using the extrapolated spectral function (red). The difference between the spectra is assumed to be a good approximation for the resonance region (blue).

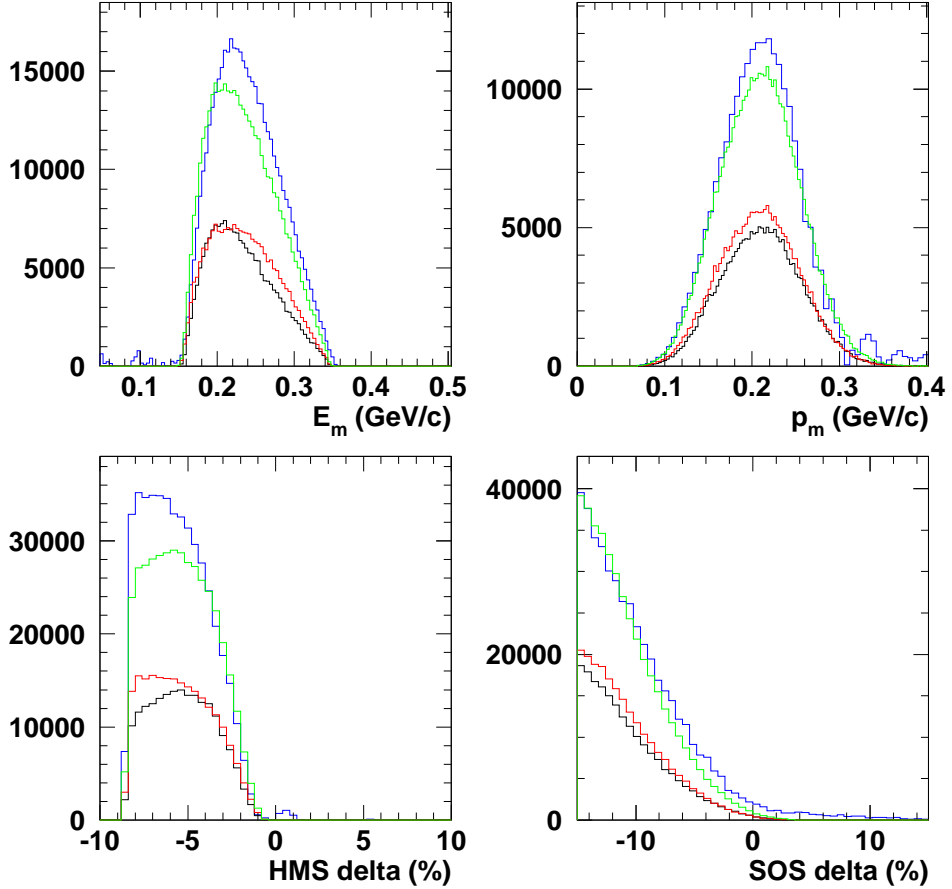


Figure 8.40: Simulation of the resonance region for kinematics kin5 using model MAID2000. The contributions from the processes  $(p,p\pi^0)$  (black) and  $(n,p\pi^-)$  (red) are summed (green). The blue curve shows the resonance region from Fig. 8.39. All spectra refer to scattering on  $^{12}\text{C}$ .

spectrum using the extrapolated spectral function. Its difference to the data in black is attributed to pion electroproduction. It is this region, which will be simulated using the formalism in sec. 8.7.1 and the cross section from the MAID models.

In Fig. 8.40 the simulation of the resonance region is shown in terms of the  $p_m$ -,  $E_m$ -spectra as well as for the distribution of the electron and proton momenta. As already mentioned two reactions have to be simulated and then summed up. The contributions from the reactions  $(p,p\pi^0)$  and  $(n,p\pi^-)$  are shown in black and red, respectively. The sum is indicated in green and compared to the resonance region in blue, which was extracted from the data

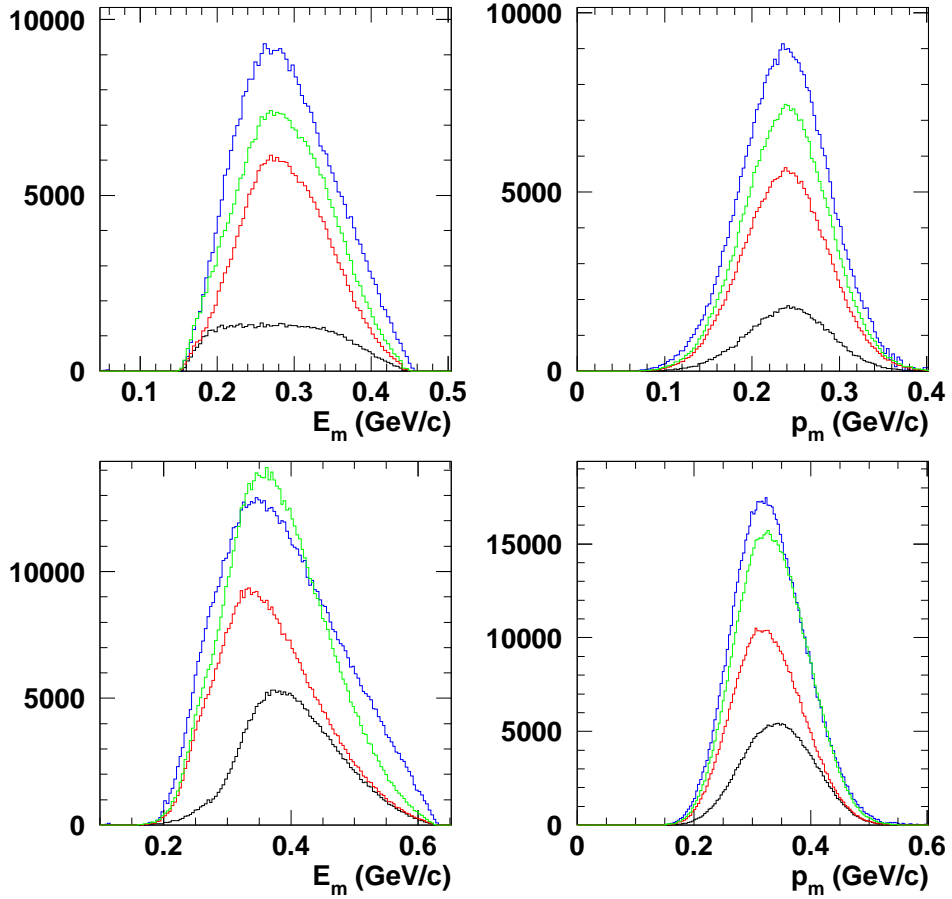


Figure 8.41: Similar to Fig. 8.40 but for kin4 (upper part) and kin3 (lower part).

as described above. The results in Fig. 8.40 refer to kinematics kin5 and  $^{12}\text{C}$ . For this simulation the model MAID2000 and the energy definition  $E_N(2)$  in Eq. 8.12 were used. With these ingredients  $\approx 90\%$  of the resonance region can be explained, which covers an invariant mass  $W$  between 1.1 and 1.5 GeV. Using MAID2003 leads to a similar result, but only 80 % of the strength is obtained. This comes mainly from a reduction of the cross section in  $(n, p\pi^-)$  compared to MAID2000. Using the energy definition  $E_N(1)$  instead of  $E_N(2)$  leads effectively to an increase in the invariant mass  $W$  of about 40 MeV. Because the present kinematics kin5 receives a significant contribution from the high energy tail of the  $\Delta$ -resonance, the yield in the simulation decreases by a factor two. This disagrees with the data and therefore it is taken as an indication that  $E_N(2)$  is the right energy definition to use. This is

supported by photoproduction experiments, where better agreement with the data was found using  $E_N(2)$  [102]. With an additional artificial shift of 30 MeV to lower  $W$  the Monte Carlo and experimental yield would be the same. Because the data obtained from a carbon target are not free from ambiguities and contributions of other reaction mechanisms, such a  $W$ -shift can not be justified. It is more likely that a broadening of the  $\Delta$ -resonance leads to more strength in the observed resonance region. In addition, a transparency factor of 0.6 was used for  $^{12}\text{C}$ , which, according to the discussion in sec. 7.2 and Tab. 8.1, has an estimated uncertainty of 10 %. The shape of the  $p_m$ -distribution is quite well described by the simulation whereas the simulated  $E_m$ -distribution is slightly tilted to smaller  $E_m$ . The momentum distributions of both the proton and the electron are reasonably well reproduced. This means that the kinematics of the dominant process in the resonance region agrees with the one used in the simulation. Two pion electroproduction should play a minor role, because it is only possible above 300 MeV missing energy.

In Fig. 8.41 the simulation of the resonance region is shown for kinematics kin4 and kin3. Here the same ingredients as in Fig. 8.40 are used. In kin4 78 % and kin3 91 % of the yield found in the resonance region is obtained with MAID2000. MAID2003 gives a yield of only 66 % and 68 %. This comes mainly from a significantly decreased cross section in the reaction ( $n, p\pi^-$ ) (Fig. 8.37 and Fig. 8.38). Because the MAID2003 fit is not constraint by data in the region needed for the present simulation no conclusion can be drawn. In addition, at higher  $W$  and  $E_m$  larger than 300 MeV the cross section for two pion production increases. The kinematics kin3 is the one most likely to be affected by two pion production. Because kin3 is dominated by the third resonance region, which is determined by  $F_{15}(1680)$ , also a broadening of the resonance might play a role. The shape of the  $E_m$ - and  $p_m$ -distribution of the resonance region in kin4 is well reproduced by the simulation, which is dominated by the second resonance region. Overall good agreement on the 20 % level is achieved between data and simulation.

It should be noted that the simulation using an Au target underestimates the data significantly compared to  $^{12}\text{C}$ . For kin5 only 62 % and for kin4 57 % of the data yield can be reproduced by the simulation using MAID2000. This deficit can probably be ascribed to the dominant contribution of rescattering at high  $E_m$ . This is obvious, if one compares the rescattering calculations for  $^{12}\text{C}$  and  $^{197}\text{Au}$  in parallel kinematics (Fig. 8.30 and 8.33). The lack of strength in the simulation would be even larger if the extrapolated tail of the spectral function would not already be increased to account partly for rescattering. Especially for moderate  $p_m$  large uncertainties are involved because the calculation of the rescattering contribution depends on the spectral

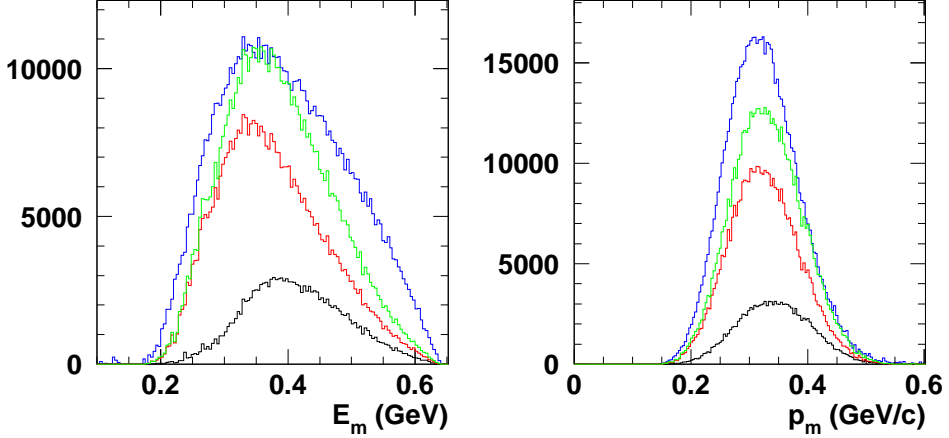


Figure 8.42: Similar to Fig. 8.41 but for kin3 and  $^{197}\text{Au}$ .

function in the single-particle region of  $^{197}\text{Au}$  (sec. 8.6.2). For larger  $p_m$  the rescattering contribution is better determined. Therefore a larger amount of the yield in the resonance region of kin3 (79 %) can be explained by the simulation as can be seen in Fig. 8.42. In addition, a broadening of the resonance in  $^{197}\text{Au}$  can be observed, if one compares the results for  $^{12}\text{C}$  in Fig. 8.41. It seems that in particular for large  $E_m$  the simulation lacks strength due to two-pion production.

#### 8.7.4 Separation of resonance and correlated region

The contribution of the resonance region can be reduced or even separated by cuts in the momentum distribution of electron and proton or in the  $p_m - \theta_{qpi}$  spectrum. The two methods exploit the fact that pion electroproduction appears at large missing energies and large missing momenta as well as large  $\theta_{qpi}$ . In Fig. 8.2 (green curve) the resonance region in kinematics kin3 was considerably reduced by cuts, which eliminate the low electron and proton momenta:  $-6\% < \text{ssdelta} < 15\%$  and  $-7\% < \text{hsdelta} < 10\%$ . The correlated region is less affected by these cuts. The cuts do not change the extracted spectral function, but limit the accessible  $E_m - p_m$ -region.

With a cut in the  $p_m - \theta_{qpi}$  plane as indicated in Fig. 8.43 by the black line, the resonance region can be separated from the correlated region. This is only possible for parallel kinematics, because in perpendicular kinematics the correlated region appears at the same angles  $\theta_{qpi}$  as the resonances. For kin3 the cut is applied at  $\theta_{qpi} = 240 \times |p_m| - 60$ . In Fig. 8.44 the yield in the correlated region left after the cut is shown in blue. The resonance region

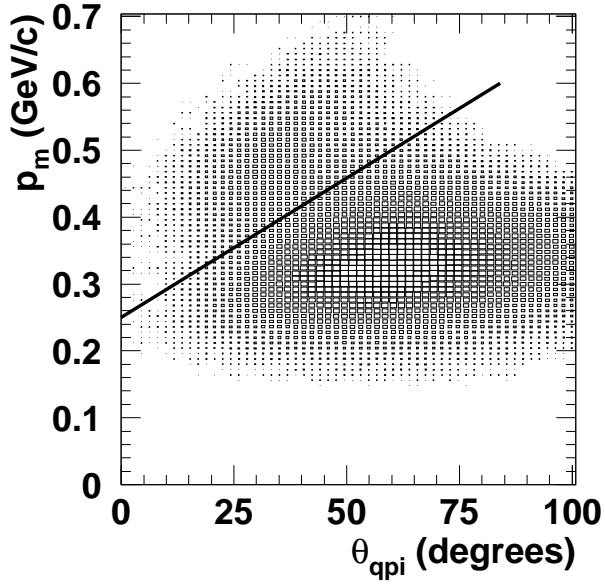


Figure 8.43: Cut indicated by the line in the  $p_m$ - $\theta_{qpi}$  plane to separate the resonance from the correlated region. Data are taken in kin3 for  $^{12}\text{C}$ .

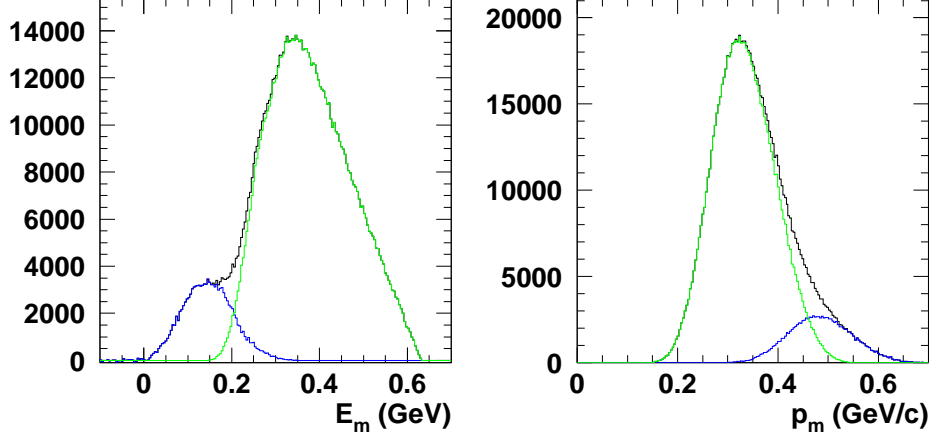


Figure 8.44:  $E_m$ - and  $p_m$ -spectra after applying the cut shown in Fig. 8.43. The spectra in green represent the difference between the data without (black) and with cut (red).

in green starts around the threshold for pion production at  $E_m \approx 150$  MeV. One should note that also the radiative tail as well as the correlated part of the spectral function at high missing energy is removed, which also appears

at large  $\theta_{qpi}$ . This can be best seen, when comparing Fig. 8.39 with Fig. 8.44. Therefore this cut can not be used for the quantitative analysis. It is useful for comparing the experimental spectra with a theory via Monte Carlo techniques if the theory does not include the resonance region.

## 9 Summary

In the '80s and '90s several experiments examined the single-particle region of many nuclei. Less protons were found at small  $E_m$  and  $p_m$  than predicted by the IPSM whereas the shape of the momentum distribution was in good agreement with the IPSM. The reason for the depletion of strength: the mean field theories neglect the repulsive part of the N–N potential, which is responsible for SRC. Due to SRC strength is shifted from small  $E_m$ ,  $p_m$  to large  $E_m$ ,  $p_m$ . This leads to the depletion of the single-particle region.

Modern many-body theories like the CBF and Green's function approach are able to treat the short-range part of the N–N potential. Their predictions agree with the reduced strength found in the single-particle region. Further, they point to the fact that a fraction of about 20 % of the protons should be found at large  $E_m$ ,  $p_m$ . In this context the experiment described in this work was proposed. The goal was to find the strength caused by SRC at large  $E_m$ ,  $p_m$  and to give insight into other reaction mechanisms, which contribute to the same region.

The high  $E_m$ – $p_m$ –region was probed via ( $e, e' p$ ) reaction for a series of nuclei using the continuous electron beam at Jlab in Hall C. The contribution of SRC is often obscured by contributions from other reaction mechanisms such as multi-step processes and isobar contributions from the resonance region. Therefore the experiment was performed in two perpendicular and three parallel kinematics. Parallel kinematics is much less affected by rescattering than perpendicular kinematics. Further, due to the transversal character of the  $\Delta$ –resonance a larger influence on the data obtained in perpendicular kinematics is expected. Because multi-step processes become more important with increasing mass number of the nucleus, different targets C, Al, Fe and Au were used.

For check-out of the setup and the analysis as well as for calibration purposes data in quasi-elastic kinematics were taken for hydrogen and carbon. As for the production runs the scattered electron was detected in the HMS and the knocked-out proton in the SOS. The elastic cross section measured

for  $Q^2$  between 0.6 and 2.2 ( $\text{GeV}/c$ )<sup>2</sup> is in good agreement with the world data set. The nuclear transparency for  $^{12}\text{C}$  is obtained from the data taken in the single-particle region for five  $Q^2$  points between 0.6 and 1.8 ( $\text{GeV}/c$ )<sup>2</sup>. The result is in good agreement with previous analyses using the same method; it also agrees with the transparency obtained from the correlated Glauber calculation, in particular for the three highest  $Q^2$  points where the Glauber theory is expected to be valid.

The spectral function was extracted from the data using the formalism of PWIA and is thus distorted by contributions from other reaction mechanisms. A reliable estimate of these contributions requires further theoretical input (s. below). Two methods were used to obtain the spectral function, the Phasespace- and Yield-Analysis. Both analyses use an iteration procedure to account for kinematics dependent processes such as radiative corrections. The two methods lead to the same result. The total systematic error of the spectral function is estimated to  $\approx 6\%$ , which was obtained after the examination of the stability of the result against the variation of several ingredients such as kinematical offsets and radiative corrections.

An unavoidable ambiguity occurs due to the choice of the off-shell e-p cross section. Different choices were tried out and their influence on the result studied. Here the version  $\sigma_{cc}$  is preferred, because best agreement for the spectral function obtained from the three different kinematics is obtained. In the cross section  $\sigma_{cc}$  one avoids to replace the energy of the proton by the on-shell value such as done by deForest. Further experiments in different kinematics would be helpful to give more insight into this long-standing problem, which becomes particularly important at large  $E_m$  and  $p_m$ .

The experimental distorted spectral functions were compared to the theoretical spectral functions from the CBF theory [22][21], the Green's function approach for finite nuclei [128] and the self-consistent Green's function for nuclear matter at finite temperature [69]. The following observations can be made:

- The difference between the spectral functions obtained in parallel and perpendicular kinematics increases with increasing  $E_m$  and  $p_m$ . At large  $E_m$  and  $p_m$  the data in perpendicular kinematics receive large contributions from multi-step processes and from the excitation to the  $\Delta$ -resonance.
- The maximum of the spectral function in parallel kinematics is shifted to lower  $E_m$  compared to the predictions of the CBF theory and Green's function approach. Surprisingly the self-consistent Green's function for nuclear matter seems to describe the data better.

- The momentum distribution, which was obtained by integrating the spectral function from 40 MeV to a variable cut-off, is approximately in agreement with the theories.
- The strength in the correlated part agrees with the theoretical one and accounts for  $\approx 0.6$  protons for  $^{12}\text{C}$  in the integration region chosen.
- The strength of the spectral function increases for  $^{197}\text{Au}$  by a factor of 1.7 compared to  $^{12}\text{C}$ .

The semi-classical approach used by Barbieri to calculate the contribution from rescattering confirms the expectation that the spectral function obtained in perpendicular kinematics is more affected by multi-step processes. The calculation can not explain the increase in the strength of the distorted spectral function from  $^{12}\text{C}$  to  $^{197}\text{Au}$ . It is expected that due to the asymmetry of protons and neutrons in heavy nuclei tensor correlations are responsible for part of the increase in strength. The large difference between the spectral function for parallel and perpendicular kinematics can not be explained entirely. Other reaction mechanisms like MEC and isobar configurations might play a role. This is not yet fully understood. It is hoped that an extended version of the code of Barbieri treating MEC will help to estimate the size of these effects in the kinematics used in the present experiment.

The resonance region is clearly visible in the data for  $E_m$  larger than 150 MeV and was simulated under the assumption of one-pion electroproduction. For this the unitary isobar model MAID was used. With MAID 2000 agreement on the 20 % level could be reached, although in nuclei other reaction mechanism and medium effects are expected to play a role.

# A The off-shell cross sections $\sigma_{cc1b}$ and $\sigma_{cc1c}$

In this section expressions for the off-shell cross sections  $\sigma_{cc1b}$  and  $\sigma_{cc1c}$  will be given. Both cross sections can be written in the form

$$\sigma = \frac{\sigma_{Mott}}{E_{on} p'} (v_m g_1 + v_e g_2), \quad (\text{A.1})$$

where  $\sigma_{Mott}$  is the Mott cross section and  $g_1$  ( $g_2$ ) are combination of the Dirac and Pauli form factors  $F_1$  and  $F_2$ . The factor  $g_1$  is equal to the square of the magnetic Sachs form factor and  $g_2$  to the structure function  $W_2$  using  $\bar{q}$ .

$$g_1 = (F_1 + \kappa F_2)^2 \quad (\text{A.2})$$

$$g_2 = F_1^2 - \frac{\bar{q}}{4M^2} \kappa^2 F_2^2, \quad (\text{A.3})$$

where  $\kappa$  is the anomalous magnetic momentum. The modified momentum transfer  $\bar{q}$  is calculated using  $\bar{\omega}$  defined in sec. 4.1.1. To write the expressions for  $v_M$  and  $v_e$  more clearly the following quantities are defined:

$$a = \frac{|\vec{q}|}{\omega} - \frac{\omega}{|\vec{q}|} \quad (\text{A.4})$$

$$b = \sqrt{\frac{Q^2}{|\vec{q}|^2} + \tan^2 \frac{\theta_e}{2}} \quad (\text{A.5})$$

$$c = 1 - \frac{\omega}{|\vec{q}|} \frac{\bar{\omega}}{|\vec{q}|} \quad (\text{A.6})$$

$$E_{in} = E_{on} - \frac{\bar{\omega}}{\bar{q}^2} (E_{on} \bar{\omega} - \vec{q} \cdot \vec{p}) \quad (\text{A.7})$$

Using  $E_{on}$ ,  $\bar{\omega}$ ,  $\bar{q}$  defined by deForest  $E_{in}$  corresponds to the sum of the energies of electron and nucleon in the initial state  $\bar{E} + E$ . For  $\sigma_{cc1b}$  one obtains [23]

$$v_m = -\frac{\bar{q}}{4} \left[ \frac{\bar{\omega}^2}{\bar{q}^2} a^2 + b^2 + \tan^2 \frac{\theta_e}{2} \right] \quad (\text{A.8})$$

$$v_e = \left[ \frac{\bar{\omega}}{|\vec{q}|} E_{in} a - b |\vec{p}'| \cos\phi \sin\gamma \right]^2 \quad (\text{A.9})$$

For  $\sigma_{cc1c}$  one has to use

$$v_m = -\frac{\bar{q}}{4} \left[ \left( \frac{\bar{\omega}^2}{\bar{q}^2} - 1 \right) c^2 + b^2 + \tan^2 \frac{\theta_e}{2} \right] \quad (\text{A.10})$$

$$v_e = \left[ E_{in} c - b |\vec{p}'| \cos\phi \sin\gamma \right]^2 \quad (\text{A.11})$$

Both cross sections contain already the kinematical factor  $E'_p |\vec{p}'|$ .

# Bibliography

- [1] D. Abbott et al., *Computer Applications in Nuclear, Particle and Plasma Physics*, Conf. Record of the 1995 IEEE 9th Real Time Conference, p. 147
- [2] D. Abbott et al., Phys. Rev. Lett. **80** (1998) 5072
- [3] P. Adderly et al., *Proceeding Mainz Parity Workshop*, 2002
- [4] A. Akmal, V.R. Pandharipande, and D.G. Ravenhall, Phys. Rev. C **58** (1998) 1804
- [5] U. Amaldi et al., Phys. Rev. Lett. **13** (1964) 341
- [6] C. Armstrong, Ph.D. thesis, College of William & Mary, Virginia, 1998
- [7] C. Armstrong, *Hall C Time of Flight Fitting Procedure*, CEBAF Hall C Internal Report, 1998
- [8] R.A. Arndt, I.I. Strakovsky, and R.L. Workman, Phys. Rev. C **56** (1997) 577
- [9] J. Arrington, *HMS/SOS Scintillator Timing Parameters*, CE-BAF Hall C Internal Report, 1994
- [10] J. Arrington, Ph.D. thesis, California Institute of Technology, 1998
- [11] J. Arrington, private communication
- [12] A. Aste, private communication
- [13] H. Baghaei et al., Phys. Rev. C **39** (1989) 177
- [14] O.K. Baker et al., Nucl. Instrum. Methods **A367** (1995) 92

- [15] M. Baldo (Editor), *Nuclear Methods and the Nuclear Equation of State*, Int. Rev. Nucl. Phys., Vol. 8, World Scientific, 1999
- [16] C. Barbieri and W.H. Dickhoff, Phys. Rev. C **68** (2003) 014311
- [17] C. Barbieri, *Proceedings 2nd Int. Conf. on Nucl. Part. Phys. with CEBAF*, Dubrovnik, 2003
- [18] C. Barbieri, *Proceedings 6th Workshop on e-m induced Two-Hadron Emission*, Pavia, 2003
- [19] M. van Batenburg, Ph.D. thesis, University of Utrecht, 2001
- [20] O. Benhar, A. Fabrocini, and S. Fantoni, Nucl. Phys. **A505** (1989) 267
- [21] O. Benhar, A. Fabrocini, and S. Fantoni, Phys. Rev. C **41** (1990) R24
- [22] O. Benhar, A. Fabrocini, S. Fantoni, and I. Sick, Nucl. Phys. **A579** (1994) 493
- [23] O. Benhar, private communication
- [24] O. Benhar, V.J. Pandharipande and S. Pieper, private communication
- [25] G. Bertsch et al., Phys. Rev. Lett. **47** (1981) 297
- [26] M. Berz, *COSY Infinity Reference Manual*, NSCL Technical Report MSUCL-977, Michigan State University, 1995
- [27] K.I. Blomquist et al., Phys. Lett. B **344** (1995) 85
- [28] K.I. Blomquist et al., Phys. Lett. B **421** (1998) 71
- [29] C. Bochna, *Unser Monitor Absolute Calibration*, CEBAF Hall C Internal Report, 1996
- [30] S. Boffi, C. Giusti, and F.D. Pacati, Nucl. Phys. **A336** (1980) 416
- [31] *Status Report on Activites in Hall A*, edited by E.J. Brash, R.D. Ransome, K. de Jager, 1999
- [32] J.F.J. van den Brand et al., Phys. Rev. D **52** (1995) 4868

- [33] R. Brockmann and R. Machleidt, in *Nuclear Methods and the Nuclear Equation of State*, edited by M. Baldo, Int. Rev. Nucl. Phys., Vol. 8, World Scientific, 1999, p. 121
- [34] S. Brodsky and G.F. de Teramond, Phys. Rev. Lett. **60** (1988) 1925
- [35] G.E. Brown and M. Rho, Nucl. Phys. **A372** (1981) 397
- [36] B.A. Brown, P.G. Hansen, B.M. Sherrill, and J.A. Tostevin, Phys. Rev. C **65** (2002) 061601(R)
- [37] J. Bunn (Contact person), *HBOOK Reference Manual*, CERN Program Library Long Writeups Y250, 1995
- [38] A.S. Carroll et al., Phys. Lett. B **80** (1979) 319
- [39] L. Cardman et al., *The Science Driving the 12 GeV Upgrade of CEBAF*, White Paper, 2001
- [40] J.M. Cavedon et al., Phys. Rev. Lett. **49** (1982) 978
- [41] G.F. Chew, M.L. Goldberger, F.E. Low, and Y. Nambu, Phys. Rev. **106** (1957) 1345
- [42] E. Christy, *Determining Kinematic Offsets From HMS Single Arm Elastics*, CEBAF Hall C Internal Report, 2001
- [43] H. Clement, P. Grabmayr, H. Röhm, and G.J. Wagner, Phys. Lett. B **183** (1987) 127
- [44] F. Coester, S. Cohen, B. Day, and C.M. Vincent, Phys. Rev. C **1** (1970) 769
- [45] O. Couet (contact person), *PAW (Physics Analysis Workstation)*, CERN Program Library Long Writeups Q121, 1995
- [46] W.J. Cummings, *SOS Handbook*, CEBAF Hall C Internal Report, 1996
- [47] J. Dechargé and D. Gogny, Phys. Rev. C **21** (1980) 1568
- [48] P. Demetriou, S. Boffi, C. Giusti and F.D. Pacati, Nucl. Phys. **A625** (1997) 513
- [49] Y. Dewulf et al., Phys. Rev. Lett. **90** (2003) 152501

- [50] W.H. Dickhoff, in *Nuclear Methods and the Nuclear Equation of State*, edited by M. Baldo, Int. Rev. Nucl. Phys., Vol. 8, World Scientific, 1999, p. 326
- [51] W.H. Dickhoff et al., Phys. Rev. C **60** (1999) 064319
- [52] A.E.L. Dieperink and I. Sick, Phys. Lett. B **109** (1982) 1
- [53] T.W. Donnelly and I. Sick, Phys. Rev. Mod. **56** (1984) 461
- [54] D. Drechsel and L. Tiator, J. Phys. G **18** (1999) 449
- [55] D. Drechsel, S.S. Kamalov, and L. Tiator, Nucl. Phys. **A645** (1999) 145
- [56] F. Duncan, J. Dunne, and S. Wood, *Hall C Cryogenic Target User Manual*, CEBAF Hall C Internal Report, 1999
- [57] J. Dunne, *Cryo and Dummy Target Information*, TJANF Memo, 1997
- [58] J. Dunne, *CMM results from tuna cans*, TJNAF Memo, 1999
- [59] D. Dutta, Ph.D. thesis, Northwestern University, 1999
- [60] R.A. Early, Nucl. Instrum. Methods **109** (1973) 93
- [61] K.Sh. Egiyan et al., Phys. Rev. C **68** (2003) 014313
- [62] R. Ent et al., Phys. Rev. C **64** (2001) 054610
- [63] *Experimental & Physics Industrial Control System (EPICS)*, Los Alamos National Laboratory, 1984
- [64] S. Fantoni and V.R. Pandharipande, Nucl. Phys. **A427** (1984) 473
- [65] T. de Forest, Nucl. Phys. **A392** (1983) 232
- [66] L.L. Frankfurt, M.I. Strikman, D.B. Day, and M. Sargsyan, Phys. Rev. C **48** (1993) 2451
- [67] L.L. Frankfurt, M.I. Strikman, and M. Zhalov, Phys. Lett. B **503** (2001) 73
- [68] T. Frick and H. Müther, Phys. Rev. C **68** (2003) 034310

- [69] Ph.D. thesis, University of Tübingen, 2004
- [70] J. Friedrich, Nucl. Instrum. Methods **129** (1975) 505
- [71] B. Frois et al., Phys. Rev. Lett. **38** (1977) 152
- [72] S. Frullani and J. Mougey, Adv. Nucl. Phys. **14** (1984) 1
- [73] Kh. Gad and H. Müther, Phys. Rev. C **66** (2002) 044301
- [74] K. Garrow et al., Phys. Rev. C **64** (2001) 064602
- [75] K. Garrow et al., Phys. Rev. C **66** (2002) 044613
- [76] H. Gao et al., Phys. Rev. Lett. **84** (2000) 3265
- [77] O. Gayou et al., Phys. Rev. Lett. **88** (2002) 092301
- [78] D. Geesaman, *Tracking in the SOS spectrometer*, CEBAF Hall C Internal Report, 1993
- [79] C. Giusti and F.D. Pacati, Nucl. Phys. **A473** (1987) 397
- [80] J.M. LeGoff et al., Phys. Rev. C **50** (1994) 2278
- [81] P. Grabmayr, Habilitationsschrift, University of Tübingen, 1991
- [82] P. Grabmayr, Prog. Part. Nucl. Phys. **29** (1992) 251
- [83] P. Gueye, M. Tiefenbacher, and C. Yan, *Hall C beam energy measurement*, CEBAF Hall C Internal Report, 1996
- [84] P. Gueye, Th. Mack, and C. Yan, *Hall C Superharp Operation Manual*, CEBAF Hall C Internal Report, 2001
- [85] P. Gueye et al., Phys. Rev. C **60** (1999) 044308
- [86] H.-W. Hammer, U.-G. Meißner, and D. Drechsel, Phys. Lett. B **385** (1996) 343
- [87] L.N. Hand, Phys. Rev. **129** (1963) 1834
- [88] L. Isaksson et al., Phys. Rev. Lett. **83** (1999) 3146
- [89] M. Jaminon and C. Mahaux, Phys. Rev. C **40** (1989) 354
- [90] S. Janssen, J. Ryckebusch, W.V. Nespen, and D. Debruyne, Nucl. Phys. **A672** (2000) 285

- [91] E. Jastrzembski, D.R. Quarrie, and W.A Watson, *Nucl. Sci. Symposium and Med. Imaging Conf.*, Conf. Record of the 1991 IEEE, vol. 1, p. 569
- [92] Y. Jin, H.P. Blok, and L. Lapikas, Phys. Rev. C **48** (1993) R964
- [93] Y. Jin, D.S. Onley, and L.E. Wright, Phys. Rev. C **45** (1992) 1311
- [94] S.S. Kamalov and S.N. Yang , Phys. Rev. Lett. **83** (1999) 4494
- [95] S.S. Kamalov et al., Phys. Rev. C **64** (2001) 032201
- [96] J.J. Kelly, Phys. Rev. C **54** (1996) 2547
- [97] D. Knödler and H. Müther, Phys. Rev. C **63** (2001) 044602
- [98] G. Krafft and A. Hofler, *How the Linac Beam Position Monitors Work*, CEBAF-TN-93-004, 1993
- [99] G.J. Kramer et al., Nucl. Phys. **A477** (1988) 55
- [100] G.J. Kramer, Ph. D. thesis, Vrije Universiteit te Amsterdam, 1990
- [101] G.J. Kramer, H.P. Blok, and L. Lapikas, Nucl. Phys. **A679** (2001) 267
- [102] B. Krusche, private communication
- [103] L. Lapikas, J. Wesseling, and R.B. Wiringa, Phys. Rev. Lett. **82** (1999) 4404
- [104] L. Lapikas et al., Phys. Rev. C **61** (2000) 064325
- [105] Z. Li, V. Burkert, and Z. Li, Phys. Rev. D **46** (1992) 70
- [106] N. Liyanage et al., Phys. Rev. Lett. **86** (2001) 5670
- [107] R.W. Lourie et al., Phys. Rev. Lett. **56** (1986) 2364
- [108] R.W. Lourie, W. Bertozzi, J. Morrison and L.B. Weinstein, Phys. Rev. C **47** (1993) R444
- [109] W.R. Leo, *Techniques for Nuclear and Particle Physics Experiments*, Springer, 1994

- [110] D. Mack and J. Volmer, *Solid target measurement for Hall C*, CEBAF Hall C Internal Report, 1997
- [111] D. Mack, private communication
- [112] C. Mahaux and H. Ngô, Nucl. Phys. **A431** (1984) 486
- [113] <http://www.kph.uni-mainz.de/MAID/maid2003/maid2003.html>
- [114] N. Makins, Ph.D. thesis, Massachusetts Institute of Technology, 1994
- [115] C. Marchand et al., Phys. Rev. Lett. **60** (1988) 1703
- [116] Y. Mardor et al., Phys. Lett. B **437** (1998) 257
- [117] L.C. Maximon, Phys. Rev. C **62** (2000) 054320
- [118] P. Mergell, U.-G. Meißner, and D. Drechsel, Nucl. Phys. **A592** (1996) 367
- [119] H. Mkrtchyan, *Fitting procedure for the calibration of the lead-glass*, private communication, 1999
- [120] L.M. Mo and Y.-S. Tsai, Rev. Mod. Phys. **41** (1969) 205
- [121] J.H. Morrison, Ph.D. thesis, Massachusetts Institute of Technology, 1993
- [122] J.H. Morrison et al., Phys. Rev. C **59** (1999) 221
- [123] H. Morita, C. Ciofi degli Atti, and D. Treleani, Phys. Rev. C **60** (1999) 034603
- [124] S. Moszkowski, Phys. Rev. **129** (1963) 1901
- [125] J. Mougey et al., Nucl. Phys. **A262** (1976) 461
- [126] J. Mougey, Ph.D. thesis, University of Paris-Sud, 1976
- [127] H. Müther, R. Machleidt, and R. Brockmann, Phys. Rev. C **42** (1990) 1981
- [128] H. Müther, G. Knehr, and A. Polls, Phys. Rev. C **52** (1995) 2955
- [129] H. Müther, in *Nuclear Methods and the Nuclear Equation of State*, edited by M. Baldo, Int. Rev. Nucl. Phys., Vol. 8, World Scientific, 1999, p. 170

- [130] H. Múther and A. Polls, Prog. Part. Nucl. Phys. **45** (2000) 243
- [131] K. Nakamura et al., Nucl. Phys. **A271** (1976) 221
- [132] H.W.L. Naus, S.J. Pollock, J.H. Koch, and U. Oelfke, Nucl. Phys. **A509** (1990) 717
- [133] T.G. O'Neill, Ph.D. thesis, California Institute of Technology, 1994
- [134] T.G. O'Neill et al., Phys. Lett. B **351** (1995) 87
- [135] G. Niculescu, *Resonant Cavities Used as Beam Current Monitors*, CEBAF Hall C Internal Report, 1996
- [136] G. Niculescu, Ph.D. thesis, Hampton University, 1998
- [137] N.N. Nikolaev et al., Nucl. Phys. **A582** (1995) 665
- [138] R.A. Niyazov et al., Phys. Rev. Lett. **92** (2004) 052303
- [139] K. Normand, private communication
- [140] J.T. O'Brien et al., Phys. Rev. C **9** (1974) 1418
- [141] G. Orlandini and L. Sarra, *Proceedings 2nd Workshop on e-m induced Two-Hadron Emission*, Gent, 1995, p. 1
- [142] V.R. Pandharipande, C.N. Papanicolas, and J. Wambach, Phys. Rev. Lett. **53** (1984) 1133
- [143] V.R. Pandharipande and S.C. Pieper, Phys. Rev. C **45** (1992) 791
- [144] V.R. Pandharipande, I. Sick, and P.K.A. deWitt Huberts, Rev. Mod. Phys. **69** (1997) 981
- [145] Particle Data Group, Phys. Rev. D **54** (1996) 1;  
K. Hagiwara et al, Phys. Rev. D 66 (2002) 010001
- [146] F. Perey and B. Buck, Nucl. Phys. **32** (1962) 353;  
F. Perey, Clementel, Villi (Editor), *Direct Interaction and Nuclear Reaction Mechanism*, Gordon & Breach, N.Y., 1963
- [147] S.K. Platchkov et al., Phys. Rev. C **25** (1982) 2318

- [148] S. Pollock, H.W.L. Naus, and J.H. Koch, Phys. Rev. C **53** (1996) 2304
- [149] D.H. Potterveld, Ph.D. thesis, California Institute of Technology, 1988
- [150] E.N.M Quint et al., Phys. Rev. Lett. **58** (1987) 1088
- [151] E.N.M Quint, Ph.D. thesis, Vrije Universiteit te Amsterdam, 1988
- [152] M. Radici, W.H. Dickhoff, and E.R. Stoddard, Phys. Rev. C **66** (2002) 014613
- [153] M. Radici, A. Meucci, and W.H. Dickhoff, Eur. Phys. J. A **17** (2003) 65
- [154] B. Reitz, Proc. of the International workshop on "Probing nucleons and nuclei via the (e,e'p) Reaction", Grenoble, France, 2003
- [155] P.U. Renberg et al., Nucl. Phys. **A183** (1972) 81
- [156] J. Ryckebusch, Phys. Lett. B **383** (1996) 1
- [157] J. Ryckebusch et al., Nucl. Phys. **A728** (2003) 226
- [158] M. Schwamb, S. Boffi, C. Giusti, and F.D. Pacati, Eur. Phys. J. A **17** (2003) 7
- [159] M. Seely, private communication
- [160] B.D. Serot and J.D. Walecka, Adv. Nucl. Phys. **16** (1994) 1
- [161] I. Sick et al., Phys. Rev. Lett. **35** (1975) 910
- [162] I. Sick and P.K.A. deWitt Huberts, Comments Nucl. Part. Phys. **20** (1991) 177
- [163] I. Sick et al., Jlab-Proposal E97-006, 1997
- [164] H.Q. Song, M. Baldo, G. Giansiracusa, and U. Lombardo, Phys. Rev. Lett. **81** (1998) 1584
- [165] G. van der Steenhoven et al., Phys. Rev. C **32** (1985) 1787

- [166] G. van der Steenhoven et al., Nucl. Phys. **A480** (1988) 547;  
G. van der Steenhoven, Ph.D. thesis, Vrije Universiteit te Amsterdam, 1987
- [167] T. Takaki, Phys. Rev. Lett. **62** (1989) 395
- [168] A. Tang et al., Phys. Rev. Lett. **90** (2003) 042301
- [169] L. Tiator et al., nucl-th/0310041, *Proceedings ICTP 4th Int. Conf. on Perspectives in Hadronic Physics*, Trieste, Italy, 2003
- [170] L. Tiator, private communication
- [171] R.K. Tripathi, J.W. Wilson, and F.A. Cucinotta, Nucl. Instrum. Methods **B145** (1998) 277
- [172] Y.-S. Tsai, Rev. Mod. Phys. **46** (1974) 815
- [173] Y.-S. Tsai, *Radiative Corrections to Electron Scattering*, SLAC Report No. SLAC-PUB-848, 1971
- [174] J.M. Udias et al., Phys. Rev. C **48** (1993) 2731
- [175] J.M. Udias et al., Phys. Rev. Lett. **83** (1999) 5451
- [176] P. Ulmer et al., Phys. Rev. Lett. **59** (1987) 2259
- [177] J. Volmer, Ph.D. thesis, Vrije Universiteit te Amsterdam, 2000
- [178] D.P. Watts, *Proceedings 4th Workshop on e-m induced Two-Hadron Emission*, Granada, 1999, p. 182
- [179] D.P. Watts et al., Phys. Lett. B **553** (2003) 25
- [180] P. Welsh, *Hall C Matrix Element Optimization Package (CMOP)*, CEBAF Hall C Internal Report, 1994
- [181] L.B. Weinstein et al., Phys. Rev. Lett. **64** (1990) 1646
- [182] L.B. Weinstein, private communication
- [183] F. Weissbach, to be published
- [184] D. van Westrum, *Measurement of Tracking Errors in the Regular and '4 of 6' Tracking Algorithm*, CEBAF Hall C Internal Report, 1996

- [185] D. van Westrum, *How to use the 'One Event Display'*, CEBAF Hall C Internal Report, 1996
- [186] D. van Westrum, Ph.D. thesis, University of Colorado, 1998
- [187] J. Wesseling et al., Phys. Rev. C **55** (1997) 2773
- [188] P.K.A. deWitt Huberts, J. Phys. G **16** (1990) 507
- [189] R. Wojcik and C. Yan, Nucl. Instrum. Methods **A484** (2002) 690
- [190] S.A. Wood, *Computer Applications in Nuclear, Particle and Plasma Physics*, Conf. Record of the 1993 IEEE 8th Real Time Conference
- [191] S.A. Wood et al., Jlab-Proposal E01-015, 2001
- [192] C. Yan et al., Nucl. Instrum. Methods **A365** (1995) 46
- [193] C. Yan et al., Nucl. Instrum. Methods **A365** (1995) 261
- [194] D.R. Yennie, S. Frautschi, and H. Suura, Ann. Phys. (N.Y.) **13** (1961) 379

## Acknowledgements

Finally I want to thank the many people who have contributed to this work. A large collaboration of the E97-006, whose experimentalists are named on the following page, has carried out the experiment. These people helped to prepare and run the experiment in summer 1999. In particular I want to mention Rolf Ent, Dave Mack, Marco Zeier and Beni Zihlmann, who spent time to discuss important questions, support me during the organization and preparation of the experiment and were always available to tackle problems.

After and during the analysis the theoretical support was important to understand and interpret the experimental results. Therefore I want to thank all the theoreticians who had a open ear for my problems. Here I want to mention in particular Omar Benhar, who already contributed to the experimental proposal, spent time to calculate the off-shell cross sections and provide me with the newest results for the nuclear transparency. With Carlo Barbieri I had many discussions and finally he contributed an important ingredient to the analysis, a reliable rescattering calculation. Then I want to thank W.H. Dickhoff, H. Müther and Tobias Frick for useful discussions and their theoretical spectral functions. Also I will not forget Andreas Aste, Kai Henken and Florian Weissbach, which took care of Coulomb corrections and radiative effects.

Further I will remember the people of the "Basel group" for discussions about everything. During the years many people joined and left the group. Therefore I will not try to name them all but mention only the ones in my closest vicinity, Giuseppe Testa and Adrian Honegger, who shared innumerable office hours with me as well as Jürg Jourdan.

I am indebted to Ingo Sick in all kind of aspects. It is due to him that I got the chance to complete this work. From the beginning he believed that I could take over the responsibility for this experiment. He was always open for discussions and full of new ideas, and I do not want to miss his valuable scientific advice. It was a pleasure to work with him.

This work is supported by the "Schweizerische Nationalfonds".

Finally I want to thank my parents for the continuous support and encouragement.

## **Experimental collaboration E97-006**

M. Hauger, A. Honegger, J. Jourdan, G. Kubon, D. Mocelj, K. Normand,  
Th. Petitjean, D. Rohe, I. Sick, F. Tiefenbacher, G. Warren  
**University of Basel, Switzerland**

C. Amstrong, R. Ent, H. Fenker, K. Garrow, A. Lung, D. Mack, J. Mitchell,  
B. Vulcan, S. Wood  
**TJANF, USA**

S. Bueltmann, D. Day, R. Lindgren, O. Rondon, M. Zeier, H. Zhu, B. Zihlmann  
**University of Virginia (UVA), USA**

R. Asaturyan, H. Mkrtchyan, S. Stepanian  
**Yerevan Physics Institute, Armenia**

K. Baker, A. Gasparian, P. Gueye, C. Keppel, E. Segbefia, L. Tang, L. Yuan  
**University of Hampton, USA**